LBNL-40406
UC-404

ERNEST ORLANDO LAWRENCE
BERKELEY NATIONAL LABORATORY

High Transition-Temperature SQUID Magnetometers and Practical Applications

Eugene Dantsker

Materials Sciences Division

May 1997

Ph.D. Thesis

For Reference

Not to be taken from this room

DISCLAIMER

This document was prepared as an account of work sponsored by the United States Government. While this document is believed to contain correct information, neither the United States Government nor any agency thereof, nor The Regents of the University of California, nor any of their employees, makes any warranty, express or implied, or assumes any legal responsibility for the accuracy, completeness, or usefulness of any information, apparatus, product, or process disclosed, or represents that its use would not infringe privately owned rights. Reference herein to any specific commercial product, process, or service by its trade name, trademark, manufacturer, or otherwise, does not necessarily constitute or imply its endorsement, recommendation, or favoring by the United States Government or any agency thereof, or The Regents of the University of California. The views and opinions of authors expressed herein do not necessarily state or reflect those of the United States Government or any agency thereof, or The Regents of the University of California.

Ernest Orlando Lawrence Berkeley National Laboratory
is an equal opportunity employer.

LBNL-40406

High Transition-Temperature SQUID Magnetometers and Practical Applications

by

Eugene Dantsker
(Ph.D. Thesis)

Department of Physics, University of California
and
Materials Sciences Division
Lawrenece Berkeley National Laboratory
University of California
Berkeley, CA 94720

May 1997

This work was supported by the Office of Basic Energy Sciences, Materials Sciences Division of the U.S. Department of Energy under contract number DE-AC03-76SF00098.

High Transition–Temperature SQUID Magnetometers and Practical Applications

by

Eugene Dantsker

B.S. (University of Maryland, College Park) 1991
M.A. (University of California at Berkeley) 1993

A dissertation submitted in partial satisfaction of the
requirements for the degree of
Doctor of Philosophy

in

Physics

in the

GRADUATE DIVISION
of the
UNIVERSITY of CALIFORNIA at BERKELEY

Committee in charge:

Professor John Clarke, Chair
Professor Theodore Van Duzer
Professor James C. Davis

1997

High Transition-Temperature SQUID Magnetometers and Practical Applications

Copyright © 1997

by

Eugene Dantsker

The U.S. Department of Energy has the right to use this document
for any purpose whatsoever including the right to reproduce
all or any part thereof

Abstract

High Transition–Temperature SQUID Magnetometers and Practical Applications

by

Eugene Dantsker
Doctor of Philosophy in Physics

University of California at Berkeley

Professor John Clarke, Chair

The design, fabrication and performance of SQUID magnetometers based on thin films of the high–transition temperature superconductor $YBa_2Cu_3O_{7-x}$ (YBCO) are described. Essential to achieving high magnetic field resolution at low frequencies is the elimination of 1/f flux noise due to thermally activated hopping of flux vortices between pinning sites in the superconducting films. Through improvements in processing, 1/f noise in single layer YBCO thin films and YBCO–$SrTiO_3$–YBCO trilayers was systematically reduced to allow fabrication of sensitive SQUID magnetometers. Both single–layer directly coupled SQUID magnetometers and multilayer magnetometers were fabricated, based on the dc SQUID with bicrystal grain boundary Josephson junctions. Multilayer magnetometers had a lower magnetic field noise for a given physical size due to greater effective sensing areas. A magnetometer consisting of a SQUID inductively coupled to the multiturn input coil of a flux transformer in a flip–chip arrangement had a field noise of 27 fT $Hz^{-1/2}$ at 1 Hz and 8.5 fT $Hz^{-1/2}$ at 1 kHz. A multiloop multilayer SQUID magnetometer had a field noise of 37 fT $Hz^{-1/2}$ at 1 Hz and 18 fT $Hz^{-1/2}$ at 1 kHz. A three–axis SQUID magnetometer for geophysical applications was constructed and operated in the field in the presence of 60 Hz and radiofrequency noise. Clinical quality magnetocardiograms were measured using multilayer SQUID magnetometers in a magnetically shielded room. The spectral density $S_\Phi(f)$ of the low frequency flux noise of SQUIDs with solid square washers scaled linearly with the cooling field B_0. By contrast, SQUIDs with narrow linewidths underwent no noise increase for cooling fields up to a threshold, that increased with decreasing linewidth. Similarly, SQUIDs whose washers are interpenetrated by an array of slots or holes so that the

remaining YBCO is in the form of narrow lines 4 μm wide exhibited no excess 1/f noise for cooling fields as high as 100 μT. Furthermore, the mutual inductance between these devices and a multiturn input coil was at least 85% of that for a solid SQUID with the same outer dimensions. Finally, a planar gradiometer is introduced, consisting of a directly coupled SQUID magnetometer inductively coupled to the smaller loop of an asymmetric, two–loop flux transformer. The baseline is 48 mm and the balance is about 1 part in 3000 with respect to fields perpendicular to the plane. The presence of the flux transformer reduces the field sensitivity of the magnetometer by only 5%.

Professor John Clarke
Dissertation Committee Chair

Contents

List of Figures vi

List of Tables x

I Introductory Material 1

1 Introduction 2
1.1 The dc SQUID 5
1.2 SQUID Operation and Readout 7
1.3 Flux Resolution and Noise 9
1.4 Designing a SQUID Magnetometer 11
1.5 High-T_c Implementation 13
1.5.1 SQUIDs at 77 K 13
1.5.2 High-T_c Technology 14

2 Equipment 18
2.1 Fabrication 18
2.1.1 Pulsed Laser Deposition System 18
2.1.2 Thermal Evaporation 20
2.1.3 Patterning 20
2.1.4 Ion Mill and Acid Etch 21
2.2 Measurement 22

II Fabrication 24

3 Single Layer YBCO Thin Films and Devices 27
3.1 A New Process for YBCO Thin Films 27
3.1.1 Choice of Substrate 27
3.1.2 Deposition Parameters 28
3.2 Bicrystal dc SQUIDs 29
3.3 Standard Fabrication of Bicrystal SQUIDs 32

4 Multilayer Devices **37**
4.1 Introduction . . . 37
4.1.1 Background . . . 37
4.1.2 Strategy . . . 39
4.2 *In situ* YBCO–STO–YBCO Trilayers . . . 41
4.3 Patterned YBCO–STO–YBCO Trilayers . . . 41
4.3.1 Edge Effects . . . 44
4.3.2 Surface Effects . . . 46
4.4 A New Multilayer Interconnect Process . . . 49

III SQUID Magnetometers **52**

5 Single Layer YBCO SQUID Magnetometers **53**
5.1 Design Considerations . . . 53
5.2 Early Directly Coupled Magnetometers . . . 57
5.3 Directly Coupled Magnetometers with Single Layer YBCO Flux Transformers 60
5.4 Recent Directly Coupled Magnetometers . . . 64

6 Flip–Chip Multiturn Magnetometers **67**
6.1 Design Considerations . . . 68
6.2 Coupling Issues . . . 68
6.3 Noise Measurements . . . 72
6.4 The Best Magnetometers . . . 74
6.5 Discussion . . . 78

7 Integrated Multiturn Magnetometers **80**
7.1 Devices . . . 80
7.2 Results . . . 82
7.3 Discussion . . . 84

8 Integrated Multiloop Magnetometers **87**
8.1 Design and Fabrication . . . 87
8.2 Measurement . . . 89
8.3 Discussion . . . 93

IV Applications **95**

9 High-T_c Three-Axis SQUID Magnetometer for Geophysical Applications **97**
9.1 Introduction: Magnetotellurics . . . 97
9.2 Construction . . . 98
9.2.1 Probe and Sensors . . . 98
9.2.2 Electronics . . . 100
9.2.3 Dewars and Shielding . . . 100
9.3 Performance . . . 101

9.4 Field Test 107
9.5 Discussion 107

10 Magnetocardiography in a Magnetically Shielded Room 109
10.1 Introduction 109
10.2 The Berlin Magnetically Shielded Room 110
10.3 Magnetometers, Electronics, and Noise 111
10.4 Magnetocardiograms 114

V SQUIDs in Magnetically Unshielded Environments 118

11 SQUIDs Cooled in Static Magnetic Fields 119
11.1 Introduction 119
11.2 Background 120
11.3 Measurement in Static Magnetic Fields 121
11.4 Large–Area Washer SQUIDs 123
11.5 Narrow Linewidth SQUIDs 126
11.6 Implications for Directly Coupled SQUID Magnetometers 131
11.7 Discussion 135

12 SQUIDs with Slots or Holes for Low Noise and Tight Coupling 137
12.1 Motivation 137
12.2 Design and Fabrication 138
12.3 Measurement 140
12.3.1 Noise 140
12.3.2 A_{eff} and Coupling 144
12.4 Implications for Flux Transformers 145
12.5 Discussion and Future Directions 145

13 A High-T_c Planar Gradiometer with an Asymmetric Flux Transformer 147
13.1 Introduction 147
13.2 Concept 148
13.3 Design and Fabrication 151
13.4 Results 152
13.5 Discussion 157

14 Conclusions and Future Directions 158

Bibliography 162

List of Figures

1.1 Magnetic field sensitivity levels required for different applications. The lengths of the lines represent the approximate frequency range of interest. 4
1.2 (a) Schematic representation of a dc SQUID. (b) Current–voltage characteristic. (c) Voltage–flux characteristic. 6
1.3 Flux–locked loop. 8
1.4 (a) Schematic representation of coupling a SQUID to a flux transformer. (b) A planar square washer SQUID. (c) A flux transformer with a multiturn input coil tightly coupled to a planar washer SQUID. 12
1.5 Top and cross–sectional views of components of an interconnect technology: (a) crossover, (b) via. 16

3.1 Scanning electron miscroscopy (SEM) image of a recent YBCO bicrystal SQUID. Dashed line indicates grain boundary. 31
3.2 Surface of a $SrTiO_3$ bicrystal near the edge after a HF etch through a photomask. The grain boundary is clearly visible in the etched region. 33

4.1 Magnetic field noise $S_B^{1/2}(f)$ and flux noise power $S_\Phi(f)$ vs frequency for a flux transformer, fabricated with the "early" process, coupled to a 40 pH bicrystal SQUID. Dashed line indicates flux noise power of the bare SQUID. 38
4.2 (a) Photograph showing the 16–turn input coil of a flux transformer. The coil, patterned in the lower YBCO layer is connected to the pickup loop (not shown). The (black) crossover is in the upper YBCO. (b) Close–up view of the via, connecting the crossover to the inner turn of the input coil. 40
4.3 Magnetic flux noise power $S_\Phi(f)$ vs frequency for an *in situ* YBCO–STO–YBCO trilayer. Dashed line indicates flux noise of bare SQUID. 42
4.4 Interconnect test structure for the YBCO–STO–YBCO trilayer process that allows independent measurements of the lower YBCO, the upper YBCO, crossover, and via. Drawing is simplified for clarity; actual structure contained two crossovers and two vias. 43
4.5 SEM image of (a) 300 nm–thick YBCO film etched in 0.05% HNO_3 with no Br etch and (b) 200 nm–thick YBCO film etched in 0.05% HNO_3 with a 10 second etch in 1% Br in methanol. 45

4.6 Magnetic field noise $S_B^{1/2}(f)$ and flux noise power $S_\Phi(f)$ vs frequency for a flux transformer with a 16–turn input coil coupled to a 40 pH bicrystal SQUID. Dashed line indicates flux noise power of the bare SQUID. Both were measured with bias reversal. 47
4.7 Atomic force microscopy (AFM) image of STO deposited on a YBCO film (a) without and (b) with an *in situ STO cap* layer 48

5.1 (a) Configuration of directly coupled magnetometer. (b) SEM image showing detail of coupling to the bicrystal SQUID. Dashed line indicates grain boundary. 55
5.2 Calculated magnetic field noise, $S_B^{1/2}$ in the thermal noise limit, vs inductance L for a directly coupled magnetometer with $I_0 = 50\,\mu A$ and R=2.0 Ω. 56
5.3 rms magnetic field noise, $S_B^{1/2}(f)$, and flux noise power, $S_\Phi(f)$, vs frequency for directly coupled magnetometer 4 measured with static current bias and bias reversal. 58
5.4 (a) $S_\Phi(f)$, vs frequency for three directly coupled magnetometers measured with bias reversal. Numbers refer to Table 5.1. (b) rms magnetic field noise, $S_B^{1/2}(f)$ vs frequency for the same devices. 59
5.5 The magnetic field noise $S_B^{1/2}$ vs frequency for a directly coupled magnetometer with (lower trace) and without (upper trace) a single–layer flux transformer shown inset. 61
5.6 (a) Configuration of a recent directly coupled magnetometer (not drawn to scale). (b) Photograph showing detail of coupling to the bicrystal SQUID. Dashed line indicates grain boundary. 65

6.1 A flux transformer. The linewidth of the pickup loop is 1 mm. The input coil (not drawn to scale) is 16 turns with a linewidth of 7 μm spaced 8 μm apart. The overall size of the input coil is about 500 × 500 μm^2. 69
6.2 Four types of dc SQUID. Dashed line indicates grain boundary. 70
6.3 Magnetic field noise $S_B^{1/2}(f)$ and flux noise power $S_\Phi(f)$ of flux transformer 3 coupled to type A/C SQUID shown inset. Dotted curve indicates $S_\Phi(f)$ of bare SQUID. 73
6.4 Magnetic field noise $S_B^{1/2}(f)$ of magnetometer with type A/C and A/A SQUIDs. Dashed line indicates $1/f^{1/2}$. 75
6.5 (a)Magnetic field noise $S_B^{1/2}(f)$ of magnetometer with type A/C and A/A SQUIDs (shown inset: dotted line indicates grain boundary.) Dashed line indicates $1/f^{1/2}$. (b)Coupling the multiturn input coil to a type A/A SQUID. The crossover, shown in light shading, covers about 90% of the slit. 77

7.1 Integrated magnetometers consisting of a flux transformer coupled to a (a) type B SQUID and (b) type C SQUID. The 16–turn input coils are in the upper YBCO films. 81
7.2 Flux noise power $S_\Phi(f)$ of small integrated magnetometer with a type A/A–80 SQUID. 83

7.3 A proposed approach for reducing the parasitic capacitance between the SQUID and the input coil. (a) Using a traditional washer SQUID, the overlap area between the input coil and SQUID is large leading to a high capacitance. (b) Placing the turns of the input coil into empty slots that interpenetrate the SQUID washer, to reduce the overlap area and the parasitic capacitance. Junctions are indicated by crosses. 85

8.1 Schematic layout of a multiloop magnetometer. For clarity, only four loops are drawn. Oppositely, shaded regions represent upper and lower YBCO films, and cross-shaded regions indicate contact between them. Junctions are indicated with crosses. 88
8.2 Photograph of multiloop magnetometer with 16 parallel loops on a 10×10 mm^2 STO bicrystal. 90
8.3 Magnetic field noise $S_B^{1/2}(f)$ obtained with bias reversal in a Conetic shield and in a YBCO tube. 92

9.1 (a) The three–axis magnetometer mount showing the there directly coupled SQUID magnetometers. (b) The entire magnetometer probe. 99
9.2 rms magnetic field noise, $S_B^{1/2}(f)$, and flux noise power, $S_\Phi(f)$, vs frequency for the x–channel SQUID magnetometer operated with bias reversal. 102
9.3 (a) Maximum amplitude of the sinusoidal flux Φ^{max} that can be applied to the x–channel SQUID without causing the feedback electronics to saturate or break the lock vs frequency. (b) Slew rate $\omega\Phi^{max}$ vs frequency for the x–channel. 104
9.4 Comparing static bias and bias reversal for the z–channel. (a) Φ^{max} vs frequency. (b) Slew rate $\omega\Phi^{max}$ vs frequency. 105
9.5 Measured frequency response of the z–channel SQUID operating in a flux–locked loop with static bias. The other two SQUID channels were operated with bias reversal. 106

10.1 The read–out SQUID electronics using additional positive feedback. (Courtesy Dietmar Drung.) 112
10.2 Voltage vs flux for the multiloop SQUID magnetometer operating with additional positive feedback. The scale is 0.25 Φ_0/div horizontal and 4 μV/div vertical. 113
10.3 Magnetic field sensitivity $S_B^{1/2}(f)$ vs frequency for the flip–chip magnetometer measured with APF using either a static bias or bias reversal in the BMSR. 115
10.4 Real–time traces of magnetocardiograms of two adult males measured using the flip–chip magnetometer inside the BMSR. The measurement bandwidth is 0.016–200 Hz. The two traces are offset for clarity. 116

11.1 Cross-sectional view of the wire-wound copper solenoid used to produce static magnetic fields perpendicular to the plane of the SQUID. 122
11.2 $S_\Phi(f)$ for the A/A SQUID (device 1) shown inset cooled in three magnetic fields 124

11.3 $S_\Phi^{1/2}$(1 Hz) for the SQUID shown inset cooled in a field of 24 μT: upper trace for D = 500 μm (device 5), lower trace after washer has been repatterned to width D = 30 μm indicated by dotted lines (device 5*). Inset is not to scale. Slit length is 100 μm. Dashed line indicates grain boundary. Spikes on traces are due to 60 Hz and its harmonics as well as other nearby electronic instruments and microphonic noise. 127
11.4 $S_\Phi^{1/2}$(1 Hz) vs cooling field B_0 for three narrow–linewidth SQUIDs. Geometry is shown in the inset. Dashed line indicates grain boundary. 129
11.5 $S_\Phi^{1/2}$(f) vs frequency for device 8 cooled in three magnetic fields. 130
11.6 $S_\Phi^{1/2}$(1 Hz) vs cooling field for device 9 with geometry shown in Figure 11.4. One other device showed similar behavior. 132
11.7 $S_\Phi^{1/2}$(1 Hz) vs cooling field for three directly coupled magnetometers with configuration shown in the inset. 133

12.1 Photographs of the photomasks for (a) a solid, thin–film SQUID, and for a SQUID penetrated by (b) 8 slots (c) 248 holes (d) 5 slots and (e) 125 holes. The outer dimensions of each device are 186 x 204 μm. (f) shows a 7–turn input coil that was coupled to the designs (a)–(c) in a flip–chip arrangement. 139
12.2 Flux noise $S_\Phi^{1/2}$(f) vs. frequency for (a) 8–slot SQUID (2) and (b) 248–hole SQUID (4) each cooled in four values of magnetic field. The spike at approximately 4.5 Hz was due to an external source of unknown origin. . . 141
12.3 Flux noise $S_\Phi^{1/2}$(1 Hz) vs. cooling field B_0 for the seven devices listed in Table 12.1 143

13.1 Asymmetric planar gradiometer consisting of a flux transformer and a directly coupled magnetometer. (a) Conceptual schematic showing key parameters. Note the coordinate axes. (b) Physical realization showing dimensions. The directly coupled magnetometer is shown in light shading. 149
13.2 (a) Signal from the flux–locked loop (FLL) for a uniform 100 Hz magnetic field applied perpendicular to the plane of the gradiometer vs. position x of the input loop relative to the magnetometer. Right–hand ordinate is balance factor. (b) Expanded view about the position of optimal balance 153
13.3 Output of the flux–locked loop for unshielded gradiometer unbalanced (upper trace) and at optimal balance (lower trace), showing reduction of the ambient noise. 155
13.4 Signal from the flux–locked loop for balanced gradiometer vs. the distance r of a wire carrying a 100 Hz current below the centerline of the gradiometer. 156

List of Tables

4.1 Deposition parameters for the new multilayer process. 50

5.1 Parameters for 4 directly coupled magnetometers. Critical current I_0 and resistance R are given per junction. 57
5.2 Parameters for the two magnetometers made from a directly coupled magnetometer coupled to a large area flux transformer. 63

6.1 Parameters for different flip–chip magnetometers using the same 16–turn flux transformer. 71
6.2 Coupling and noise data for five flip–chip magnetometers all made with the same type A/C SQUID. d is the input coil thickness. (U)/(L) refer to placement of input coil in upper/lower YBCO film. 72
6.3 Parameters for two flip–chip magnetometers made with the same 16–turn flux transformer coupled to a type A/C and a type A/A SQUID. 76

7.1 Parameters for different integrated magnetometers with multiturn flux transformers. 84

8.1 Parameters for multiloop magnetometers 1 and 2 at 77 K. For magnetometer 2, 2a refers to the Conetic shield, 2b to the YBCO shield. 89

11.1 Flux noise of six SQUIDs measured at 1 Hz for three values of magnetic field. D is the outer width of the SQUID washer, ℓ the length of the slit, and L the estimated inductance. 125
11.2 Parameters for seven narrow–linewidth SQUIDs. Critical current I_0 and resistance R are per junction. Devices 6–9 are bare SQUIDs. Devices 10–12 are directly coupled magnetometers. B_T is the threshold cooling field at which the noise at 1 Hz begins to increase. 128

12.1 Critical current I_0 and resistance R per junction for SQUIDs with configurations of Figure 12.1; A_{eff} is the effective area and M_i the mutual inductance to a 7–turn input coil. In the first column, letters in parentheses refer to Figure 12.1. 140

Acknowledgments

My foremost thanks go to Professor John Clarke for always focusing the efforts of this project on topics that were both interesting and important, maintaining a level of professional enthusiasm, and supplying great advise on both SQUIDs and the stock market.

I was introduced to the delicate art of high-T_c thin film fabrication by Jack Kingston and Rasmus Kromann. Upon their departure, our group was joined in rapid succession by David Nemeth, Dieter Koelle, and Frank Ludwig. Together with Andy Miklich, the five of us formed a team that I wish to acknowledge as a whole; for several years (and several hundred samples), we worked to develop a low noise multilayer technology for sensitive SQUID magnetometers. I would like to acknowledge David for his great skill and good humor that made work with him anything but boring. I would like to thank Andy and Dieter for teaching me SQUID characterization and noise measurement methods and for help in fitting the three–axis magnetometer into the dewar. Frank's fabrication skill and patience were responsible for our most sensitive SQUID magnetometers and his dry wit kept me alert.

I would like to thank Reinhold Kleiner for help with measurements and acknowledge his deep theoretical knowledge of superconductivity revealed to me over many discussions. I thank Per-Åke Nilsson for timely help with SQUID fabrication. I thank Saburo Tanaka for many noise measurements of SQUIDs cooled in magnetic fields. With great sadness, I acknowledge Oliver Froehlich for building the probe for the planar SQUID gradiometer and for help with initial measurements before his shocking death December 14, 1996. I would like to thank Saburo Tanaka, Konstantin Kouznetzov and Helene Grossman for additional help with the gradiometer.

I would like to thank Tom Lee for friendship over the last six years, a great collaboration on his scanning SQUID microscope, and many useful discussions on SQUIDs, electronics, and the job market. I thank Tim Shaw for great comradery and discussions on noise, vortices, and software. I thank Teressa Ho, Alex Rimberg, Cagliyan Kurdak, Dinh Ton, Beth Chan, Yann Chemla, and Greg Nichols for sharing lab space, equipment and expertise.

I was fortunate to benefit from numerous collaborations with many other groups and individuals. At Conductus, I would like to thank Ward Ruby and Kookrin Char for providing us with YBCO films on 50 mm substrates. I thank Joe Longo and Vlad Vinetskiy

for lending us prototype SQUID electronics for the three–axis magnetometer. I thank Mark Teepe and Luke Lee for depositing a YBCO film on a $SrTiO_3$ bicrystal when our equipment was down. I thank Z. Lu, Vlad Matijasevic and Kookrin Char for coevaporating a YBCO film on a 100 mm wafer that was used to pattern the flux transformer for the planar gradiometer. I would like to acknowlege Kookrin Char and Luke Lee for many beneficial discussions on device fabrication, and Andrei Matlashov - on electronics and design.

At the Phisikalisch-Technische Bundesanstalt Institut Berlin (PTB) I would like to thank Dietmar Drung, Silvia Knappe and Hans Koch for a fruitful collaboration on the multiloop magnetometer. I thank Silvia also for prividing us with SEM images of our films. I thank Dietmar for another excellent collaboration on magnetocardiography using our SQUIDs and his electronics, and for many late nights at the PTB during my visit there. I thank the entire staff of the Cryogenics and Biomagnetics groups at PTB for their hospitality during my visit in July, 1995 and for providing funding for that trip.

I thank Neil Alford and Tim Button of ICI Superconductors for several YBCO–coated YSZ tubes which I used as shields in noise measurements of our most sensitive devices. I thank Ruth Ellen Thomson at NIST, Boulder for AFM images of our multilayer structures; I thank Frank Ogletree at LBNL, Berkeley for subsequently teaching me to use an AFM. I would like to thank Professor John Clem for theoretical insight into our scheme for eliminating flux noise in field–cooled SQUIDs. I thank Michael Mück for usefull discussions on SQUID linearity and flux noise during his visit to our lab.

The photolithography portion of this work was carried out at the Berkeley Microfabrication Laboratory ("Microlab") of the Electrical Engineering and Computer Science Department at the University of California, Berkeley and I would like to acknowledge the help offered by its staff and fellow colleagues. In particular, I would like to thank Marilyn Kushner for making most of the masks and proving some invaluable advise on various processing aspects.

Back at the Physics Department, I would like to acknowledge the expertise of the Machine Shop staff who made many of the components that were used to carry out this work. In particular, I wish to thank George Weber for often helping me translate a concept into a mechanical part. I would also like to acknowledge the staff at the Electronics Shop, particularly John Davis and Levern Garner for helpful advice on circuit design and for teaching me to make printed circuit boards. I would like to also thank our building manager, Abram Hardin, for his expert handling of our day–to–day operations interrupted

by occasional crises. I thank Lynn Pelosi and Joseph Matia for operating purchasing and supply and for friendly chats.

I thank John Clarke's administrative assistant, Barbara Salisbury, for being a great liaison with lab administrative policy and for expertly producing all manuscripts.

I gratefully acknowledge financial support from a National Defense Science and Engineering Graduate Fellowship during my first three years at UC Berkeley. Funding was also provided by the Director, Office of Energy Research, Office of Basic Energy Sciences, Materials Sciences Division of the U.S. Department of Energy under contract number DE-AC03-76SF00098 and by the California Competitive Technology Program.

I owe a debt of gratitude to Dr. Chandra S. Pande for giving me my start in research at the Naval Research Laboratory nearly ten years ago.

Most of all I would like to thank my parents and my sister for years of unconditional love, encouragement and friendship.

Part I

Introductory Material

Chapter 1

Introduction

From a functional point of view, a Superconducting QUantum Interfererence Device (SQUID) is a detector of magnetic flux and a transducer of flux into voltage. As a sensor of flux, the SQUID surpasses the resolution of any other available sensor. This fact makes the SQUID an attractive device for a range of applications where one measures small physical quantities that can be readily converted into flux, for example, current, voltage, displacement, magnetic field and magnetic field gradient. As with any other sensor or amplifier, the functionality of a SQUID is limited by its intrinsic noise, by one's ability to efficiently couple a signal into it, and by one's ability to read out the response.

Since its invention in 1964[1], the SQUID has undergone extensive theoretical and experimental investigation both to understand its complex non-linear nature and to improve it for greater sensitivity and more functionality in various applications. These efforts led to extensive theoretical descriptions of the signal and noise theory of the SQUID in various frequency ranges, which in turn led to optimized, more useful devices, surpassing the sensitivity of competing voltmeters, low-noise amplifiers and magnetometers. The fact remains, however, that the SQUID has faced a share of problems in entering the mainstream of sensors and amplifiers. Perhaps the main impediment was the need to operate the SQUID at cryogenic temperatures, namely in liquid helium, whereas most conventional sensors and amplifiers operate at room temperature. The need for cryogenics has placed the SQUID into the hands of a limited research community, mainly low–temperature physicists. Over the years, improvements in SQUID technology allowed large numbers of sensitive, reproducible devices to be fabricated and become commercially available, for example, for multichannel array systems in biomagnetic sensors[2, 3, 4]. The applications, however, largely remained

limited to research at a relatively small number of institutions capable of supporting a cryogenic infrastructure.

In 1986, the community was shaken up by the discovery of superconductivity in the ceramic LaBaCuO by Bednorz and Müller[5], followed shortly after by the synthesis of $YBa_2Cu_3O_{7-x}$(YBCO)[6] with a transition temperature (T_c) of 92 K, above the boiling point of liquid nitrogen (77 K). While promises of levitating trains and lossless power cables circulated in the media, numerous researchers worldwide turned to fabricating thin films of the new high–transition temperature (high-T_c) superconductors intrigued by the possibility of SQUIDs and other superconducting electronics that can operate in liquid nitrogen. The result of the worldwide effort over the past 10 years has been an extraordinary amount of progress – from the early granular YBCO thin films to a complete high–quality multilayer technology based on the new materials.

This thesis represents a portion of that effort. I will describe the design, fabrication and performance of high-T_c SQUID magnetometers sufficiently practical to be used in applications. A magnetometer is perhaps one of the more obvious configurations of a SQUID; examples of applications of sensitive magnetometers include biomagnetic diagnostics – magnetocardiography and magnetoencephalography, geophysical surveying and prospecting techniques such as magnetotellurics, and non–destructive evaluation (NDE), for example, of subsurface cracks in airplane frames. All of these applications have already been demonstrated with low-T_c SQUID magnetometers with the sensor cooled in liquid helium. The term "practical" carries several underlying requirements. In the very least, the SQUID magnetometer must be sensitive enough to detect the signal being measured, which places an upper limit on its noise. The SQUID must also be able to operate under conditions that are commensurate with the application, for example, in a magnetically–noisy hospital, an airplane hangar or just in the magnetic field of the Earth. In some applications, biomagnetics, for example, one wishes to have an array of as many as 256 closely–spaced magnetometers suspended above the patient's heart or surrounding the head. In that case, small sensor size becomes an important requirement.

Figure 1.1 shows schematically the required magnetic sensitivity levels and frequency ranges for the applications listed above. The advantage of a SQUID–based magnetometer over competing magnetic sensors such as induction coils, Hall probes and flux–gates lies in its unique combination of extremely high sensitivity, broad bandwidth (up to 10's of GHz) and small size. The emergence of high-T_c SQUID magnetometers removes the ne-

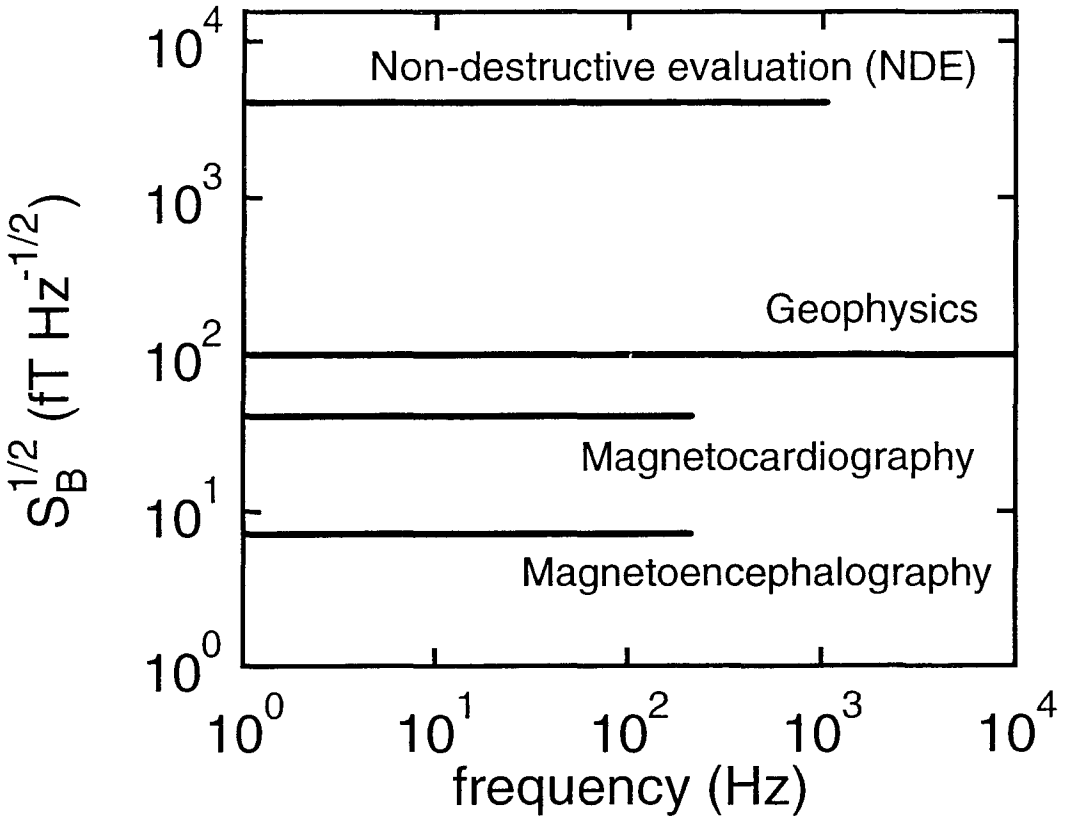

Figure 1.1: Magnetic field sensitivity levels required for different applications. The lengths of the lines represent the approximate frequency range of interest.

cessity for liquid helium, substituting it with liquid nitrogen which is less expensive, easier to handle and store, and evaporates much more slowly. The objective of this project was, therefore, to develop a technology for high-T_c SQUID magnetometers that could compete with their low-T_c counterparts. It will become clear that this was not a straightforward task. The main reason had to do with the low–frequency measurements required by these applications. As with many other physical systems, the noise of a SQUID at low frequencies f scales as 1/f, and in the early high-T_c devices the level of the 1/f noise was extremely high. This noise limited their field sensitivity, rendering them useless in many applications. A significant part of this project became a systematic effort to understand and reduce this excess noise.

In the remainder of this chapter, I will present an introduction to SQUID theory, operation, and optimization with respect to noise and sensitivity, and then extend the discussion into the realm of high–T_c superconductors, focusing on the requirements for the new technology and the issues involved with operating SQUIDs at 77 K. In Chapter 2, I give a description of the fabrication and measurement equipment used to carry out the work presented in the remainder of this thesis. In Chapters 3 and 4, I describe the fabrication of both single layer and multilayer SQUID magnetometers and outline optimization of the process to reduce the low–frequency 1/f noise. Chapters 5–8 present four different types of magnetometers that were fabricated, focusing on their design and overall sensitivity. I turn to applications carried out with these magnetometers in Chapters 9 and 10. Finally in Chapters 11–13, I discuss the issues involved with operating SQUID magnetometers in a magnetically unshielded environment. I draw conclusions and discuss future directions in Chapter 14.

1.1 The dc SQUID

The magnetometers described in this work are based on the dc SQUID[1] shown schematically in Figure 1.2(a). The SQUID consists of two Josephson junctions[8] connected in parallel in a superconducting loop of inductance L. Each junction has a critical current I_0, a shunt resistance R, and a capacitance C. In the limit of low capacitance the current–voltage (I–V) characteristic of each junction is well described by the resistively–shunted

[1]For a more comprehensive introduction to SQUIDs, see, for example, ref. [7].

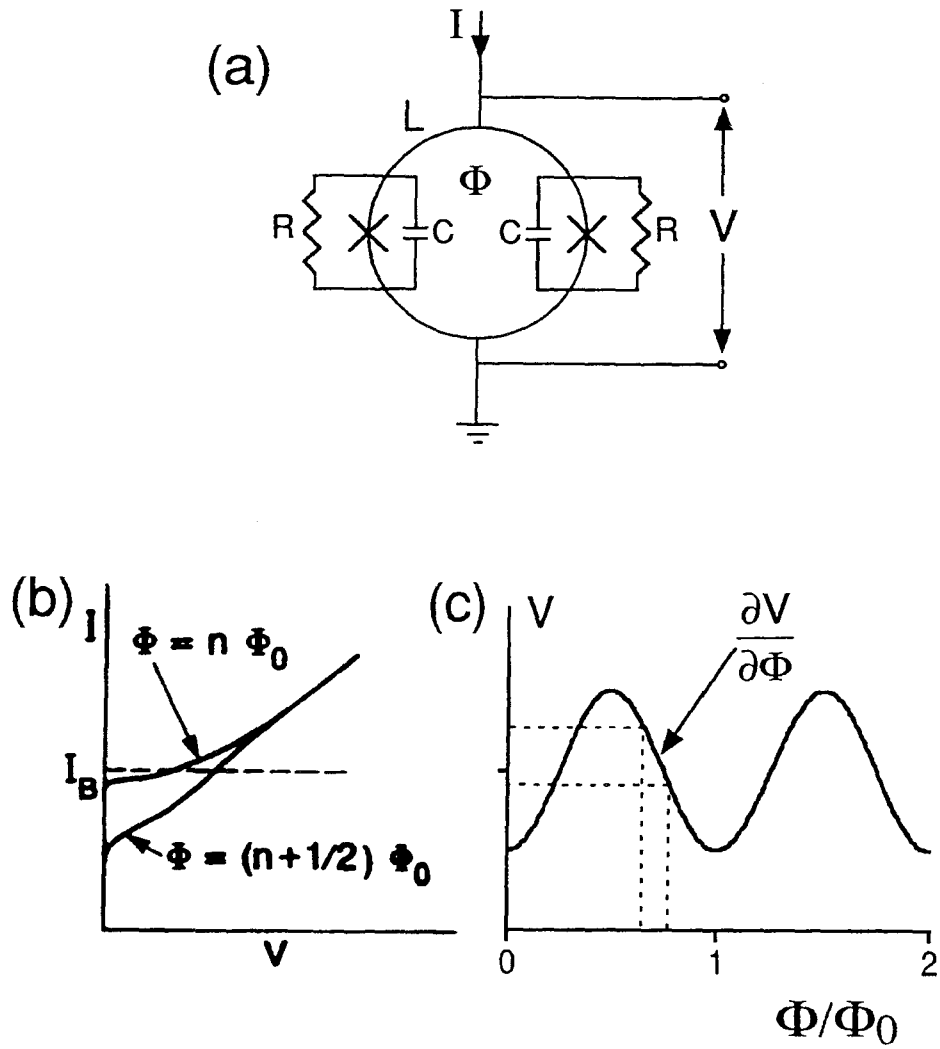

Figure 1.2: (a) Schematic representation of a dc SQUID. (b) Current–voltage characteristic. (c) Voltage–flux characteristic.

junction (RSJ) model [9, 10] which predicts V=0 for $I < I_0$ and

$$V = I_0 R\sqrt{(I/I_0)^2 - 1} \tag{1.1}$$

for $I > I_0$. If the absence of an applied flux, the I–V characteristic of the SQUID, shown in the upper plot of Figure 1.2(b), resembles that of a single junction (Eq. 1.1) with critical current $2I_0$ and resistance R/2. As the flux is increased, the critical current of the SQUID is reduced, reaching a minimum whenever the flux $\Phi = (n + 1/2)\Phi_0$, where the flux quantum $\Phi_0 = h/2e \approx 2.07 \times 10^{-15}$Wb and n is an integer. Correspondingly, the critical current becomes a maximum when $\Phi = n\Phi_0$. In practice, one applies a static current $I_B > I_0$ to the SQUID and measures the voltage which oscillates as a function of the applied flux with a period of Φ_0 as shown in Figure 1.2(c). The SQUID then can be used as a flux–to–voltage transducer with transfer function V_Φ defined as the slope $\partial V/\partial\Phi$ of the voltage–flux (V–Φ) characteristic at the steepest point. Normally one biases the SQUID at the value of I where V_Φ is a maximum. Computer simulations of Tesche and Clarke [11] show that for the reduced inductance $\beta \equiv 2I_0L/\Phi_0 = 1$, $V_\Phi \approx R/L$. Although this result must be modified for SQUIDs operating at 77 K (see Section 1.5), the basic message still applies: to increase the transfer function one strives to reduce L and increase R.

1.2 SQUID Operation and Readout

As seen in Figure 1.2(c), the SQUID response is very nonlinear, and for normal operation the SQUID must be biased with a static flux at the steepest part of the V–Φ curve. In the simplest mode of operation, one simply reads the voltage across the SQUID which, of course, limits its operation to signals $\Phi \ll \Phi_0$. To extend the linearity range we operate the SQUID in a feedback mode called the flux–locked loop, shown schematically in Figure 1.3. One flux biases the SQUID at either $n\Phi_0$ or $(n + 1/2)\Phi_0$ and applies a modulating flux in the form of a square wave with a peak–to–peak amplitude $\Phi_0/2$ at a frequency usually between 100 kHz and 1 MHz. The SQUID then acts as a mixer between the high–frequency modulating flux and the applied quasistatic flux. The mixed signal, in the form of an alternating voltage across the SQUID, is then stepped up by the transformer, amplified, and demodulated by the lock–in detector referenced to the modulation frequency. The output of the lock–in is integrated and fed back to the SQUID via the resistor R_F and the feedback/modulation coil coupled to the SQUID with mutual inductance M_F.

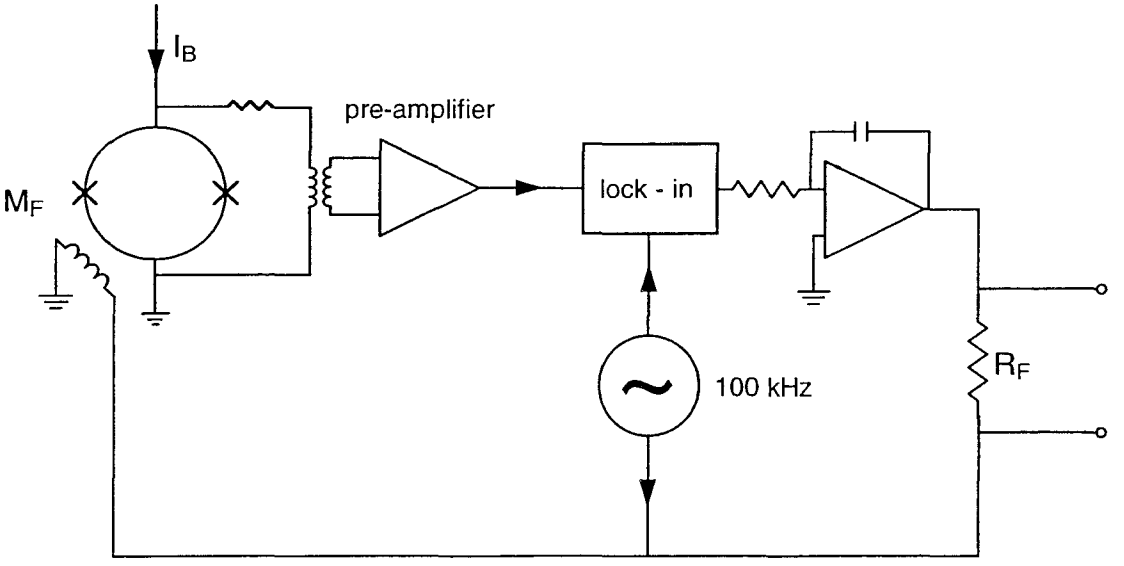

Figure 1.3: Flux–locked loop.

To illustrate the function of the flux–locked loop, consider a flux $\Phi(f)$ applied to the SQUID, where f is much less than the modulation frequency. The flux–locked loop then generates a feedback flux $\Phi_F(f)$ related to $\Phi(f)$ by $\Phi_F(f) = G(f)[\Phi(f) - \Phi_F(f)]$, where $G(f) = V_\Phi G_T G_A G_I R_F/M_F$ is the open–loop gain and G_T, G_A, and G_I are the individual gains of the transformer, amplifier and integrator, respectively. If $G(f) \gg 1$, the feedback flux equals the applied flux and the voltage measured across R_F is given by $(M_F/R_F)\Phi(f)$.

The flux modulation used in this technique eliminates the effects of 1/f noise and drift in the bias current and the amplifier. The use of feedback extends the linearity range of the SQUID response over many flux quanta since the net flux actually present in the SQUID is $\Phi(f)/G(f)$.

1.3 Flux Resolution and Noise

The smallest amount of flux that a SQUID can detect is limited by its intrinsic noise. This is not to be confused with the environmental or *extrinsic* noise which simply obscures the signal being measured. At high frequencies the noise of a SQUID is frequency–independent (or "white"), and arises from the Nyquist voltage fluctuations across the resistive shunts. Computer simulations[11] show that for a SQUID with $\beta = 1$ operated near T=4.2 K the spectral density of the voltage noise is approximately $16k_BTR$ and the corresponding flux noise is

$$S_\Phi(f) = \frac{16k_BTR}{V_\Phi^2} = \frac{16k_BTR}{(R/L)^2} \tag{1.2}$$

where, again, the form of the transfer function strictly only applies to low-T_c SQUIDs. However, the underlying message, that higher temperatures and lower transfer functions increase the SQUID noise, is still valid. This thermal noise represents the lowest limit to the SQUID's ability to resolve flux. For practical SQUIDs, flux resolutions of $(1 - 10) \times 10^{-6}\Phi_0\,\mathrm{Hz}^{-1/2}$ are readily achieved.

At lower frequencies, the flux noise of a SQUID scales as approximately 1/f and becomes much higher than the thermal noise. The exact frequency onset of this noise usually depends on the materials nature of the SQUID and the operating temperature. There are two known sources of the 1/f noise. The first arises from fluctuations in the critical current I_0 of the junctions. It can be related to trapping and releasing of charge carriers by defects in the barrier which raise and lower the barrier potential with a characteristic time and

amplitude. Fortunately, this noise source can be substantially reduced with a suitable modulation technique. Since there are two junctions in parallel undergoing I_0 fluctuations, the overall critical current fluctuation of the SQUID can be thought of as consisting of two modes. One is an "in–phase" mode in which the critical current of both junctions fluctuates with the same polarity. This mode produces voltage fluctuations across the SQUID and effectively shifts the $V - \Phi$ characteristic along the voltage axis. The ac flux modulation scheme described in the previous section eliminates this noise source since the readout is insensitive to the dc level of the $V - \Phi$, provided that the modulation frequency is much greater than the frequency of the fluctuations. The second, "out–of–phase" mode, in which the junctions fluctuate antisymmetrically, generates current around the SQUID loop thereby creating flux fluctuations in the SQUID which shift the $V - \Phi$ characteristic along the Φ axis. This noise is not reduced by the standard flux–locked loop, but can be reduced by the so–called bias reversal scheme [12]. In our implementation of this scheme, the SQUID is operated in the usual flux–locked loop, flux–modulated at 100 kHz with a peak–to–peak amplitude $\Phi_0/2$. Synchronously with this modulation the bias current I through the SQUID is reversed at 2 kHz, a frequency less than the modulation frequency but greater than the onset frequency of the 1/f noise. This flips the $V - \Phi$ curve about the V=0 axis. Simultaneously with the bias current reversal, the flux though the SQUID is shifted by $\Phi_0/2$ to recover the phase of the original $V - \Phi$ curve. Now, if an external flux is applied to the SQUID, the SQUID responds with a directional shift in the $V - \Phi$ curve along the Φ–axis regardless of the sign of the bias current. On the other hand, the flux generated by an out–of–phase current fluctuation changes sign every time the bias current is reversed. Provided that the bias reversal frequency is much higher than the fluctuation frequency, the time average of the flux produced by the fluctuation is zero. This scheme has been found to reduce the 1/f noise in both high- and low-T_c SQUIDs by several orders of magnitude in power, to the level of the white noise at frequencies down to 1 Hz or less.

The second source of 1/f noise in SQUIDs arises from thermally activated hopping of flux vortices among the pinning sites in the superconducting films. Because it couples to the SQUID as an externally–applied flux signal, this noise cannot be eliminated by the modulation and bias reversal schemes described above. One can only hope to reduce it through improvements in fabrication or possibly design. This noise source is particularly significant in high-T_c SQUIDs where pinning energies are low and operating temperatures are high. Much more will be said about this source of 1/f noise in the remainder of this

work.

1.4 Designing a SQUID Magnetometer

The capability of a SQUID to resolve small magnetic fields is limited by the magnetic *field noise* or *field resolution* $S_B(f)$ given by

$$S_B(f) = \frac{S_\Phi}{(A_S)^2} = \frac{1}{(A_S)^2}\frac{16k_BTR}{(R/L)^2} \tag{1.3}$$

where A_S is the *effective sensing area* of the SQUID. To minimize $S_B(f)$, one must increase A_S but to reduce the *flux* noise $S_\Phi(f)$, one must keep the inductance and thus the SQUID size small. The most common way to reconcile these conflicting requirements is to couple the SQUID to a *flux transformer* as illustrated schematically in Figure 1.4(a). A flux transformer is a closed loop of superconductor consisting of a large–area pickup loop and a (usually) multiturn input coil coupled to the SQUID via the mutual inductance M_i. A magnetic field B applied to the pickup loop generates a superconducting screening current $J_T = BA_p/(L_p + L_i)$ where A_p and L_p are the area and inductance of the pickup loop, respectively, and L_i is the inductance of the input coil. The current couples a flux J_TM_i into the SQUID. Thus the total effective area of the magnetometer defined as flux in the SQUID per unit applied field is

$$A_{eff} = A_s + A_p\frac{M_i}{L_p + L_i} = A_s + A_p\frac{\alpha\sqrt{L_iL}}{L_p + L_i} \tag{1.4}$$

where α is the coupling coefficient between the input coil and the SQUID inductance and A_s is the effective area of the bare SQUID. It is straightforward to show that A_{eff} is a maximum when $L_i = L_p$, yielding

$$A_{eff} = \frac{1}{2}\alpha A_p\sqrt{\frac{L}{L_p}}, \tag{1.5}$$

where we neglect A_s which is usually small.

Equation 1.5 stresses the need to couple the input coil inductively to the SQUID with very high coupling efficiency. The most common way to achieve tight coupling is by fabricating the input coil of the flux transformer as a planar spiral in a film directly over a SQUID, in a square washer configuration [13]. Figures 1.4(b) and 1.4(c) show the geometry of the square washer SQUID and the planar flux transformer with a multiturn input coil,

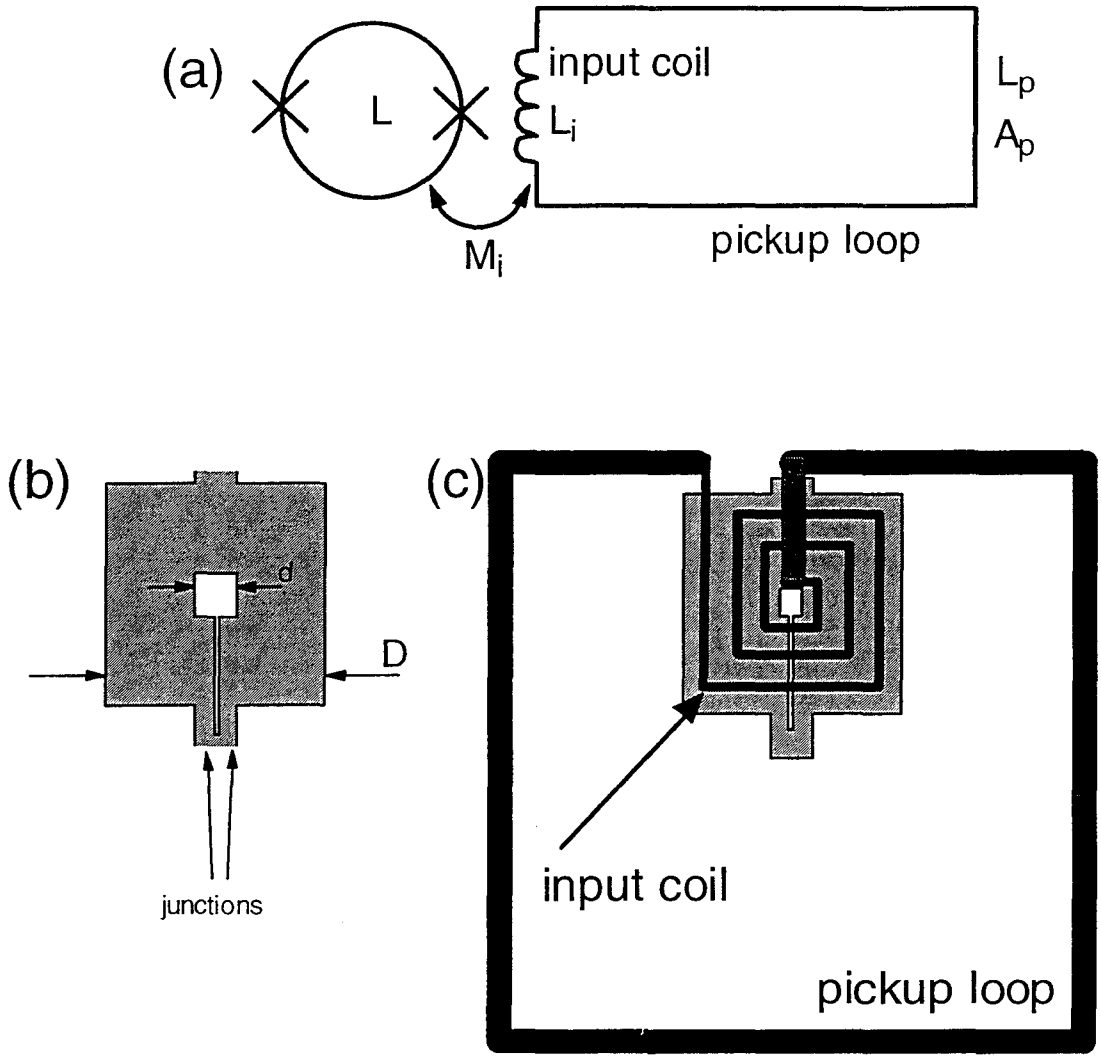

Figure 1.4: (a) Schematic representation of coupling a SQUID to a flux transformer. (b) A planar square washer SQUID. (c) A flux transformer with a multiturn input coil tightly coupled to a planar washer SQUID.

respectively. Ketchen and Jaycox[13, 14] showed that for a washer SQUID with inner and outer dimensions d and D, $L \approx 1.25\mu_0 d$ in the limit d $\lesssim$ D/3. They gave the following expressions in the "tight–coupling" limit where $\alpha \approx 1$

$$L_i = n^2 L + L_s, \tag{1.6}$$

$$M_i = nL, \tag{1.7}$$

where n is the number of turns in the input coil and L_s is the stripline inductance of the coil. By combining Equations 1.4, 1.6, and 1.7, one can show that A_{eff} is a maximum for $n = \sqrt{L_p/L}$, provided $L_i = L_p$. The effective area is then given by

$$A_{eff} = A_s + \frac{1}{2} A_p \sqrt{\frac{L}{L_p}}. \tag{1.8}$$

Conventionally one defines the gain of the flux transformer as A_{eff}/A_s.

For low-T_c SQUIDs, one integrates the flux transformer and the SQUID on the same chip, separated by a thin insulating layer. With high-T_c SQUID magnetometers it also became popular to fabricate each device on a separate chip and align them face–to–face in a"flip-chip" arrangement.

1.5 High-T_c Implementation

1.5.1 SQUIDs at 77 K

Before we explore the materials and the fabrication requirements needed to produce sensitive high-T_c SQUID magnetometers, let us briefly consider the implications for a SQUID operating at 77 K as opposed to 4.2 K. One immediately suspects that for a temperature almost 20 times higher, thermal fluctuations become much more important. Indeed, even in low-T_c SQUIDs, thermal fluctuations tend to "noise round" the I-V characteristics of the junctions by generating some dissipation below the critical current I_0 [15] which decouples the two sides of the junction. Thus, the thermal energy must be considerably less than the Josephson coupling energy; this condition may be written as

$$\frac{I_0 \Phi_0}{2\pi} \gtrsim 5 k_B T \tag{1.9}$$

where the factor of 5 is a result of computer simulation [16]. For T=77 K, we find the constraint $I_0 \gtrsim 16\mu$A.

Furthermore, the transfer function V_Φ at 77 K is not well described by the expression R/L obtained for low-T_c SQUIDs[11]. For a series of high-T_c SQUIDs Koelle *et al.*[17] found exprimentally that V_Φ scaled closer to $1/L^2$. Taking into account the effects of thermal noise, Enpuku *et al.*[18] obtained an analytical expression for the transfer function

$$V_\Phi = \frac{4I_0R}{\Phi_0(1+\beta)}\left(1-\sqrt{\frac{L}{L_T}}\right) \tag{1.10}$$

where $L_T = \Phi_0^2/4\pi k_B T$. At T=4.2 K, L_T = 6nH and for practical SQUID inductances V_Φ reduces to $\approx$R/L for $\beta = 1$, but at 77 K, L_T=321 pH and the transfer function is significantly reduced for inductances above about 100 pH, placing an addtional constraint on the SQUID parameters. Reinhold Kleiner[19] did extensive numerical simulations to explore the dependence of the SQUID transfer function and energy resolution on both temperature and inductance, finding Equation 1.10 to agree with the simulations for $0.08 \lesssim L/L_T \lesssim 0.4$ but underestimate V_Φ outside this range.

1.5.2 High-T_c Technology

We now turn to the technological requirements for fabricating a high-T_c SQUID magnetometer of the type shown in Figure 1.4(c), involving a planar SQUID coupled to a flux transformer with a multiturn input coil. The basic ingredient for this technology is a high–quality thin film of a high-T_c superconductor. Mostly for historical reasons, YBCO is the standard material, partly because of the enormous effort already invested into its development. Because of the anisotropy of the electrical transport properties in YBCO, films must be grown with the c–axis oriented normal to the surface to allow high critical currents in the plane. Oxygen plays a key role in determining the superconductivity of YBCO. Therefore films must be grown either in the presence of oxygen (*in situ*) or the growth must be followed by a subsequent annealing step (*ex situ*). The most common *in situ* techniques for growing YBCO thin films are pulsed–laser deposition (PLD), magnetron sputtering and co–evaporation. PLD is the method used in this work as described in Chapter 2. An appropriate substrate also must be chosen, ideally one with the same a and b lattice constants as YBCO. Other perovskites such as $SrTiO_3$ (STO), $LaAlO_3$, $NdGaO_3$ as well as MgO, sapphire and yttrium–stabilized zirconia (YSZ) have all been used. Of these, STO has the best lattice match to YBCO; the remaining substrates often require a buffer layer to facilitate good growth. In general, one would like the YBCO film to have T_c above 77 K,

ideally as high as 92 K, comparable to the bulk material. For good electrical transport, the critical current density (J_c) should be as high as possible. The latter requires that the film be free of defects, grain boundaries (except for twin boundaries), and that it grows epitaxially, with the c–axis perpendicular to the substrate.

One also requires a method for making Josephson junctions or weak links in the YBCO films. The junctions should be reproducible, have a I_0R product above 100 μV and, in particular, have a high voltage–state resistance R, of say a few ohms, for the SQUID to have a useful transfer function. Until recently, the most common junctions used in high-T_c SQUIDs involved a grain boundary across a narrow bridge patterned in the film. In fact, the first high-T_c junctions were fabricated in granular films by patterning a bridge across the naturally-occurring grains [20]. Since then, film quality improved as did the methods for producing an intentional grain boundary. The most straightforward type of grain boundary junction is made on a bicrystal substrate which contains a prefabricated grain boundary that propagates into the YBCO film grown on the bicrystal. Narrow bridges patterned in the YBCO, crossing the boundary, exhibit RSJ I–V characteristics. In another method called the step–edge junction, one ion mills a vertical step in a region of the substrate. A YBCO film grown over the step contains grain boundaries where the film crosses the upper and the lower corners of the step. Todate, the most successful high-T_c SQUID magnetometers were made with junctions using one of these two methods. Other junction technologies are described in ref [7] and [21] and some of them are making their way into high-T_c devices.

The third requirement for high-T_c SQUID magnetometers is a multilayer interconnect technology. It is clear from Figure 1.4(c) that the strip connecting the inner turn of the multiturn input coil to the pickup loop must be made in a separate layer to prevent it from shorting the rest of the turns. One must use a compatible insulating film to isolate the two superconducting layers except where intentional connections, or vias, are required. Figure 1.5 shows the two essential circuit components of an interconnect technology: a crossover, where two films of superconductor are separated by an insulating layer, and a via, where two films are connected through a window in the insulator. The basic component of this structure is a YBCO/insulator/YBCO trilayer. All three films of this trilayer must maintain epitaxy to avoid grain boundaries and attain good transport in both superconducting films. The insulating material must be free of pinholes and be both chemically and structurally compatible with YBCO. Usually a substrate material such as STO is a good choice. In addition to the insulator, the critical parts of a crossover are the edges, where

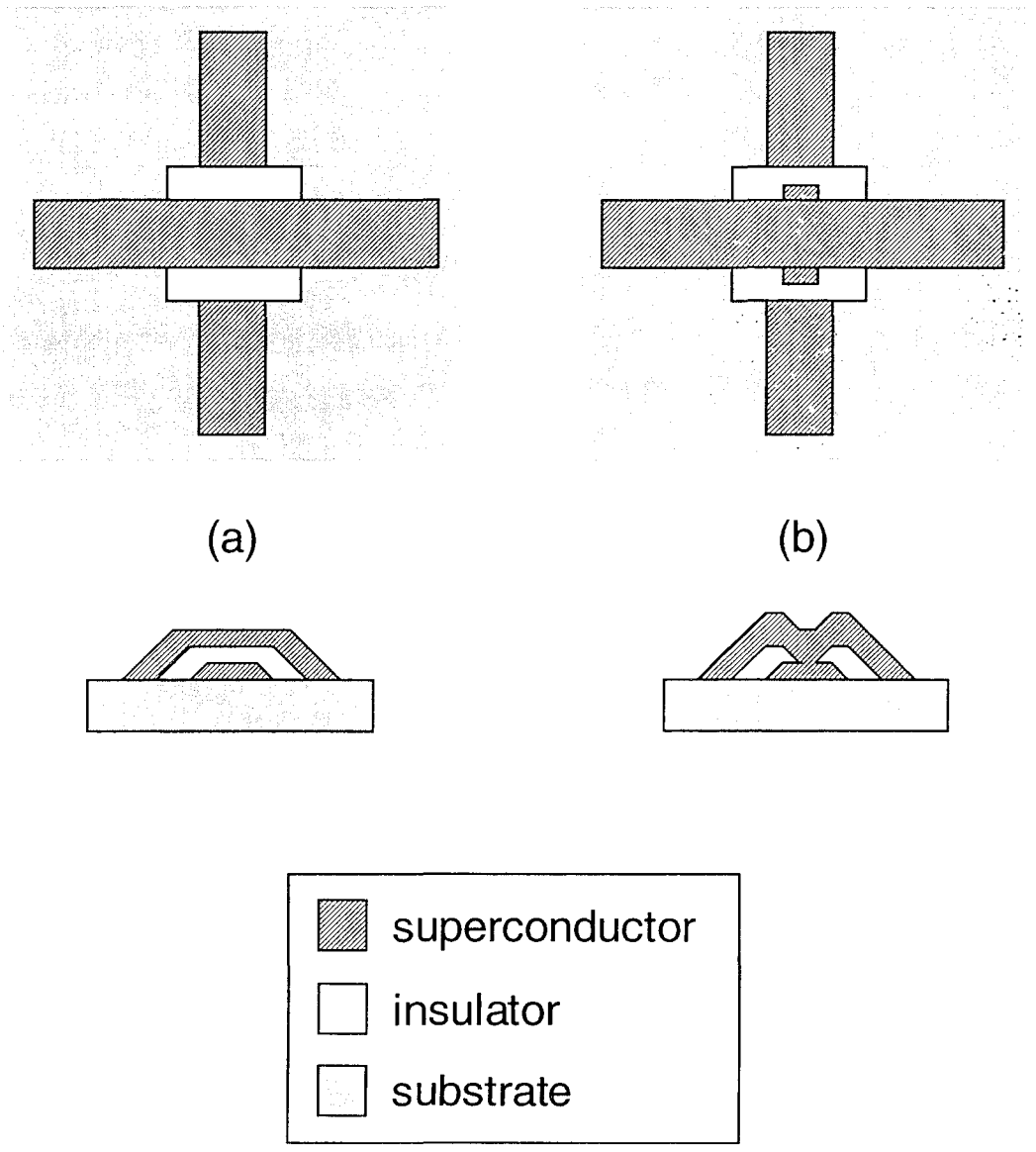

Figure 1.5: Top and cross–sectional views of components of an interconnect technology: (a) crossover, (b) via.

grain boundaries can form in the insulator and propagate through the upper YBCO. For a via contact, the ability to achieve a high critical current density is an obvious requirement.

The final criterion for SQUID magnetometers made from YBCO is the need for a technology that does not create excess noise in the device. I mentioned in Section 1.4 that 1/f noise in a SQUID can originate from flux vortices that hop under thermal activation between pinning cites in the SQUID body. A multilayer flux transformer, as we shall see, is even more susceptible to this vortex motion. Weak pinning sites can form in both superconducting layers, especially in regions that underwent processing, such as crossovers, vias and surfaces exposed to chemical etchants or photoresist. Vortex–antivortex pairs are created in the superconducting films when the device is cooled through T_c, even in nominally zero field. While some of these pairs annihilate during cooling, a number of the vortices are weakly pinned so that thermal activation at 77 K results in random hopping between sites, coupling flux noise into the SQUID. This problem is even more evident when the SQUID magnetometer is cooled in a finite static magnetic field, such as that of the Earth, in which case there is an excess of vortices that can generate noise.

Chapter 2

Equipment

In the following sections, I will describe and discuss the equipment and some of the standard procedures that were used to carry out this work. The equipment falls into two categories, fabrication and measurement.

2.1 Fabrication

2.1.1 Pulsed Laser Deposition System

There are several available techniques for fabricating *in situ* thin films of YBCO and other perovskites. Arguably the most common one is pulsed laser deposition (PLD), although off–axis sputtering and co–evaporation[22] have also been used with acceptable results. Our PLD system was built by Fred Wellstood and Jack Kingston; details of its original construction can be found in ref. [23]. Over the years it underwent upgrades; the most recent was the replacement of the laser. I will give a brief description of its current state and operating procedure.

The PLD system consists of a laser, an optical imaging system, and a vacuum chamber with target and sample holders. We use a Lambda Physik Compex 200 excimer laser, mounted on a rigid table and reinforced for safety. It uses a gas mixture of F_2, Kr, and Ne which must be replaced after approximately 3 weeks of normal use. The laser operates at a wavelength of 248 nm and can generate up to 10 pulses/second with a maximum energy of about 700 mJ/pulse. By regulating the energy internally and using a circular aperture 7.9 mm in diameter, we produce a uniform beam with a typical energy of about 75 mJ/pulse.

We use an external energy meter to measure and set the beam energy prior to each film deposition.

The optical imaging system consists of two planar mirrors and a planoconcave lens. The optical elements are mounted on standard light tracks. The beam follows a zigzag path that almost doubles back on itself, emerging from the laser, reflecting from one mirror close to the vacuum chamber, reflecting from another mirror close to the laser, and finally passing through the lens into the chamber. The length of the optical path is adjusted for optimal fluence on the target of 2.25 J cm^{-2} and an optimal spot size 2.5 mm^2 on target.

The stainless steel vacuum chamber is evacuated by a diffusion pump backed by a mechanical roughing pump. Both pumps use liquid nitrogen cold traps. The base pressure is usually 1 X 10^{-6} Torr. The walls of the chamber contain electrical feedthroughs for the substrate heater, pressure sensors and a thermocouple. There are two quartz windows, one that admits the laser beam into the chamber and another that allows us to observe the plume.

The chamber contains the substrate heater block, a holder for six targets and a shutter. The heater block is made from Hanes alloy with an embedded resistive cartridge heater. Except for the front face where the substrate is mounted, the heater block is surrounded by a stainless steel radiation shield. Normally we remove the heater block to mount the substrate. We place a sheet of Ag foil, slightly larger than the substrate, on the heater block, apply a layer of Ag paste onto roughly the inner 2/3 of the foil area, mount the substrate on top and clamp it down with a Hanes alloy clip that resembles a rectangular loop. This ensures good thermal contact and allows us to remove the substrate after deposition without breaking it. After mounting the heater block into the chamber, we attach current leads to the heater and insert the tip of a thermocouple into a hole drilled in the block. We regulate the temperature of the heater block using a programmable Omega temperature controller which uses the thermocouple as a temperature sensor. We make the final temperature adjustments by reading the temperature of the heater block with an infrared pyrometer, which looks through a window in the lid of the vacuum chamber into another hole in the heater block. The pyrometer provides a more reliable reading of temperature than the thermocouple, especially in low ambient pressures where the thermal contact between the thermocouple and the heater block can be poor. We regulate the ambient O_2 pressure by throttling the gate valve and bleeding O_2 into the chamber through a needle valve.

The six–target system allows us to change targets using a rotary feedthrough without breaking vacuum; this is essential for *in situ* multilayers. Each pressed–powder target is a disk 25 mm in diameter and 7 mm thick. Prior to deposition, we remove and polish the targets, in order to remove the laser markings from the previous deposition. We use 400 grit sand paper for a rough polish, followed by 600 grit for a finer polish. Finally, we wipe the target surface on a latex glove and gently blow off any remnant particles with compressed N_2 gas parallel to the surface, before remounting the target. For each deposition, the target is moved into position in front of the laser beam and held in contact with a rotating disk, which rotates the target about its center at about 1 revolution per second. The laser beam strikes the target about 2 mm from the edge, thereby ablating material at a different spot with each strike. This ensures more uniform target wear and prevents boulders in our thin films. In front of the target is a water–cooled Cu sheet with a rectangular opening 10 x 20 mm^2 which allows the beam to strike the target and the plume of the ablated material to emerge. The plume extends toward the heated substrate, thereby depositing material with each pulse of the laser. A shutter in front of the heater block allows us to ablate material off the target without depositing it onto the substrate. Just before each deposition, we close the shutter and clean the target by ablating material at 10 Hz for 1–2 minutes.

2.1.2 Thermal Evaporation

We deposit metallic thin films by thermal evaporation, using a Varian Model 3118 Evaporator. Their most common use is to form contacts between YBCO SQUIDs or magnetometers and external wiring. Typically we evaporate 50–100 nm of Ag through a shadow mask onto freshly deposited YBCO films, covering the area of the film where contact pads will be patterned. We usually attain very low contact resistances between the Ag and the YBCO, on the order of $\mu\Omega$'s. We do not post–anneal the Ag.

2.1.3 Patterning

We pattern our devices by photolithography at the Berkeley Microfabrication Lab, which is a Class 100 clean room. We begin by spinning Shipley 1400-31 (more recently S1818) photoresist onto the chip at 6000 rpm. We then bake the photoresist, to harden it, on a hot plate at 70°C for 6 minutes. Our masks are laid out using a CAD program and

transfered to emulsion or chrome plates. We use a Cannon 4X Projection Mask Aligner to transfer the mask pattern to the resist. We develop the resist in a 1:1 solution of Microdeposit Developer Concentrate and DI water. This procedure and equipment generally allow us to pattern structures as small as 1 μm.

2.1.4 Ion Mill and Acid Etch

We transfer a pattern from the resist onto the underlying YBCO by exposing the surface to a beam of high–energy Ar ions, which bombard and thereby remove the material not covered by the resist. Our ion mill system consists of a vacuum system, an ion source, a neutralizer and a cooled sample stage. The vacuum system consists of a commercial stainless steel vacuum chamber which is evacuated by a cryopump. The base pressure is about 1 X 10^{-7} Torr. The chamber has two windows that allow us to observe the progress of the milling. It also has electrical feedthroughs for the ion source, the neutralizer and the Faraday cup used to measure the beam current.

To generate the beam of Ar ions, we use a Nordiko 5 cm RF Ion Source mounted on a Conflat flange that fits onto the chamber. The advantage of the RF ion mill is that it does not use a filament which would radiate heat onto our sample. We operate the ion source at an accelarating voltage of about 500 V to generate a beam current of 120–180 μA cm^{-2}. We also use a Nordiko rf neutralizer mounted inside the chamber to supply a beam of electrons at about 70° to the ion beam in order to prevent the ions from charging up the dielectric substrate.

The sample is clamped to a copper stage connected to a shaft that extends through a copper block. The shaft is rotated from outside the chamber using a feedthrough and a system of gears, thereby allowing continuous rotation of the sample during the ion milling. The copper block contains a U–shaped copper tube, whose ends extend outside the chamber for flowing either chilled water or liquid nitrogen to cool the block. The sample stage is in thermal contact with the copper block through heat–conducting vacuum grease, which also allows free rotation of the stage. The entire assembly is mounted on a Conflat flange which fits into a mating hole in the lid of the chamber and can be rotated with respect to the ion beam so that films can be milled at any angle to the substrate.

The ion mill is a convenient, universal *dry etching* technique used for YBCO, $SrTiO_3$, Ag, or any other material we pattern. Its main advantage lies in one's ability to

mill at an arbitrary angle to the surface, which is important if one must make either very vertical, well–defined edges or, alternatively, edges sloped at a shallow angle to facilitate good epitaxial growth of subsequent layers. Several chemical *wet etching* techniques are also available. YBCO and PBCO can be etched in a weak solution of HNO_3, which we used until the ion mill came online. Wet etching has the advantage of speed – 2 to 3 minutes for 150 nm of YBCO – and it is the only technique available to us for etching large wafers (50 mm and up). Unlike the ion mill, however, it is nondirectional and it is difficult to control the final size of very small features, on the order of 1–2 μm. In general, we now only use wet etching when ion milling is impractical; for example, for YBCO on large wafers (see Chapters 5 and 13).

2.2 Measurement

Most of the experiments discussed in this work involved measuring the flux noise of high-T_c SQUIDs or magnetometers in liquid nitrogen at 77 K. The cryostat was a 5 liter superinsulated fiberglass dewar surrounded by three concentric high–permeability (mu–metal) shields. A number of probes were used, although I made most of the later measurements using one in particular, which I had modified over the years for best performance, as the measurements became more demanding. In its latest incarnation, the "noise probe" consists of a 1.2 m–long, 12.5 mm-diameter stainless steel rod with an O–ring Quick–Connect seal that allows it to slide down to various levels into the dewar. The probe can be used to measure up to five SQUIDs at the same time. At the bottom end of the probe are five sets of cold electronics each consisting of a transformer, to couple the signal from the SQUID to the room–temperature preamplifier, and several resistors in series with the bias currents. Each hand–wound transformer has a 3 turn primary and a 90 turn secondary coil wound about a ferrite core[24]. The transformer has a voltage gain of 30 up to at least 100 kHz; the gain drops to 6 at 500 kHz.

For mounting the SQUID chip, I used one of two "probe attachments". On the "horizontal attachment" the SQUID chip is mounted with its plane parallel to the axis of the dewar and shields. The "vertical attachment" mounts the SQUID with its plane perpendicular to the axis of the dewar. The SQUID chip is glued to a custom–made printed circuit board with Cu contact pads that are attached to the leads of the SQUIDs with 25 μm Al wire bonds. Cu wires connect the pads to the cold electronics. Modulation and

feedback signals are supplied by one of several coils mounted on the probe attachment. The horizontal attachment also has a 20×30 mm^2 field coil for measuring the effective area of a SQUID or magnetometer. With the vertical attachment, I measure the effective area using a long solenoid (See Chapter 11).

All copper wires in the probe are in twisted pairs. All wires that carry a high–frequency signal, namely the modulation signal and the output of the transformer secondary, are surrounded by grounded CuNi tubes to prevent crosstalk and for external rf shielding. At the top end of the probe is an aluminum box containing connections for each of the 5 SQUID channels as well as ones for the modulation/feedback coils and a Pt thermometer.

In addition to the mu–metal shields surrounding the dewar, I used either a cold Co-netic or Cryoperm shield placed around the SQUID mount or, more recently, a superconducting shield that consists of a 125 mm–long YSZ tube covered on both surfaces by a 1 μm–thick layer of YBCO. For additional rf shielding, all noise measurements were conducted is a Cu–mesh shielded room in the second basement of Birge Hall.

The SQUID control electronics were inherited from former group members with only minor modifications. It allowed the SQUID to operate in a flux–locked loop with 100 kHz flux modulation. The 2 kHz bias reversal electronics were designed and built by Andy Miklich. Noise spectra were read on a spectrum analyzer, connected to the output of the flux–locked loop, and downloaded into a personal computer.

Part II

Fabrication

In this part, I give a semi-historical overview of the fabrication and processing technology used to make our thin-film YBCO devices. As with any new technology, the processing underwent a significant evolution over the course of this research and, in fact, became a major part of it. The requirements for the technology were discussed in Section 1.5, but the evolution was largely driven by the final criterion, the need for YBCO thin films and YBCO/insulator/YBCO multilayers that are not plagued by 1/f noise, which limited the performance of earlier devices. This noise is generated by the thermally-activated hopping of flux vortices between pinning sites in the superconducting films. In Chapter 3, I will focus on single thin films of YBCO and highlight innovations in the fabrication relevant for SQUIDs and magnetometers with low 1/f noise. In Chapter 4, I will turn to multilayer devices, namely flux transformers, which require both a suitable interconnect technology as well as low noise in all superconducting layers. I will end each chapter by outlining the final "standard" process now used to fabricate each type of device. In the course of these two chapters, I will show plots of the flux noise for some model SQUIDs and magnetometers to point out various fabrication improvements that led to lower noise; however, I will postpone a detailed discussion of the final design and magnetic field sensitivity of the best SQUID magnetometers until Part III.

To set the scene, by 1991 an immense amount of effort in the development of a high-T_c fabrication technology was expended by my predecessors[1] in the Clarke Group, not the least of which was the construction of the pulsed laser deposition (PLD) system described in Chapter 2. They developed deposition parameters to grow epitaxial *in situ* YBCO thin films, with transition temperatures as high as 88 K, on $SrTiO_3$-buffered MgO substrates. They developed an interconnect technology based on YBCO-$SrTiO_3$-YBCO multilayers with patterning initially done with shadow masks, but subsequently replaced by photolithography and wet etching or ion milling. Finally, they applied the interconnect technology to fabricate flux transformers which operated at temperatures above 77 K. They coupled the flux transformers to both high- and low-T_c SQUIDs in a flip-chip arrangement and measured gains in effective area as high as 83. A full description of the interconnect technology prior to 1992 can be found in refs. [25] and [23].

Although, what I will now call the "early" process, was generating functional flux transformers, it had several shortcomings which still had to be resolved. First, the

[1] Jack Kingston, Fred Wellstood and Rasmus Kromann.

yield of devices that operated above 77 K, with all vias carrying a supercurrent and all crossovers insulating, was about 1 in 2. Second, the transport properties, even of devices that functioned at 77 K, were only marginally acceptable; as an example, for a typical functional flux transformer with a 10–turn input coil and two vias, the T_c was about 83 K and the J_c about $5 \times 10^4 \mathrm{Acm}^{-2}$ at 77 K, considerably below the reported values for bare YBCO thin films. Finally, as I shall describe in detail in Chapter 4, these flux transformers were plagued by excessive amounts of low–frequency 1/f noise generated by the motion of flux vorices in the superconducting films. The development of the "early" process was driven by a need for high–quality YBCO thin films and a high–T_c interconnect technology, which it largely fulfilled. Its benchmarks were mostly transport and epitaxial properties of the thin films as characterized by electrical measurements and X–ray diffractometry, respectively. The new processes, which I will presently describe, developed by the next generation[2], can be regarded as successive refinements of the "early" process with particular focus on the flux noise, in addition to transport and epitaxy.

[2]Myself along with Frank Ludwig, David Nemeth, Dieter Koelle, Andy Miklich, and John Clarke.

Chapter 3

Single Layer YBCO Thin Films and Devices

3.1 A New Process for YBCO Thin Films

It is now well established that the 1/f noise of YBCO thin films decreases substantially as their crystalline quality is improved. These findings were initially reported by Ferrari *et al.*[26] who used a low-T_c SQUID at 4.2 K to measure the flux noise of YBCO films at temperatures around 77 K. As a result, we made systematic efforts to optimize the quality of our YBCO thin films. The properties of the film are controlled by a set of fabrication parameters that include: choice of substrate, deposition rate, laser energy, substrate temperature and ambient O_2 pressure. In what we can call a high–quality film, these properties include a high degree of epitaxy, high T_c and J_c, and low levels of flux noise, associated with the hopping of vortices. A change in a single parameter, often requires a change in another parameter; for example, YBCO films with highest T_c are grown at 770°C on $SrTiO_3$–buffered MgO substrates but at 810°C on $SrTiO_3$ substrates. In the remainder of this section, I will highlight the main features of our new process for YBCO thin films developed between 1992 and 1993, pointing out major changes from the earlier process.

3.1.1 Choice of Substrate

In the "early" process, we deposited YBCO thin films on MgO subtrates buffered with about 40 nm of $SrTiO_3$. The buffering helped reduce the lattice mismatch and allowed

patterning of the YBCO by acid etch, since MgO also etches in HNO_3 whereas $SrTiO_3$ does not. The main advantage of MgO was that the substrates were relatively inexpensive (about \$5 for 12.5mm × 12.5mm × 1mm); they are also easy to cleave and to polish. The main disadvantage was lattice–mismatch to YBCO, which generated 45° angle grain boundaries and depressed the T_c to 88 K. It also created stress–induced defects in the YBCO which likely led to the elevated levels of 1/f flux noise. In the course of optimizing the "new" process, we experimented with MgO, as well as YSZ and $SrTiO_3$ substrates for growing YBCO thin films. Tim Shaw periodically measured the noise of our YBCO thin films using a low–T_c SQUID and these measurements pointed to $SrTiO_3$ as the substrate of choice for YBCO films with lowest noise. The lattice constant of the cubic structure of $SrTiO_3$ is 3.91 Å, within a few percent of the orthorombic YBCO (a= 3.83Å, b=3.89Å), and considerably closer than either MgO (a=b=4.21Å) or YSZ (a=b=5.15Å). It is therefore likely that the improved lattice match to YBCO improved the quality of our films with respect to flux noise. $SrTiO_3$, however, carries two important disadvantages. The first is cost, about \$140 for 12.5mm × 12.5mm × 1mm, the most expensive of all substrates now used to grow YBCO films. The second is a very large dielectric constant, about 10^3, which perhaps is not a very important factor for low–frequency applications such as magnetocardiography, but may limit certain high–frequency applications like NQR. Nonetheless, we now use $SrTiO_3$ almost exclusively for all of our YBCO films and devices.

3.1.2 Deposition Parameters

In addition to switching substrates, we also made substantial improvements in the film quality by altering parameters associated with the actual deposition of the film. These parameters include: laser energy, aperture size, beam fluence, laser spot size on the target, plume size and shape, distance between the target and the substrate, substrate temperature and ambient O_2 pressure. Once again, all of these parameters are interrelated and were optimized by making a large number of samples which were all thoroughly characterized, discussed and catalogued. I will confine the present discussion to final results [27].

We reduced the deposition rate from 0.2 nm/pulse to 0.07 nm/pulse. This was done through a combination of reducing the area of the aperture at the output of the laser from 84 mm^2 to 49 mm^2, readjusting the position of the optics to focus a spot about 2.5 mm^2 onto the target (a spot 6 mm^2 was previously used), and reducing the laser power.

This resulted in a beam fluence of about 2.25 J cm^{-2} on target. We moved the substrate closer to the target (within 5 cm) and readjusted the plume so that only its tip touched the substrate during deposition. We re-optimized the YBCO deposition temperature and O_2 pressure to 810°C and 210 mT, respectively. We also found that thicker films tend to have poorer quality, possibly due to a breakdown in crystallinity in the upper regions. Most of our single layer YBCO films are, therefore, now less than 200 nm thick, whereas in the past they were 300–400 nm.

This optimization was driven by feedback supplied by measurements of T_c and J_c by electric transport, film epitaxy and content of c–axis growth by X–ray diffractometry, and flux noise measurements with a low-T_c SQUID. For single YBCO films, 100–200 nm thick, deposited with our optimized process, we measured $T_c = 91 - 92$ K and $J_c = (3 - 10) \times 10^6 \mathrm{Acm}^{-2}$. Measurements of X-ray diffraction spectra indicated a negligible amount of a–axis growth and no 45° grain boundaries, suggestive of excellent epitaxy. Flux noise measured at 77 K with a low–T_c SQUID was limited by the intrinsic noise of the SQUID itself, about $13\mu\Phi_0\mathrm{Hz}^{-1/2}$ at 1 Hz in, in contrast with the "early" process which yielded YBCO films with noise levels at 1 Hz not lower than $250\mu\Phi_0\mathrm{Hz}^{-1/2}$ at 40 K [26]. It was gratifying that the new process yielded YBCO films with low noise as well as good epitaxy and transport, all essential parameters for a complete high–T_c electronics technology and an important first step in the development of low–noise YBCO SQUIDs and SQUID magnetometers.

3.2 Bicrystal dc SQUIDs

Until early 1992, all high-T_c SQUIDs made in our group were based on biepitaxial junctions [28] which suffered from several significant shortcomings. First, they often did not function at 77 K. Second, their low I_0R products limited the SQUID transfer coefficient V_Φ to a few $\mu V/\Phi_0$ which resulted in high white noise. Third, the SQUIDs were plagued by excess 1/f noise at low frequencies, which was not entirely due to critical current fluctuations and therefore could not be removed by bias reversal. By the spring of 1992, $SrTiO_3$ bicrystal substrates were commercially available and we began fabricating bicrystal SQUIDs. In the bicrystal process, one starts with a boule of single–crystal $SrTiO_3$ and cuts a wedge out of it at a specified angle. The remaining pieces are then re-fused and the resulting bicrystal boule is sectioned into (100)–oriented wafers with a grain boundary down the middle creating an

in–plane misorientation between the two halves at an angle typically 24° or 36°. A YBCO film grown on the bicrystal substrate replicates the grain boundary and narrow bridges patterned across the boundary exhibit RSJ behavior [29, 30].

Since bicrystal SQUIDs require only a single layer of YBCO, they were very well suited to our new process described in Section 3.1. In our first devices, we deposited about 200 nm of YBCO onto $10 \times 10\,\mathrm{mm}^2$ $SrTiO_3$ bicrystals with 24° angles of misorientation and patterned typically 12 SQUIDs with 2–3 μm-wide junctions in each film using conventional photolithography. In the early bicrystals the grain boundary was very visible and one could easily align to it the microbridges that formed the junctions. We wet etched the YBCO in a 0.05% aqueous solution of HNO_3 and allowed the etchant to slightly undercut the bridges, thereby controlling their final widths[1]. Andy Miklich characterized the SQUIDs and found them all functional at 77 K with current–voltage characteristics resembling the RSJ model with I_0R products ranging from 100 to 200 μV and voltage–flux characteristics with modulation depths around 15 μV for SQUIDs with L $\approx$ 40pH. Details of these measurements can be found in refs. [31] and [32]. Furthermore, he measured the flux noise in some of these SQUIDs by operating each in a flux–locked loop both with a static bias and with bias reversal. With static bias, the power spectrum scaled approximately as 1/f between 0.1 Hz and 1 kHz and became white above 5 kHz. However, with bias reversal the 1/f noise was dramatically reduced, by about two orders of magnitude in power at 1 Hz, suggesting that it largely originated from critical current fluctuations. With bias reversal the noise was white down to about 10 Hz, increasing to $17\,\mu\Phi_0\,Hz^{-1/2}$ at 1 Hz. The noise at 1 Hz in this SQUID was of the order of that in an unpatterned YBCO thin film ($13\,\mu\Phi_0\,\mathrm{Hz}^{-1/2}$), as measured with a low-T_c SQUID (see Section 3.1.2), suggestive of a certain consistency in our new process; the slightly elevated noise of the SQUID may have been due to the effects of patterning and the presence of edges. In short, the noise in bicrystal SQUIDs operated with bias reversal appears to be limited by thermal noise, and is white down to very low frequencies. The white noise normally depends on the SQUID inductance L as well as the I_0R product but is typically around $(5 - 15)\,\mu\Phi_0\,\mathrm{Hz}^{-1/2}$, and, in more recent bicrystal SQUIDs, extends to below 1 Hz.

We have been fabricating exclusively bicrystal SQUIDs since that initial success. Figure 3.1 shows a scanning electron micrograph of a recent (1996) bicrystal SQUID. The

[1]Ion milling later proved to be a better technique for this.

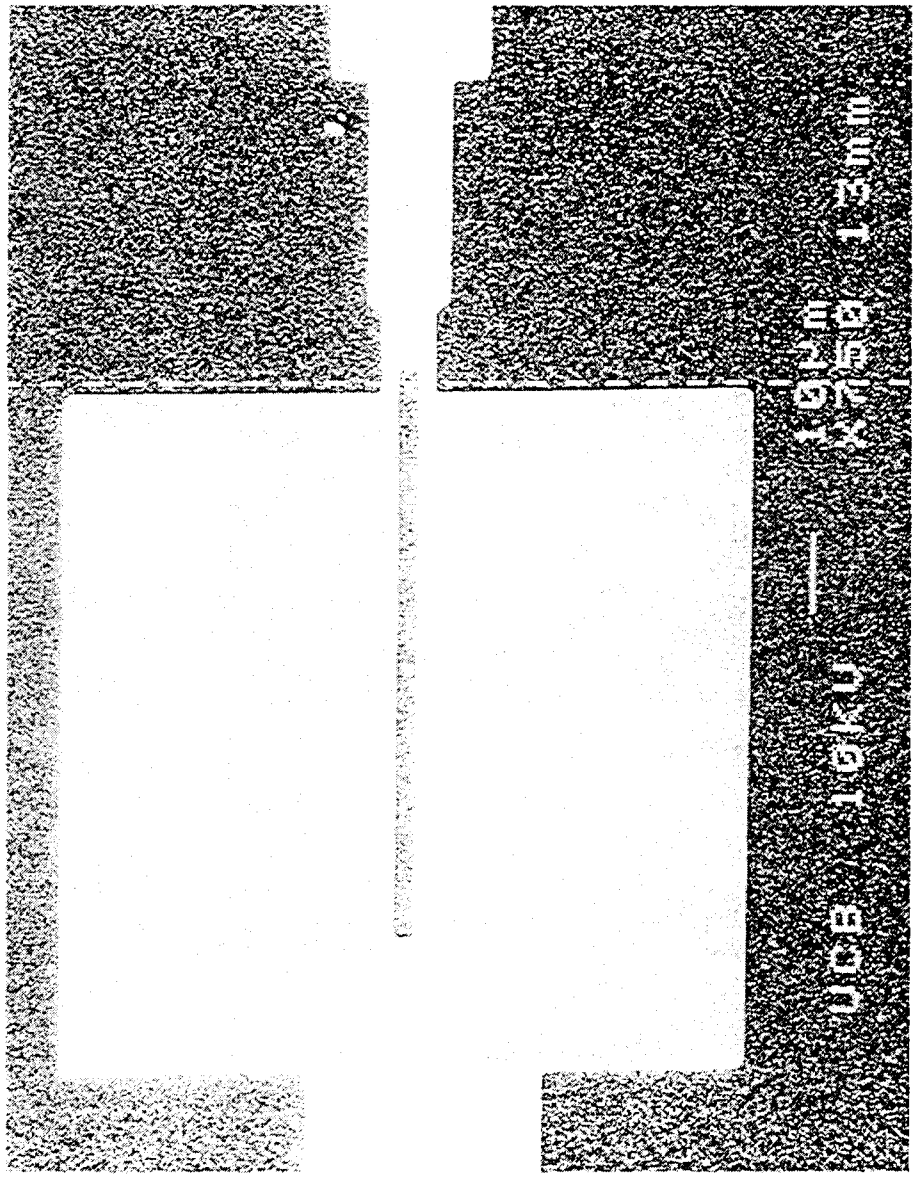

Figure 3.1: Scanning electron miscroscopy (SEM) image of a recent YBCO bicrystal SQUID. Dashed line indicates grain boundary.

YBCO film was 150 nm thick. The grain boundary, indicated by the dashed line, intersects the two bridges, 2 μm wide and 4 μm long, to form the junctions. The width of the bridges was determined by the critical current density of the YBCO film across the bicrystal line, usually 10^4–10^5 A cm^{-2}. The length of the junctions is kept short so that they contribute only minimally to the overall inductance L of the SQUID. For this particular SQUID the parameters were: L=40 pH, $I_0 = 120\mu$A, R = 1.1Ω, $V_\Phi = 32\mu V/\Phi_0$. In general, bicrystal SQUIDs proved sufficiently reliable in my experience. They are relatively simple to fabricate, requiring only one deposition step followed by one patterning step. On a given chip, the yield of devices that operate above 77 K is nearly always 100 percent and their I_0R products are usually between 100 and 200 μV. They suffer from a few disadvantages, however. One is that the SQUIDs must be confined to a line along the grain boundary and cannot be placed at arbitrary locations on the substrate. For a magnetometer, that requires only one SQUID, this is not a significant concern. Another disadvantage is cost; a 10mm $\times$ 10mm $\times$ 0.5mm $SrTiO_3$ bicrystal costs \$350–\$400. The final, and what I believe is the main disadvantage of bicrystals, is that it is not a well–controlled technology. Critical current density across the grain boundary, sometimes drifts from one batch of substrates to another (even for nominally identical angles) and the researcher does not have exclusive control over the properties of the junctions; some of that control is in the hands of the bicrystal supplier. In 1992, bicrystals offered the most reliable high-T_c junction technology available. The main drawback of other junction technologies such as biepitaxy [28], noble–metal SNS [33], step–edge [34] and ramp–edge [35] was low voltage–state resistance R. By now, the latter two have largely caught up to bicrystals with resistances reported in the range of a few ohms and I_0R products of 100–200 μV at 77 K. Several groups have used them in SQUIDs and magnetometers with great success (see for example refs. [36, 37, 38, 39]).

3.3 Standard Fabrication of Bicrystal SQUIDs

I will now outline the process that I use to fabricate bicrystal dc SQUIDs for most devices discussed in this thesis. The process underwent some refinement since our first devices and I will simply give the latest version which has been "standard" since about 1994. I divided the process into several steps as shown below. I refer the reader to Chapter 2 for equipment–specific details.

(1) Cleaning 1: To remove any residual wax and dirt, I agitate the $SrTiO_3$ bicrystal

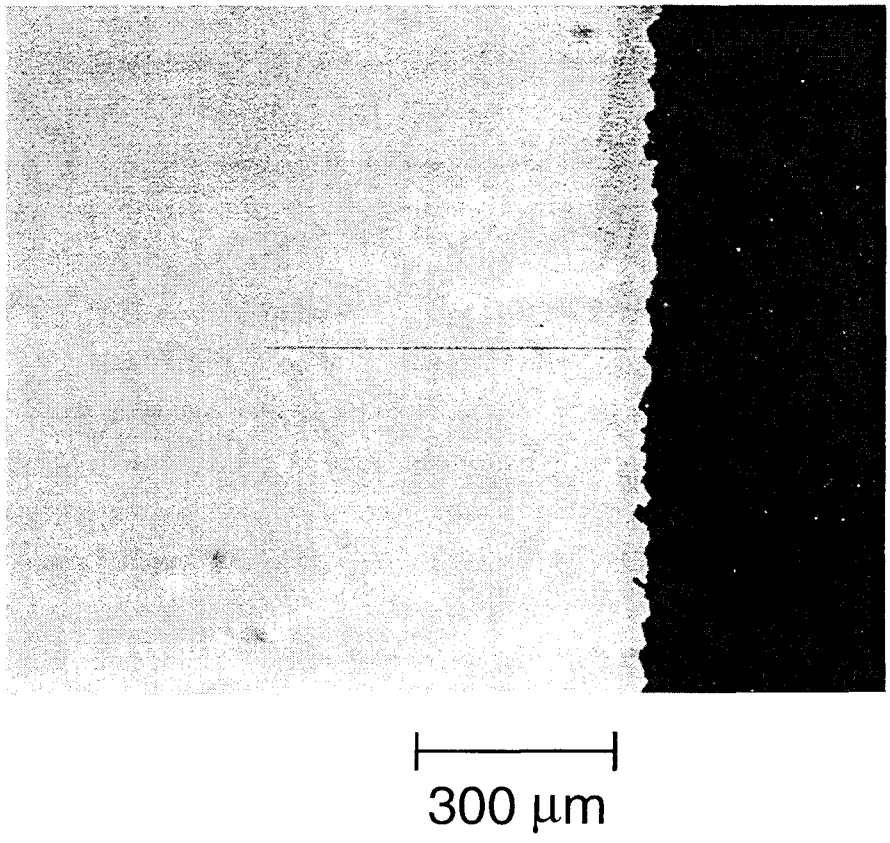

Figure 3.2: Surface of a $SrTiO_3$ bicrystal near the edge after a HF etch through a photomask. The grain boundary is clearly visible in the etched region.

in a beaker of trichloroethane for 3–4 minutes in an ultrasonic bath, followed by identical cleanings in isopropyl alcohol and methanol. I then rinse it with methanol and blow it dry with compressed N_2 gas. I inspect the surface under an optical microscope for any unremoved contaminants or solvent residue and repeat the cleaning steps as necessary.

(2) HF etch: Due to improvements in the quality of the bicrystals, we can no longer see the grain boundary under the microscope of the mask aligner. We must therefore define it artificially in order to later align it to the junctions. I spin photoresist onto the surface of the clean substrate and pattern a photomask which covers the entire surface except for two windows, about 0.5×0.5 mm^2, at the outer edges of the grain boundary. I then immerse the substrate into a 9% aqueous solution of hydrofluoric acid (HF) which etches the exposed $SrTiO_3$ surfaces with preferential etching along the grain boundary. I etch for about 15 seconds with slight agitation. Figure 3.2 shows the HF etched surface of a bicrystal with the grain boundary clearly visible. The grain boundary has an apperant width of about 1 μm and remains visible even when YBCO is deposited onto the bicrystal.

(3) Cleaning 2: I remove the photoresist by spraying the surface with acetone followed by ultrasonic agitation in a beaker of acetone. I then repeat the steps of (1) beginning with isopropyl alcohol.

(4) Preparing the PLD Chamber: I remove and polish the YBCO target that will be used, as described in Chapter 2, to remove the laser markings from the previous deposition. At this time, I also thoroughly clean the vacuum chamber with methanol to remove any YBCO from the previous deposition that may cover the chamber walls or fixtures. Usually there is significant covering of the fixtures closest to the plume. I found that if one does not clean the chamber every time, there is a marked degradation in the quality of the deposited films(lower T_c, to begin with, followed by increased 1/f noise), likely due to contamination from the amorphous YBCO in the chamber that may resputter onto the substrate.

* NOTE: Even with this regular cleaning procedure, after approximately every 100 depositions I notice a slight degradation in film quality, and then I usually remove parts from the chamber and clean them, along with the chamber itself, with 10% HNO_3 in DI water followed by methanol.

(5) Mounting the substrate: I mount the bicrystal onto the Hanes alloy heater block using the procedure described in Chapter 2. The Hanes alloy clip is in the form of a rectangular loop which grips two parallel sides of the substrate by about 0.5 mm and I

orient the grain boundary parallel to those sides, so that all of it, including the HF–etched edges, will be covered by YBCO. I then place the heater block into the chamber and attach the current leads and the thermocouple.

(6) Pumpdown and heating: I pump the chamber down to a base pressure of about 3×10^{-6} Torr. I then heat the substrate from room temperature to 810°C in 30-40 minutes. I check the temperature with the infrared pyrometer and inspect the surface of the substrate through the quartz window to make sure that it glows bright–red, an indication of good thermal contact.

(7) Preparing the laser: Simultaneously with step (6), I power up the laser and fire it at 1 Hz onto an external energy meter placed in front of the circular 7.9 mm–diameter aperture which sits in front of the output mirror. I adjust the internal laser energy so that the energy through the aperture is 75 mJ per pulse.

(8) Cleaning the target and depositing the film: Next I regulate the ambient O_2 pressure in the chamber to 210 mT and readjust the temperature. I then cover the substrate with the shutter, move the YBCO target into position, start it rotating, and fire the laser onto the rotating target at 10 Hz for 1–2 minutes to clean the surface. During this time, I orient the heater block so that the plume will reach the substrate in the center and normal to the surface. I then close the laser shutter, open the substrate shutter, reset the laser to fire at 5 Hz, and reopen the laser shutter to begin the YBCO deposition. At our deposition rate (Section 3.1), a 120–150 nm–thick film is deposited in about 12 minutes.

* NOTE: Until recently, we preceded the YBCO deposition by first depositing a 10 nm–thick buffer layer of STO at 760°C and 150 mT O_2. Its function was to smooth out any surface roughness in the substrate. I since discovered that it can actually add to the roughness and left that step out.

(9) Annealing: Following the YBCO deposition, I reduce the temperature to 780°C, and let in about 400 Torr of O_2 over a few minutes. I then cool the substrate to 450°C in 20 minutes. This is regulated by the temperature controller, which at the end of the cycle shuts off the heater which then cools to room temperature.

(10) Ag evaporation: Once it cools, I (carefully) remove the bicrystal from the heater block, attach it to a glass slide with double–sided tape, and cover the length of the grain boundary by a 4 mm-wide strip of Al foil which serves as a shadow mask. I evaporate 50 nm of Ag onto the substrate to cover the outer parts of the YBCO film which will be used for contact pads.

(11) Patterning: I spin photoresist onto the surface and bake it for 6 minutes on a hot plate at 70°C. I first pattern the bicrystal with the same mask that I used to define the windows for the HF etch in step (2). This removes the photoresist from the regions where the grain boundary is visible. I then align the SQUID mask over the bicrystal using the Canon 4X Mask Aligner. At the outer edges of the mask are alignment marks, a series of double rectangles separated vertically by 4 μm, the same as the lengths of the junctions, and spaced horizontally every 20 μm. By aligning the etched grain boundary to fall between these rectangles, I ensure that the grain boundary will intersect the junctions of all SQUIDs on the mask. The contact pads of the patterned SQUIDs fall onto the Ag–covered YBCO.

(12) Ion milling: Once patterned, I place the substrate into the vacuum chamber of the Nordiko ion mill, pump to a base pressure of 5×10^{-7} Torr and ion mill the surface at normal incidence for about 20 minutes or until the YBCO is milled through. I have made SQUIDs in this manner using both water and liquid nitrogen for cooling the substrate during milling, and both with and without rotation of the substrate, with comparable results. I then remove the photoresist with acetone in an ultrasonic bath.

(13) Wirebonding: Typically I make 12–15 SQUIDs on one chip. To test the SQUIDs, I glue the chip to a standard testing package which has 68 gold contacts for wire bonds. I make electrical connections between the Ag–covered contact pads of the SQUIDs and the gold pads of the package by ultrasonic bonding 25 μm diameter Al wires.

(14) Testing: I plug the test package into a mating piece on a cryogenic insert which has a field coil near the package and 72 banana connections at the top allowing electrical access to the SQUIDs from outside the cryostat. I lower the insert into a Dewar of liquid nitrogen surrounded by three concentric mu-metal shields and measure the I-V and the V-Φ characteristics of each SQUID in turn. This convenient procedure allows me to select a SQUID with the most optimal parameters for subsequent experiments.

Chapter 4

Multilayer Devices

4.1 Introduction

4.1.1 Background

As stated earlier, a flux transformer requires two superconducting layers separated by an insulating layer. The two superconducting layers must not short together except where one intentionally connects them through vias in the insulator. These are essential requirements of a multilayer interconnect technology, a necessary but, as we shall see, not sufficient condition for a practical SQUID magnetometer based on a flux transformer. Using the interconnect technology developed in our group prior to 1992, we could successfully fabricate multiturn flux transformers operating at 77 K [40, 32]. In this process, the first YBCO film, typically 300 nm thick was deposited on a $SrTiO_3$–buffered MgO substrate and patterned by wet etching in a 0.05–0.1% aqueous solution of HNO_3. The resist was stripped and the sample was immersed for a few seconds in a 1% solution of Br in methanol to etch the YBCO surface. Then the 400 nm–thick $SrTiO_3$ layer was deposited. Vias in the $SrTiO_3$ were patterned by photolithography and milled using an older Ag ion mill at an angle of 60°. After stripping the resist, we deposited a second YBCO film, typically 400 nm thick, and patterned it with an acid–etch.

With this interconnect process, former members of the group fabricated both flip–chip [40] and integrated [41] SQUID magnetometers. At the time, however, the noise in biepitaxial SQUIDs that were used in these devices limited the performance of the magnetometers. In 1992, we began fabricating the much quieter bicrystal SQUIDs using the

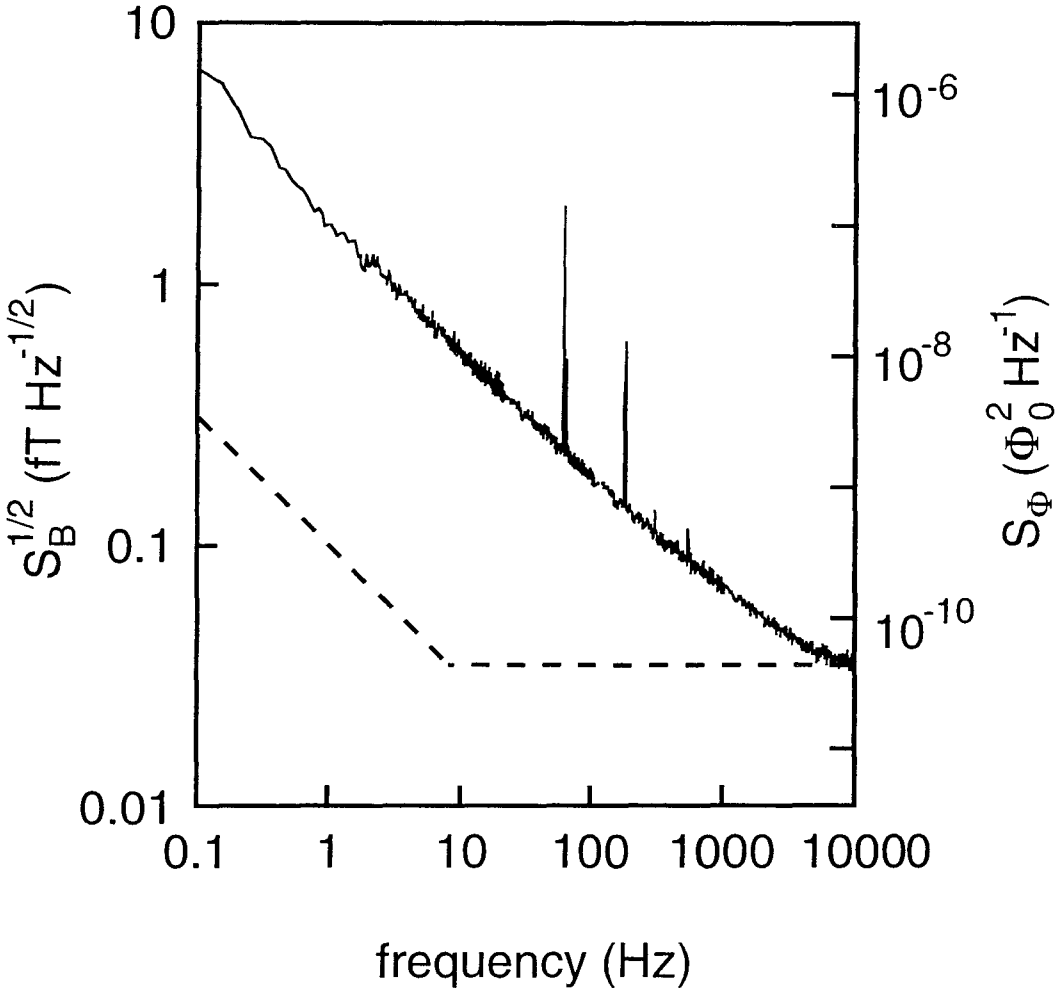

Figure 4.1: Magnetic field noise $S_B^{1/2}(f)$ and flux noise power $S_\Phi(f)$ vs frequency for a flux transformer, fabricated with the "early" process, coupled to a 40 pH bicrystal SQUID. Dashed line indicates flux noise power of the bare SQUID.

process described in Chapter 3. Shortly after measuring the noise of our first bicrystal SQUID, Andy Miklich coupled it to a flux transformer, made with the "early" process, in a flip–chip arrangement[32]. The transformer had a 81 mm^2 pickup loop and a 5–turn input coil; the SQUID was a 500-μm square washer with an inductance of 40 pH. Figure 4.1 shows the magnetic field sensitivity $S_B^{1/2}(f)$ and the equivalent flux noise power $S_\Phi(f)$ for this flip–chip magnetometer cooled in liquid nitrogen and measured in a flux–locked loop with bias reversal. The flux noise of the bare SQUID is indicated by the dashed line. The flux transformer increased the effective area of the SQUID by a factor of about 60, yielding a white noise of about 36 fT $Hz^{-1/2}$. However, at frequencies below a few kHz the noise power scaled as 1/f, caused by the motion of flux vortices in the YBCO films of the transformer. The high level of magnetic flux noise at 1 Hz limited the magnetic field resolution to 1.7 pT $Hz^{-1/2}$, rendering this device about 3 orders of magnitude less sensitive than the best low-T_c SQUID magnetometers and not very useful for most practical applications. These results stressed the need to improve our interconnect technology to obtain much lower levels of flux noise in our processed multilayers.

4.1.2 Strategy

The excess 1/f noise of a flux transformer is caused by the thermally–activated hopping of flux vortices among weak pinning sites in the YBCO films. An obvious strategy to lower this noise is to reduce the number of those sites by improving the quality of the films. Figure 4.2(a) shows a photograph of the input coil of a typical flux transformer. An enlargement of the inner via is shown in Figure 4.2(b). Within these regions one sees both single layer YBCO films and trilayers of YBCO–$SrTiO_3$–YBCO, as well as superconducting crossovers and a via – all are essential components of a multilayer flux transformer and all are potential regions for weak pinning cites. Therefore, we tackled the problem of reducing 1/f noise in the flux transformers by systematically improving the quality of each component in turn. We began by optimizing single layer YBCO films for low flux noise as measured with a low–T_c SQUID. These efforts led to the process for low noise YBCO films and, consequently, low–noise bicrystal SQUIDs, as described in Chapter 3. Next, we turned to *in situ* trilayers of YBCO–$SrTiO_3$–YBCO, followed by *ex situ* trilayers, patterned trilayers (crossovers and vias) and, finally, complete flux transformers. Driven by this strategy, we decided to focus on a flip–chip magnetometer as our near–term goal. We would use a YBCO

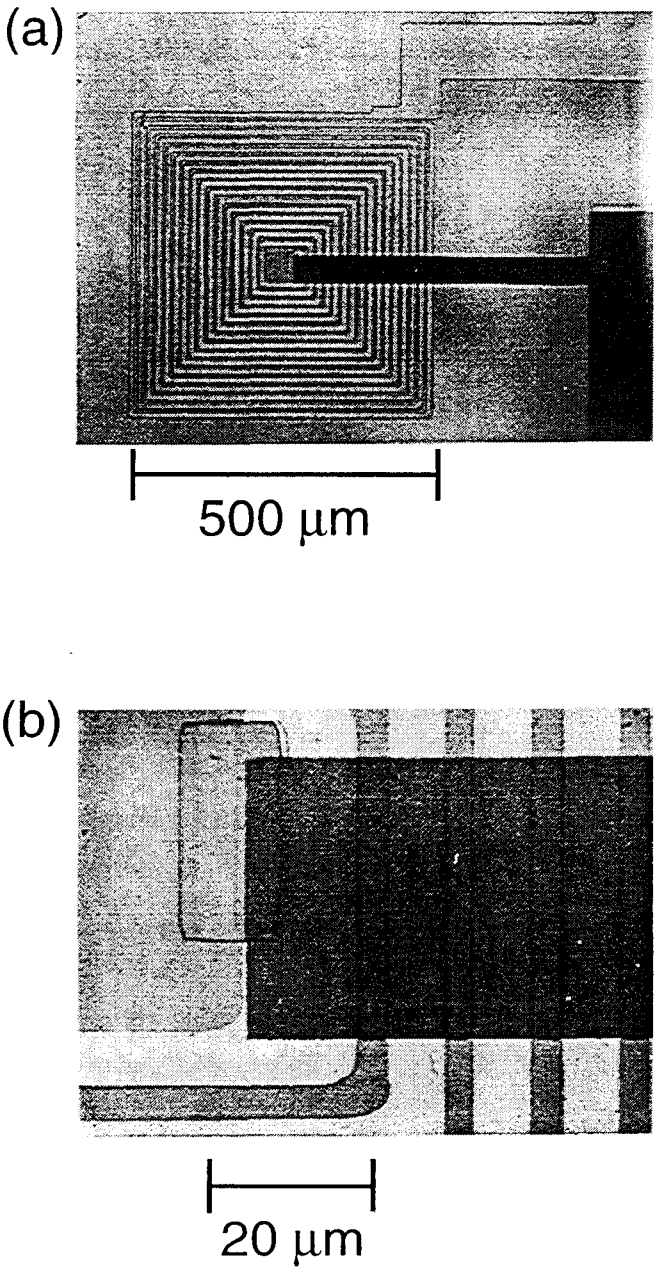

Figure 4.2: (a) Photograph showing the 16–turn input coil of a flux transformer. The coil, patterned in the lower YBCO layer is connected to the pickup loop (not shown). The (black) crossover is in the upper YBCO. (b) Close–up view of the via, connecting the crossover to the inner turn of the input coil.

bicrystal SQUID to both characterize the noise in the components and to form the final magnetometer.

4.2 *In situ* YBCO–STO–YBCO Trilayers

To decouple the effects associated with photolithography and other processing steps on the noise increase, we first examined multilayer films grown *in situ*, that is, without breaking vacuum between depositions. We continued using STO as the insulating layer because of its excellent lattice match to YBCO. We concentrated on YBCO–STO–YBCO trilayers, the most fundamental component of a multilayer flux transformer. We made the trilayers on STO substrates using the same deposition rate and laser beam parameters developed in the course of our work on single–layer YBCO films (Chapter 3). The key changes from the "early" multilayer process [25] that yielded substantial improvements in the quality of the new trilayers were thinner films for all three layers and a lower substrate temperature for the deposition of the upper YBCO film. In the optimized trilayer process, we deposited a 10 nm STO buffer onto a STO substrate at a temperature T=760°C and ambient O_2 pressure p=150 mTorr, followed by 120 nm of YBCO (T=810°C, p=210 mTorr), 250 nm of STO (p=760°C, p=150 mTorr), and 250 nm of YBCO (T=790°C, p=210 mTorr). We typically measured $T_c = (88 - 89)$ K and $J_c = (2 - 3) \times 10^6$ for the upper YBCO film. X–ray diffraction measurements indicated a high degree of crystalline quality: the full–width at half maximum of the rocking curve of the (005) peak was below 0.3°. To investigate the flux noise of trilayer films, we coupled them to our YBCO bicrystal SQUID in a flip–chip arrangement and measured the noise at 77 K. Figure 4.3 shows that the presence of the trilayer did not increase the 1/f noise of the SQUID over its rms value of $S_\Phi^{1/2}(1\mathrm{Hz}) = 15\mu\Phi_0\,\mathrm{Hz}^{-1/2}$. By comparison, the flux noise of the *in situ* trilayers fabricated with the "early" process was always above $100\mu\Phi_0\,\mathrm{Hz}^{-1/2}$ [27].

4.3 Patterned YBCO–STO–YBCO Trilayers

The noise of our *in situ* trilayers is in principle low enough to make multiturn flux transformers which do not couple excess low–frequency flux noise into the SQUID. However, each film in the multilayer structure must be patterned, which produces edges over which subsequent layers must grow with a high degree of crystalinity. Furthermore,

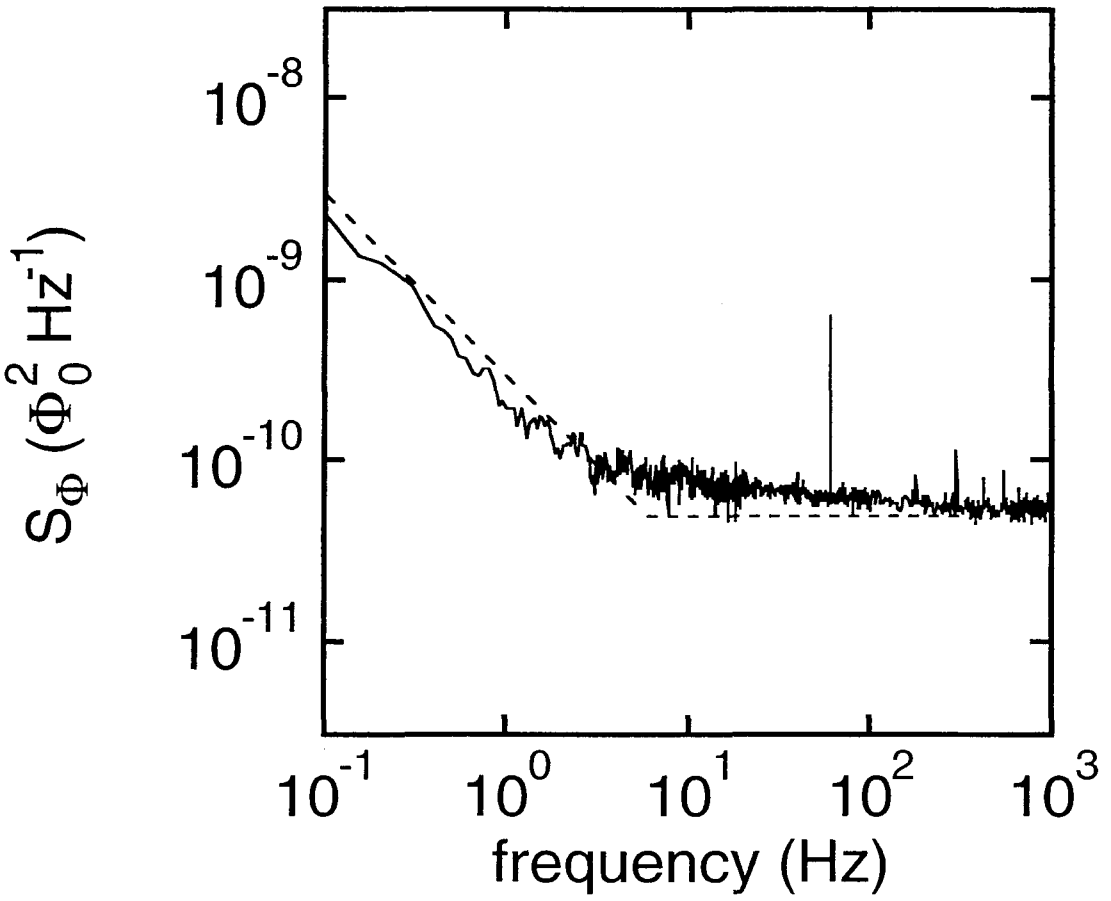

Figure 4.3: Magnetic flux noise power $S_\Phi(f)$ vs frequency for an *in situ* YBCO–STO–YBCO trilayer. Dashed line indicates flux noise of bare SQUID.

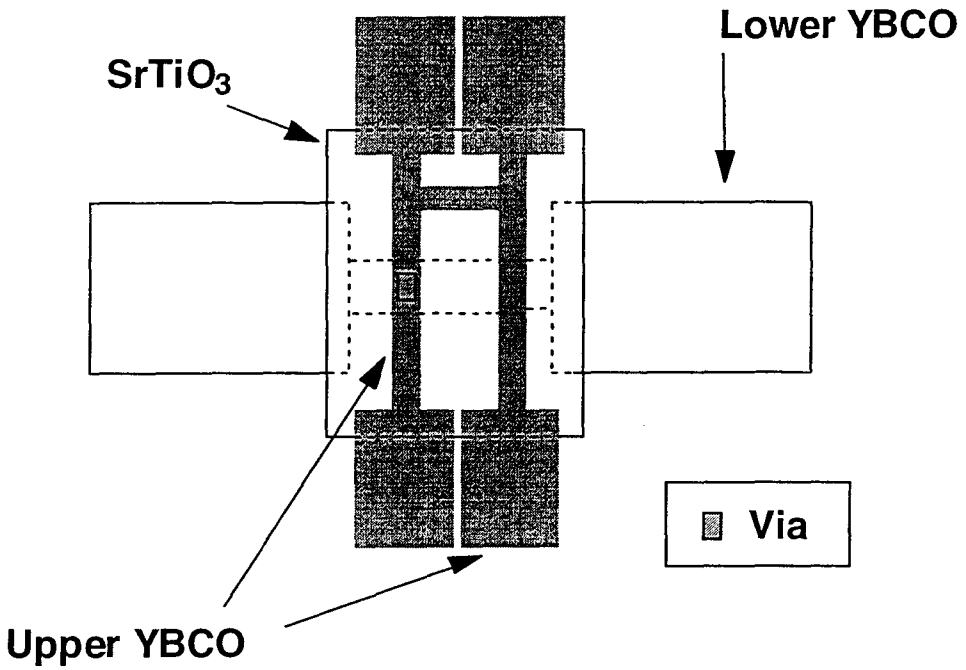

Figure 4.4: Interconnect test structure for the YBCO–STO–YBCO trilayer process that allows independent measurements of the lower YBCO, the upper YBCO, crossover, and via. Drawing is simplified for clarity; actual structure contained two crossovers and two vias.

the patterning exposes each film to photolithographic chemical processing which can affect the growth of subsequently deposited films. To study the transport properties of the various transformer components, we fabricated interconnect test structures (Figure 4.4) to enable us to make independent electrical measurements of the lower and upper YBCO films, the crossover where the upper YBCO passes over the edges produced by the lower film, the via connecting them through the insulating layer, and the insulation itself. To investigate the flux noise of these processed multilayers we periodically made flux transformers and coupled them to a SQUID in a flip–chip arrangement.

4.3.1 Edge Effects

In our initial work to improve the multilayer interconnect process we used film thicknesses and deposition parameters that yielded the low–noise *in situ* trilayers, but borrowed some of the patterning techniques from the "early" process developed by our predecessors [42, 25]. Following that process, we wet etched the lower YBCO film in 0.05% HNO_3 and etched it for 5–6 seconds in a 1% solution of Br in methanol. We then deposited the STO insulating layer and cut vias with the Ar ion mill at a 60° angle of incidence. In contrast to the former process, the ion milling also removed all of the lower YBCO film in the window area, leaving only a beveled edge to make contact to the upper YBCO film, which was also wet etched.

We found that $J_c(77\ \mathrm{K})$ for the upper YBCO film remained at $(2-3)\times 10^6 \mathrm{Acm}^{-2}$ even where it crossed the edges of the lower YBCO strip, at least one order of magnitude improvement over the "early" process which used thicker YBCO and STO films. To investigate this further, we performed[1] scanning electron microscopy (SEM) of wet–etched YBCO films of different thicknesses exposed to a Br etch. Figure 4.5 shows SEM images of the edges of YBCO (a) 300 nm thick without the Br etching and (b) 200 nm thick after a 10 s Br etch. We see that the edge of a wet–etched YBCO film is nearly perpendicular to the substrate. The Br etch rounds the upper part of this edge; for thicknesses below 150 nm, the entire edge tends to become beveled. Thus the Br etch can produce reasonably smooth edges for thinner films, but steep edges remain for thicker films, which may have introduced disorder and grain boundaries into the "early" interconnect process resulting in low critical currents at 77 K. Note, however, that the surfaces in Figure 4.5 have been roughened by

[1]Thanks to Silvia Knappe.

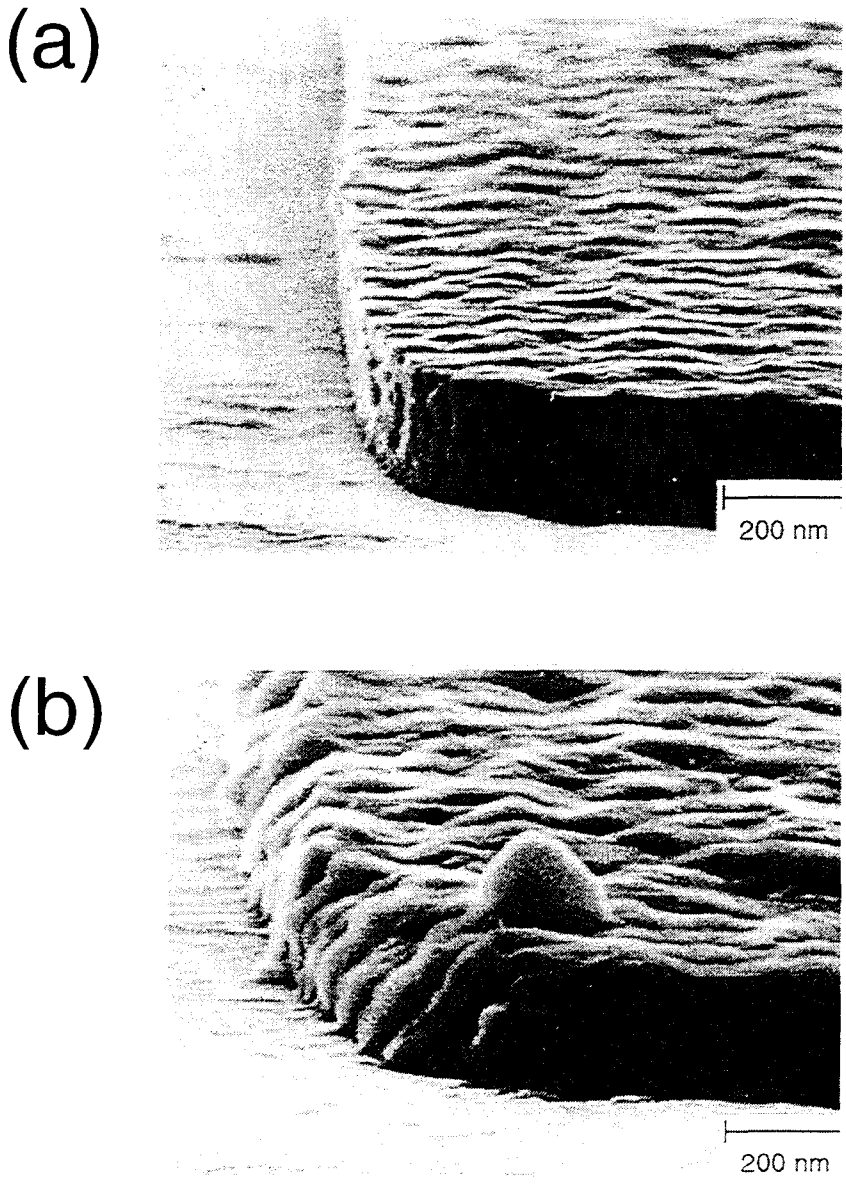

Figure 4.5: SEM image of (a) 300 nm–thick YBCO film etched in 0.05% HNO_3 with no Br etch and (b) 200 nm–thick YBCO film etched in 0.05% HNO_3 with a 10 second etch in 1% Br in methanol.

the etching process.

For 30μm–wide via contacts to a 100 nm–thick lower YBCO film the critical current I_c(77 K) was typically 15 mA, corresponding to $J_c \approx 5 \times 10^5 \mathrm{Acm}^{-2}$. Although this value is almost one order of magnitude lower than for single films, it is adequate for flux transformers. The resistivity of the STO, measured between the upper and the lower YBCO films over an area of $20 \times 100\,\mu\mathrm{m}^2$, was typically $10^8\,\Omega\,\mathrm{cm}$ or higher, at 77 K [27].

4.3.2 Surface Effects

At this stage, Frank Ludwig, David Nemeth and I used the above interconnect technology to fabricate a series of flux transformers with pickup loop areas of either 68 or 81 mm^2, and mostly with 16–turn input coils. The input coil and the pickup loop were patterned in the lower YBCO film, with linewidths of 7 μm and 1 mm, respectively. The input coil was 500 μm across. Out of eight flux transformers, seven operated at 77 K, indicating that the fabrication process was fairly reproducible. Dieter Koelle and Andy Miklich coupled each transformer in turn to a 500 μm bicrystal SQUID in a flip–chip arrangement. Figure 4.6 shows $S_B^{1/2}(f)$ and $S_\Phi(f)$ vs frequency for the best magnetometer out of this series, measured with bias reversal. The gain in effective area was 70, yielding $S_B^{1/2}$(1kHz)=30 fT Hz$^{-1/2}$ and $S_B^{1/2}$(1Hz)=340 fT Hz$^{-1/2}$. The latter value represented a factor of five improvement over the best flip–chip magnetometer fabricated with the "early" process. Nevertheless, the rms flux noise at 1 Hz was still a factor of five above that of the bare SQUID, implying that noise from the flux transformer still dominated at low frequencies.

To investigate the origin of the low–frequency noise, on some of the flux transformer chips we patterned single layer, bilayer, and trilayer test regions which underwent the same processing as the rest of the transformer and which could be positioned directly over the SQUID. We found that the 1/f noise of processed *ex situ* trilayers was much higher than in the *in situ* trilayers described earlier, although we could not rule out the possibility that the YBCO films at the edges of the via and crossover also contributed to the noise.

To decouple the effects of processing on the surface from those on the edges, we studied the growth of STO on a YBCO film that had been subjected to the usual processing but not patterned: Frank Ludwig deposited a 120 nm–thick YBCO film on a STO substrate buffered with 10 nm of STO, spun on photoresist, developed, and removed it with acetone

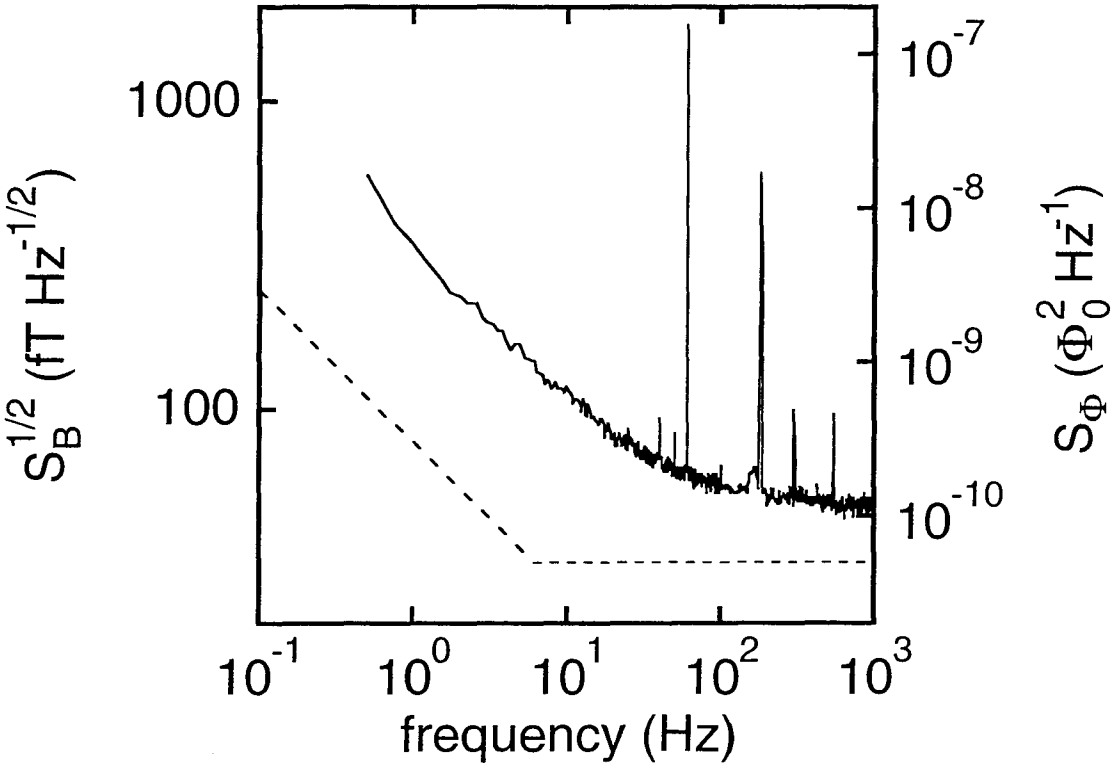

Figure 4.6: Magnetic field noise $S_B^{1/2}(f)$ and flux noise power $S_\Phi(f)$ vs frequency for a flux transformer with a 16–turn input coil coupled to a 40 pH bicrystal SQUID. Dashed line indicates flux noise power of the bare SQUID. Both were measured with bias reversal.

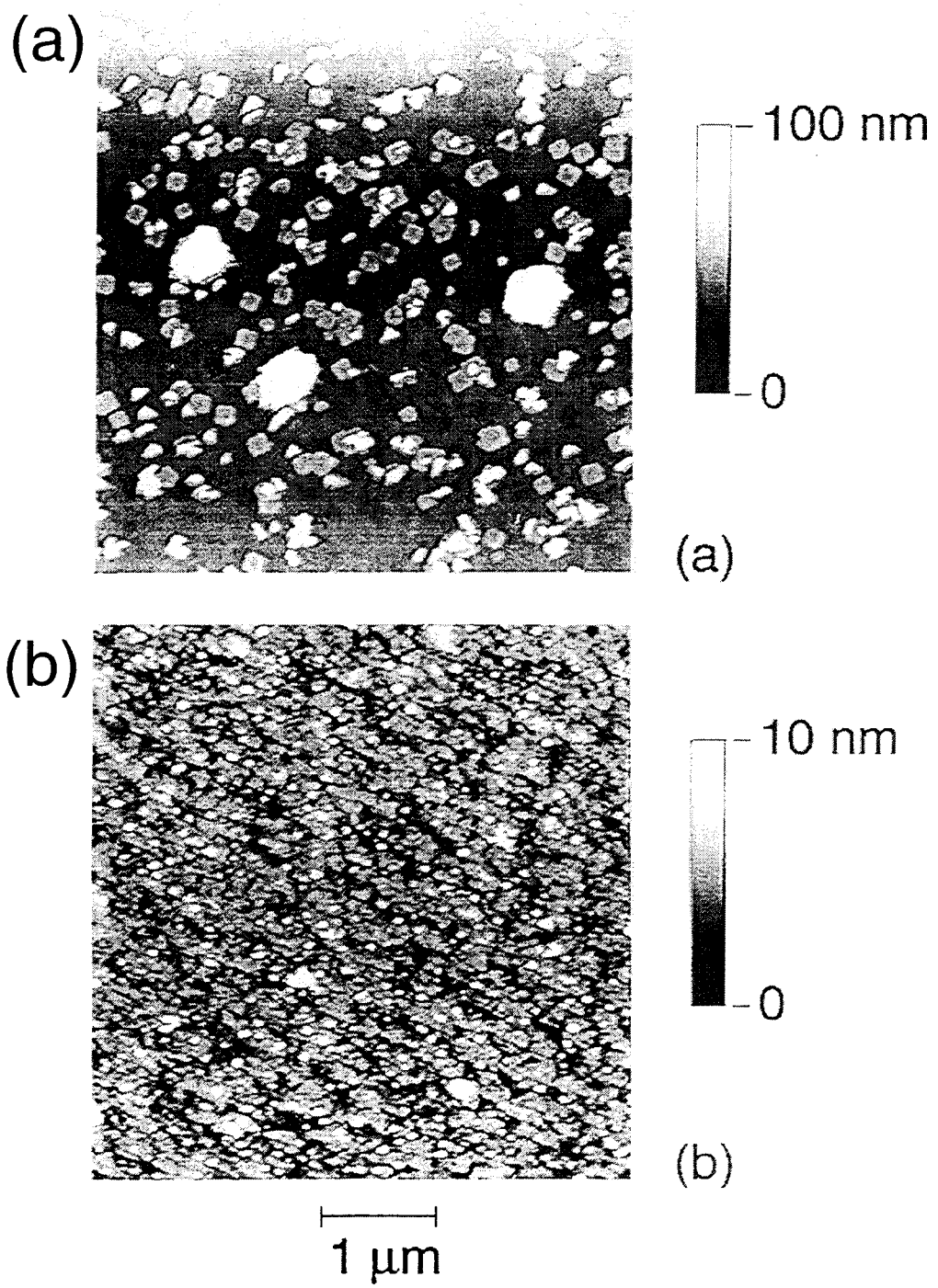

Figure 4.7: Atomic force microscopy (AFM) image of STO deposited on a YBCO film (a) without and (b) with an *in situ STO cap* layer

and then etched the sample for 5 s in a 1% solution of Br in methanol. He then deposited a 250 nm–thick STO film. The surface of the bilayer imaged with an atomic force microscope[2] is shown in Figure 4.7(a). In addition to several large (100–150 nm high) particles, there are many plate–like particles, typically 200 nm on a side and 20 to 25 nm high, on a relatively smooth surface with a roughness of a few nm. It is very likely that the poor growth in the STO film, which obviously determines the structure of the upper YBCO film, is induced by damage on the lower YBCO film produced by photoresist and Br etching.

We took several measures to reduce the exposure of the lower YBCO film to chemical processes that could potentially damage the surface. We stopped using Br to round or bevel the edges of the YBCO. Also we chose not to pattern the YBCO films by wet etching in HNO_3. Instead, we ion milled the film at a 60° angle of incidence while rotating the substrate about an axis normal to its surface on a water–cooled stage, to both pattern and create beveled edges in all directions. Furthermore, like some other groups [43, 44], we capped the lower YBCO film with a thin *in situ* STO film before the first patterning. Figure 4.7(b) shows the surface of a bilayer in which Frank capped the lower YBCO film with a 15 nm–thick *in situ* STO film before exposing it to photoresist. As before, he deposited a 230 nm–thick film of STO after removing the resist. The particles evident in Figure 4.7(a) are no longer present and the overall surface roughness is 2–3 nm.

4.4 A New Multilayer Interconnect Process

We modified our fabrication process by introducing the capping step as well as the other modifications mentioned in the last section. Frank Ludwig was instrumental in developing the final "standard" version of this process which I will briefly describe [45]. The thicknesses and deposition parameters for each layer are listed in Table 4.1. The procedures regarding cleaning the chamber, polishing the targets, mounting the sample, etc., described in Section 3.3 for a single layer deposition, apply here for each individual layer.

After depositing the lower YBCO film, it is capped by a 15 nm–thick *in situ* STO layer. The sample is then cooled to 500°C in 30 minutes and held at that temperature for an additional 30 minutes to oxygenate the lower YBCO film fully, before cooling it to room temperature. The capped lower YBCO film is then patterned by standard photolithography. To bevel the edges of the film, after the photoresist is developed, it is baked for 10 minutes

[2]Thanks to Ruth Ellen Thomson.

Layer	Thickness (nm)	Deposition temperature (°C)	Oxygen pressure (mTorr)	T_c (K)	J_c(77 K) (10^6 A cm^{-2}
lower YBCO	120–150	810	210	85	1–2
STO cap	15	760	150	–	–
STO insulator	230	760	150	–	–
upper YBCO	250	790	210	89	3

Table 4.1: Deposition parameters for the new multilayer process.

at 120°C to round the edges of the resist. The structure is then ion milled at a 60° or 45° angle of incidence while the substrate rotates on a water cooled stage.

After the photoresist is stripped in acetone, the sample is remounted into the deposition chamber, heated to 760°C in 250 mT of O_2, and a 230 nm–thick STO insulator film is deposited. In our prior process a 20 minute cooldown from 780°C to 450°C in 0.8 atm of O_2 was sufficient to oxygenate the lower YBCO film fully after it had been covered by the 230 nm–thick STO film. However, the high crystalline quality of the STO insulator with the capping process inhibits oxygen diffusion into the lower YBCO film. Therefore to re-oxygenate the lower YBCO film a longer anneal is required; the film is cooled to 500°C in 30 minutes in 0.8 atm O_2 and held at that temperature for 3 hours before cooling to room temperature. Vias are then patterned in the STO, as before, and ion milled at a 60° angle of incidence, while the substrate rotates on a water cooled stage, to create beveled edges for an in–plane contact between the upper and the lower YBCO films. Finally, after stripping the resist, the substrate is replaced in the chamber, heated in 250 mT of O_2 to 790°C, and the upper YBCO film is deposited. The upper YBCO is patterned by photolithography and ion milling at normal incidence.

The key component of this new multilayer process is the capping of the lower YBCO film by a 15 nm–thick STO cap which, evidently, is less susceptible to photolithographic processing than uncapped YBCO. However, the high crystalline quality of both the cap and the subsequently grown STO insulation layer, make it difficult to keep the lower YBCO oxygenated. Our first several flux transformers made with this process, but without special annealing steps, did not work at 77 K; we discovered that the T_c of the lower YBCO was about 40 K. Using the longer anneal times at 500°C, we succeeded in

improving the T_c to 85 K and $J_c(77\ K)$ to $(1-2)\times 10^6 A\,cm^{-2}$, but we never fully recovered the parameters that we routinely measured in bare YBCO films, namely $T_c = 90 - 92$ K and $J_c = (3-10)\times 10^6 A\,cm^{-2}$. On the other hand, crossovers fabricated with this process typically have $T_c = 89$ K and $J_c = 3\times 10^6 A\,cm^{-2}$.

This process yielded our lowest–noise multilayers todate and was consequently used to fabricate flux transformers for flip–chip magnetometers as well as integrated magnetometers and multiloop magnetometers. Details of these devices are described in Part III: Magnetometers – in Chapters 6, 7, and 8, respectively. Grundler *et al.* [43] have used a similar technique to protect the surface of their lower YBCO film from chemical processing. Alternatively, Shen *et al.* [46] do not cap the lower YBCO, but rather strip the damaged layer using an O_2 plasma etch.

Part III

SQUID Magnetometers

Chapter 5

Single Layer YBCO SQUID Magnetometers

For reasons outlined in Chapter 4, the development of a magnetometer based on a SQUID, coupled to a flux transformer, required us to overcome a number of materials and processing challenges in order to bring down the level of the 1/f noise in our multilayer structures. On the other hand, our SQUIDs and single layer films made with the process described in Chapter 3 typically exhibited no 1/f flux noise above 1 Hz. Therefore concurrently with our work on improving multilayers, we considered various magnetometer designs that could be made from single YBCO films. In this chapter I describe some of our more successful single layer devices. It will become apparent that, although they are ultimately not as sensitive as multilayer magnetometers of equal size, properly designed single layer magnetometers can be sufficiently sensitive and useful in a number of applications which will be described in Chapters 9 and 13.

5.1 Design Considerations

As was discussed in Section 1.4, to convert a flux-sensitive SQUID into a field-sensitive magnetometer one must increase its effective area while maintaining low SQUID inductance. We considered several approaches to this, constricted to single layer YBCO films on a 10 x 10 mm^2 bicrystal. One method was simply to increase the outer dimension D of the SQUID washer [47] thereby using flux focusing to enhance the area [48, 17]. The rather large area of the YBCO, however, limited our ability to use bias reversal due to flux

motion in the film[17].

A more successful approach called a *directly coupled magnetometer* [49] is illustrated in Figure 5.1 and the rest of the chapter will be devoted to this device. It consists of a square pickup loop of YBCO directly connected to opposite sides of the SQUID body. A magnetic field applied to the magnetometer induces a superconducting screening current in the loop which is injected directly into the body of the SQUID. Since the junctions are biased in the voltage state, the current couples to a fraction α_d of the SQUID inductance L, just below the junctions in Figure 5.1(b). The effective area of this magnetometer is therefore

$$A_{eff} = A_s + \alpha_d L \frac{A_p}{L_p} \tag{5.1}$$

where A_p and L_p are the area and inductance of the pickup loop, respectively, and A_s is the effective area of the bare SQUID (negligible in most cases). It is instructive to compare Equation 5.1 with the equivalent expression for a SQUID of inductance L, inductively coupled to a flux transformer with a n-turn input coil. We showed in Section 1.4 that the effective area of an optimized SQUID magnetometer in the tight coupling limit is $A_{eff} = A_p/2n$ where $n = \sqrt{L_p/L}$. Therefore, for a pickup loop of given size and shape, there is a factor of $n/2 = (\sqrt{L_p/L})/2$ gained in effective area by coupling to the SQUID via an input coil, whose inductance is matched to that of the pickup loop, over direct coupling.

To maximize A_{eff} in Equation 5.1, we must maximize the ratio A_p/L_p and use the largest SQUID inductance L permitted by other constraints. For a square pickup loop of outer width D_p and inner width d_p, A_p/L_p approaches a maximum of $D_p/1.25\mu_0$ in the limit[1] $d_p < \frac{1}{3}D_p$ [14]. If one increases L, one must take account of the corresponding decrease in the SQUID transfer function V_Φ and therefore the increase in the flux noise power $S_\Phi(f) = S_V(f)/V_\Phi^2$. Thus to estimate the magnetic field noise $S_B^{1/2}(f) = S_\Phi^{1/2}(f)/A_{eff}$ we take $S_V(f) \approx 16k_BTR$ and use Equation 1.10 for V_Φ at 77 K

$$V_\Phi = \frac{4I_0R}{\Phi_0(1+\beta)}\left(1 - \sqrt{\frac{L}{321pH}}\right) \tag{5.2}$$

where $\beta = 2LI_0/\Phi_0$. Figure 5.2 shows the calculated values of $S_B^{1/2}(white)$ versus the SQUID inductance L where we assumed $I_0 = 50\,\mu$A and $R = 2\,\Omega$. There is a shallow

[1]In this limit the pickup loop resembles a square washer; therefore as shown by Ketchen and Jaycox [14] $L_p \approx 1.25\mu_0 d_p$ and $A_p \approx d_p D_p$.

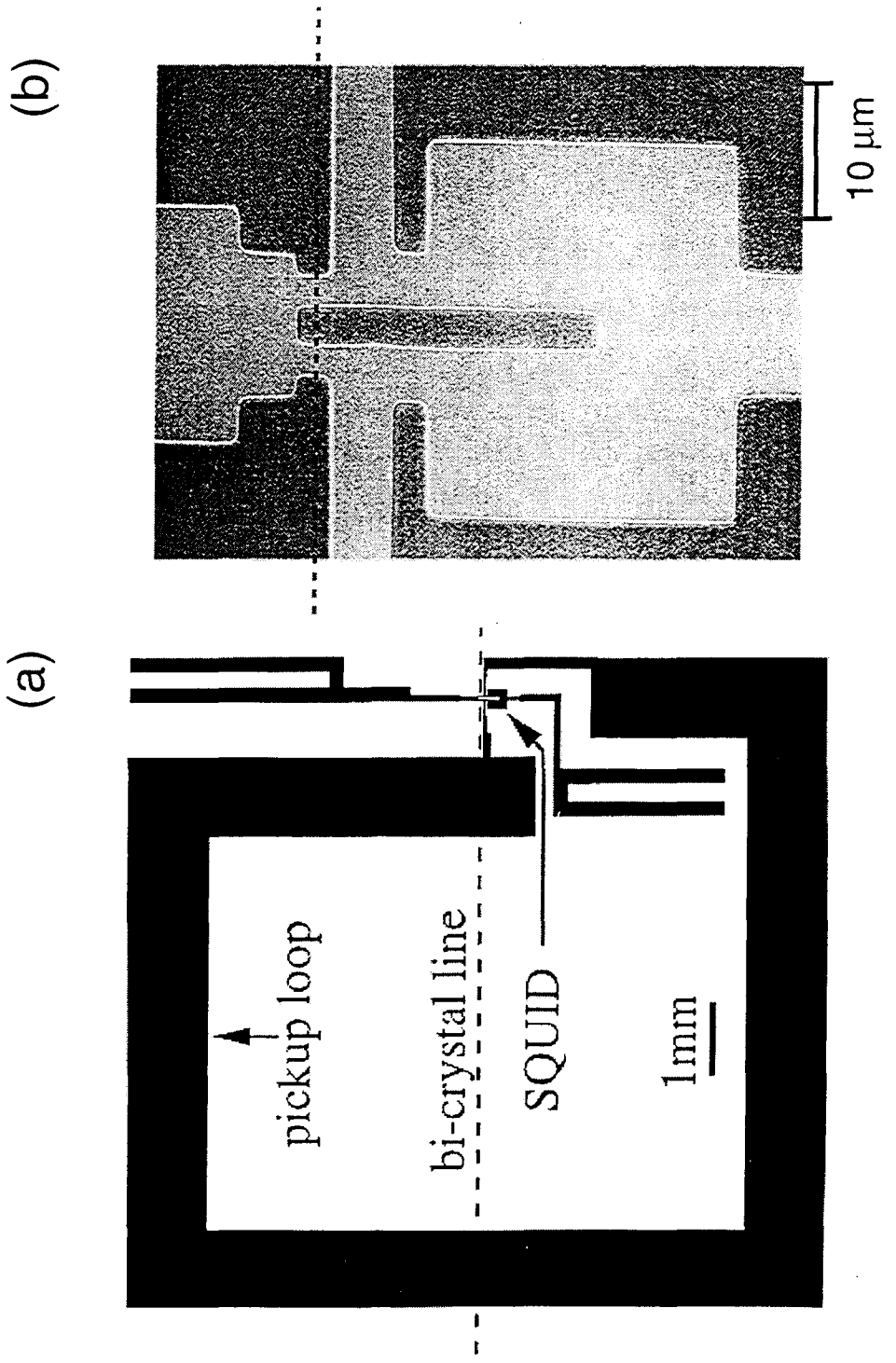

Figure 5.1: (a) Configuration of directly coupled magnetometer. (b) SEM image showing detail of coupling to the bicrystal SQUID. Dashed line indicates grain boundary.

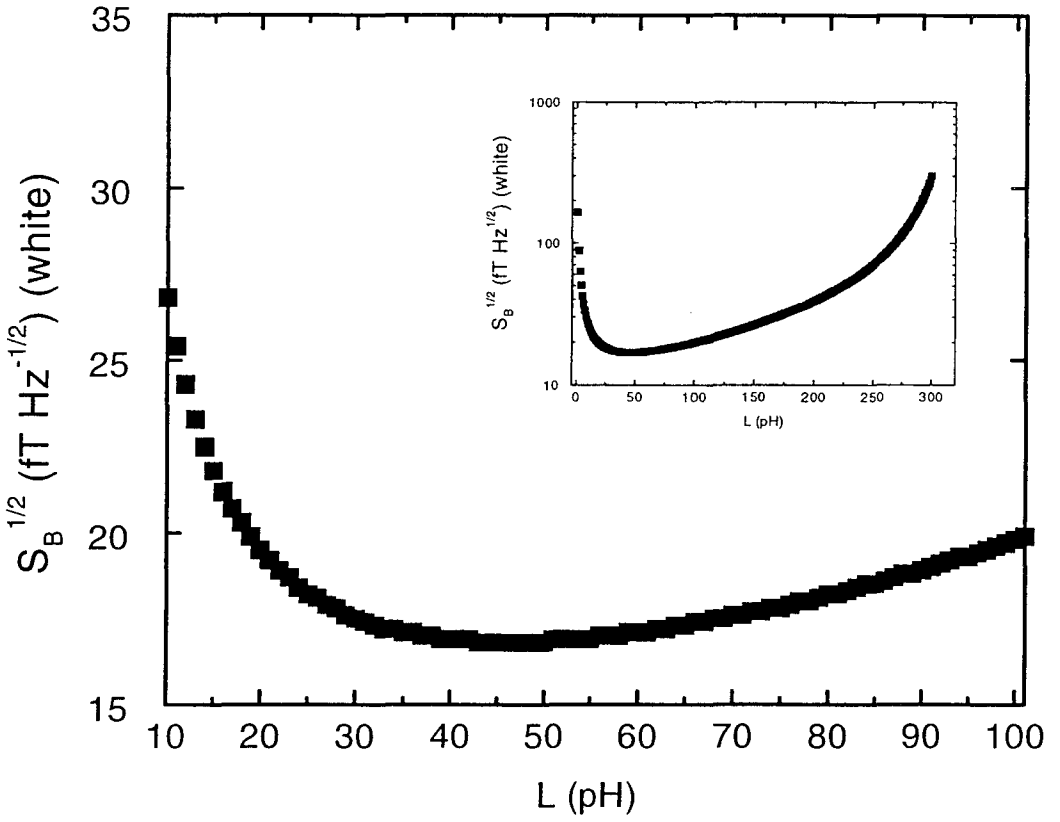

Figure 5.2: Calculated magnetic field noise, $S_B^{1/2}$ in the thermal noise limit, vs inductance L for a directly coupled magnetometer with $I_0 = 50\,\mu A$ and R=2.0 Ω.

Device(#)	I_0 (μA)	R (Ω)	L (pH)	V_Φ ($\mu V/\Phi_0$)	A_{eff} (mm^2)	$S_\Phi^{1/2}$(white) ($\mu\Phi_0\,Hz^{-1/2}$)	$S_B^{1/2}$(white) ($fT\,Hz^{-1/2}$)
1 (833)	45	2.1	145	7.1	0.29	40	290
2 (981)	70	3.2	40	93	0.13	6	105
3 (984)	70	2.3	40	73	0.14	14	210
4 (1019)	45	3.4	20	220	0.086	3.9	93

Table 5.1: Parameters for 4 directly coupled magnetometers. Critical current I_0 and resistance R are given per junction.

minimum in the field noise between 20 pH and 90 pH with an absolute minimum near 50 pH.

5.2 Early Directly Coupled Magnetometers

We now turn to the measured performance of various directly coupled magnetometers made by our group. Andy Miklich and Dieter Koelle were primarily responsible for the pioneering work (1992–1993) described in this section [17]. We fabricated a total of four devices whose geometry is shown in Figure 5.1 and their various parameters are listed in Table 5.1. Each magnetometer was patterned in a 200 nm–thick YBCO film, deposited on a 10x10 mm^2 STO bicrystal, and etched in an 0.05% aqueous solution of HNO_3 (devices 1-3) or by ion milling (device 4). As shown in Figure 5.1, one set of bias leads was placed inside the pickup loop. All leads were subsequently covered with 50 nm of Ag through a shadow mask and repatterned by ion milling.

Each magnetometer was characterized in liquid nitrogen in a dewar surrounded by three mu–metal shields; a cold Conetic shield surrounded the SQUID mount. For noise measurements, the SQUID was operated in a 100 kHz–modulated flux–locked loop with a static bias and with bias reversal. Figure 5.3 shows the rms magnetic field resolution, $S_B^{1/2}(f)$, and the equivalent flux noise power, $S_\Phi(f)$, for device 4 measured using both biasing techniques. With static bias the flux noise power scales approximately as 1/f for frequencies below 1 kHz. As was the case with our bare SQUIDs, the use of bias reversal here reduces the 1/f noise dramatically, by more than two orders of magnitude in power at 1 Hz. This indicates that the primary source of 1/f noise were critical current fluctuations in the junctions. Operated with bias reversal, the noise spectrum is white down to a few Hz.

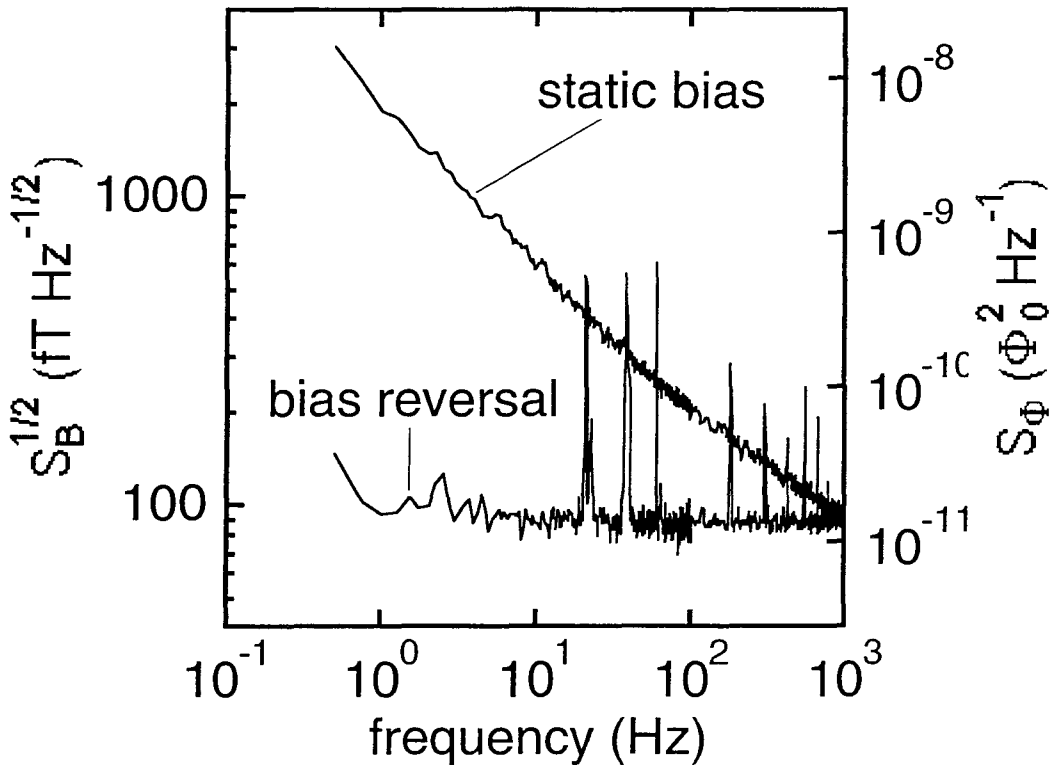

Figure 5.3: rms magnetic field noise, $S_B^{1/2}(f)$, and flux noise power, $S_\Phi(f)$, vs frequency for directly coupled magnetometer 4 measured with static current bias and bias reversal.

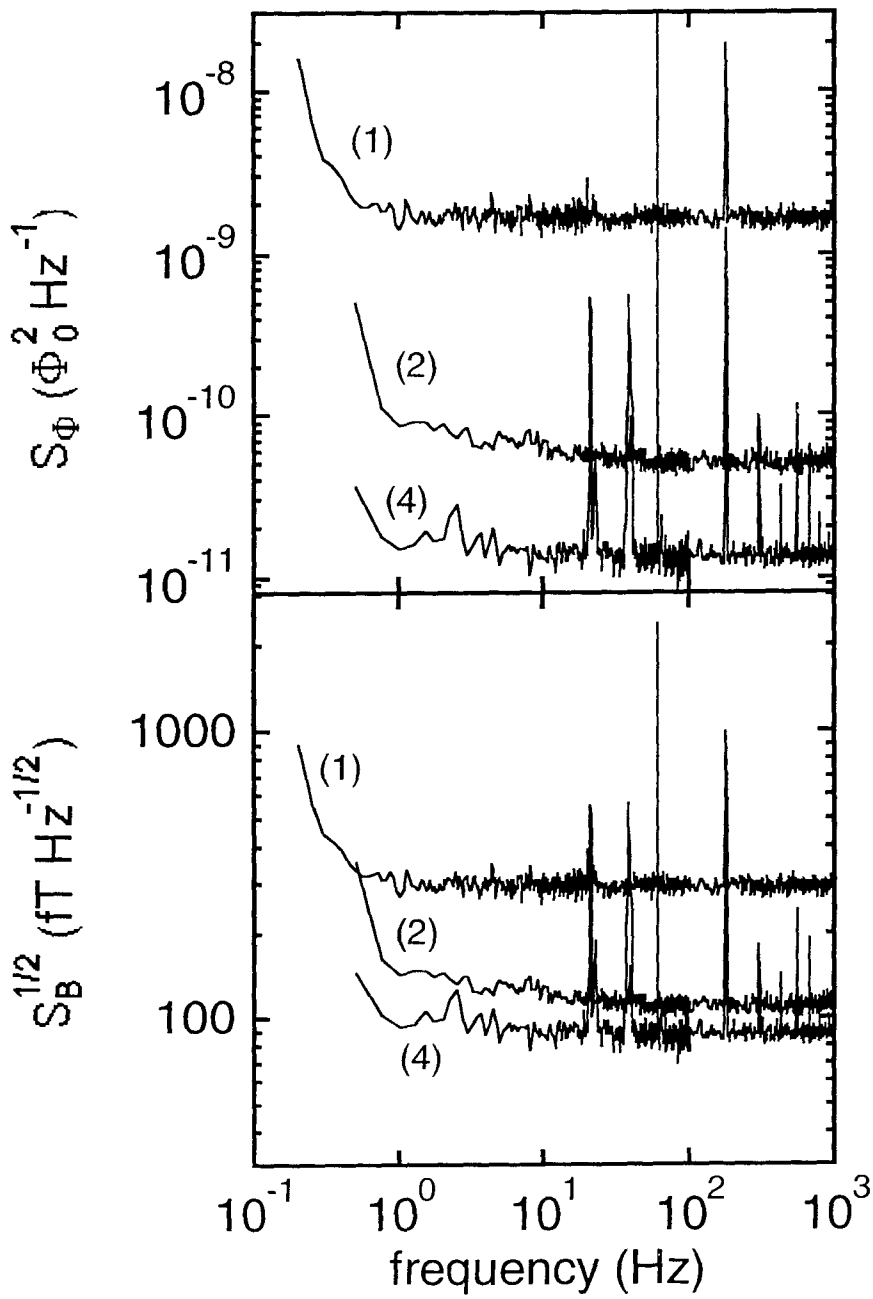

Figure 5.4: (a) $S_\Phi(f)$, vs frequency for three directly coupled magnetometers measured with bias reversal. Numbers refer to Table 5.1. (b) rms magnetic field noise, $S_B^{1/2}(f)$ vs frequency for the same devices.

We now compare the designs and relative performances of the directly coupled magnetometers listed in Table 5.1. Figure 5.4(a) compares the flux noise power for devices 1, 2, and 4 (device 3 was nominally identical to device 2), all measured with bias reversal. Figure 5.4(b) compares the measured magnetic field resolution for those devices. Devices 1–3 had pickup loops of outer dimensions 8×9 mm^2 and a linewidth of 1 mm. Of those, device 1 had a SQUID with an inductance of 145 pH which resulted in a rather small transfer function V_Φ of 7.3 $\mu V/\Phi_0$ at 77 K, limiting the flux noise $S_\Phi^{1/2}$ to 40 $\mu\Phi_0 Hz^{-1/2}$ in the white noise region. Reducing the SQUID inductance to 40 pH in devices 2 and 3 increased the transfer function to 93 and 73 $\mu V/\Phi_0$, respectively, decreasing the flux noise. Device 4 used a pickup loop with a linewidth of 2 mm and a SQUID with an inductance of 20 pH. The lower inductance helped raise V_Φ to 220 $\mu V/\Phi_0$ thereby reducing the flux noise to $3.9\,\mu\Phi_0\,Hz^{-1/2}$, while the larger linewidth increased A_p/L_p, thus raising the effective area. In general, lowering the SQUID inductance, in all cases, also reduced the effective area, however, the greater relative reduction in flux noise increased the net magnetic field resolution [albeit by progressively smaller factors as seen in Figure 5.4(b)].

The best directly coupled magnetometer (device 4) had a magnetic field resolution of 93 fT Hz$^{-1/2}$ at frequencies down to below 1 Hz. This resolution appeared adequate for a number of applications, some of which will be outlined in Part III. By contrast, at that time our best magnetometer based on a SQUID and a multilayer flux transformer had a white noise level of 40 fT Hz$^{-1/2}$, but the 1/f noise due to vortex motion in the multilayers limited the field resolution at 1 Hz to about 340 fT Hz$^{-1/2}$. The higher sensitivity at low frequencies and the relative ease of fabrication, requiring only one deposition and patterning step, made the directly coupled magnetometers somewhat more attractive and precipitated further work on single layer devices.

5.3 Directly Coupled Magnetometers with Single Layer YBCO Flux Transformers

To increase further the effective area of a directly coupled SQUID magnetometer we coupled it to a single–layer flux transformer patterned in a YBCO film on a 50 mm wafer [50]. The films were fabricated by Ward Ruby and Kookrin Char at Conductus by laser–depositing 200 nm of YBCO on 50 nm–diameter YSZ substrates buffered with 20 nm

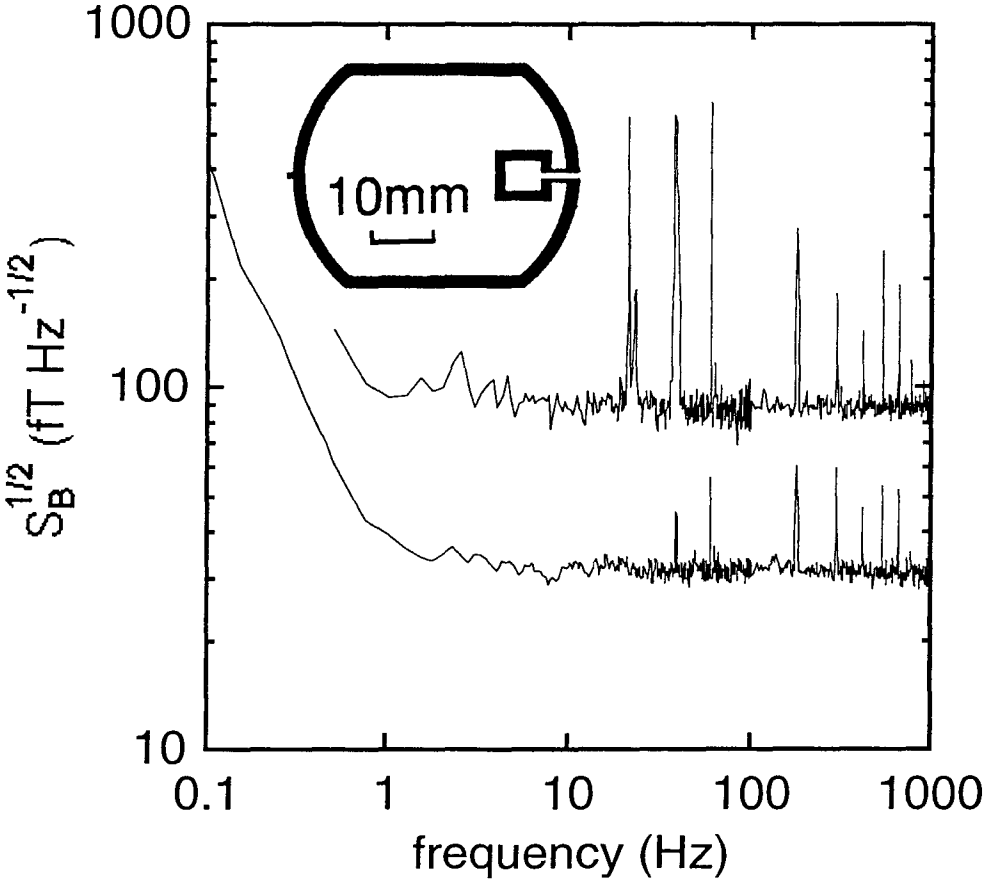

Figure 5.5: The magnetic field noise $S_B^{1/2}$ vs frequency for a directly coupled magnetometer with (lower trace) and without (upper trace) a single–layer flux transformer shown inset.

of CeO_2. I made two of these flux transformers, patterning each using the Kasper Contact Aligner followed by etching in a 0.05% aqueous solution of HNO_3. The transformer (inset Figure 5.5) consists of a pickup loop of area A_p and inductance L_p and an input loop of area A_i and inductance L_i which is inductively coupled to the pickup loop of the directly coupled magnetometer hereafter refered to as the "coupling loop" (area A_c, inductance L_c). We can estimate the effective area of the coupled device by calculating the net flux in the SQUID per unit of the applied magnetic field to obtain

$$A_{eff} \approx \frac{\alpha_d L}{L_c}\left[A_c \pm \frac{\alpha_m\sqrt{L_c L_i}(A_p \mp A_i)}{L_p + L_i}\right] \tag{5.3}$$

where α_m is the coupling coefficient between the input loop and the coupling loop. The first term corresponds to the effective area of the directly coupled magnetometer alone and the second term describes the contribution from the flux transformer. The plus/minus refers to placing the input coil inside/outside the pickup loop. For our dimensions it is easy to show that placing the input loop inside, as shown in the inset of Figure 5.5, gives the greater effective area.

Table 5.2 summarizes the parameters of the two magnetometers that were made using directly coupled magnetometer devices 2 and 4 from Section 5.2. The input loop of each of the two flux transformers was made to resemble the coupling loop of the corresponding directly coupled magnetometer. Dieter Koelle aligned each pair of devices face–to–face in a flip chip arrangement. Due to the presence of the wire bonds the separation was at least 100 μm; nonetheless the estimated coupling coefficients α_m were as high as 0.9, indicating the efficient coupling attained between two planar loops whose vertical separation is much smaller than their width. We measured the effective area A_{eff} of each combined magnetometer using a pair of external Helmholtz coils or a calibrated field coil on our noise probe. The measured effective areas were 0.46 and 0.29 mm^2 for magnetometers 1 and 2, respectively, corresponding to a gain of 3.5 and 3.4 over the effective area of the directly coupled magnetometer alone. From Equation 5.3 we estimate A_{eff} to be 0.46 and 0.26 mm^2, in rather good but, given the uncertainties in our estimated parameters, perhaps fortuitous agreement. The lower trace in Figure 5.5 is the measured magnetic field resolution for the best device (device 2). The upper trace is the field resolution without the flux transformer. Both were measured with bias reversal. For the combined magnetometer, the field noise is 31 fT Hz$^{-1/2}$ down to 5 Hz increasing to 39 fT Hz$^{-1/2}$ at 1 Hz. The less sensitive device (device 1) had a field noise of 44 and 49 fT Hz$^{-1/2}$ in the white noise limit and at 1 Hz,

Device	L (pH)	α_d	L_c (nH)	A_c (mm^2)	L_i (nH)	α_m	L_p (nH)	A_p (10^{-3} m^2)	A_{eff} (mm^2)
1	40	0.9	14	52	13	0.7	85	1.33	0.46
2	20	0.8	11	47	10	0.9	85	1.33	0.29

Table 5.2: Parameters for the two magnetometers made from a directly coupled magnetometer coupled to a large area flux transformer.

respectively.

In both devices the flux transformer did not add significantly to the 1/f noise of the bare directly coupled magnetometer. We can estimate the contribution of the 1/f noise in the film of the transformer to the noise in the SQUID following the model of Ferrari *et al.* [51]. Vortices that move under thermal activation in a direction radial to the YBCO pickup loop, induce a superconducting screening current in the transformer that couples a noise flux into the coupling loop of the directly coupled magnetometer resulting in flux noise in the SQUID. As a vortex moves a distance δr, it changes the flux in the transformer by approximately $\delta r \Phi_0/w$, where w is the linewidth of the transformer loop, resulting in a screening current that couples a flux

$$\delta\Phi_S \approx \left(\frac{\alpha_d L}{L_c}\right)\left(\frac{\alpha_m\sqrt{L_i L_c}}{L_p + L_i}\right)\left(\frac{\Phi_0}{w}\right)\delta r \tag{5.4}$$

into the SQUID. Given $\mathcal{N}$ vortices per unit area in the film, each with a spectral density for radial motion $S_r(f)$, the corresponding flux noise in the SQUID is

$$S_\Phi(f) = \mathcal{N} S_r(f)\int_A \left(\frac{\partial \Phi_S}{\partial r}\right)^2 dA \tag{5.5}$$

where the integral is taken over area A of the YBCO in the pickup loop. Thus the total contribution to the SQUID flux noise by vortex motion in the pickup loop of the magnetometer is

$$S_\Phi(f) \approx \mathcal{N} S_r(f)\Phi_0^2\left(\frac{\alpha_d^2 L^2}{L_c^2}\right)\frac{\alpha_m^2 L_i L_c}{(L_p + L_i)^2}\left(\frac{\ell}{w}\right) \tag{5.6}$$

where ℓ is the perimeter of the flux transformer loop. If we take $L_i \approx L_c$, we can see immediately that the presence of the term $L^2/(L_p + L_i)^2$ makes this noise contribution rather small. In ref. [51] it is shown that $\mathcal{N} S_r(f)\Phi_0^2 \lesssim S_\Phi^U(f)$, where $S_\Phi^U(f)$ is the spectral density of the flux noise produced by the *unpatterned* film of the transformer as measured by a SQUID placed directly over it. Thus, for device 2 we obtain $S_\Phi(f) \lesssim 10^{-5} S_\Phi^U(f)$, where we take $\ell \approx 132$ mm, w=2 mm, and the parameters in Table 5.2. Evidently, these large flux

transformers themselves can have rather high levels of flux noise without degrading the low frequency performance of the magnetometer. This result will be especially significant when we consider cooling these devices in ambient magnetic fields (Chapter 11).

5.4 Recent Directly Coupled Magnetometers

Recently, I have made a number of modifications and improvements to our original directly coupled magnetometer shown in Figure 5.1. Most of the improvements were motivated by the optimization discussion in Section 5.1. The latest design is illustrated in Figure 5.6. First, I increased the linewidth of the pickup loop in order to maximize A_p/L_p to $D_p/1.25\mu_0$. The pickup loop now resembles a square washer with inner dimension $d_p = 2\,\mathrm{mm}$ and outer dimension $D_p = 9.5\,\mathrm{to}\,10\,\mathrm{mm}$. Second, I set the SQUID inductance L to 50 pH which, based on Figure 5.2, is optimal for low magnetic field noise. Third, I changed the structure of the current bias and voltage leads as shown in Figure 5.6(b). Now all the leads are outside the pickup loop and wire bonds are not in the way of flip–chip coupled devices like the magnetometer in the previous section and the gradiometer described in Chapter 13. Having the pads close to the edge of the device also reduces parasitic inductance between the wire bonds and the magnetometer which would otherwise limit our ability to use bias reversal. Since I now only have access to the side of the SQUID below the grain boundary, I cannot run a current symmetrically through the SQUID. Therefore I used three current leads in order to bias the junctions symmetrically as shown in Figure 5.6(b). Fourth, I made the SQUID linewidth 4 μm to eliminate the excess 1/f noise generated in the SQUID when it is cooled in an ambient static magnetic field (see Chapters 11 and 12.) Furthermore, in order to reduce the noise coupling between the vortices in the pickup loop and the SQUID, I separated the SQUID on three sides by 120 μm from the nearest YBCO material.

In the present design the SQUID consists of two parallel 4 μm–wide strips separated by a slit 4 μm wide and 45 μm long and the bicrystal junctions are 1 μm wide and 4 μm long, giving L = 50 pH (which includes a small contribution from the kinetic inductance). I estimate the inductance of the pickup loop using $L_p \approx 1.25\mu d_p + L_{sl}$ where L_{sl} is the inductance of the 10 μm–wide slit, giving $L_p \approx 3.2\,\mathrm{nH} + 1\,\mathrm{nH} \approx 4.2\,\mathrm{nH}$. Using Equation 5.1, we obtain $A_{eff} \approx 0.28\,\mathrm{mm}^2$ where I took $\alpha_d = 0.9$. To date, I have made three directly coupled magnetometers with this configuration. The measured effective areas varied

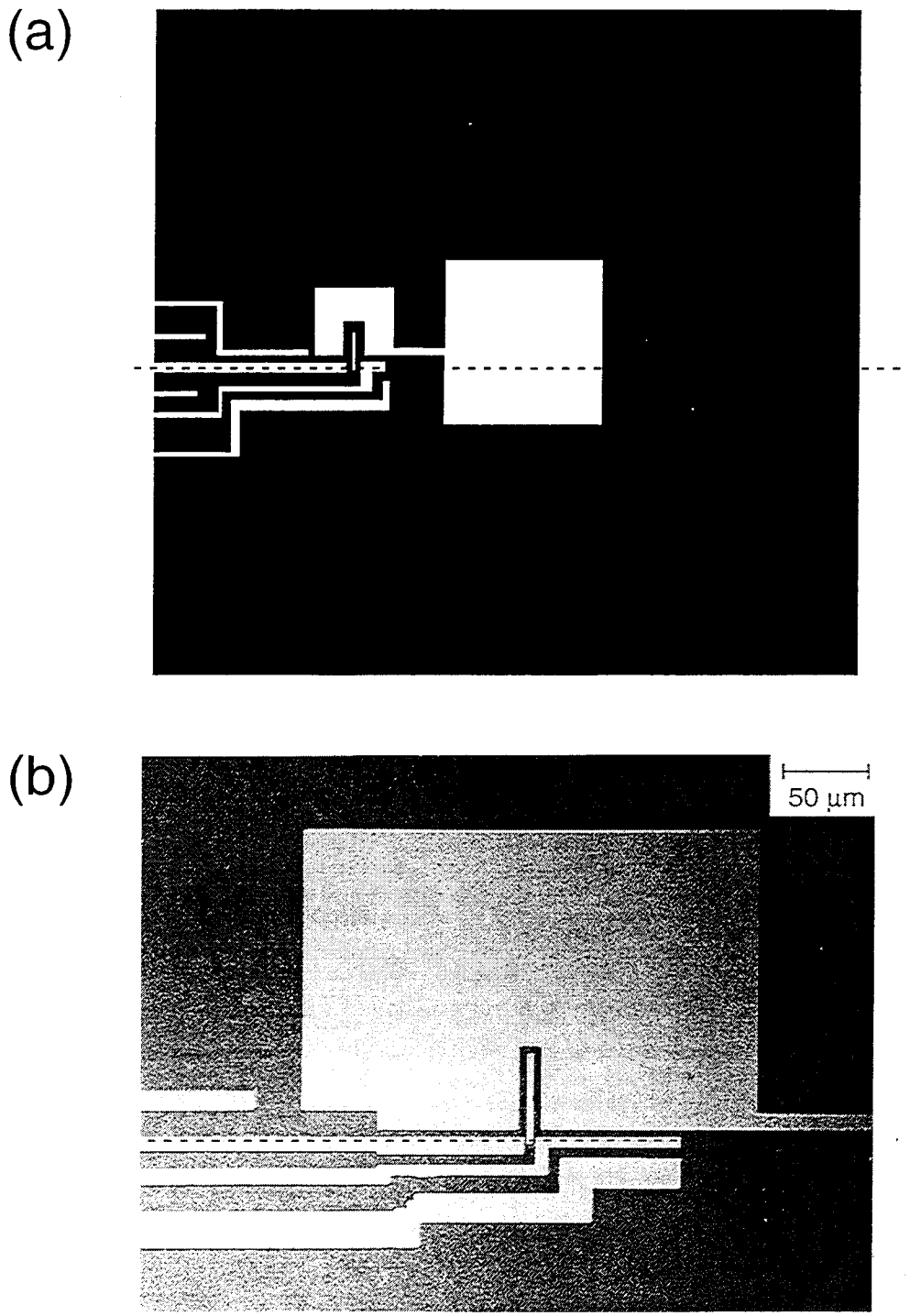

Figure 5.6: (a) Configuration of a recent directly coupled magnetometer (not drawn to scale). (b) Photograph showing detail of coupling to the bicrystal SQUID. Dashed line indicates grain boundary.

between 0.28 and 0.29 mm^2, in excellent agreement with the calculation and comparable to device 1 in Section 5.2 which used a SQUID with an inductance 3 times greater. The flux noise $S_\Phi^{1/2}(1\text{Hz})$ of one device was 14.8 $\mu\Phi_0\,\text{Hz}^{-1/2}$ corresponding to a field noise of 110 $\text{fT}\,\text{Hz}^{-1/2}$. The somewhat high flux noise was due to unusually high critical currents in the junctions resulting in $\beta \approx 5$. A factor of 3 reduction in the field noise should be possible for a SQUID with more typical junction parameters.

Over the past 5 years, several other groups reported SQUID magnetometers, based on a single layer of YBCO, with impressive performance. Zhang *et al.* [47] based their device on a rf SQUID with a 10 x 10 mm^2 flux–focusing washer and achieved a field noise at frequencies down to below 1 Hz of 170 fT $Hz^{-1/2}$. The noise was further reduced to 24 fT $Hz^{-1/2}$ with the addition of a single layer YBCO flux transformer on a 50 mm wafer [37]. The group at Conductus developed directly coupled magnetometers based on a dc SQUID with bicrystal junctions, and through improvements in design and junction quality achieved field noise levels at 1 Hz of 65 fT $Hz^{-1/2}$ for a device on a 10 x 10 mm^2 bicrystal [52] and 26 fT $Hz^{-1/2}$ for one on a 20 x 20 mm^2 bicrystal [53, 54]. It is interesting to note that since the first reports on high-T_c single layer SQUID magnetometers, the majority of workers have focused on these devices in lieu of multilayer magnetometers. The attraction lies mainly in less rigid fabrication requirements, since attaining high–quality low–noise single films of YBCO appears to be straightforward whereas the transport and noise properties of a comparable multilayer device technology are rather more difficult to control. I emphasize that for a given physical size, a magnetometer based on a SQUID coupled to a multilayer flux transformer offers a key advantage, in terms of greater effective area, over a directly coupled magnetometer. The best single layer magnetometers described here, are all about 50 mm across and for applications where few sensor channels are used and sensor size is not important, they are perfectly adequate. An example of such an application is a three–axis SQUID magnetometer for geophysical surveying described in Chapter 9. On the other hand, for an array of a large number of closely–spaced sensors used, for example, in biomedical applications, a smaller, equally sensitive magnetometer, based on a multilayer technology, is essential.

Chapter 6

Flip–Chip Multiturn Magnetometers

The larger single layer magnetometers discussed in the last chapter are, in principle, sensitive enough to be useful, for example, to detect a magnetocardiogram. However, the large size prevents one from achieving a reasonably dense array of sensors and confines one to systems with just a few channels. To achieve comparable or better performance in areas of say $10 \times 10\,\mathrm{mm}^2$, one must couple the SQUID to a flux transformer with a multiturn, *multilayer* input coil. Multilayer devices require considerably tighter control of fabrication parameters and, until recently, their excessive 1/f noise rendered them inferior to single layer devices at low frequencies. Over the last few years, however, improvements in processing of YBCO–STO–YBCO multilayers systematically brought down that noise [27, 45, 55].

The SQUID magnetometers described in this chapter are based on a bicrystal SQUID coupled to a flux transformer on a separate substrate, in a flip–chip arrangement. The flux transformers were fabricated using the multilayer process that involved *in situ* capping of the lower YBCO film with a thin layer of STO [45] as described in Chapter 4. This was the process that ultimately yielded flux transformers with the lowest 1/f noise. All measurements described here were performed in liquid nitrogen using the noise probe with the horizontal attachment. Shielding was provided by three mu-metal shields surrounding the dewar and either a cold 7–layer shield of Conetic foil or a YBCO shield surrounding the SQUID mount. To form a magnetometer, a transformer was placed over the SQUID with a

3 μm mylar foil separating them. The input coil was aligned over the SQUID washer with a lateral precision of 4–5 μm.

6.1 Design Considerations

To obtain low magnetic field noise $S_B^{1/2}(f) = S_\Phi^{1/2}/A_{eff}$, one must not only reduce the flux noise in the films but also maximize the effective area A_{eff} of the magnetometer through a suitable design of both the flux transformer and the SQUID. Figure 6.1 shows the configuration of our flux transformer. As shown in Section 1.4, A_{eff} is a maximum for $L_i = L_p$ and is given by Equation 1.5.

$$A_{eff} = \frac{1}{2}\alpha A_p \sqrt{\frac{L}{L_p}} \tag{6.1}$$

where, again, L is the SQUID inductance and α is the coupling coefficient between the SQUID and the input coil. Assuming that L is an independent parameter, we must maximize both α and the ratio $A_p/\sqrt{L_p}$. For a pickup loop with outer dimension D_p and inner dimension d_p, the area A_p is between $D_p d_p$ and $((D_p + d_p)/2)^2$ [48] and the inductance is given by [56]

$$L_p \approx \frac{1.86}{\pi}\mu_0 \left(\frac{D_p + d_p}{2}\right)\left[ln\frac{D_p + d_p}{D_p - d_p} + 0.42\right] \tag{6.2}$$

In our samples the outer dimension D_p is limited by the substrate size to 10 mm. Thus, for a maximum value of $A_p/\sqrt{L_p}$ we obtain the optimum d_p between 7 and 8 mm. Therefore the optimal linewidth of the pickup loop is about 1 mm yielding $L_p \approx 20\,nH$. This is in contrast to the directly coupled magnetometer for which the optimal pickup loop resembles a washer.

To maximize the coupling coefficient α, we should consider the exact geometry of the SQUID. Figure 6.2 shows four configurations of SQUIDs that were tested in the course of these experiments. For most of the SQUIDs we chose $L = 40\,pH$ to maintain a sizable transfer function. In the tight coupling limit, A_{eff} is maximum for $n = \sqrt{L_p/L}$, where n is the number of turns in the input coil; therefore we chose $n = 16$. This exhausts the predictions we can easily make *a priori*. To gain further insight into the nature of coupling between a given SQUID and the input coil of a flux transformer we must turn to experiment.

6.2 Coupling Issues

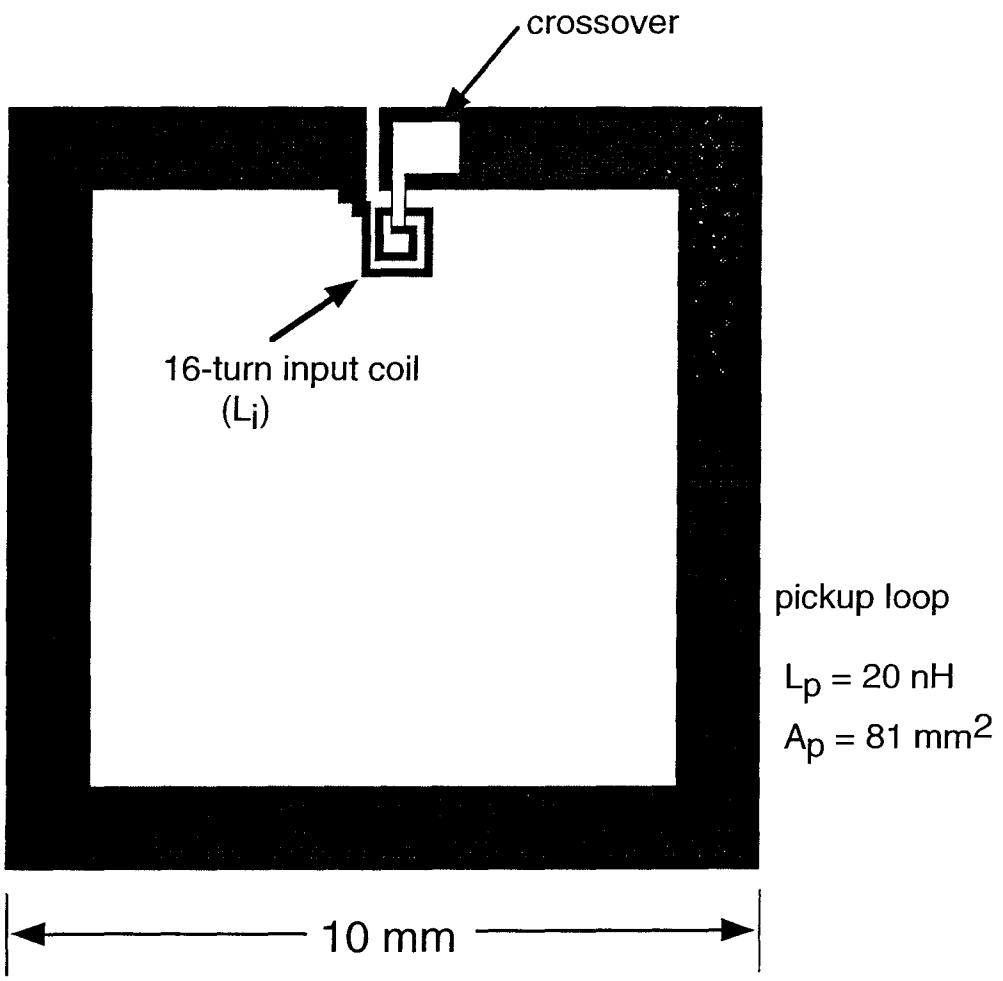

Figure 6.1: A flux transformer. The linewidth of the pickup loop is 1 mm. The input coil (not drawn to scale) is 16 turns with a linewidth of 7 μm spaced 8 μm apart. The overall size of the input coil is about 500 $\times$ 500 μm^2.

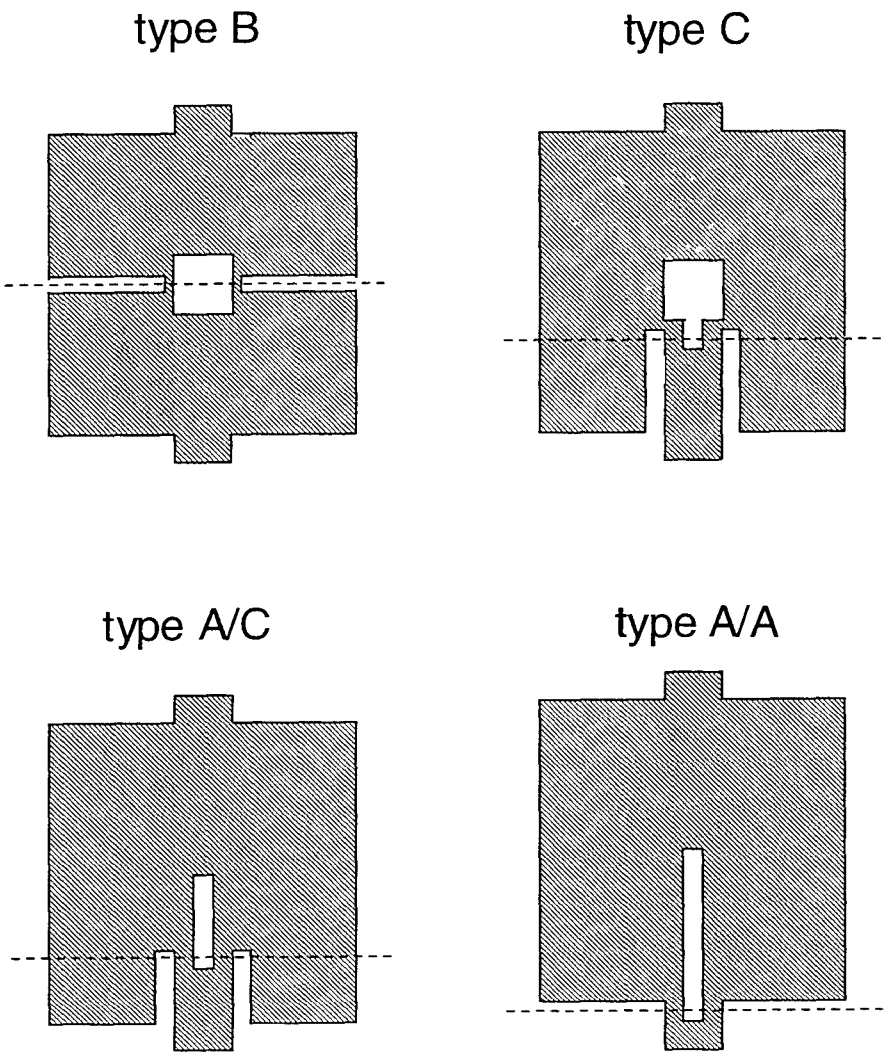

Figure 6.2: Four types of dc SQUID. Dashed line indicates grain boundary.

SQUID type	B	C	A/C	A/A
L (pH)	40	40	40	80
$A_s(mm^2)$	0.0077	0.0087	0.015	0.024
$A_{eff}(mm^2)$	0.44	0.54	0.96	–
g	57	62	63	–
M_i(pH)	310	340	550	–
L_i(nH)	39	32	28	–
α	0.25	0.30	0.52	–

Table 6.1: Parameters for different flip–chip magnetometers using the same 16–turn flux transformer.

Table 6.1 summarizes a series of measurements in which we coupled a flux transformer with a 16–turn input coil to each of three SQUIDs whose geometries are shown in Figure 6.2. In all SQUIDs the outer dimension is 500 μm. Type B SQUID was our earliest configuration in which the junctions are placed inside the washer thereby allowing one to easily calculate the inductance using $L = 1.25\mu_0 d$ [13]. Its effective area A_s, however, is smaller than that of the other devices because part of the applied flux leaks out through the two slits. In the type C SQUID, the slits are rotated toward each other by 90° and the washer must contain a small slit in addition to the square hole in order to define the junctions. In the type A/C SQUID the hole is replaced by a slit 100 μm long and 4 μm wide still giving L=40 pH; now, however, the junctions are closer to the edge thereby shortening the two outer slits with the resulting increase in the effective SQUID area. Finally, in the type A/A SQUID the junctions are placed entirely outside the SQUID which results in the largest effective SQUID area, but we can no longer maintain an inductance of 40 pH for a 500 μm washer. The estimated inductance for this device is 80 pH.

We measured A_s and A_{eff} (the effective area of the bare SQUID and the magnetometer) using a calibrated field coil. After these measurements, we cut the pickup loop of the flux transformer and injected a current through it to directly measure M_i. We calculated L_i from Equation 1.4 using the estimated values $L_p = 20\,nH$ and $A_p = 81\,mm^2$, and α using $M_i = \alpha\sqrt{L_i L}$. We see that the coupling for the type A/C SQUID is considerably more efficient than for the other two devices and the effective area of the magnetometer A_{eff} scales with α, as expected from Equation 1.5. Also the coupling efficiency appears

#	d (nm)	A_{eff} (mm^2)	Gain	$S_\Phi^{1/2}$(1 Hz) ($\mu\Phi_0\,Hz^{-1/2}$)	$S_\Phi^{1/2}$(1 kHz) ($\mu\Phi_0\,Hz^{-1/2}$)	$S_B^{1/2}$(1 Hz) (fT $Hz^{-1/2}$)	$S_B^{1/2}$(1kHz) (fT $Hz^{-1/2}$)
1	100(L)	0.42	29	22	7	108	36
2	100(L)	0.34	24	17	9	105	53
3	120(L)	0.80	55	28	12	74	31
4	250(U)	0.53	36	50	8	196	31
5	250(U)	1.02	70	...	...	...	...

Table 6.2: Coupling and noise data for five flip–chip magnetometers all made with the same type A/C SQUID. d is the input coil thickness. (U)/(L) refer to placement of input coil in upper/lower YBCO film.

to scale with the effective area of the bare SQUID. Although we did not independently measure α for the type A/A SQUID, one can draw from the data that its large effective area should contribute to even more efficient coupling than the A/C SQUID resulting in greater A_{eff}, although its larger inductance would also increase the flux noise.

6.3 Noise Measurements

Using the multilayer process described Section 4.4, Frank Ludwig fabricated a series of flux transformers, all with 16–turn input coils, and pickup loops with outer dimension of 10 mm and a linewidth of 1 mm, as specified in the discussion of Section 6.1. We then coupled each flux transformer to the same type A/C SQUID with an inductance of 40 pH and an effective area of 0.014 mm^2. In these measurements we used a cold shield of 7 turns of Conetic foil. All measurements were made using bias reversal.

Table 6.2 summarizes the effective areas and magnetic flux and field noise levels at 1 Hz and 1 kHz for five different magnetometers. In the first three devices the input coil was patterned in the lower YBCO layer. In the next two, we reversed the order, patterning the input coil in the upper YBCO film; the lower film was patterned into a *crossunder*. Figure 6.3 shows the magnetic field noise $S_B^{1/2}(f)$ and flux noise power $S_\Phi(f)$ for magnetometer 3. At 1 Hz, the rms field noise was 74 fT $Hz^{-1/2}$, at the time the lowest value achieved in a multilayer device. The dashed line represents the flux noise of the bare SQUID. At low frequencies the increase in the flux noise of the magnetometer over that of the SQUID is likely due to 1/f noise generated in the transformer. The increase at 1 kHz, at the time, was

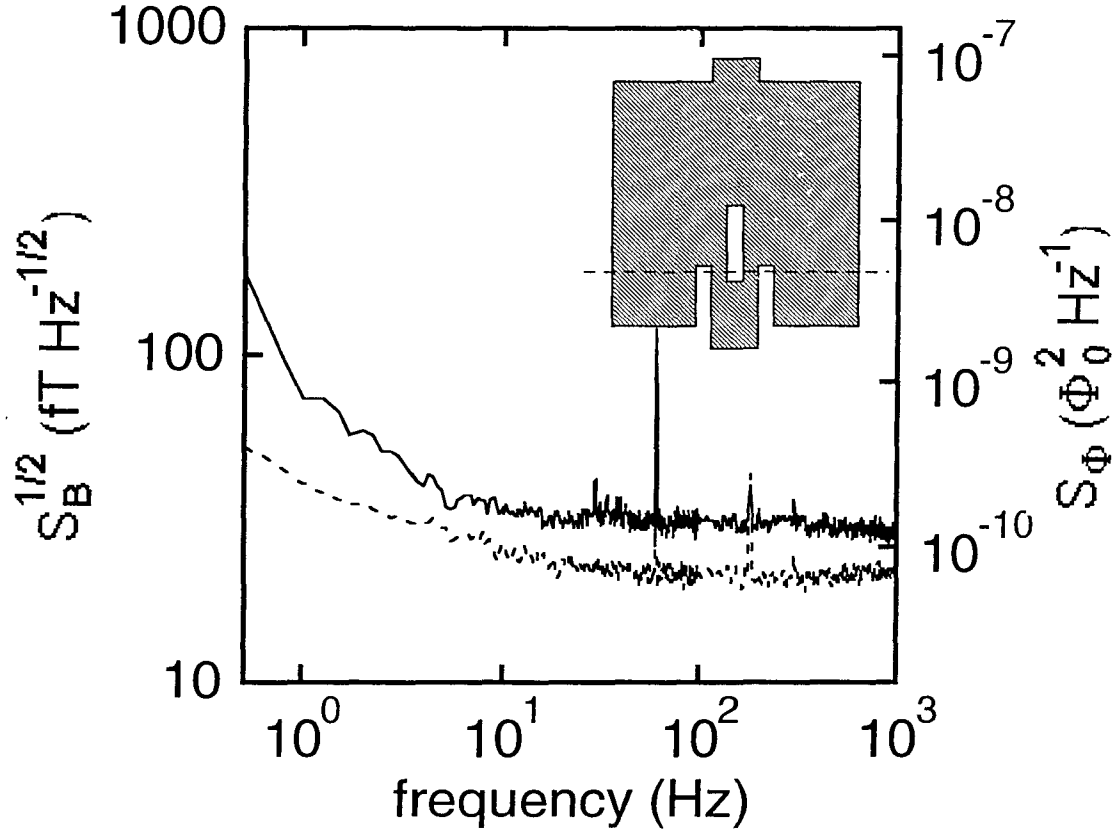

Figure 6.3: Magnetic field noise $S_B^{1/2}(f)$ and flux noise power $S_\Phi(f)$ of flux transformer 3 coupled to type A/C SQUID shown inset. Dotted curve indicates S_Φ(f) of bare SQUID.

unclear, although later we realized that the magnetometer was picking up Nyquist noise from the Conetic shield (see Chapter 8).

With regard to 1/f flux noise, there are two coupling mechanisms, as identified by Ferrari *et al.* [51]. First, *direct noise* is produced by the motion of vortices in close proximity to the SQUID, i. e. the input coil and the crossover or crossunder. The SQUID *directly* senses changes in flux as the vortices move. The second mechanism, called *indirect noise*, arises from the motion of vortices perpendicularly across the linewidth of the flux transformer. This motion generates a screening current in the closed loop of the transformer which couples a noise flux into the SQUID via the input coil. Vortices anywhere in the flux transformer, including the pickup loop, can thus produce indirect noise. On occasion we tried to identify the main contribution to the 1/f noise by cutting the pickup loop, which should remove the indirect noise. In some cases the 1/f noise decreased suggesting that the main contribution to the noise was indirect. At other times the 1/f noise was unchanged, pointing to direct noise. In the course of three years of measurements, neither one coupling mechanism can be said to have dominated the 1/f noise in our flip–chip magnetometers.

We can draw two general conclusions from the data in Table 6.2. First, the 1/f noise seems to be higher when the input coil is patterned in the upper YBCO film. One simple reason is that upper YBCO must grow on surfaces that underwent photolithographic processing, as described in Chapter 4, therefore its quality may be less than that of the lower YBCO. Since the input coil contains considerably more material than the crossover, one can speculate that this would result in higher direct noise. The fact that the input coil lines are more narrow than the crossover would also result in an increase in indirect noise. Second, there is a tendency for the gain to decrease with decreasing film thickness, probably because of an increase of the self–inductance of the input coil which would lead to greater mismatch to the inductance of the pickup loop. Thus, modest improvement in performance might be achieved by patterning the input coil in a film with a thickness of 150–200 nm, provided that the thicker lower film does not adversely affect the growth of the upper film.

6.4 The Best Magnetometers

To achieve even higher magnetic field resolution, I coupled the flux transformer 3 (Table 6.2) to several new SQUIDs. Twelve SQUIDs, six type A/C and six type A/A, were patterned in a 250 nm–thick YBCO film deposited at Conductus on a STO bicrystal.

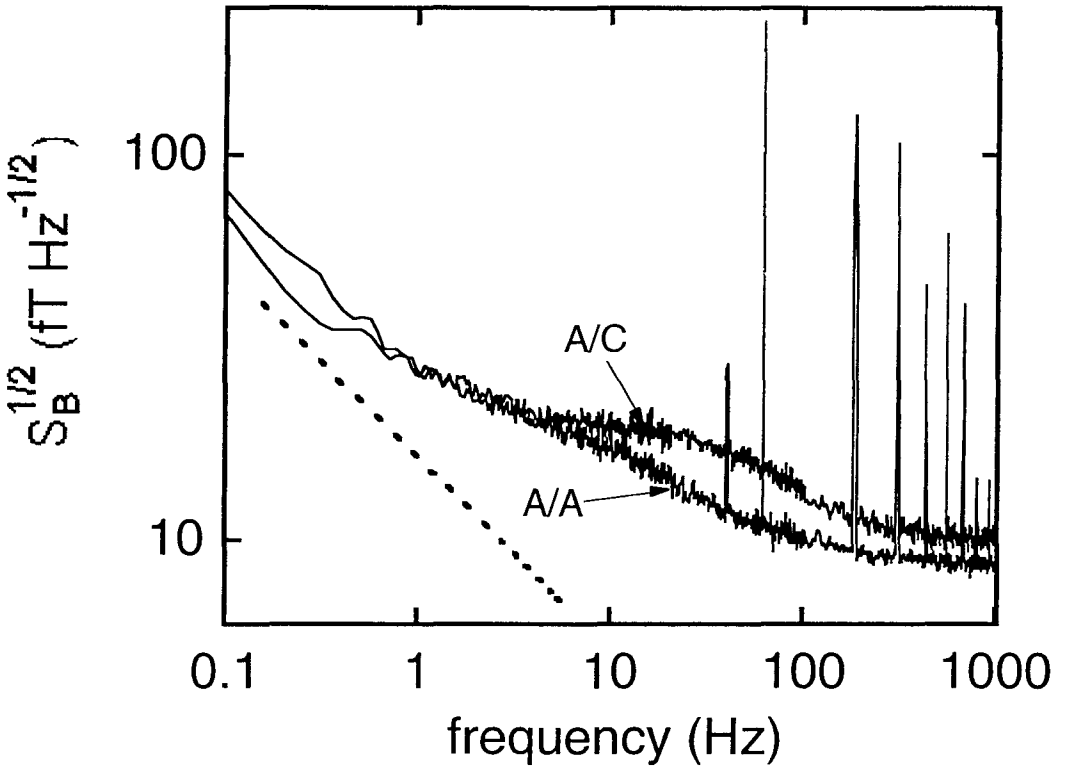

Figure 6.4: Magnetic field noise $S_B^{1/2}(f)$ of magnetometer with type A/C and A/A SQUIDs. Dashed line indicates $1/f^{1/2}$.

SQUID	R (Ω)	L (pH)	V_{pp} (μV)	A_s (mm^2)	L^c (pH)	V^c_{pp} (μV)	A_{eff} (mm^2)
A/C	5.8	40	66	0.011	30	90	0.68
A/A	8.6	75	55	0.024	30	108	1.2

Table 6.3: Parameters for two flip–chip magnetometers made with the same 16–turn flux transformer coupled to a type A/C and a type A/A SQUID.

Each SQUID had an outer dimension of 500 μm, a slit width of 4 μm, and junction width between 1 and 3 μm. The resistance per junction R in these SQUIDs, ranging from 2.4 to 8.6 Ω, was higher than for the SQUID in the previous section resulting in higher values of the peak–to–peak voltage modulation V_{pp}, and hence lower flux noise. I selected the SQUID of each type that produced the highest value of V_{pp}, listed in Table 6.3 [57, 55].

The magnetic field noise achieved with the transformer coupled to each SQUID is shown in Figure 6.4, both cases measured inside the YBCO shield. The field noise at lowest frequencies scales as $1/f^{1/2}$ for both magnetometers and at 1 Hz is 27 fT Hz$^{-1/2}$. As the frequency is increased, the noise spectrum appears Lorenzian suggestive of a random telegraph signal (RTS) produced by a single vortex hopping between two sites. Above 100 Hz, the noise becomes white with values of 9.5 and 8.5 fT Hz$^{-1/2}$ for the A/C and A/A devices, respectively. To date, this is the lowest magnetic field noise achieved with a high-T_c SQUID magnetometer of this size.

The fact that the field noise at low frequencies is identical for both magnetometers suggests that the dominating noise mechanism is *indirect noise.* We can derive this result by considering a vortex displacement δr across a width w of the transformer loop. Following the model of Ferrari *et al.* [51], this generates a flux change $\delta\Phi = \Phi_0 \delta r/w$ and a current around the transformer which couples a flux $\delta\Phi_s = (M_i \Phi_0 \delta r)/w(L_i + L_p)$ into the SQUID. For $\mathcal{N}$ vortices, each with a spectral density for radial motion $S_r(f)$, the resulting flux noise in the SQUID is

$$S_\Phi(f) = \frac{\mathcal{N} S_r(f)\, \Phi_0^2 M_i^2}{(L_p + L_i)^2} \left(\frac{\ell_i}{w_i} + \frac{\ell_p}{w_p} \right) \tag{6.3}$$

where $w_i(w_p)$ and $\ell_i(\ell_p)$ are the linewidth and length of the input (pickup) loop, respectively. Therefore the field noise $S_B(f) = S_\Phi(f)/A^2_{eff}$ is independent of M_i.

Figure 6.5(a) shows the magnetic *flux* noise power of the type A/A SQUID with and without the flux transformer. Below about 11 Hz, the flux noise is clearly still dominated

SQUID inductance, while maintaining efficient coupling, by covering part of the SQUID slit with the crossover. Although this can be done in an integrated magnetometer, it would require a total of three superconducting layers [41].

On the other hand, the coupling efficiency between the SQUID and the input coil is expected to be higher in an integrated device since the vertical separation between them is much smaller and their relative lateral positioning can be controlled more precisely. We address this issue in the following chapter.

Chapter 7

Integrated Multiturn Magnetometers

A device in which both the SQUID and the flux transformer are fabricated on the same chip has been the mainstay of low-T_c SQUID magnetometers [61]. Integrated high-T_c magnetometers have also been made for some time [58, 41, 59, 60, 46]. Until recently, however, the excessive 1/f noise in these devices rendered them impractical for sensitive field measurements. In the course of the development of our low–noise multilayer process, we focused on flip–chip magnetometers. Once the process was established, we investigated integrated devices as well.

7.1 Devices

Our integrated magnetometers were fabricated on STO bicrystals using the process described in Chapter 4. Our intent was to investigate the reproducibility of the fabrication technique and the coupling efficiency to SQUIDs with different geometries. Therefore our samples contained 10 magnetometers on a single 10×10 mm^2 STO bicrystal. In each magnetometer the SQUID was either in the upper or the lower YBCO layer; the SQUID body served as the crossover or crossunder, so that we required only two superconducting layers [41]. On each chip we had two SQUIDs of washer types B, C, and A/C, each with an outer size D of 500 μm and and estimated inductance L of 40 pH coupled to a 16–turn input coil. We also had two type A/A SQUIDs with D=400 μm and L=80 pH (A/A–80), coupled to a 12–turn input coil, and two smaller type A/A SQUIDs with D=200 μm and L=40 pH

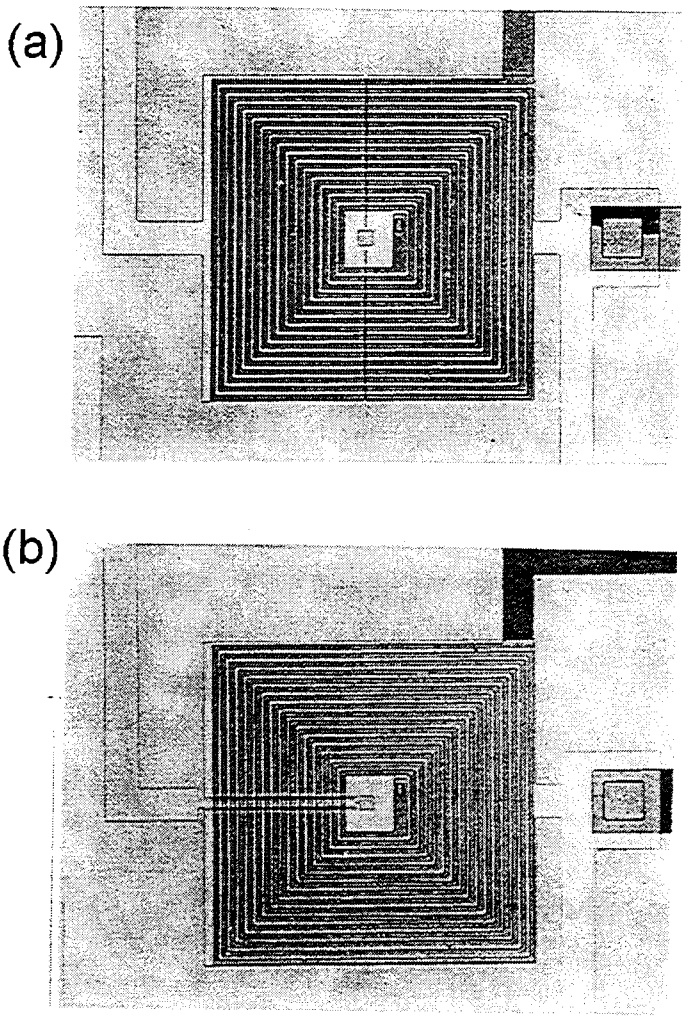

Figure 7.1: Integrated magnetometers consisting of a flux transformer coupled to a (a) type B SQUID and (b) type C SQUID. The 16–turn input coils are in the upper YBCO films.

(A/A-40), coupled to an 8–turn coil. To accommodate 10 magnetometers on a chip, the pickup loop areas were correspondingly smaller than the usual 10 × 10 mm^2. The pickup loop inductance and area were estimated to be L_p=5 nH and 3.2 mm^2, respectively, for the type B, C, A/C, and A/A–80 SQUIDs, and 2 nH and 1.8 mm^2 for the A/A-40 device.

Figure 7.1 shows two of the integrated magnetometers with a type B and a type C SQUID. In both cases the input coil is in the upper YBCO film.

7.2 Results

Out of six integrated magnetometers with the SQUID patterned in the upper YBCO film, only one exhibited flux modulation at 77 K. Evidently the grain boundary did not transfer well through the underlying layers. On the other hand, 11 out of 15 devices with the input coil in the lower YBCO layer functioned at 77 K. Furthermore, the I-V and the V-Φ characteristics for most of the integrated devices exhibited pronounced resonances due to the large dielectric constant of the STO separating the SQUID from the input coil. The resonances, caused by the stray capacitance between the SQUID and the input coil, combined with the input coil inductance, have also been observed by other groups [59, 46]. They are often seen in low-T_c SQUIDs with integrated input coils.

We measured the flux noise of the two best integrated magnetometers, one with a type A/A-40 SQUID and one with a type A/A–80 SQUID. Figure 7.2 shows the flux noise power $S_\Phi(f)$ vs. frequency for the latter device. The flux noise is 19 $\mu\Phi_0 Hz^{-1/2}$ at 1 kHz and 24 $\mu\Phi_0 Hz^{-1/2}$ at 1 Hz, corresponding to a field noise of 250 fT $Hz^{-1/2}$ and 320 fT $Hz^{-1/2}$, respectively. The high field noise was due to the small effective area, 0.15 mm^2, about a factor of 10 less than what one might achieve with a 10 × 10 mm^2 pickup loop. For the type A/A-40 device, the rms flux noise was 15 $\mu\Phi_0 Hz^{-1/2}$ at 1 kHz and 20 $\mu\Phi_0 Hz^{-1/2}$ at 1 Hz, respectively. The rms flux white flux noise of this device was about a factor of two higher than the value we usually obtained for single layer SQUIDs with the same inductance. The higher noise was caused by the low values of I_0R, about 50 μV, a factor of about three less than the values typically obtained for bicrystal junctions.

To investigate the coupling between the input coil and the SQUID, we cut open the pickup loops to inject a current into the input coil and thereby measure the mutual inductance M_i as we did with the flip–chip magnetometers in Section 6.2. The corresponding results are shown in Table 7.1 for all five SQUID configurations. As with the flip–chip

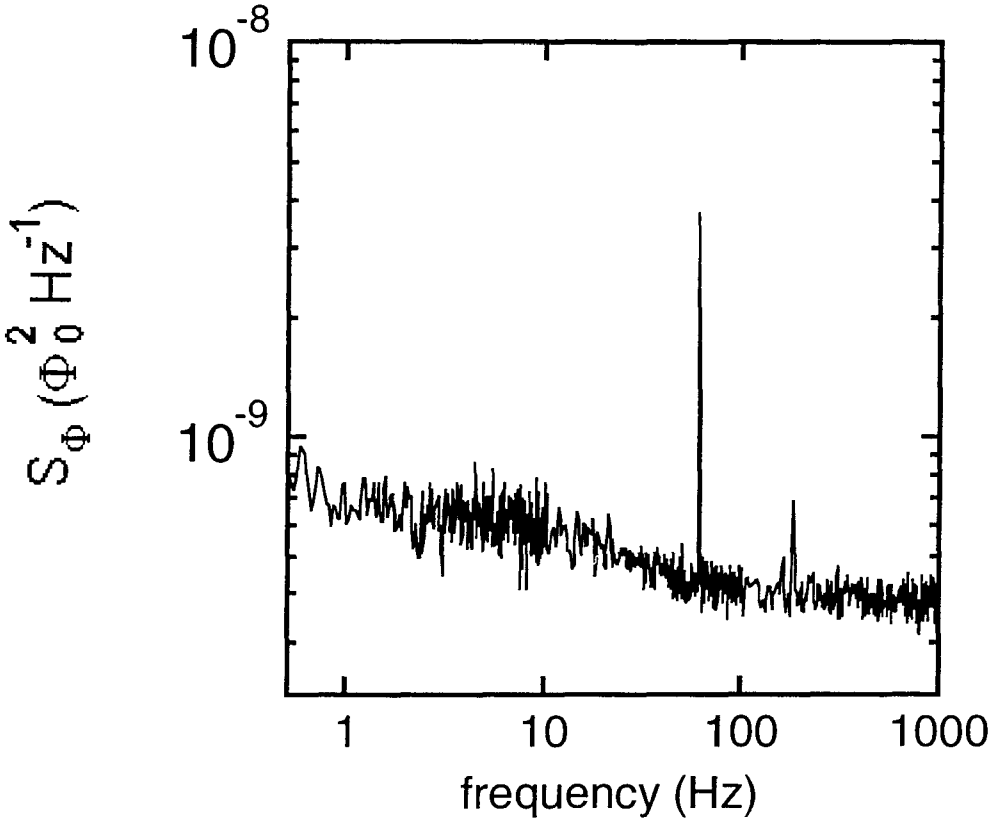

Figure 7.2: Flux noise power $S_\Phi(f)$ of small integrated magnetometer with a type A/A–80 SQUID.

SQUID type	B	C	A/C	A/A–40	A/A–80
$A_s(mm^2)$	0.0069	0.0065	0.012	0.021	0.0061
$A_{eff}(mm^2)$	0.033	0.037	0.077	0.12	0.06
n	16	16	16	12	8
M_i(pH)	450	375	650	960	310
L_i(nH)	50	34	27	25	9
α	0.32	0.32	0.62	0.67	0.52

Table 7.1: Parameters for different integrated magnetometers with multiturn flux transformers.

magnetometers, the coupling efficiency for the A/C SQUID is clearly higher than for the type B and C SQUIDs. The inferred values for α for all integrated devices appear to be slightly higher than for the corresponding flip–chip devices (Table 6.2), but, given the uncertainties, the improvements may be only marginal. The coupling efficiencies for both type A/A devices were also clearly higher than for the type B and C SQUIDs. The highest coupling coefficient obtained was α=0.67 for the A/A–80 device.

7.3 Discussion

From these results, it is clear that we gained only a marginal improvement in coupling efficiency by integrating the input coil with the SQUID as compared to a flip–chip device. On the other hand, because the I_0R product of these junctions is lower than in single layer bicrystal SQUIDs, the flux noise has increased. The reduction in the I_0R product is likely due to poor oxygen diffusion into the junctions through the upper YBCO and STO films. In the next chapter I will describe an integrated magnetometer with bicrystal junctions, made in the lower YBCO film, having much higher I_0R products. This, however, only points to a certain lack of control of oxygen in multilayer structures, and in particular in junctions, through a suitable annealing method.

The presence of resonances in the V-Φ characteristic can be reduced by using an insulating layer with a lower dielectric constant, such as CeO_2 or $NdGaO_3$. The resonances could also be damped with a resistor shunting the two junctions [62], although the noise may also increase. Alternatively, one could replace the solid washer SQUID with a SQUID

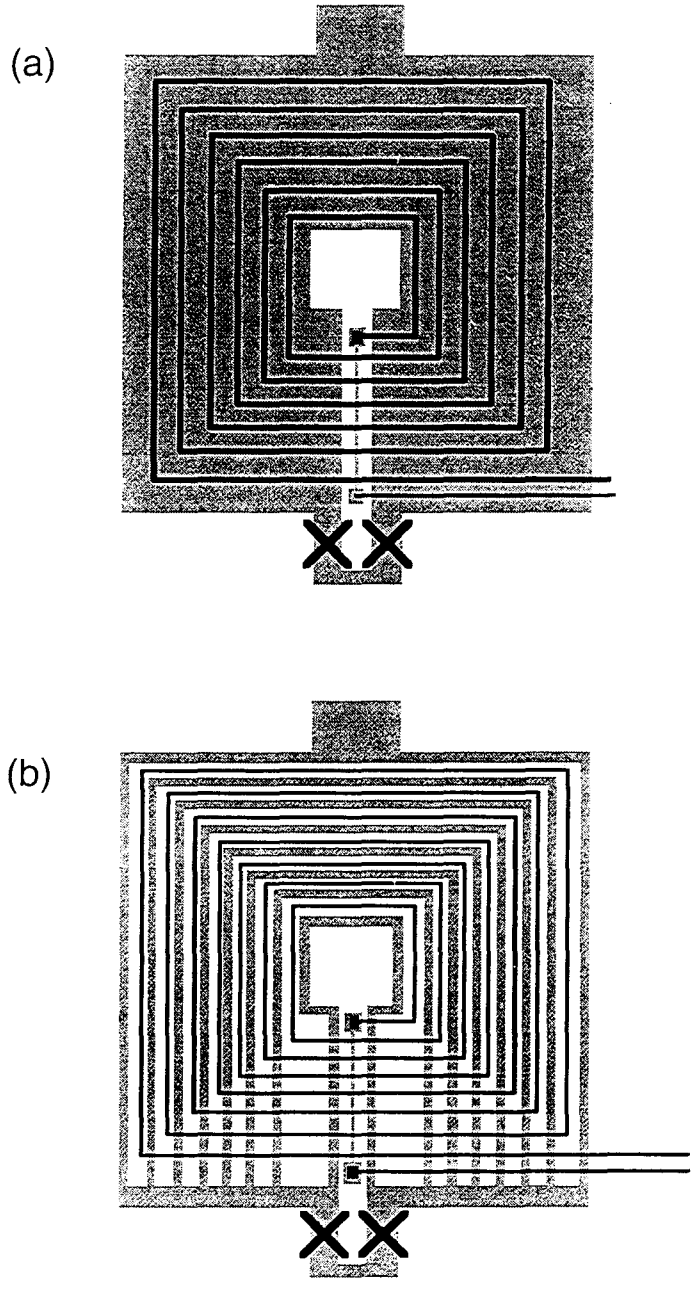

Figure 7.3: A proposed approach for reducing the parasitic capacitance between the SQUID and the input coil. (a) Using a traditional washer SQUID, the overlap area between the input coil and SQUID is large leading to a high capacitance. (b) Placing the turns of the input coil into empty slots that interpenetrate the SQUID washer, to reduce the overlap area and the parasitic capacitance. Junctions are indicated by crosses.

interpenetrated by slots [63]. Then the turns of the input coil can be placed inside the slots, thereby significantly reducing the parasitic capacitance between the SQUID and the input coil while retaining efficient coupling [63]. This approach, shown in Figure 7.3 may be very beneficial for low-T_c SQUIDs as well.

To date the most sensitive monolithic magnetometer involving a high-T_c SQUID and a multiturn flux transformer was fabricated on a 10×10 mm^2 bicrystal by Shen *et al.* [46]. The device had a magnetic field noise of 9.7 fT Hz$^{-1/2}$ at 1 kHz and 53 fT Hz$^{-1/2}$ at 1 Hz [64]. The low white noise was due to the high resistances of the bicrystal junctions, about 9 Ω. Multilayer magnetometers thus have achieved very low field noise levels, largely due to a systematic reduction of the 1/f noise in the multilayers. The magnetic field sensitivity is now largely limited by the thermal noise of the SQUID, which depends significantly on junction parameters. There is a need to improve the reproducibility and yield of high-T_c junctions before one can attain a high yield of integrated magnetometers with very low field noise. Until then, the flip–chip approach is probably a more efficient method since the yield of SQUIDs can be increased by fabricating a large number in one run on a single substrate and selecting the SQUIDs with optimal parameters.

Chapter 8

Integrated Multiloop Magnetometers

8.1 Design and Fabrication

The purpose of coupling a flux transformer to a SQUID was to increase the effective sensing area while keeping the SQUID inductance low. An alternative approach is the multiloop magnetometer, or fractional turn SQUID, originally proposed and demonstrated by Zimmerman [65] in an rf SQUID machined from bulk niobium. Subsequently, Drung *et al.* [66] developed multiloop dc SQUIDs based on niobium thin films and used them in multichannel biomagnetic sensors [67]. A simplified layout of the magnetometer is shown in Figure 8.1. The essential idea is to connect N superconducting loops in parallel to a pair of junctions thereby reducing the overall SQUID inductance while keeping the effective area constant. The parallel connection is done at the central hub of this "cartwheel" via coplanar lines or "spokes". The effective inductance is given by

$$L_{eff} = \frac{L_p}{N^2} + \frac{L_s}{N} + L_j \tag{8.1}$$

and the effective area by

$$A_{eff} = \frac{A_p}{N} - A_s. \tag{8.2}$$

Here L_p and A_p are the inductance and area of the large outer loop, L_s and A_s are the average inductance and area of one spoke, L_j is the inductance of the connections from the pickup loops to the junctions, and N is the number of loops.

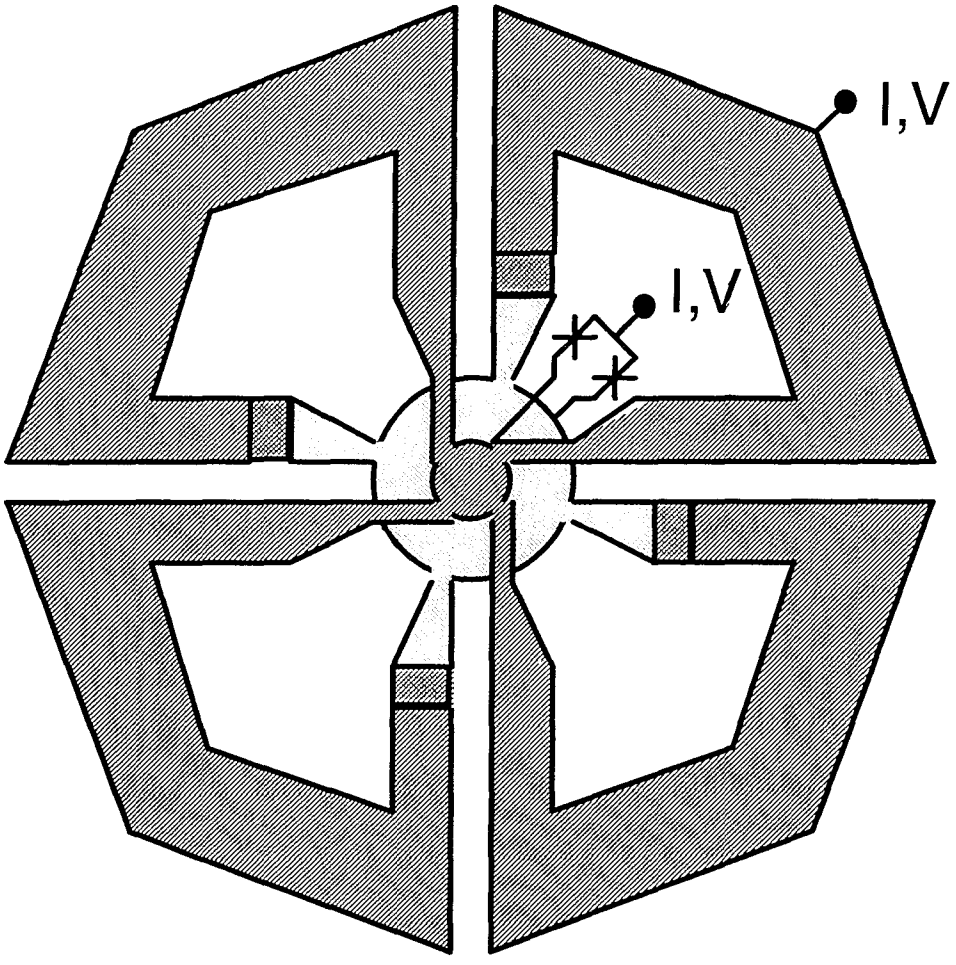

Figure 8.1: Schematic layout of a multiloop magnetometer. For clarity, only four loops are drawn. Oppositely, shaded regions represent upper and lower YBCO films, and cross-shaded regions indicate contact between them. Junctions are indicated with crosses.

					Static bias		Bias reversal	
	A_{eff}	I_0	R	V_{pp}	$S_B^{1/2}$(1Hz)	$S_B^{1/2}$(1kHz)	$S_B^{1/2}$(1Hz)	$S_B^{1/2}$(1kHz)
	(mm^2)	(μA)	(Ω)	(μV)	(fT Hz$^{-1/2}$)	(fT Hz$^{-1/2}$)	(fT Hz$^{-1/2}$)	(fT Hz$^{-1/2}$)
1	1.84	290	0.78	2.5	610	80	305	140
2a	1.89	13	10	20	130	23	53	25
2b	1.89	13	10	20	104	17	37	18

Table 8.1: Parameters for multiloop magnetometers 1 and 2 at 77 K. For magnetometer 2, 2a refers to the Conetic shield, 2b to the YBCO shield.

A complete design theory for multiloop SQUID magnetometers including some insight into high-T_c implementation was recently outlined by Drung *et al.* [67]. Constricted to a physical size of 10 × 10 mm^2, niobium multiloop magnetometers typically have 8 parallel pickup loops with a total inductance L_{eff} of 400–500 pH. Because we need to achieve a lower inductance for the higher temperature operation [18], we chose 16 loops.

It is clear that the multiloop magnetometer is a multilayer device, requiring at least two superconducting layers separated by an insulating layer. Using masks designed by Dietmar Drung and Silvia Knappe, Frank Ludwig fabricated two multiloop magnetometers, each on a 10 × 10 mm^2 STO bicrystal, utilizing the same multilayer fabrication process used to make our integrated magnetometers [68]. A photograph of the complete 16–loop device is shown in Figure 8.2. The outer diameter of the magnetometer is 7 mm. In the center of the magnetometer is a patterned YBCO–STO–YBCO trilayer. Each pickup loop, most of which is patterned in the upper YBCO film, makes contact with the lower YBCO through one of 16 vias in the STO. The two bicrystal junctions had a nominal width of 2.5 μm and were patterned in the lower YBCO film. The films were patterned so that no narrow lines, other than the junctions, cross the grain boundary. For this magnetometer we estimated, $L_p = 12.2\,\mathrm{nH}$, $A_p = 34.5\,\mathrm{mm}^2$, $L_s = 1.17\,\mathrm{nH}$, $A_s = 0.39\,\mathrm{mm}^2$, and $L_j = 24\,\mathrm{pH}$, yielding an estimated inductance $L_{eff} = 145\,\mathrm{pH}$ and an effective area $A_{eff} = 1.77\,\mathrm{mm}^2$.

8.2 Measurement

I characterized each magnetometer in liquid nitrogen in a dewar surrounded by a triple mu–metal shield. The parameters are listed in Table 8.1. The two measured effective

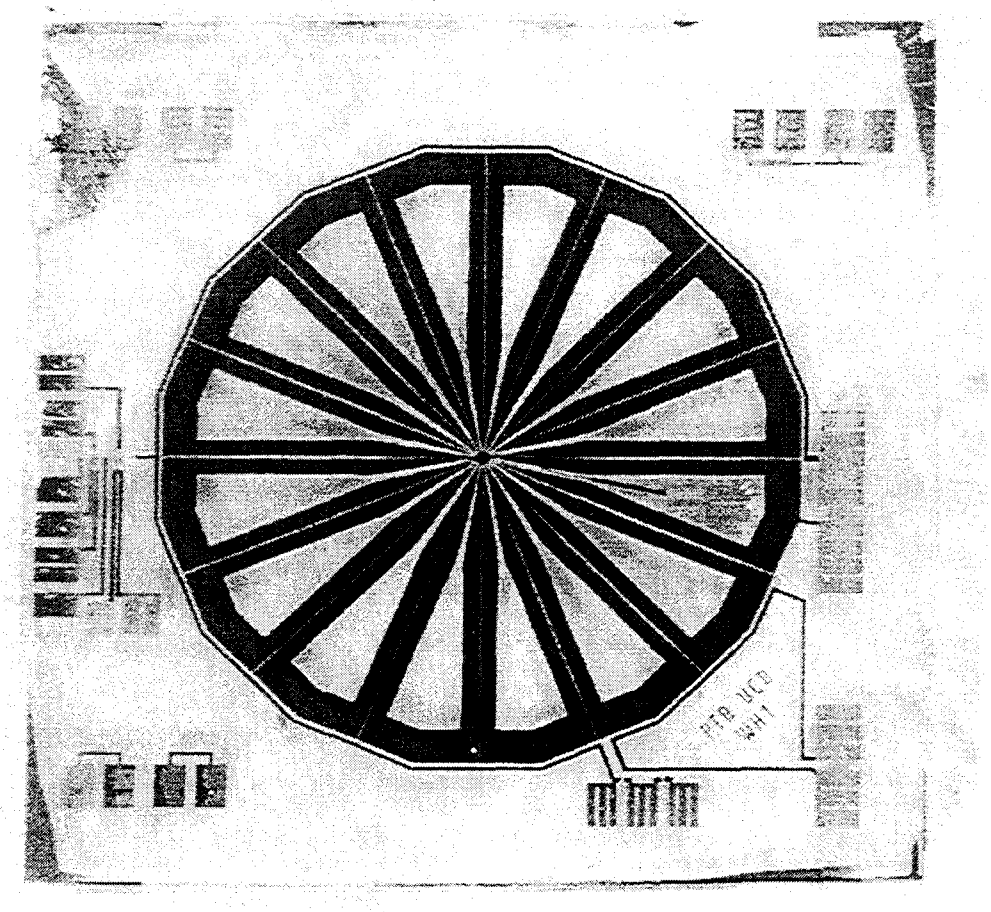

Figure 8.2: Photograph of multiloop magnetometer with 16 parallel loops on a 10 × 10 mm^2 STO bicrystal.

areas are comparable and slightly higher than our estimated value. There is a striking difference between the values of I_0 and of the asymptotic resistance R in the two SQUIDs. For magnetometer 1, I_0 is considerably higher than the value we usually obtain for bicrystal junctions of the same width and film thickness, and the resistance is correspondingly lower; the I_0R product, however, is at the upper end of what we usually expect, over 200 μV. The high critical current yielded $\beta = 2I_0L_{eff}/\Phi_0 \approx 40$, a value substantially higher than the optimum value of approximately unity. The low resistance reduced V_{pp} to 2.5 μV. These substantial differences between the two devices were, in part, a result of our patterning process. To pattern the lower YBCO film we normally use a resist mask 1.5 μm thick. However, the 45° ion milling angle likely produced junctions substantially wider than the nominal 2.5 μm. In the second device, we used a thinner resist, 0.8 μm thick, which resulted in a noise–rounded critical current of 4.3 μA. Numerical simulations [19] indicate that the noise–free critical current per junction was about 13 μA, corresponding to $\beta \approx 1.8$. The resistance R was 10 Ω per junction yielding an I_0R product of about 130 μV. Although the use of a thinner resist did result in a lower I_0 for device 2, the resist thickness cannot possibly account for for the factor of 20 difference in I_0 between the two devices. Oxygen diffusion in and out of the junctions during annealing steps may have played a significant role.

To measure the noise, I initially enclosed each magnetometer in a 7–layer Conetic shield and immersed it in liquid nitrogen. Each device was flux modulated at 100 kHz and operated in a flux–locked loop. Table 8.1 lists the magnetic field noise, $S_B^{1/2}(f)$, at 1 Hz and at 1 kHz for both magnetometers operated with a static bias and with bias reversal. In the case of the static bias current, device 1, which had a low V_{pp}, exhibited a substantially higher white noise than device 2. When I used bias reversal, the 1/f noise of both magnetometers was reduced. The residual value of $S_B^{1/2}(1Hz)$ in magnetometer 1, however, was much higher than in magnetometer 2. With regard to the white noise, the level increased markedly in magnetometer 1, from 80 to 140 fT Hz$^{1/2}$, when I used bias reversal. The increase was due to a parasitic mutual inductance of 7–8 pH between the bias current leads and the magnetometer, which caused a flux change of roughly $4\Phi_0$ when the bias current was reversed. Thus, it was difficult to set up the flux bias condition for the reversal scheme accurately, which resulted in loss of signal, reducing the effective transfer coefficient and increasing the white noise.

For magnetometer 2, the bias current was about 10 μA so that the flux generated

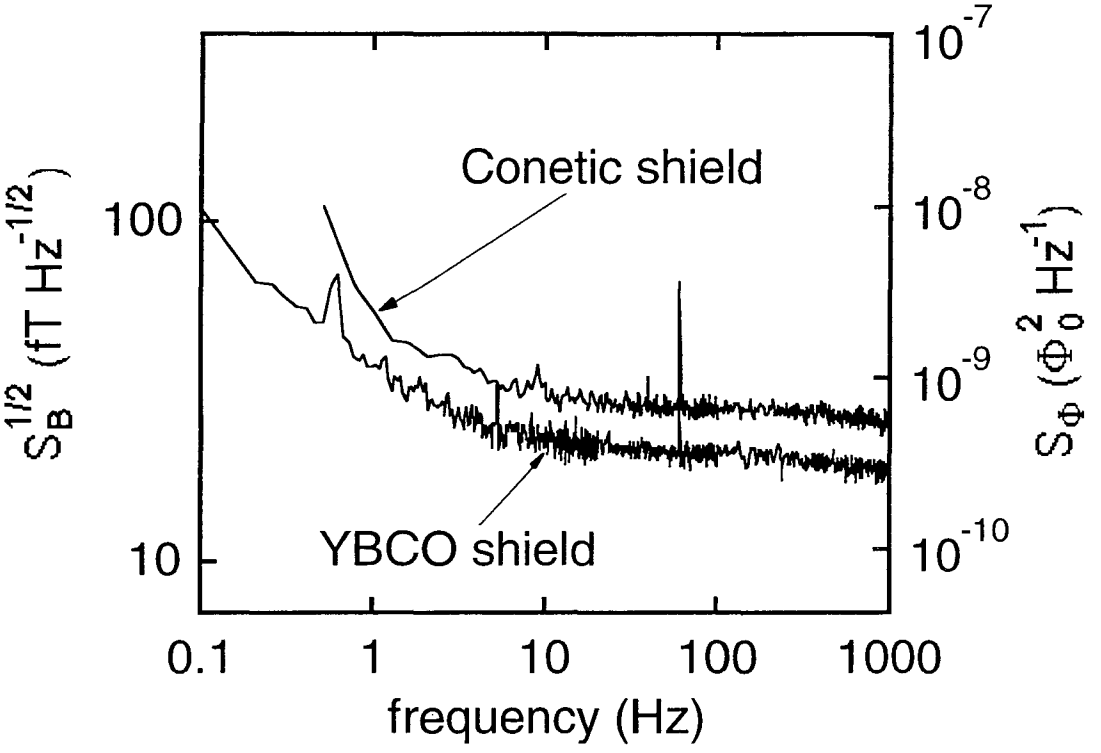

Figure 8.3: Magnetic field noise $S_B^{1/2}(f)$ obtained with bias reversal in a Conetic shield and in a YBCO tube.

by the bias reversal was small, less than $0.1\Phi_0$. To reduce the parasitic inductance further, the wire bonds were made to intersect the outer loop radially and halfway between adjacent spokes. With bias reversal, the noise levels at 1 kHz and 1 Hz were 25 and 53 fT $Hz^{-1/2}$, respectively. The corresponding spectrum is plotted in the upper trace of Figure 8.3. The noise at low frequencies increased more rapidly than $1/f^{1/2}$, due to drifts in the residual magnetic field not entirely attenuated by the shields. Drifts of several Φ_0 could be observed over a period of a few minutes or much more rapidly when metal objects were moved within 5 meters of the experiment, in spite of the magnetic shielding. I subsequently replaced the Conetic shield with a shield consisting of a YSZ tube with a length of 125 mm and inner and outer diameters of 25 and 32.5 mm, coated on both sides with a thick film of YBCO[1] [69]. The resulting magnetic field noise is plotted in the lower curve of Figure 8.3, and the values at 1 kHz and 1 Hz appear in Table 8.1. We note first that the white noise has decreased from 25 to 18 fT $Hz^{-1/2}$, indicating that a significant level of Nyquist noise was generated by the Conetic shield[2]. Second, the power spectrum is less steep, approximately 1/f, at low frequencies, and the noise at 1 Hz with bias reversal has been reduced from 53 to 37 fT $Hz^{-1/2}$. Evidently the upturn in the upper trace was produced by drift in the ambient field and not intrinsic to the device. The superconducting shield greatly stabilized the drift.

8.3 Discussion

The multiloop magnetometer had a diameter of only 7 mm, yet the measured effective area was 50% greater than that of our best flip–chip magnetometer of slightly larger size. The sensitivity achieved with device 2 is adequate for magnetocardiography (see Chapter 10) and the low field noise at 1 Hz was a further confirmation that our multilayer process is capable of producing high quality films with low 1/f noise. The noise above a few Hz was, once again, limited by the thermal noise of the SQUID which was largely influenced by the SQUID inductance of 145 pH, higher than the usually preferred 40–80 pH.

The yield of these integrated magnetometers critically depends on the correspond-

[1]Courtesy of Tim Button, ICI.

[2]Our earlier devices were not sensitive enough to detect this Nyquist noise, with the possible exception of the directly coupled magnetometer coupled to a single–layer flux transformer (device 2 in Section 5.3.) That device was nearly as large as the inner diameter of the Conetic shield. Close observation reveals that addition of the flux transformer reduced the white noise by a smaller factor than the corresponding increase in effective area, suggesting that part of the net white noise was of external origin.

ing yield of junctions with high values of the I_0R product. The difference between the junction parameters of the two nominally identical magnetometers points to a need for greater control of junction reproducibility to attain higher yield.

A nearly identical multiloop magnetometer, but with step–edge junctions, was fabricated by Reimer *et al.* [38] at the University of Hamburg. They attained a field noise of 31 fT $Hz^{-1/2}$ and 94 fT $Hz^{-1/2}$ at 1 kHz and 1 Hz, respectively [70]. An interesting extension of that work, recently developed by Scharnweber and Schilling [39] was to connect the multiple pickup loops to a multiturn input coil, inductively coupled to a washer SQUID with an inductance of 90 pH. This allows one to use a SQUID of lower inductance than the parallel inductance of the pickup loops.

Part IV

Applications

The ultimate goal of our efforts described in the last chapters was to develop high-T_c SQUID–based magnetometers suitable for practical applications. This prescription carries several requirements which lagely depend on the application. In the very least, these devices must offer a functional and/or financial advantage over competing sensors such as low-T_c SQUIDs, induction coils, Hall probes, etc. In some cases, they may be the only solution. I will focus on two specific applications, geophysics and magnetocardiography, where I had some direct involvement in the course of this work. In Chapter 9, I will describe a prototype high-T_c three–axis SQUID magnetometer for geophysical applications and in Chapter 10, I will discuss measurements of magnetocardiograms using high-T_c SQUID magnetometers. Other noteworthy practical applications of SQUIDs include non–destructive evaluation and its extension, scanning SQUID microscopy [71, 72] where a SQUID is used as a local probe of magnetic field on a microscopic scale. The latter is of particlar interest with the advent on high-T_c SQUIDs which operate at considerably higher temperatures than low-T_c devices and can therefore be placed considerably closer to a room–temperature sample [73, 74].

Chapter 9

High-T_C Three-Axis SQUID Magnetometer for Geophysical Applications

9.1 Introduction: Magnetotellurics

Magetotellurics is a geophysical surveying method in which one measures the components of the fluctuating electric and magnetic fields at the surface of the Earth to infer the resistivity of the ground as a function of position and depth. Electric fields are measured with buried electrodes whereas SQUID magnetometers have been demonstrated as suitable sensors of the magnetic field in this technique. In the 1970's and early 1980's Professor Clarke's group carried out magnetotelluric surveys using a pair of three–axis SQUID magnetometers positioned at two remote sites, in order to cross–correlate the measurements and remove bias due to local noise [75, 76]. Each three–axis magnetometer consisted of three low-T_c SQUID magnetometers positioned orthogonally on a cryogenic insert that was lowered into a dewar of liquid helium. The technique proved successful although the need to use liquid helium was recognized as an obvious hindrance.

At present, most magnetotelluric surveys are performed using induction coils, typically 1–2 m long, 60 mm in diameter and weighing about 7 Kg each [77]. They are capable of very high field resolutions; for example, Model BF-4 from ElectroMagnetic Instruments, Inc. has a field resolution of better than 100 fT $Hz^{-1/2}$ in a frequency range between 1 Hz

and 1 kHz [77]. At low frequencies f, however, the noise power of induction coils scales as $1/f^3$. The advantage of SQUID magnetometers over induction coils lies in high field sensitivity over a much greater bandwidth, particularly at low frequencies, and in portability and ease of deployment, since all three SQUIDs can be mounted orthogonally on one fixed probe. The main disadvantage is the need for cryogenics – until recently – a dewar filled with liquid helium. Furthermore, many geophysical surveys are carried out at remote locations for many months and the need to refill the helium presents a serious limitation. The emergence of high-T_c SQUIDs promises to alleviate this limitation, since liquid nitrogen has a much slower boil–off rate. Therefore, a portable high-T_c three–axis SQUID magnetometer that weighs about 20 Kg and holds liquid nitrogen for a few months presents itself as a promising application of the new technology.

By the summer of 1993 we had developed the single–layer directly coupled magnetometers described in Section 5.2. The magnetic field noise levels of these devices were around 100 fT $Hz^{-1/2}$ and we felt that they were sufficient to explore the possibility of a three–axis magnetometer based on them. This was our first multichannel high-T_c SQUID system (and, to my knowledge, the second in the world at the time, after the Superconducting Sensor Lab's 16 channel magnetocardiography system [78]). In addition, the system presented a new challenge: to operate high-T_c SQUID magnetometers completely unshielded, in the presence of power line and radio frequency noise. This required us to consider previously un-examined issues of dynamic range, slew rate and frequency response.

9.2 Construction

9.2.1 Probe and Sensors

For the high-T_c three–axis magnetometer [79] I used one of the original low–T_c three–axis probes [76], having stripped the wiring and re–machined the mount to accommodate three planar sensors where originally three cylindrical SQUIDs were used. I used devices 1, 2 and 3 from section 5.2 for the three orthogonal channels y, z and x with the z–channel vertical. Their parameters are summarized in Table 5.1. Each magnetometer was glued to a Si wafer, about 20 mm by 12 mm, along with a printed circuit board with 4 gold-plated copper pads. Electrical contact was made to each SQUID with Al wire bonds. The SQUIDs were mounted on a G–10 fiberglass stage machined to provide three orthogonal

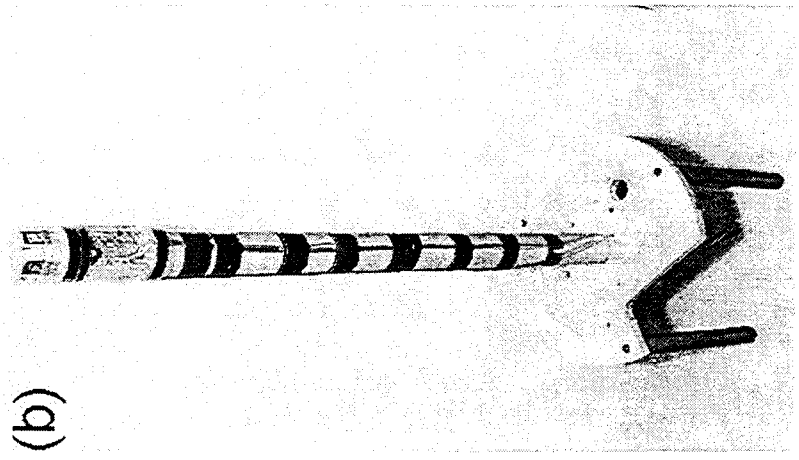

(b)

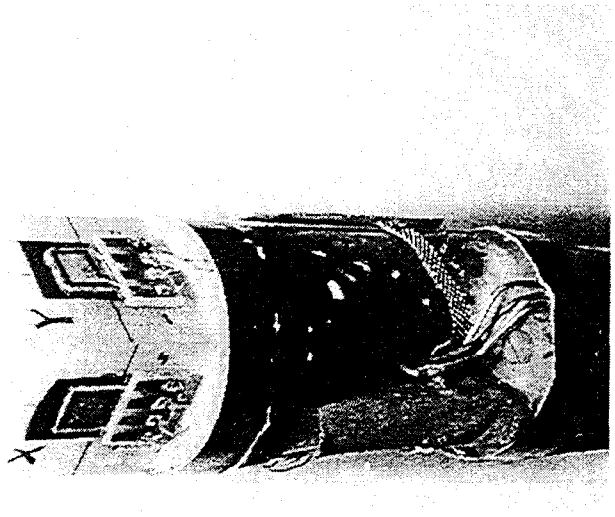

(a)

Figure 9.1: (a) The three–axis magnetometer mount showing the there directly coupled SQUID magnetometers. (b) The entire magnetometer probe.

surfaces. The modulation/feedback flux was supplied by a 50–turn coil of 150 μm diameter insulated copper wire set into the G-10 fiberglass surface beneath each SQUID. A photograph of the stage is shown in Figure 9.1(a) displaying the three SQUID magnetometers and the associated cold electronics. The stage was mounted at the lower end of a cylindrical fiberglass tube about 0.7 m long and 30 mm in diameter. At the top end of the probe, a 12 mm–thick Al plate served as a cap for the dewar and a mount for the three flux–locked loop packages. The plate also contained a blow–off valve and a fill line for the liquid nitrogen. Figure 9.1(b) shows the entire probe.

9.2.2 Electronics

To reduce crosstalk between channels, each SQUID was supplied with three twisted pairs of wires – one for current bias (manganin), one for modulation/feedback (copper) and one for output voltage (copper) – each surrounded by a grounded CuNi tube. The alternating voltage developed across each SQUID was coupled to its preamplifier via a cold, transformer consisting of a 10–turn primary and a 50–turn secondary Cu coils wound on a ferrite core; the inductances were 6.3 and 158 μH, respectively. Each transformer had a bandwidth of over 500 kHz. The three transformers were isolated from each other by grounded Cu mesh screens.

We used three sets of flux–locked loop electronics lent to us by Conductus. The flux–locked loop for each SQUID was housed in a metal box, grounded to the Al plate at the top of the probe. A single 500 kHz oscillator supplied flux modulation and the reference for the mixers for all three channels. Two of the three sets of electronics could be operated with bias reversal at 2 kHz. Each flux–locked loop was operated by a separate remote controller.

9.2.3 Dewars and Shielding

As will be seen in subsequent sections, we operated the three–axis magnetometer in two separate dewars. To characterize the instrument in the laboratory we used a 5 liter fiberglass dewar small enough to fit into our mu-metal shields. When deployed in the field, the magnetometer probe was inserted into a portable 25 liter fiberglass dewar originally used for magnetotelluric measurements with low–T_c SQUIDs [76]. To provide screening against radio and television stations and other sources of rf interference, the dewar was completely enclosed in Cu mesh, except for the top, where the screening was completed by

the Al cap. Thus the electronics, probe wiring and magnetometers were surrounded by a Faraday cage.

9.3 Performance

To assess the performance of the three–axis magnetometer, I first operated it in the 5 liter dewar surrounded by three concentric mu–metal shields. The dewar was enclosed in a copper mesh room for additional rf screening. All three SQUIDs were operated in flux–locked loops using either static bias or bias reversal. Figure 9.2 shows the rms magnetic field noise $S_B^{1/2}(f)$ and the equivalent flux noise power $S_\Phi(f)$ for the x–channel SQUID, operated with bias reversal, while the y and z–channels were also operating. There is a large spike near 30 Hz due to microphonics caused by the heavy Al plate at the top of the system. Other spikes are due to 60 Hz and its harmonics. Apart from these spikes, the noise is approximately white at frequencies above 10 Hz with a magnetic field noise of 170 fT $Hz^{-1/2}$, corresponding to a flux noise of 12 $\mu\Phi_0 Hz^{-1/2}$, about the same as measured before [17]. The noise power spectrum was unaffected by the operation of the other two SQUIDs. The z–channel SQUID, which was of identical design, had a similar performance with a white noise of 180 fT $Hz^{-1/2}$. The white noise of the y–channel was much higher, however, 1450 fT $Hz^{-1/2}$, about a factor of 5 greater than measured originally [17]; by then, this magnetometer was about 2 years old and had probably undergone damage after many thermal cycles.

We now turn to a discussion of slew rate, dynamic range and frequency response. When a flux $\Phi(\omega)$ is applied to the SQUID at frequency $f = \omega/2\pi$, the flux–locked loop gives rise to a feedback flux

$$\Phi_f(\omega) = \Phi(\omega)\frac{g(\omega)}{1+g(\omega)} \tag{9.1}$$

where $g(\omega)$ is the open loop gain. The error flux in the SQUID in the presence of an applied flux is $\Phi_e(\omega) = \Phi(\omega) - \Phi_f(\omega) = \Phi_f(\omega)/g(\omega)$. Because the system will lose lock if the error flux exceeds $\Phi_0/4$, the maximum slew rate is given by $| d\Phi_e/dt |^{max} = \omega\Phi_0/4$, provided the feedback amplifier does not saturate. Therefore the maximum flux that can be applied is

$$\Phi^{max}(\omega) = [1+g(\omega)]\Phi_0/4 \tag{9.2}$$

and the maximum slew rate for the applied flux is given by

$$[d\Phi(\omega)/dt]^{max} = [1+g(\omega)]\omega\Phi_0/4. \tag{9.3}$$

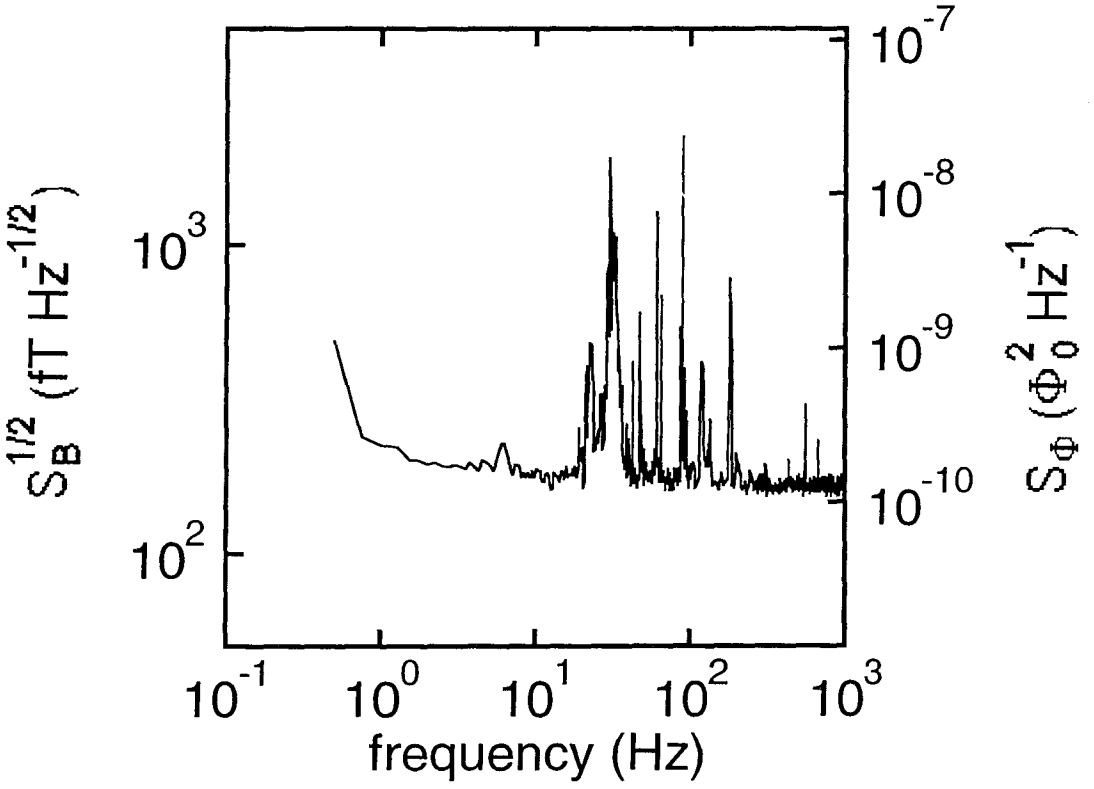

Figure 9.2: rms magnetic field noise, $S_B^{1/2}(f)$, and flux noise power, $S_\Phi(f)$, vs frequency for the x–channel SQUID magnetometer operated with bias reversal.

I determined the dynamic range and slew rate for each channel from the maximum sinusoidal flux $\Phi(t) = \Phi(\omega)\sin\omega t$, that could be applied (via the modulation coil) without causing the electronics to saturate or the feedback loop to unlock. Figure 9.3(a) shows the maximum amplitude $\Phi^{max}(\omega)$ vs frequency for the x–channel. At frequencies below 900 Hz, Φ^{max} is limited by the maximum current the electronics can feed back, equivalent to $\pm 19\Phi_0$. Given the rms flux noise measured with bias reversal, this corresponds to a dynamic range of $\pm 1.6 \times 10^6\,\mathrm{Hz}^{1/2}$ in the white noise region. Above 900 Hz, $\Phi^{max}(\omega)$ falls off as $1/\omega$ as expected for a feedback loop with a single–pole integrator. Figure 9.3(b) shows the slew rate $\omega\Phi^{max}(\omega)$ vs frequency, again for the x–channel. The maximum flux slew rate is $1.1 \times 10^5\,\Phi_0\,\mathrm{s}^{-1/2}$ at 900 Hz corresponding to a field slew rate of 1.6 mT s^{-1}. Above 900 Hz the slew rate is independent of frequency. I note that the data in Figure 9.3 were obtained with a static bias current. Figure 9.4 compares Φ^{max} and the slew rate $\omega\Phi^{max}$ for the z–channel measured with a static bias and with bias reversal. Bias reversal lowers the open–loop gain somewhat, reducing the slew rate by a factor of 1.5.

I determined the small signal frequency response $\mid \Phi_f(\omega)/\Phi(\omega) \mid = g(\omega)/[1 + g(\omega)]$ of each channel by applying white noise over a 100 kHz bandwidth to the magnetometer and measuring the output of the flux–locked loop. Figure 9.5 shows the response of the z–channel, operated with static bias, with the other two channels operating with bias reversal. The large peaks at 2 kHz and its harmonics are the result of these bias reversals. The 3 dB point in the roll–off in the response is beyond 100 kHz; with bias reversal the 3 dB point is reduced to about 90 kHz. Unfortunately we did not have a way of adjusting the open loop gain of the flux–locked loops. Both the slew rate and the frequency response data represent the best achieved with the gains available.

Another important issue for the three–axis magnetometer is the orthogonality of the three channels, that is the response of two of the channels when a magnetic field is applied to the third channel. Orthogonality is obviously limited by the extent to which one can mount the three magnetometers orthogonally; it is also limited by crosstalk among the channels, notably among the modulation and feedback coils. To determine the orthogonality, I removed the magnetic shields and placed the dewar in the center of pair of a Helmholtz coils with a diameter of about 1.2 m, mounted with their axis horizontal to the floor. Since the magnetometer was no longer shielded, I first determined a set of frequencies where the intrinsic noise was not obscured by signals from power lines and laboratory equipment. I then injected a small alternating current at one of those frequencies into the coils

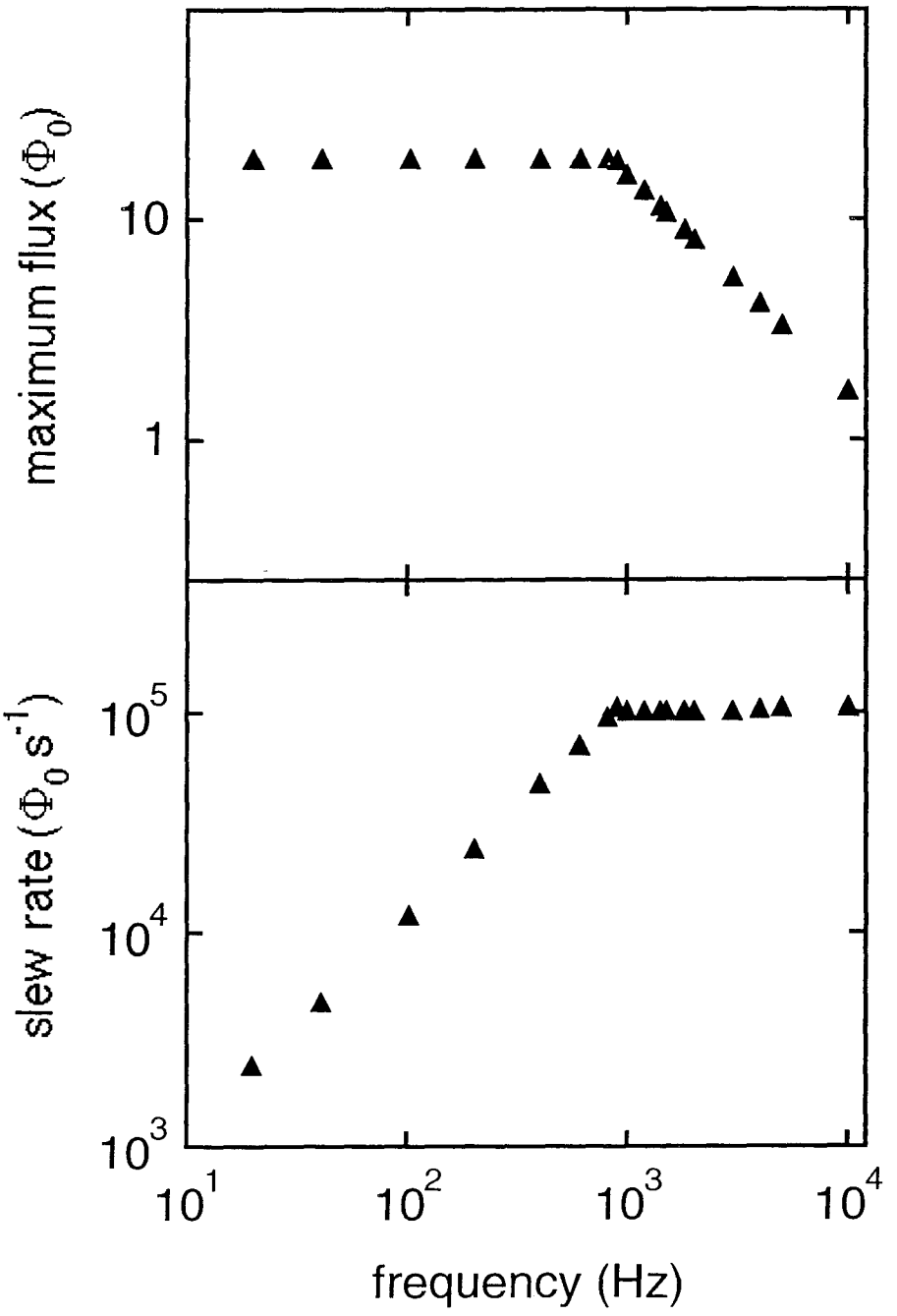

Figure 9.3: (a) Maximum amplitude of the sinusoidal flux $\Phi^{\max}$ that can be applied to the x–channel SQUID without causing the feedback electronics to saturate or break the lock vs frequency. (b) Slew rate $\omega\Phi^{max}$ vs frequency for the x–channel.

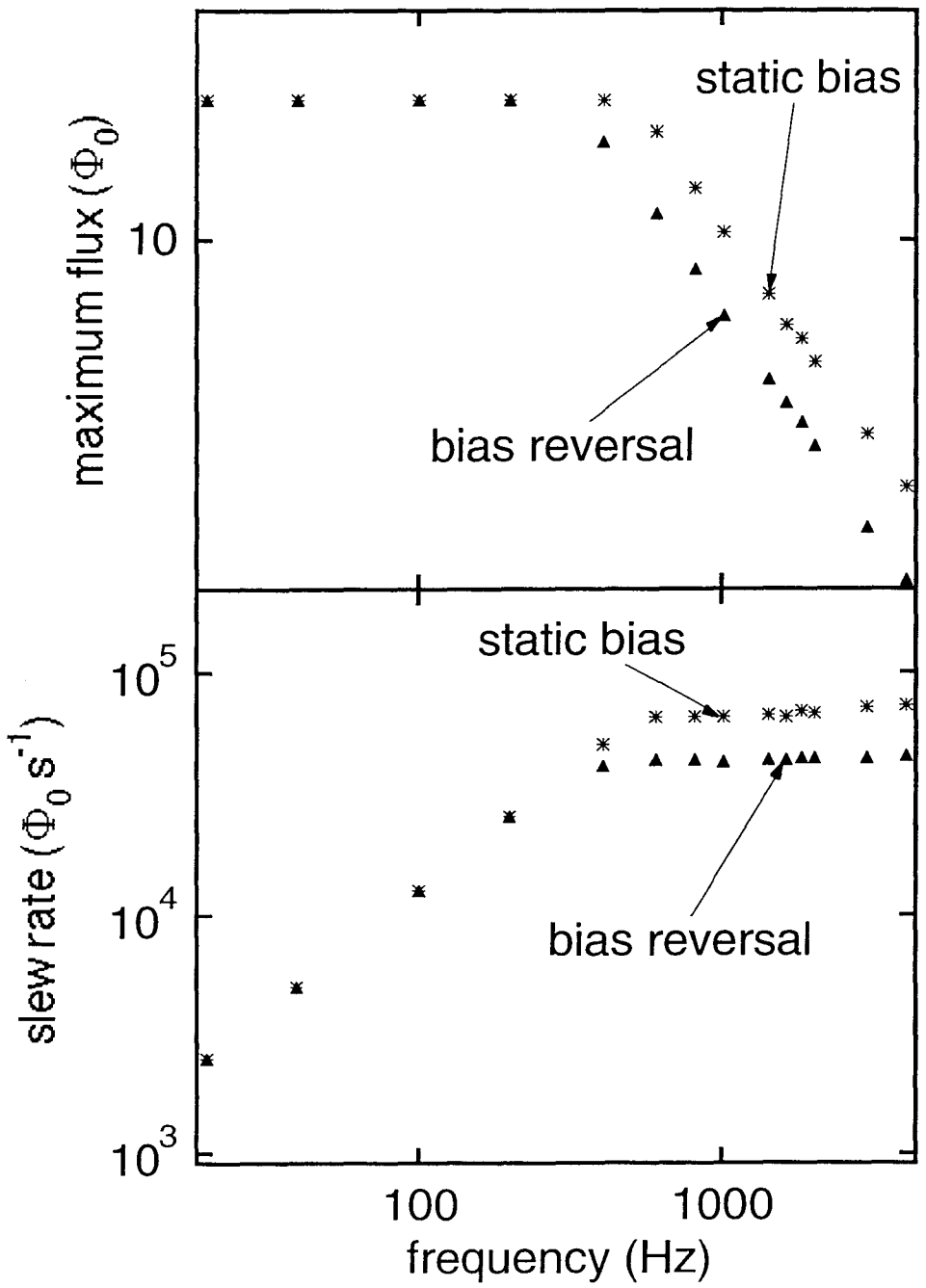

Figure 9.4: Comparing static bias and bias reversal for the z–channel. (a) $\Phi^{\max}$ vs frequency. (b) Slew rate $\omega\Phi^{max}$ vs frequency.

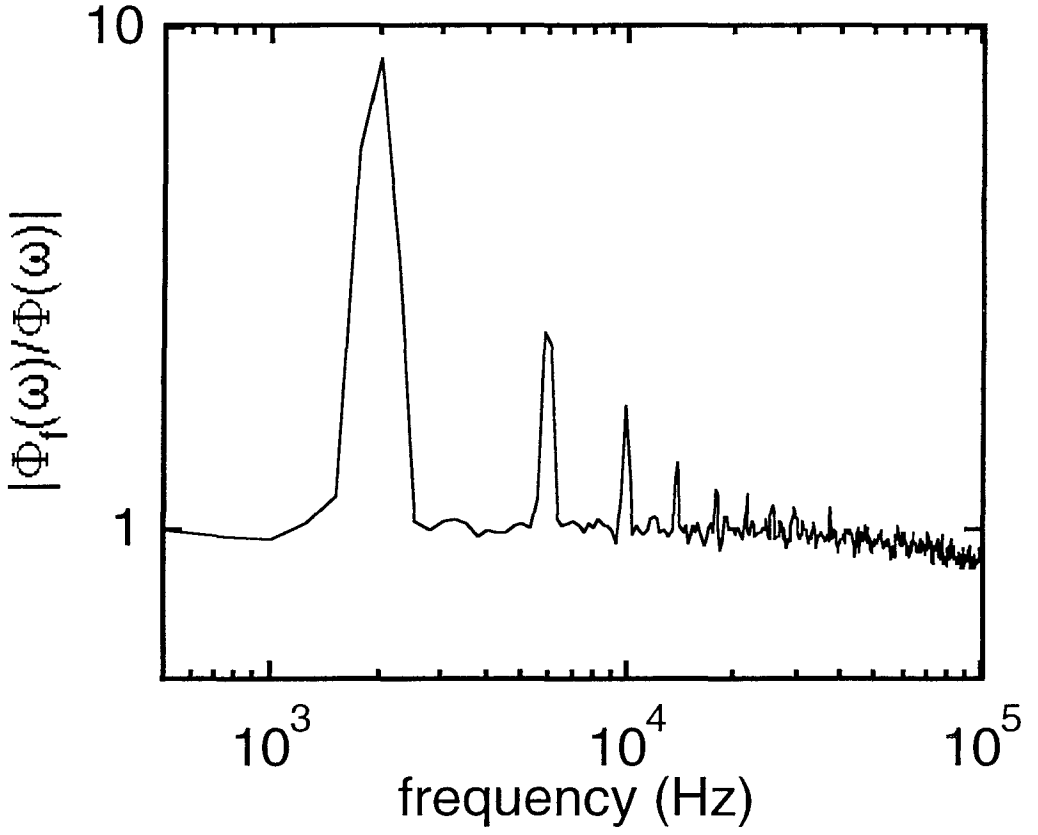

Figure 9.5: Measured frequency response of the z–channel SQUID operating in a flux–locked loop with static bias. The other two SQUID channels were operated with bias reversal.

and rotated the cryostat until the y–channel response was a minimum, and the x–channel therefore aligned with the axis of the Helmholtz pair. The responses for all three channels were measured with a lock–in amplifier for a range of frequencies from 100 to 500 Hz. Subsequently, I rotated the magnetometer so that the x–channel response was a minimum and repeated the measurements. We concluded that the signals from the two off–axis channels ranged from 0.5% to 1% of the channel aligned with the Helmholtz pair.

9.4 Field Test

To test the magnetometer outside the laboratory, we operated it in the rf–shielded 25 liter dewar on the Faculty Glade at UC Berkeley about 50 m from the nearest building. The magnetometer probe was lowered into the liquid nitrogen after the dewar was in place, and the dewar was not moved during the subsequent measurements. The three sets of electronics and a portable oscilloscope were powered by lead–acid batteries. Each SQUID was operated in a flux–locked loop, with bias reversal for the z–channel. The ambient magnetic field noise was dominated by 60 Hz oscillations from nearby power lines, varying from 20 to 200 nT peak to peak. Their presence made the setting up of the bias reversal somewhat difficult to monitor. The x and z–channels remained locked for the entire observation time of 40 min, while the y–channel, for which I used the set of electronics with the lowest loop gain, lost lock once, after the first 15 min of this period. The largest observed quasiperiodic change in magnetic field was in the z direction, with a total excursion of about $6\Phi_0$, corresponding to about 100 nT, well within the dynamic range.

Finally, I made an assessment of the liquid nitrogen hold time for the 25 liter dewar by monitoring the level on the nitrogen over a period of a few days. In the absence of the magnetometer probe, I found that 1 liter boils off in 4.5 days, corresponding to a total hold time of 16 weeks; in the presence of the probe the boil off rate increased substantially, to 1 liter in 3 days. Calculating the thermal conduction through the wires, CuNi tubing and the G-10 fiberglass probe, one can almost exactly account for the loss in hold time.

9.5 Discussion

The prototype three–axis magnetometer fulfilled two anticipated requirements for a geophysical system based on high-T_c SQUIDs. First, the SQUID flux–locked loops re-

mained locked in the presence of the 60 Hz and rf fields in the unshielded environment, indicating that the system had sufficient slew rate and frequency response as well as suitable rf shielding. Second, the liquid nitrogen hold time of nearly 3 months is considerably greater than with an equivalent low-T_c system. There are, however, a number of improvements one would wish to make in a second generation system. First, it should be possible to increase the hold time substantially through the use of a properly designed dewar with particular attention paid to heat leaks through the support structure and wiring. We have since acquired a commercial liquid nitrogen dewar that weighs about 15 kg, measures 0.4 m in diameter, and boils off liquid nitrogen at a rate of 0.1 liters per day [80]. With high-T_c SQUIDs, one can also consider using a cryocooler, possibly powered by solar cells. Second, substantial improvements should, and by now – can, be made to the magnetometers and the readout electronics. The lowest magnetic field noise in the directly coupled SQUID magnetometers used in this prototype was 170 fT $Hz^{-1/2}$. Much more sensitive single- and multilayer devices are available by now with white noise levels at least an order of magnitude less (see, for example, Sections 5.3–5.4 and Chapters 6 and 8). Another crucial issue concerns the increase in the low–frequency 1/f noise when the high-T_c SQUIDs are cooled in the Earth's magnetic field [81]. We can now eliminate this excess 1/f noise through the use of specially–designed SQUIDs and magnetometers described in Chapters 11 and 12 [82, 63]. It would also be prudent to add a heater to the SQUID stage that enables one to raise and lower the temperature to release trapped flux after the three–axis magnetometer is moved into position. Finally, to further increase the slew rate, one should use a two–pole integrator in the flux–locked loop [61].

Today there appears to be a resurgence in magnetotellurics due to the rising cost of oil. In addition, a technique that involves lowering magnetometers into boreholes for cross–borehole sounding is another possible application of a compact three–axis SQUID system. With the improvements listed above, we may well expect to meet the requirements of sensitivity, portability and long–term durability for a geophysical system based on high-T_c SQUID magnetometers.

Chapter 10

Magnetocardiography in a Magnetically Shielded Room

10.1 Introduction

Biomagnetism is a very promising application of SQUID–based magnetometers, particularly because no other magnetic sensor of suitable size has the required field resolution to detect magnetic signals generated within the body. In fact, most of the (low-T_c) SQUID systems sold in the last 10 years were multichannel biomagnetic sensors mainly designed to diagnose the brain (magnetoencephalography or MEG) [3, 4, 83] and also used in heart diagnosis (magnetocardiography or MCG). The use of these systems falls roughly into two categories. In the first scenario, one measures the magnetic field over an area in front of the patient's chest or around the head, using an array of SQUID sensors, and attempts to reconstruct and localize the source. This technique has been used with some success, for example to locate sources of focal epilepsy [84]. In a less ambitious problem, magnetocardiography is used as a diagnostic tool to screen for certain heart conditions which have a distinct signature in the time domain. Whereas the first category is largely a research tool, the second is more likely to provide one with specific, immediate information.

An obvious question is whether magnetocardiography provides information not available through other means such as electrocardiography (EKG) or echocardiography. This question largely remains open because suitable biomagnetic systems, consisting of 50 to 300 SQUID sensors, have not been available until recently. Another reason is that

simple medical diagnostics have not been the highest priority for researchers involved in biomagnetism. I am aware of two heart conditions that were shown to have a distinct magnetic signature. One involves stress–induced reversal of the QRS complex as detected by MCG whereas only the usual frequency increase is detected by EKG [85]. Another is arrhythmia, or sudden cardiac death, which causes the deaths of an estimated 300,000 to 400,000 people in the United States each year. Recently a method was developed at the Benjamin Franklin Hospital in Berlin for identifying and quantifying the risk for sudden cardiac death using MCG. In this method, the fragmentation of the QRS complex, caused by the arrhythmia, is converted into a risk index for sudden cardiac death. Although, a larger sample of patients will be required to establish this method of diagnosis conclusively, it has the attractiveness of speed and reliability, as well as requiring no placement of electrodes on the patient. More recently, the group from KFA–Jülich, in collaboration with Benjamin Franklin Hospital in Berlin, conducted MCG measurements on arrhythmia patients using a high–T_c SQUID magnetometer vis-a-vis a low-T_c single channel SQUID system, and found comparable levels of performance, in terms of identifying risk (see ref. [86] and references therein). There is now more activity than ever in MCG, specifically in cardiac diagnosis, and the two findings that I listed are testimonial to this work.

By the summer of 1995 we had developed the multilayer magnetometers described in Chapters 6, 7, and 8. Their field sensitivities were on par with some of the low-T_c SQUID magnetometers routinely used in magnetocardiography and certainly among the best of the high-T_c devices. I was curious to assess their capability as biomagnetic sensors. I collaborated with Dietmar Drung at the Phisikalisch-Technische Bundesanstalt Institut Berlin (PTB) in a project whose main objective was to obtain clinical quality magnetocardiograms using high-T_c SQUID magnetometers. The other objective was to operate the magnetometer using an alternate readout scheme called additional positive feedback (APF) [70].

10.2 The Berlin Magnetically Shielded Room

The measurements described here were performed in the Berlin Magnetically Shielded Room (BMSR) at the Phisikalisch-Technische Bundesanstalt Institut Berlin (PTB). The BMSR was build in 1980 by Vacuumschmeltze GMBH Hanau expressly for biomagnetic measurements in an environment of low background noise. It was designed to provide

electromagnetic screening at frequencies from dc to GHz. The BMSR is a cube with inner dimensions $2.25 \times 2.25 \times 2.25$ m^3 and outer dimensions $4.6 \times 4.6 \times 4.6$ m^3. The shielding is provided by six layers of high–permeability alloy and an eddy current shield of copper plates. The magnetic screening factor of the room is 10^6 at frequencies down to 2 Hz and about 10^5 at 1 Hz [87].

Work at the BMSR has focused on magnetocardiography and studies of the peripheral nerve system using a 37 channel SQUID array [88] based on niobium multiloop magnetometers [66]. An 83 channel system was subsequently developed [89]. High-T_c SQUIDs have rarely been used and only in collaboration with other groups.

10.3 Magnetometers, Electronics, and Noise

For this experiment I used the multiloop magnetometer (device 2, Section 8.2) and a flip–chip magnetometer consisting of a multiturn flux transformer (device 3, Section 6.3) coupled to a type A/C SQUID. To operate the magnetometers, we used a readout technique called additional positive feedback (APF) developed by Dietmar Drung [66]. The circuit is illustrated in Figure 10.1. The most obvious differences between APF and the flux modulated flux–locked loop (FLL), used in our group, is the absence of a transformer, an oscillator and a mixer in the former. The function of the transformer is to step up the SQUID signal above the voltage noise at the input of the preamplifier and one of the purposes of modulating the flux is to mix the SQUID signal up in frequency, above the 1/f knee of the preamp. Alternatively, in the APF technique, the voltage across the SQUID is fed back as an additional flux via the resistor R_a and a coil L_a with mutual inductance to the SQUID M_a. The effect is to steepen the V–Φ characteristic at every other working point thereby increasing the transfer coefficient to $V_\Phi = V_{\Phi,i}/(1 - G_a)$ where $V_{\Phi,i}$ is the transfer coefficient without APF and

$$G_a = \left(M_a + \frac{\partial \Phi}{\partial I}\right) \frac{V_{\Phi,i}}{R_a} \tag{10.1}$$

is the APF gain. The values of R_a and M_a must be accurately adjusted so that $G_a \lesssim 1$. Normally we use $G_a \approx 0.9$. An example of a V-Φ characteristic of a SQUID operating with APF is shown in Figure 10.2. By effectively increasing the transfer coefficient, one can now couple the SQUID signal directly to the preamplifier, thereby reducing the preamplifier noise contribution.

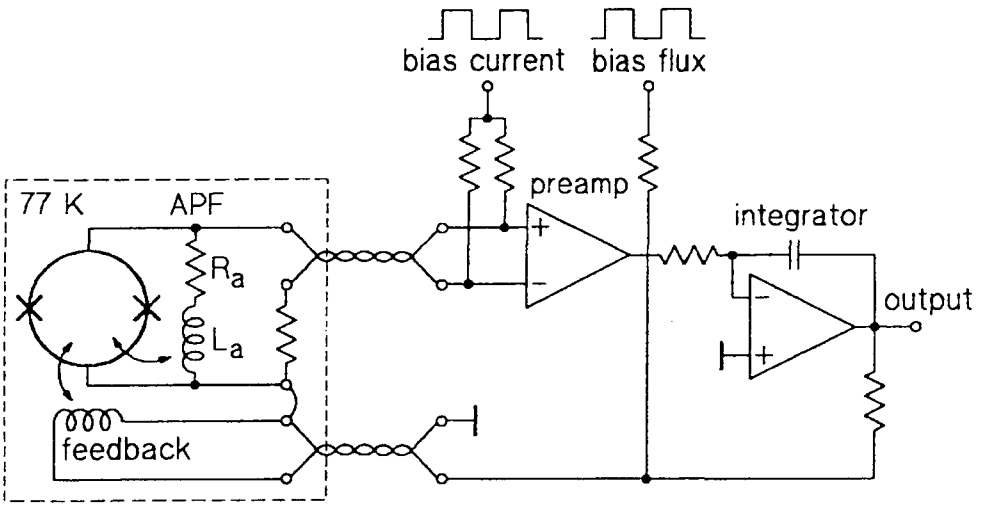

Figure 10.1: The read–out SQUID electronics using additional positive feedback. (Courtesy Dietmar Drung.)

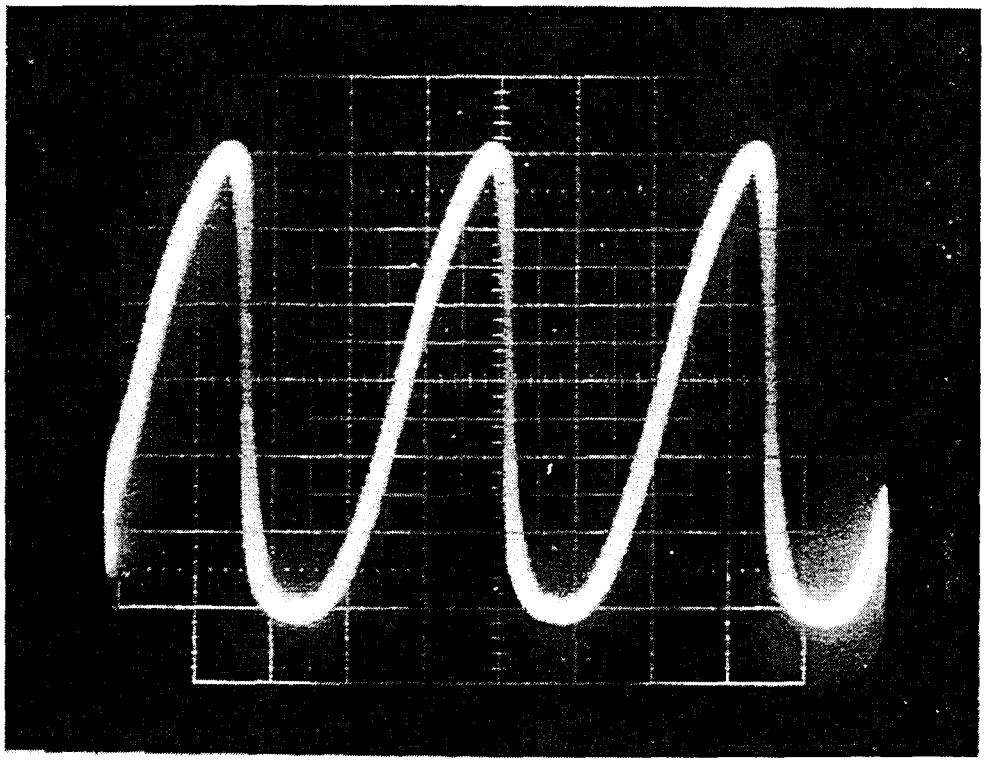

Figure 10.2: Voltage vs flux for the multiloop SQUID magnetometer operating with additional positive feedback. The scale is 0.25 Φ_0/div horizontal and 4 μV/div vertical.

The second function of the traditional FLL is to remove the "in–phase" component of the 1/f noise produced by critical current fluctuations. The "out–of–phase" component is removed by bias reversal. With static bias, the APF scheme does not suppress either component. However, it was shown that combining APF with a combination of bias current and flux reversal one can effectively suppress the noise due to critical current fluctuations [90]. The addition of bias reversal to the APF circuit is indicated in Figure 10.1. Bias reversal frequencies of either 15 kHz (flip–chip) or 9 kHz (multiloop) were used in these measurements.

Each magnetometer was mounted on a probe and inserted into a low–noise biomagnetic dewar filled with liquid nitrogen. The plane of the magnetometer chip was parallel with the bottom of the dewar and the separation between the magnetometer and the outer bottom wall of the dewar was about 13 mm. Once the dewar was moved into the BMSR, the magnetometer was warmed above T_c to release trapped flux and cooled again. All measurements were done with the BMSR door closed. Figure 10.3 shows the magnetic field noise vs frequency for the flip–chip magnetometer measured both with a static bias and with bias reversal. The background noise of the BMSR, as measured by a low-T_c SQUID system at the same location, is indicated. The use of bias reversal suppressed the 1/f noise substantially, but there was still residual non–thermal noise at frequencies below about 10 Hz. The measured noise in this device was 16 fT $Hz^{-1/2}$ and 135 fT $Hz^{-1/2}$ at 1 kHz and 1 Hz, respectively. The field noise of the multiloop magnetometer was 13 fT Hz−1/2 at 1 kHz, a value somewhat below the one that I recorded at Berkeley (18 fT $Hz^{-1/2}$) using a YBCO shield [68] (Chapter 8), suggesting that the shield contributed nonnegligible noise. At 1 Hz, the noise was 110 fT $Hz^{-1/2}$, about a factor of 3 higher than the previously recorded value of 37 fT $Hz^{-1/2}$. It is likely that a defect had developed in this multilayer device during the 8 months of storage since original testing.

10.4 Magnetocardiograms

Figure 10.4 shows magnetocardiograms recorded using the flip–chip magnetometer from two healthy adult male volunteers. In each measurement, the dewar was placed into a mobile gantry inside the BMSR and the subject lay on his back below the dewar. Once the dewar was positioned over the subject, the magnetocardiograms were recorded in real time in a 200 Hz bandwidth. In addition to the large QRS complex one can clearly see the

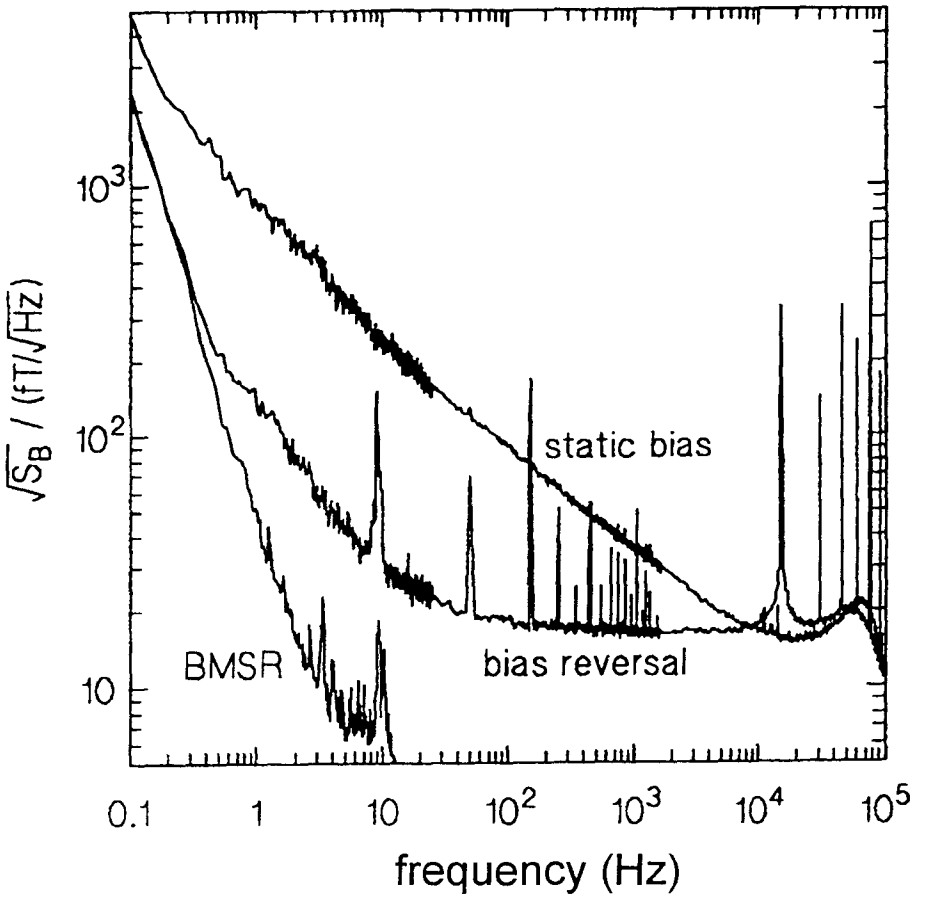

Figure 10.3: Magnetic field sensitivity $S_B^{1/2}(f)$ vs frequency for the flip–chip magnetometer measured with APF using either a static bias or bias reversal in the BMSR.

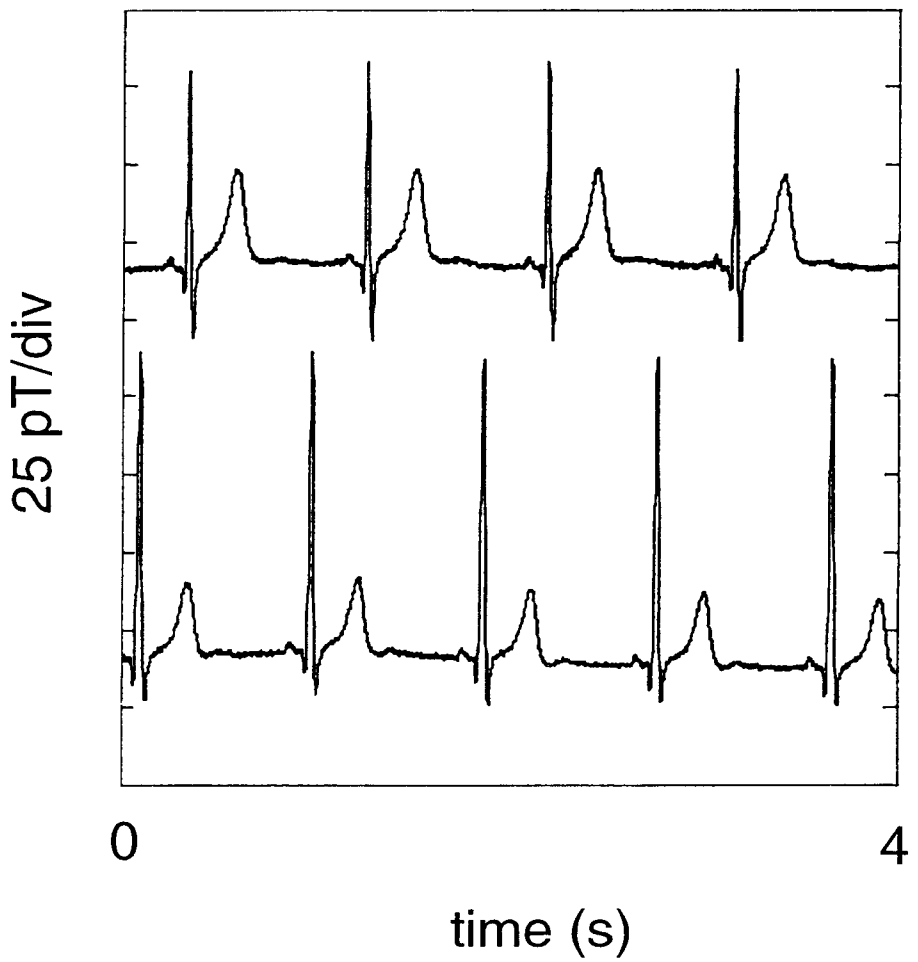

Figure 10.4: Real–time traces of magnetocardiograms of two adult males measured using the flip–chip magnetometer inside the BMSR. The measurement bandwidth is 0.016–200 Hz. The two traces are offset for clarity.

P–wave, just in front, and the T–wave that follows. The noise level was about 2 pT in a 200 Hz bandwidth. Some of the noise was due to 50 Hz powerline signals not entirely screened by the BMSR, suggesting that a gradiometer might still be beneficial.

The quality of these real–time magnetocardiograms is sufficient for clinical applications. In fact, on the scale of Figure 10.4, we could barely distiguish this MCG from one measured from the same subject using a low-T_c SQUID system. This demonstrates that high-T_c SQUID magnetometers have reached a noise level adequate for magnetocardiography. Two improvements, however, are still desired (in my opinion) that would make high-T_c SQUID magnetometers sufficiently attractive to replace their low-T_c counterparts. One is a multichannel sensor array of, say, 50 channels. That would certainly require a greater yield of sensitive high-T_c SQUID magnetometers and the ability to move their fabrication closer to mass production. The other is the ability to operate these magnetometers with less – or even no – magnetic shielding. Possible solutions to this problem are addressed in the remainder of this thesis.

Part V

SQUIDs in Magnetically Unshielded Environments

Chapter 11

SQUIDs Cooled in Static Magnetic Fields

11.1 Introduction

Chapters 5–8 described the extensive improvements in magnetic flux and field noise as well as in compactness of our high-T_c SQUID magnetometers. Two important applications of these devices were illustrated in Chapters 9 and 10 and several others were referenced. One more issue, however, must be resolved before the word "Practical" can be justified in the title of this thesis. All measurements described in Part III were performed with the SQUID magnetometer cooled and operated inside magnetic shields which attenuated the ambient static and time-varying magnetic fields by factors as high as 10^4. The magnetocardiograms described in Chapter 10 were obtained in the Berlin Magnetically Shielded Room (BMSR) which attenuates external fields by as much as 10^6 [87]. It is, however, essential for some applications that the SQUID be cooled and operated in the ambient environment, without magnetic shielding. For example, one of the envisioned instruments for nondestructive evaluation (NDE) is a hand-held scanner that can analyze a sample as large as an airplane wing [91]; it is impractical to shield an object of this size. For geophysical applications such as magnetotellurics, one measures fluctuating magnetic fields at the surface of the earth, and has no option other than to operate the magnetometer unshielded. For biomagnetic measurements the issue may relate more to cost than necessity. Magnetically–shielded rooms (MSR's) large enough to enclose a patient and multiple

SQUID sensors are commercially available and have been widely used with LTS SQUIDs. The cost of an MSR is substantial – typically around $1M – and unless the MSR can be eliminated, the financial savings offered by the transition from liquid helium to liquid nitrogen–cooled SQUID systems are difficult to justify.

A SQUID exposed to the ambient environment is adversely affected by a variety of sources. They can be categorized into *extrinsic* sources – arising directly from the environment – and sources *intrinsic* to the SQUID. Examples of extrinsic or environmental noise sources include power lines (typical amplitudes 20–200 nT at 50 or 60 Hz), computer displays (40 to 80 Hz), lasers, elevators and automobiles. These external magnetic sources as well as their harmonics and intermodulations obscure the signal of interest such as a magnetocardiogram. These effects are not exclusive to high-T_c SQUIDs – they affect any magnetometer and their reduction requires a gradiometer or a system of active cancellation which will be discussed in Chapter 13.

In this and the next chapter we focus on the effect of unshielded cooling and operation on the *intrinsic* properties of the SQUID [82, 92]. In particular we discuss the implications of cooling a high-T_c SQUID in the static magnetic field of the Earth – about 50 μT at our location. The most noticeable effects are the reduction of the critical current resulting in a consequent reduction of the transfer function increasing the white noise, and the increase in the low-frequency flux noise.

11.2 Background

Ferrari *et al.* [26] used a low-T_c dc SQUID to measure the flux noise in YBCO films cooled to 77 K in static magnetic fields B_0 and found that at low frequencies the spectral density $S_\Phi(f)$ scaled as 1/f for cooling fields above a few μT. Furthermore $S_\Phi(f)$ increased linearly with B_0. The excess noise was attributed to the thermally–activated hopping of weakly–pinned flux vortices frozen into the film during cooling. Given that the hopping of each vortex is an uncorrelated event with a characteristic duration, the resulting ensemble of random–telegraph signals produces a 1/f spectrum, consistent with the measurements. The observed linear increase of $S_\Phi(f)$ with B_0 is also consistent with uncorrelated vortex motion since $S_\Phi(f)$ is expected to be proportional to the number of vortices and hence to B_0. Even in the quietest YBCO film, the noise at 1 Hz measured in a B_0 of 50 μT was an order of magnitude higher than the corresponding value obtained in zero field. These

findings were expected to have serious implications for SQUIDs made from these films.

The earliest investigations of the effects of cooling a high-T_c SQUID and a directly coupled magnetometer in static magnetic fields B_0 were conducted by Miklich *et al.* [81]. They found that the critical current of their 3μm–wide bicrystal junctions decreased by a factor of nearly 2, when they were cooled in a 100 μT field, due to flux penetration into the junctions enhanced by the flux–focusing of the SQUID washer. More importantly they found that the 1/f flux noise at low frequencies increased substantially when the devices were cooled in fields comparable to that of the Earth and the spectral density $S_\Phi(f)$ scaled linearly with B_0. For example, in one 250 $\times$ 250 μm^2 square–washer SQUID the noise at 1 Hz increased from 20 $\mu\Phi_0 Hz^{-1/2}$ in nominally zero field to 200 $\mu\Phi_0 Hz^{-1/2}$ when cooled at B_0 = 50 μT. Even if coupled to the best flux transformer desribed in Chapter 6, this excess noise would limit the magnetic field resolution to about 400 fT $Hz^{-1/2}$, an order of magnitude higher than the most sensitive devices in zero field. Comparable increases in 1/f noise with magnetic field were reported by Glyantsev *et al.* [93]. Recently Schmidt *et al.* [94] reported the operation of high-T_c dc SQUID magnetometers in the Earth's field without a substantial increase in low–frequency noise but gave no details of the design. Faley *et al.* [95] presented data showing little increase in the flux noise at 1 Hz, more than 50 $\mu\Phi_0 Hz^{-1/2}$, at fields up to 100 μT, and ascribed this behavior to the geometry of their ramp–type junctions.

11.3 Measurement in Static Magnetic Fields

To investigate the effects of cooling a SQUID or a SQUID magnetometer in a static magnetic field while excluding the influence of other noise sources I used the vertical attachment to the noise probe as illustrated in Figure 11.1. The SQUID chip was mounted on top of the G-10 fiberglass block in the center a solenoid of about 1500 turns of Cu wire wrapped in a single layer about a plastic tube. The solenoid provided a static magnetic field (perpendicular to the chip) at 16.4 μT/mA supplied by a lead-acid battery. To screen against the earth's magnetic field and its fluctuations the solenoid was placed in a cryoperm shield with one endcap and the dewar was surrounded by a triple mu-metal shield. In our earlier measurements we used a cylindrical shield of YBCO on a YSZ tube [69] placed inside the solenoid and cooled with the SQUID to stabilize the field against drift. We later discarded the shield having found that it can actually generate excess noise (particularly in

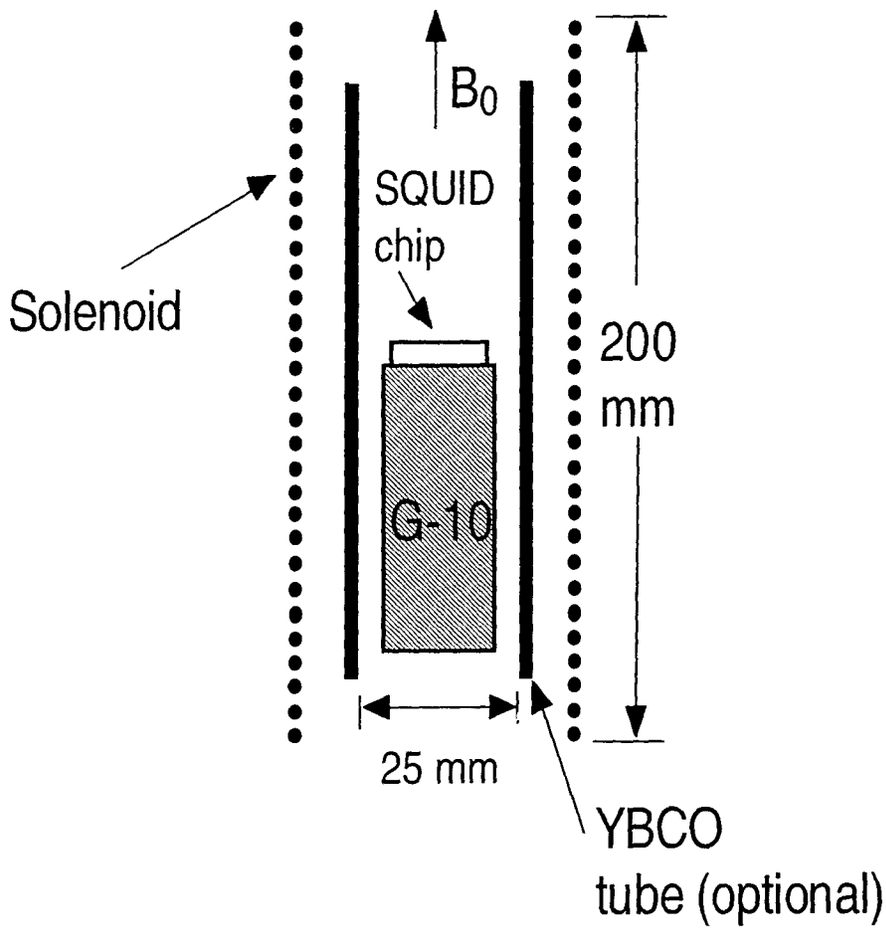

Figure 11.1: Cross-sectional view of the wire-wound copper solenoid used to produce static magnetic fields perpendicular to the plane of the SQUID.

fields above 50 μT) and that the field can be kept from drifting if the battery is first allowed to partially discharge.

In a typical measurement we supplied a current to the solenoid and then lowered the entire assembly into liquid nitrogen. After characterizing the SQUID, we re-adjusted the current to the next value, lifted the probe above the level of the nitrogen and lowered it again, thereby cooling the SQUID in the new field. (More recently Saburo Tanaka hermetically-sealed the SQUID chip in a package equipped with a heater which now allows us to raise and lower the temperature in about 5 minutes – this proved to be a convenient technique for removing trapped flux.) Since a complete characterization of the field dependence of $S_\Phi(f)$ of a SQUID usually took about one week, we typically wired up to three SQUIDs on the chip simultaneously and measured each in turn before changing B_0. The SQUID was operated in the 100 kHz flux-locked loop. Since we were specifically interested in examining the excess 1/f *flux* noise, all SQUIDs described here were operated with the 2 kHz bias reversal scheme. In contrast with the work by Miklich *et al.* [81] we observed no change in the critical current for cooling fields up to 60 μT, likely because most of the junctions were 1 μm wide and therefore had a smaller flux capture area.

11.4 Large–Area Washer SQUIDs

As described in Parts I and III, a magnetometer consisting of a square–washer SQUID inductively coupled to a flux transformer in either a flip-chip [45] or integrated [64] arrangement combines high magnetic field sensitivity with small sensor size. The outer dimension of the SQUID washer is usually made large, say 500 μm, to facilitate efficient coupling to the multiturn input coil. Consequently we first re–examined the dependence of the flux noise on the ambient static field for these large–area SQUIDs. Two years prior to this, Andy Miklich measured the field dependence of one of our 250 $\times$ 250 μm^2 washer SQUIDs and found that the flux noise power increased linearly with the cooling field, reaching a value of 200 $\mu\Phi_0/Hz^{1/2}$ for B_0=50 μT. [81] We were interested in seeing the field dependence of the flux noise for our more recent SQUID designs (types A/A and A/C – see Figure 6.2) and, in particular, whether the recent processing improvements reduced the noise at B_0=50 μT. Table 11.1 summarizes the dimensions and noise performance at three values of B_0 for three A/A SQUIDs and two A/C SQUIDs. Spectral density $S_\Phi(f)$ vs. frequency for device 1 is plotted in Figure 11.2 for the three cooling fields. All SQUID

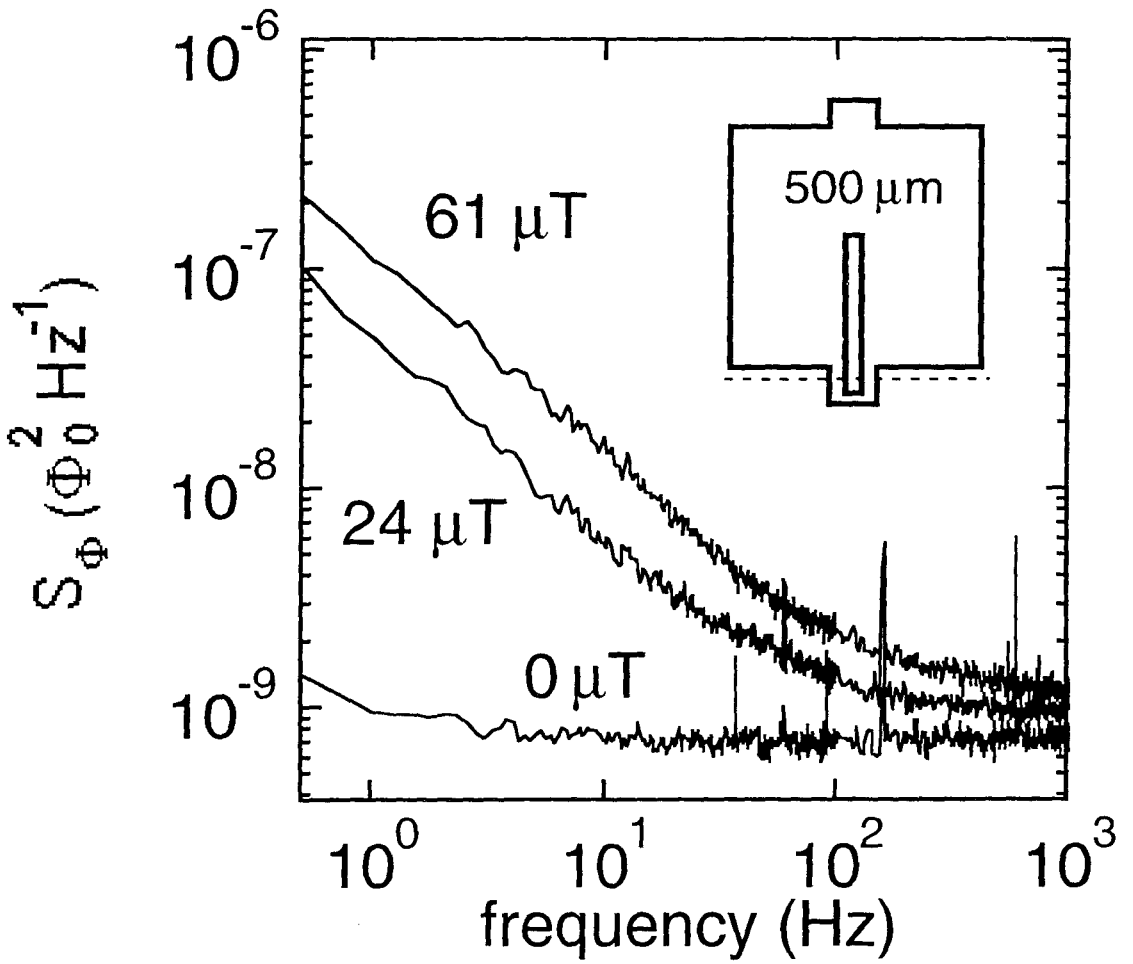

Figure 11.2: $S_\Phi(f)$ for the A/A SQUID (device 1) shown inset cooled in three magnetic fields

Device No.	D (μm)	ℓ (μm)	L (pH)	$S_\Phi^{1/2}(1\text{Hz})(\mu\Phi_0\text{Hz}^{-1/2})$ 0 μT	24 μT	61 μT
1	500	250	80	31	220	330
2	500	250	80	24	240	380
3	500	250	80	16	250	400
4	500	100	40	33	120	...
5	500	100	40	5	130	180
5*	30	100	40	8	11	170

Table 11.1: Flux noise of six SQUIDs measured at 1 Hz for three values of magnetic field. D is the outer width of the SQUID washer, ℓ the length of the slit, and L the estimated inductance.

washers had an outer dimension D of 500 μm and an inner slit of length ℓ and width 4 μm. The junction widths were 1 μm and 2 μm for the A/A and A/C SQUIDs respectively.

At B_0=0 μT the noise for all five SQUIDs was white at frequencies down to 1 Hz as illustrated in the example of Figure 11.2. For higher fields, however, the spectral density $S_\Phi(f)$ at low frequencies increased significantly, scaling as 1/f. In all cases S_Φ(1 Hz) scaled linearly with B_0, as in the observations of Miklich *et al.* [81], suggesting that the excess noise arises from uncorrelated motion of flux vortices. It is interesting to note the reproducibility of $S_\Phi^{1/2}$(1 Hz) at B_0=24 μT and B_0=61 μT seen in Table 11.1 for all devices of a given type. Also at a given B_0, $S_\Phi^{1/2}$(1 Hz) is about a factor of 2 lower for the A/C SQUIDs than for the A/A SQUIDs. Although the first observation indicates the reproducibility of our film fabrication process, we have no immediate explanation for the systematic dependence of the 1/f noise on these SQUID geometries. It might be interesting to analyze more samples and to image vortex distributions in both types of washer using, for instance, a scanning SQUID microscope [96].

We were more concerned, however, with the alarmingly high levels of flux noise in both types of SQUID cooled in magnetic fields comparable to the Earth's. Magnetometers based on these SQUIDs simply would not have enough field resolution for most practical applications in the ambient static field. To reduce this noise we first set out to make higher quality YBCO films. By that time, we systematically had transition temperatures (T_c) of 92 K and critical current densities (J_c) as high as 10^7 A/cm^2 at 77 K, but a remaining quality factor was the roughness of the film. I examined the SQUID washers with an atomic

force microscope and found that the films contained a large number of "stalagmites" about 1000 Å high and spaced every 1–2 μm. I could subsequently reduce this surface roughness to about 10 Å by leaving out the STO buffer layer and by not using the Hanes alloy clip to press the substrate to the heater block; the quality of the films (T_c, J_c) was otherwise unchanged. The removal of surface roughness in the YBCO had no effect on the SQUID noise in zero field nor, unfortunately, on the excess 1/f noise when the SQUIDs were cooled in higher fields.

11.5 Narrow Linewidth SQUIDs

Because of the 1/f scaling and linearity with B_0 we concluded that the cause of the excess 1/f noise, described in the previous section, was thermally–driven hopping of flux vortices that enter the SQUID washer when it goes through the superconducting transition in a magnetic field. To eliminate this noise, the vortices must be either kept from moving or from entering the film in the first place. If one reduces the size of the SQUID washer there will be fewer vortices. On the other hand, as one reduces the washer linewidth w, each remaining vortex might couple more flux into the SQUID per hop. One can also argue that reducing w to a value smaller than the vortex–vortex separation, approximately $(\Phi_0/B_0)^{1/2}$, would make it energetically unfavorable for vortices to penetrate the film. The latter argument is consistent with John Clem's theoretical treatment of flux penetrating a strip of width w going through a superconducting transition in a magnetic field B_0 [97]. He showed that for fields below the *vortex exclusion field*

$$B_T = \pi\Phi_0/4w^2 \tag{11.1}$$

vortices should not enter the strip. Above this field, vortices are expected to penetrate the film.

To test these arguments I repatterned device 5, as shown in the inset of Figure 11.3, to remove the material outside the dotted lines, reducing the outer dimension D from 500 μm to 30 μm and thereby reducing the linewidth w to 13 μm. As we see in Figure 11.3 and Table 11.1 (device 5*), the noise measured in B_0=24 μT is dramatically reduced, by more than two orders of magnitude in power. The noise spectrum of the repatterned device is approximately white at frequencies down to 10 Hz and increases slowly at lower frequencies. At 61 μT, however, the noise at 1 Hz is not significantly different from that in

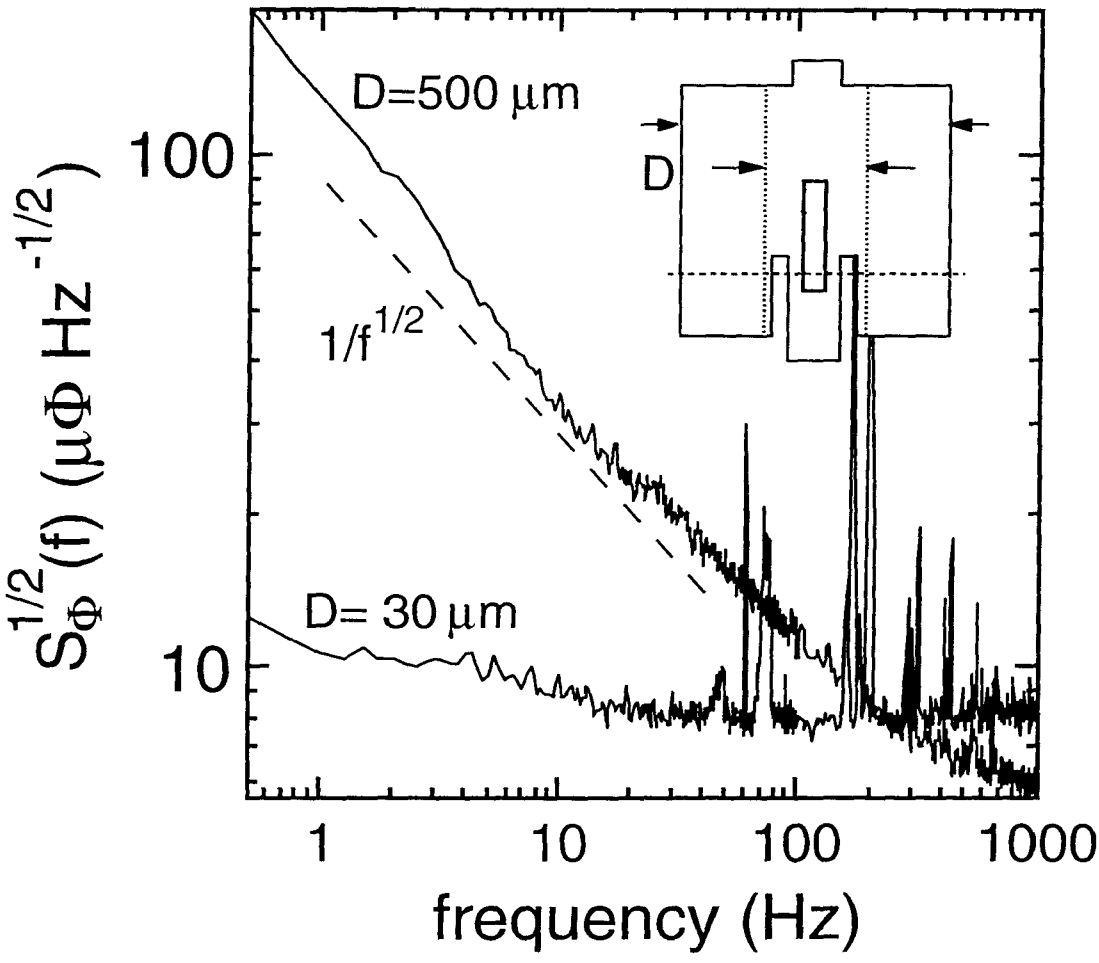

Figure 11.3: $S_\Phi^{1/2}$(1 Hz) for the SQUID shown inset cooled in a field of 24 μT: upper trace for D = 500 μm (device 5), lower trace after washer has been repatterned to width D = 30 μm indicated by dotted lines (device 5*). Inset is not to scale. Slit length is 100 μm. Dashed line indicates grain boundary. Spikes on traces are due to 60 Hz and its harmonics as well as other nearby electronic instruments and microphonic noise.

Device No.	D (μm)	w (μm)	ℓ (μm)	I_0 (μA)	R (Ω)	L (pH)	B_T (μT)
6	20	8	48	65	1.8	40	26
7	30	13	55	88	1.1	40	20
8	30	13	55	74	1.4	40	19
9	20	8	24	130	1.2	20	N/A
10	30	13	55	62	1.8	40	20
11	12	4	40	54	2.0	40	33
12	12	4	40	45	2.2	40	33

Table 11.2: Parameters for seven narrow–linewidth SQUIDs. Critical current I_0 and resistance R are per junction. Devices 6–9 are bare SQUIDs. Devices 10–12 are directly coupled magnetometers. B_T is the threshold cooling field at which the noise at 1 Hz begins to increase.

the original device. This reduction in 1/f noise is a graphic illustration of the role of SQUID geometry and, in particular, supports the assertion that sufficiently narrow linewidths in a SQUID washer exclude vortices.

To investigate further the effect of SQUID configuration on the flux noise, I fabricated a series of SQUIDs with values of D ranging from 12 to 30 μm and linewidths w correspondingly ranging from 4 to 13 μm. (See inset to Figure 11.4). The length ℓ of the 4 μm–wide slit was adjusted to keep the estimated inductance L of each SQUID loop at either 20 or 40 pH. Figure 11.4 shows the behavior of three of these devices, fabricated in the same film. Additional parameters are summarized in Table 11.2. For devices 7 and 8 (D=30 μm, w=13 μm), $S_\Phi^{1/2}$(1 Hz) is constant up to $B_0 \approx 20\mu$T above which the noise increases rapidly with field. We interpret the magnetic field at which the noise abruptly increases as the threshold field B_T for vortex entry when the SQUID is cooled. For device 6 (D=20 μm, w=8 μm) B_T is somewhat greater, about 26 μT, as one might expect for the SQUID the smaller linewidth. The threshold values of B_0 estimated from Equation 11.1 are 10 and 25 μT, respectively, the latter in rather good agreement with the measurement.

Figure 11.5 shows noise spectra for device 8 cooled in three magnetic fields. At $B_0 = 19.5\,\mu$T the noise below about 5 Hz has increased slightly above the zero–field level. The onset of vortex entry must occur at a cooling field just below this value. At $B_0 = 23.4\,\mu$T, $S_\Phi^{1/2}$(1 Hz) has increased by about a factor of 3 over the zero–field value. The power spectrum below about 200 Hz scales approximately as $1/f^{0.4}$; this slope is more

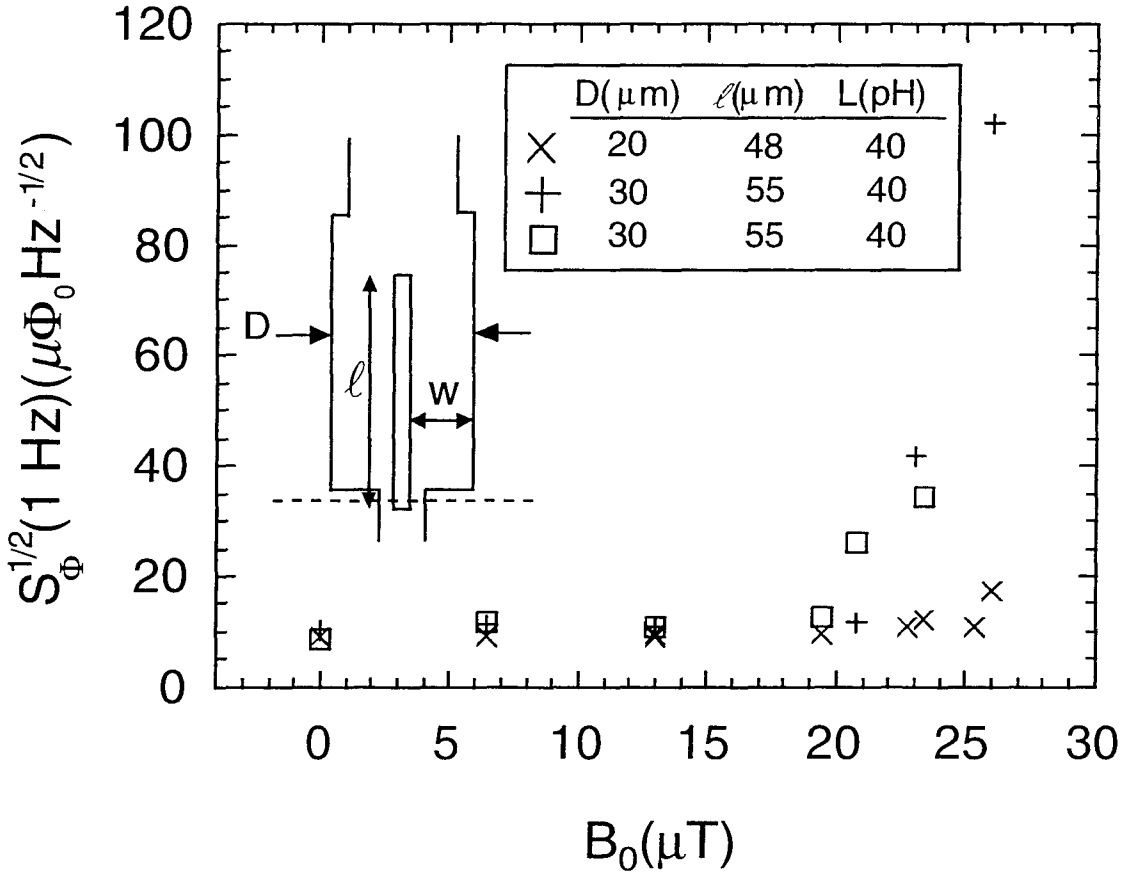

Figure 11.4: $S_\Phi^{1/2}(1\ \mathrm{Hz})$ vs cooling field B_0 for three narrow–linewidth SQUIDs. Geometry is shown in the inset. Dashed line indicates grain boundary.

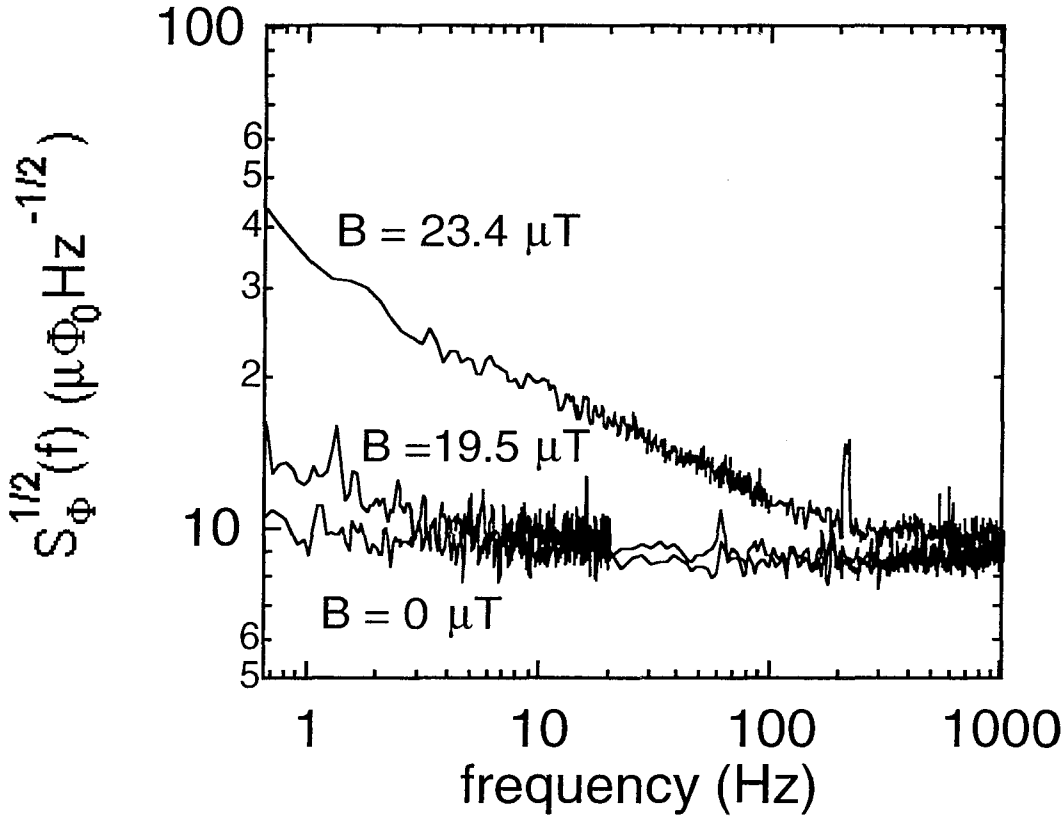

Figure 11.5: $S_\Phi^{1/2}(f)$ vs frequency for device 8 cooled in three magnetic fields.

shallow than what we usually observe for large-area SQUIDs (see for example Figures 11.2 and 11.3).

Of the 9 narrow-linewidth SQUIDs that we investigated on this bicrystal, 7 showed the behavior displayed in Figure 11.4. The other two exhibited a rather different behavior shown in Figure 11.6 for device 9, in which $S_\Phi(1\ \mathrm{Hz})$ increased linearly with B_0. Clearly vortices are not excluded from these SQUIDs even for very small cooling fields. It is likely that variation in film quality, particularly at the edges, contribute to this effect. More will be said about edges at the end of this chapter.

On a separate bicrystal I fabricated 10 small directly coupled magnetometers consisting of a SQUID, whose outer dimension D ranged from 12 to 30 μm, coupled to a pickup loop 1.8 mm by 3.8 mm and 4 μm wide. The effective areas of these magnetometers were comparable to those of the large-washer A/C and A/A SQUIDs. Figure 11.7 shows $S_\Phi^{1/2}(1\ \mathrm{Hz})$ vs. B_0 for three of these devices. For D=30 μm (w=13 μm), the noise increases at about 20 μT as before, while for the two devices with D=12 μm (w=4 μm), the threshold is about 33 μT. For this linewidth Equation 11.1 predicts a threshold field of $B_T \approx 100\mu$T. This discrepancy may be a further illustration of film quality variation at the edges. The increase of $S_\Phi^{1/2}(1\ \mathrm{Hz})$ with B_0 above the threshold is indicative of increasing numbers of vortices penetrating the SQUID loop. In that case, however, one expects the noise *power* $S_\Phi(1\ \mathrm{Hz})$ to scale as B_0. The quadratic scaling seen here is, as yet, difficult to explain but we may be seeing just the *onset* of vortex penetration which may depend of the geometry. It may be interesting to measure the noise in these devices at greater cooling fields and also to re-examine the vortex distribution using an imaging technique such as scanning SQUID microscope.

11.6 Implications for Directly Coupled SQUID Magnetometers

From the foregoing discussion it is clear that SQUIDs with narrow linewidths are immune to ambient field–cooling up to a threshold field whereas large-area SQUIDs generate excess 1/f noise for cooling fields as low as a few μT. Even though they are small in size and effective area, the new SQUIDs are ideally suited for directly coupled magnetometers that must operate in the unshielded environment. We therefore turn to a discussion of the

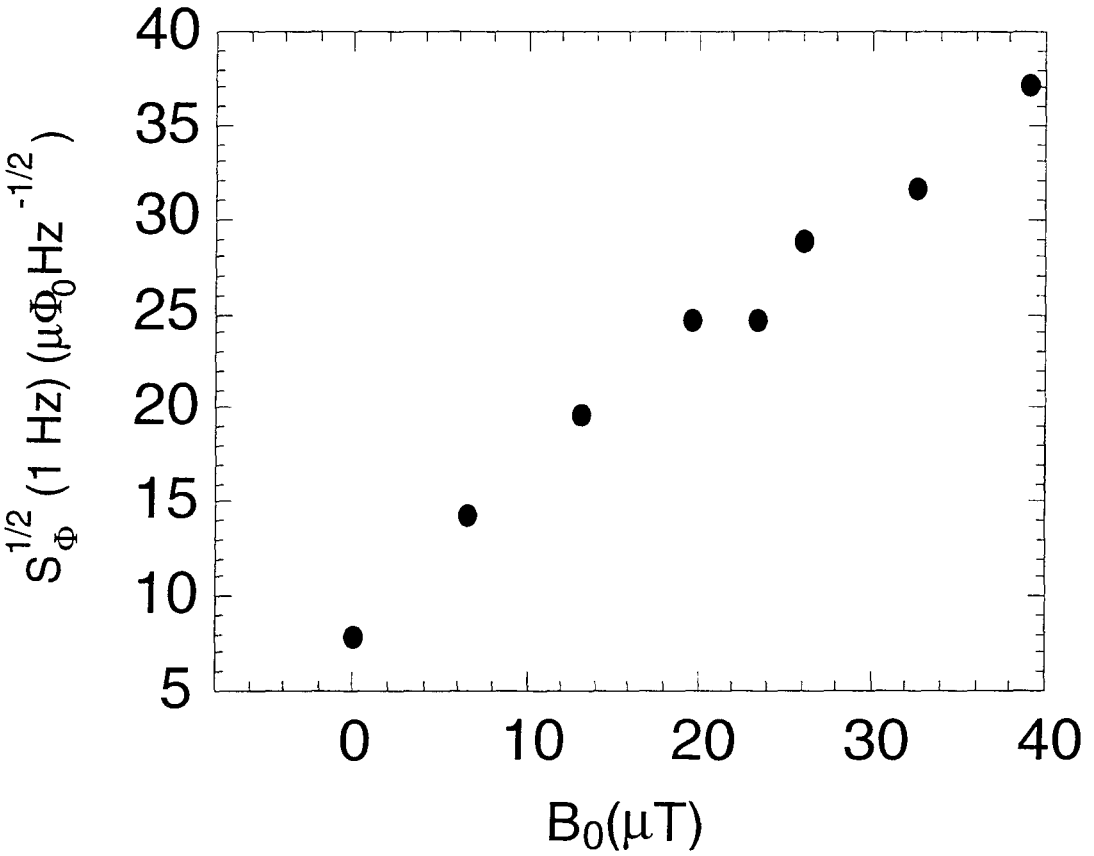

Figure 11.6: $S_\Phi^{1/2}$(1 Hz) vs cooling field for device 9 with geometry shown in Figure 11.4. One other device showed similar behavior.

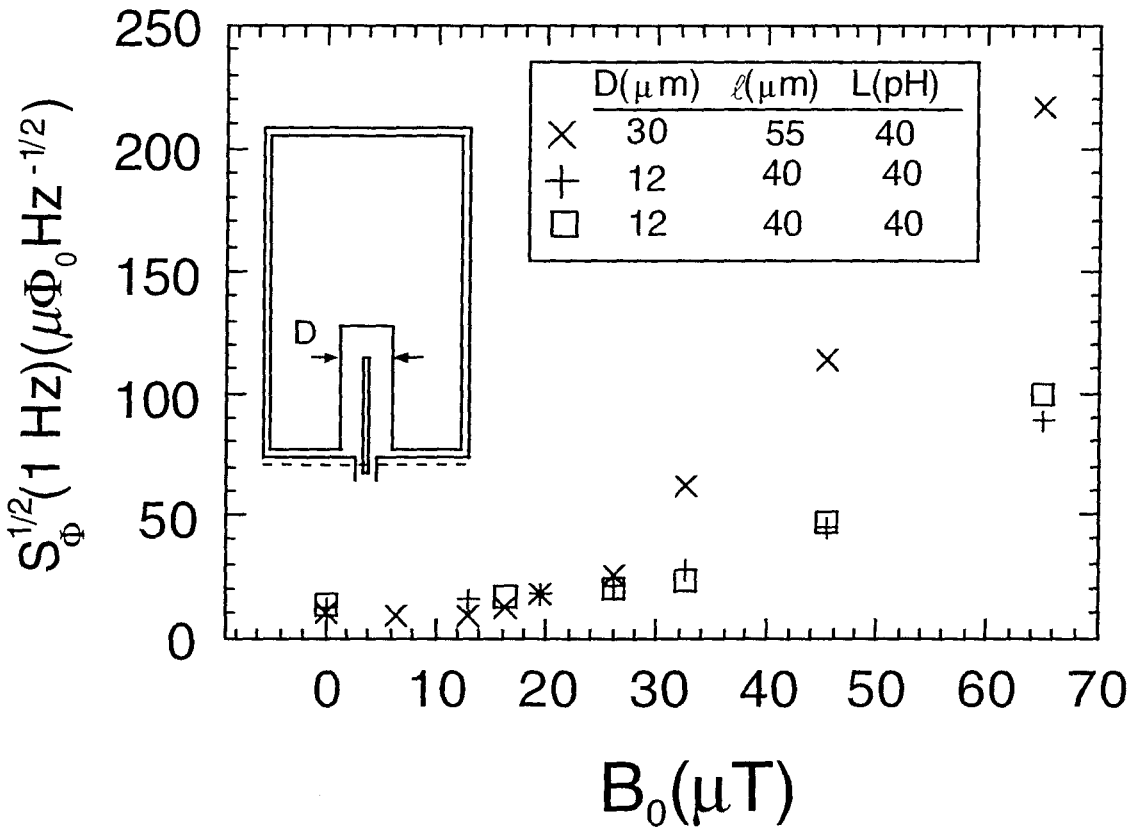

Figure 11.7: $S_\Phi^{1/2}(1\ \text{Hz})$ vs cooling field for three directly coupled magnetometers with configuration shown in the inset.

implications of these results for directly coupled magnetometers to complement the design discussion of Chapter 5.

Consider a directly coupled dc SQUID magnetometer, optimized for maximum field sensitivity, shown in Figure 5.6. The pickup loop is square with inner and outer dimension d_p and D_p and inductance L_p. We also define the linewidth of the pickup loop $w_p = (D_p - d_p)/2$. As shown in section 5.4, the design that yields the highest effective area A_{eff} for a magnetometer on a 1 cm^2 substrate uses a washer pickup loop with $w_p \geq 3\,mm$. This means that even in relatively low cooling fields, a large number of vortices penetrates the loop. We can estimate the contribution of these vortices to the 1/f noise using the model of Ferrari *et al.* [51], originally devised to estimate noise in flux transformers, modified for directly coupled magnetometers. In simple terms, vortex motion in the pickup loop generates screening currents which, in turn, couple flux noise into a fraction α_d of the SQUID inductance L. Consider a vortex displacement δr across the pickup loop. This results in an applied flux change $\delta\Phi \approx \Phi_0 \delta r/w_p$ and a screening current $J \approx -\Phi_0 \delta r/w_p L_p$ which couples flux $\delta\Phi_S \approx \alpha_d L J \approx -(\Phi_0 \alpha_d L)\delta r/(w_p L_p)$ into the SQUID. For $\mathcal{N}$ uncorrelated vortices per unit area in the YBCO film, each with a spectral density for radial motion $S_r(f)$, the spectral density of the flux noise in the SQUID is given by

$$S_\Phi(f) = \mathcal{N} S_r(f) \int_A \left(\frac{\partial \Phi_S}{\partial r}\right)^2 dA \tag{11.2}$$

where the integral is taken over area A of the YBCO in the pickup loop. Thus for the directly coupled magnetometer the total contribution to the SQUID flux noise by the vortex motion in the pickup loop is

$$S_\Phi^{(in)}(f) = 4\mathcal{N} S_r(f) \frac{\Phi_0^2 L^2 \alpha_d^2}{L_p^2} \left(\frac{D_p + d_p}{D_p - d_p}\right) \tag{11.3}$$

where (in) indicates that the noise is *indirect*, coupled into the SQUID via a screening current.

We can now make an order–of–magnitude estimate for this noise. In ref. [51] it is shown that $4\mathcal{N} S_r(f)\Phi_0^2 \approx S_\Phi^U(f)$, where $S_\Phi^U(f)$ is the spectral density of the flux noise produced by an *unpatterned* film as measured by a low-T_c SQUID of given dimensions placed directly over it. Tim Shaw has measured the flux noise of a number of our laser–depositted YBCO films, cooled to 77 K in various magnetic fields, using an appropriate low-T_c SQUID held at 4.2 K and typically found for B_0=50 μT, $S_\Phi^U(1Hz) \lesssim 10^{-9}\Phi_0^2 Hz^{-1}$ [81, 26]. We

take typical parameters for a directly coupled magnetometer from the design in Section 5.4: $\alpha_d \approx 0.9$, L $\approx$ 50pH, $L_p \approx 4\,nH$, $d_p = 2\,mm$ and $D_p = 10\,mm$. Inserting these values into Equation 11.3 we find $S_\Phi(1Hz) \approx 10^{-4} S_\Phi^U(1Hz) \approx 10^{-13}\,\Phi_0^2\,Hz^{-1}$. This spectral density corresponds to rms flux noise of $S_\Phi^{1/2}(1Hz) \approx 0.3\,\mu\Phi_0 Hz^{1/2}$, considerably lower than the intrinsic noise measured for any of our SQUIDs in any field (or indeed for any SQUID reported in the literature.) We can thus conclude that the 1/f noise contribution of the pickup loop is entirely negligible, even though the film is penetrated by vortices. The noise of a directly coupled magnetometer cooled in a static magnetic field may still be dominated by the *direct* flux noise of the SQUID and of the film in the pickup loop in close proximity to the SQUID. The SQUID flux noise can be eliminated by using a narrow–linewidth SQUID and the remaining direct noise can be reduced by keeping the SQUID sufficiently distant, say 100 μm, from any wide films (See Figure 5.6).

It is interesting to note that if one makes the pickup loop larger, the contribution of the 1/f noise in the loop to the magnetic *field* noise becomes even smaller. Recall that the effective area of the magnetometer is given by

$$A_{eff} = \alpha_d L \frac{A_p}{L_p}. \tag{11.4}$$

We keep the linewidth w_p fixed and increase the size of the loop. To convert Equation 11.3 into magnetic field noise we divide it by the A_{eff}^2 and find

$$S_B^{1/2}(f) = \frac{1}{\sqrt{2}} \frac{1}{A_p} \left(\frac{D_p + d_p}{w_p} \right)^{1/2} \left(S_\Phi^U\right)^{1/2}(f) \tag{11.5}$$

meaning that $S_B^{1/2}$ scales as $D_p^{-3/2}$ (since $A_p \sim D_p^2$). This rather remarkable result indicates that the signal–to–noise ratio of a SQUID magnetometer scales as $r^{3/2}$, where r is the size of the pickup loop, and that the 1/f noise contribution from the pickup loop structure of any magnetometer is negligible provided the loop is sufficiently large.

11.7 Discussion

In this chapter I have shown that the 1/f flux noise of dc SQUIDs cooled in a magnetic field can be dramatically lowered by reducing the linewidth of the device. Vortices are excluded from the film for cooling fields B_0 below a threshold, which increases with decreasing linewidth. The measured threshold fields, however, were not in full agreement

with the prediction $B_T = \pi\Phi_0/4w^2$ [97]. In particular, the measured threshold field of 33 μT for the devices with the 4 μm linewidths was below the Earth's magnetic field of 50 μT whereas Equation 11.1 predicts $B_T \approx 100\,\mu T$. It would be highly desirable to increase this threshold field by at least a factor of 2. Furthermore in two devices, the 1/f noise increased linearly with magnetic field. At this stage in our work, we suspected variations in the quality of the films, particularly at the edges, to be responsible for these sample–to–sample variations and disagreement with theory (a suspicion proved to be correct). I note that Sun *et al.* [98] in their work on magnetic hysteresis found that the applied magnetic field at which vortices entered the film depended critically on the quality of the edges and that improved edge quality significantly increased the threshold field for flux entry.

These narrow linewidth SQUIDs are, in principle, very useful elements for any SQUID–based instrument that must operate in the Earth's magnetic field. Examples include a voltmeter [99] and a scanning SQUID microscope [73, 74]. As far as sensitive magnetometers are concerned, in the case of a single–layer directly coupled SQUID magnetometer it is straightforward to make the SQUID with narrow linewidths (shown in Figure 5.6); the 1/f noise in the pickup loop is expected to be negligible as was shown in the previous section[1]. The best directly coupled magnetometers on a 10 × 10 mm^2 substrate have a field resolution of about 50 fT Hz$^{-1/2}$ down to 1 Hz [53], adequate for most geophysical applications. For higher field sensitivity one would need to use a multilayer flux transformer but the limited coupling efficiency of the narrow linewidth SQUID would make this approach impractical. The solution to all of these problems is addressed in the next chapter.

[1] I have made a number of directly coupled magnetometers on 10 × 10 mm^2 bicrystal substrates shown in Figure 5.6. At this time we have used these devices in the gradiometer described in Chapter 13 but we have not yet measured their field noise.

Chapter 12

SQUIDs with Slots or Holes for Low Noise and Tight Coupling

12.1 Motivation

The narrow linewidth SQUIDs introduced in the last chapter exhibit no excess 1/f noise when cooled in a static magnetic field B_0 up to a threshold field B_T. These devices are ideally suited for directly coupled magnetometers and we showed that the 1/f noise contribution from the pickup loop is negligible. However, we also showed in Part III that for a pickup loop of a given size, the highest field sensitivity can be achieved by means of a superconducting flux transformer with a multiturn input coil inductively coupled to the SQUID[1]. There appears to be a trade-off: as we reduce the linewidth of the SQUID washer, we also reduce its coupling efficiency to the input coil. In this chapter, I introduce a new type of SQUID design which combines the narrow–linewidth principles, resulting in no excess 1/f noise in static magnetic fields, with the tight coupling efficiency of a traditional square–washer SQUID [63].

Another issue addressed in this chapter is the fact that although in Chapter 11 B_T increased with decreasing values of the linewidth w, its value was not in full agreement with the prediction of Equation 11.1. In particular, we did not break the "50 μT barrier" for $w = 4\,\mu m$, whereas the prediction was for $B_T \approx 100\,\mu T$. It was suggested that rough edges in the films were responsible for this discrepancy. I will presently show that improvement

[1]Another viable alternative is the multiloop SQUID magnetometer introduced in Chapter 8, since all linewidths can, in principle, be made narrow.

in edge quality does indeed increase the threshold field to the predicted value.

12.2 Design and Fabrication

The desired requirements for our new SQUIDs are: (1) no excess 1/f flux noise in ambient magnetic fields and (2) efficient coupling to a planar multiturn input coil. The traditional square–washer SQUID shown in Figure 12.1(a) fulfills the second requirement but not the first as shown in the last chapter. Figures 12.1(b) and (c) illustrate designs that fulfill both. The guiding principle in these designs is to maintain narrow linewidths for the YBCO films: I chose a value of 4 μm, for which the predicted vortex entry field is 100 μT [97]. In Figure 12.1(b) the washer contains 8 slots, each 8 μm wide, that separate 9 YBCO strips, each 4 μm wide. One can alternatively regard this structure as 8 pickup loops of a directly coupled magnetometer connected in parallel to a single SQUID. Figure 12.1(c) shows our second design in which 248 holes, each 8 x 8 μm^2 divide the square washer into a grid of 4 μm–wide lines. In Figures 12.1(d) and (e) I have reduced the number of slots to 5 and the number of holes to 125, respectively, leaving a superconducting band 40 μm wide around three sides of the devices. This was done to determine whether vortices a given distance from the SQUID slit couple significant amounts of 1/f noise. All five devices have outer dimensions of 186 x 204 μm^2. The innermost slit is 4 μm wide and 100 μm long.

I estimate the inductance of the solid washer SQUID [Figure 12.1(a)] to be 40 pH (including contributions from the junctions and kinetic inductance). The inductance of the devices containing holes [Figure 12.1(c) and (e)] is likely to be comparable. The inductances of the devices with slots [Figure 12.1(b) and (d)] are more difficult to calculate; I estimate the inductance of the innermost loop to be 90 pH, a value that is reduced by the parallel inductances of the remaining loops.

While fabricating these devices I was continually concerned with the question of rough edges raised in the last chapter. I re–examined those SQUIDs using both scanning electron and optical microscopy and found that the edges on one side of the SQUID slits were indeed more rough than on the other. Using the mask for the new devices, I first made several test exposures and developments of the photoresist on Si wafers and saw lateral edge roughness (a series of submicron meanders along the edge line) in the photomask itself. I attributed this to insufficiently optimized exposure and development parameters[2] and re-

[2]Shortly prior to this, the Microlab switched photoresists from Shipley 1400-31 to S1818.

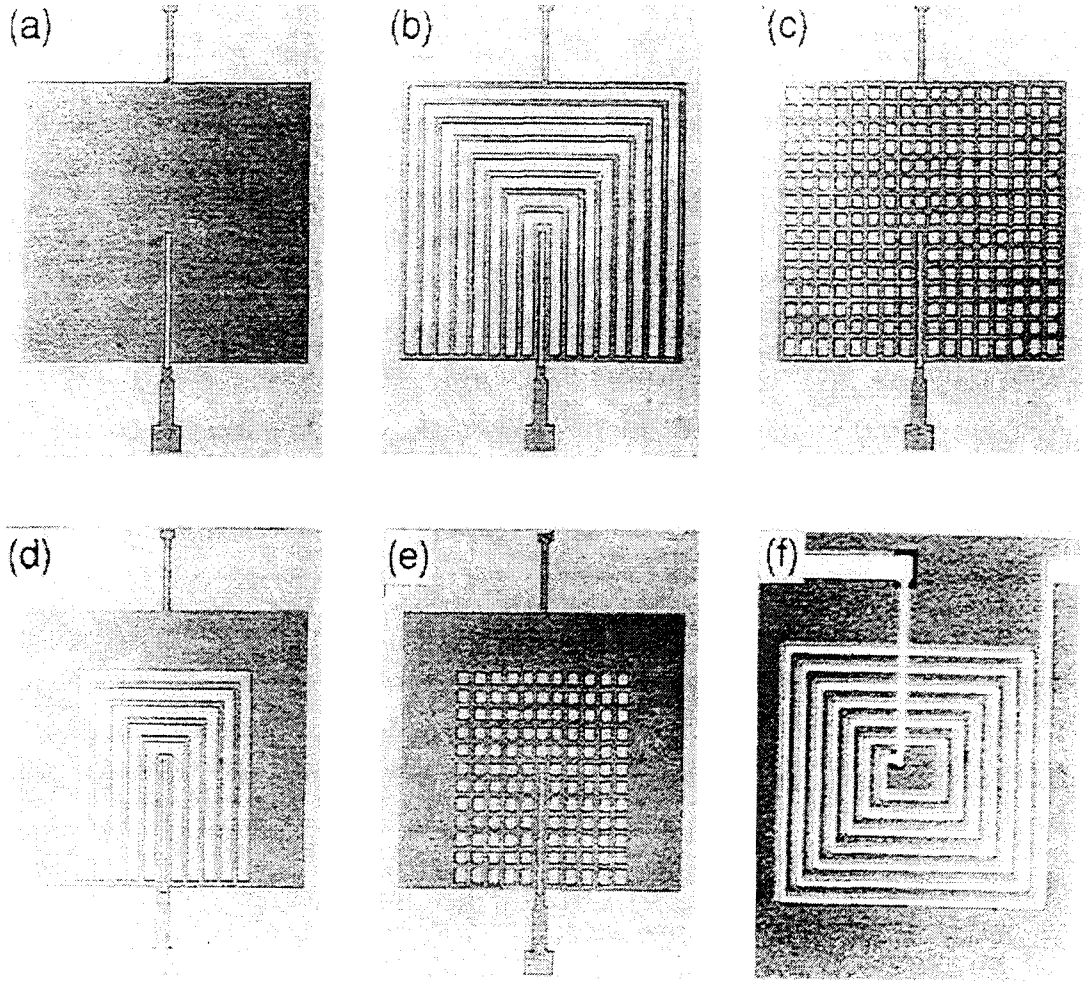

Figure 12.1: Photographs of the photomasks for (a) a solid, thin–film SQUID, and for a SQUID penetrated by (b) 8 slots (c) 248 holes (d) 5 slots and (e) 125 holes. The outer dimensions of each device are 186 x 204 μm. (f) shows a 7–turn input coil that was coupled to the designs (a)–(c) in a flip–chip arrangement.

	SQUID	I_0 (μA)	R (Ω)	A_{eff} ($10^{-3}mm^{-2}$)	M_i (pH)
1	solid (a)	19	3.8	5.01	148
2	8 slots(b)	40	2.0	5.45	125
3	8 slots(b)	35	2.0	5.58	-
4	248 holes(c)	18	2.6	5.95	129
5	5 slots(d)	21	2.0	6.81	-
6	125 holes(e)	12	3.4	6.18	-
7	125 holes(e)	60	2.2	6.67	-

Table 12.1: Critical current I_0 and resistance R per junction for SQUIDs with configurations of Figure 12.1; A_{eff} is the effective area and M_i the mutual inductance to a 7–turn input coil. In the first column, letters in parentheses refer to Figure 12.1.

tuned the parameters[3] until the edges looked very smooth (as seen under a high–power optical microscope). I patterned the SQUIDs in a 150 nm-thick film of YBCO on a 10 × 10 mm^2 STO bicrystal using photolithography and argon ion milling at normal incidence without substrate rotation. The edges of the patterned YBCO films looked more smooth than in the devices in Chapter 11. I suspect that the observed roughness was reduced when both the photomask and subsequently the YBCO edges were very close to vertical. I made 12 SQUIDs on the bicrystal, 2 to 3 of each type illustrated in Figures 12.1(a)–(e). The bridges across the bicrystal boundary forming the junctions were approximately 1 μm wide. The critical current and resistance per junction are listed in Table 12.1 for each of the 7 SQUIDs that were investigated.

12.3 Measurement

12.3.1 Noise

Sabu Tanaka and I measured the flux noise of these SQUIDs using the apparatus and procedure described in section 11.3. Figure 12.2 shows the rms flux noise $S_\Phi^{1/2}(f)$ for SQUIDs with (a) 8 slots [Figure 12.1(b)] and (b) 248 holes [Figure 12.1(c)], each cooled in four different magnetic fields. In Figure 12.2(a) there is no increase in the noise for cooling fields up to 60 μT. At 130 μT, however, the noise at 1 Hz has increased by a factor of 2, indicating that flux entered the YBCO film at a value between 60 and 130 μT. In Figure 12.2(b), the low-frequency noise is unchanged for cooling fields up to 80 μT. At 100 μT, the

[3]No point in listing them. I am sure they drifted by now.

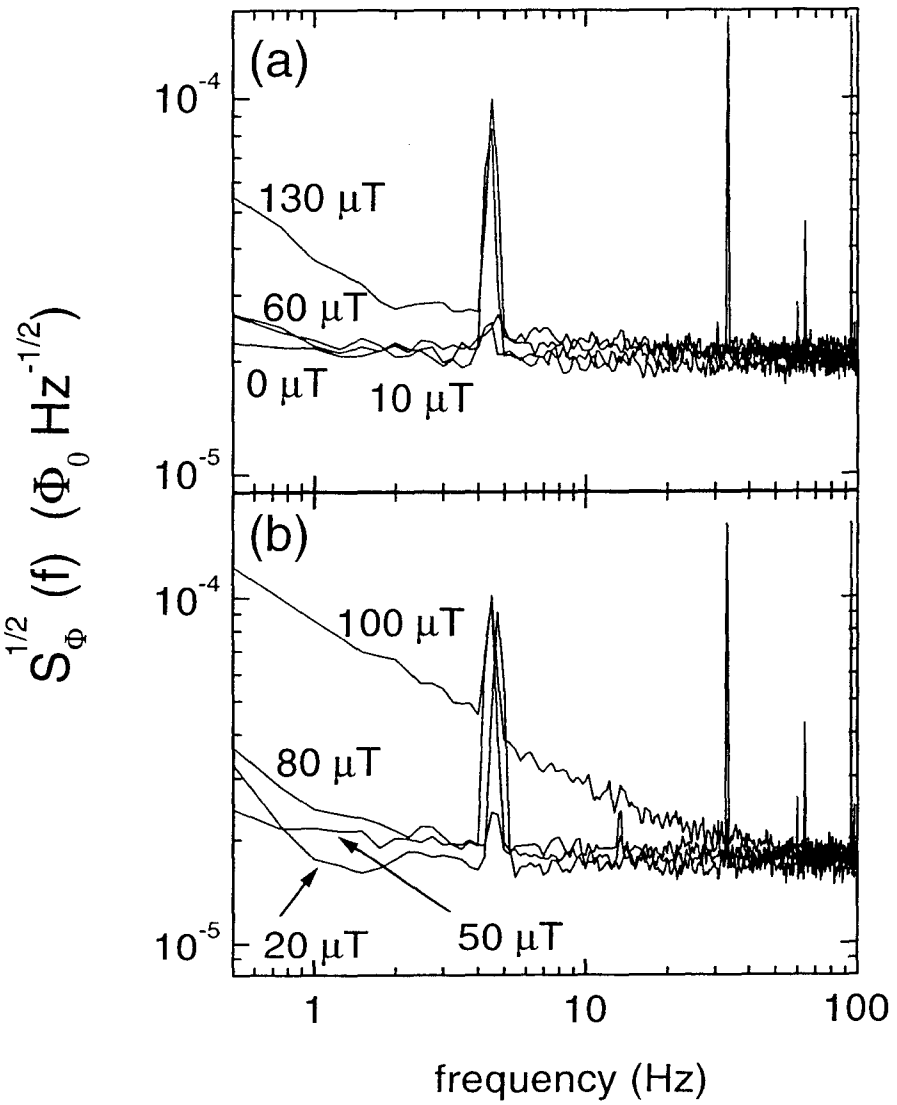

Figure 12.2: Flux noise $S_\Phi^{1/2}(f)$ vs. frequency for (a) 8–slot SQUID (2) and (b) 248–hole SQUID (4) each cooled in four values of magnetic field. The spike at approximately 4.5 Hz was due to an external source of unknown origin.

noise below about 50 Hz increased substantially, by a factor of about 5 at 1 Hz, and $S_\Phi^{1/2}(f)$ scales approximately as $1/f^{1/2}$ in this frequency range. Flux vortices must have entered the YBCO film at a value between 80 and 100 μT. I note that in both cases the white noise remains constant for all values of magnetic field, an observation consistent with the fact that the critical currents of the SQUIDs did not vary systematically with the field.

Figure 12.3 shows the flux noise at 1 Hz, $S_\Phi^{1/2}(1\text{ Hz})$, vs. cooling field B_0 for all seven SQUIDs. For the solid SQUID, $S_\Phi^{1/2}(1\text{ Hz})$ increases rapidly with B_0 to a value of 230 $\mu\Phi_0\text{Hz}^{-1/2}$ at 20 μT, a value similar to that for large–washer SQUIDs described in Chapter 11. For the device with 5 slots and one of the devices with 125 holes, the noise increase is similar to that of the solid SQUID although the actual values of the noise are somewhat less. Evidently flux vortices enter the outer band of YBCO and couple significant amounts of excess 1/f noise. The second device with 125 holes, however, is markedly less noisy, although $S_\Phi^{1/2}(1\text{ Hz})$ increases linearly with B_0. This different behavior between two nominally identical devices implies that variation in edge quality still remains a factor. For the devices with 8 slots and 248 holes the noise is virtually independent of the cooling field B_0 up to a threshold. The best SQUID, one with 8 slots, exhibits no significant increase in $S_\Phi^{1/2}(1\text{ Hz})$ for values of B_0 up to above 100 μT. At 130 μT, the noise has increased slightly, by less than a factor of 2 above the zero field value, suggesting that vortex entry ocurred somewhat below this cooling field. The threshold field appears to be a little above the predicted value of 100 μT. For the second SQUID with 8 slots, there is a small increase in the noise at 80 μT. Again the difference in threshold field between two nominally identical devices suggests a materials variation. For the SQUID with 248 holes, vortex entry ocurrs between 80 and 100 μT. The value of B_T is lower than that of the better of the two devices with slots: this may be a materials issue, but I note that the result is consistent with the fact that the largest linewidth of the YBCO film, at each intersection of two lines, is $4\sqrt{2}\,\mu$m. For the SQUID with slots, on the other hand, there is only a small number of such wider regions.

In short, SQUIDs completely interpenetrated with slots or holes showed no significant increase in the 1/f flux noise when cooled in magnetic fields up to a threshold, consistent with the theory that narrow linewidths exclude vortices. Improvements in edge quality raised the threshold field for flux entry to the value predicted by Equation 11.1 for w=4 μm. The solid square–washer SQUID behaved as one might expect for a washer

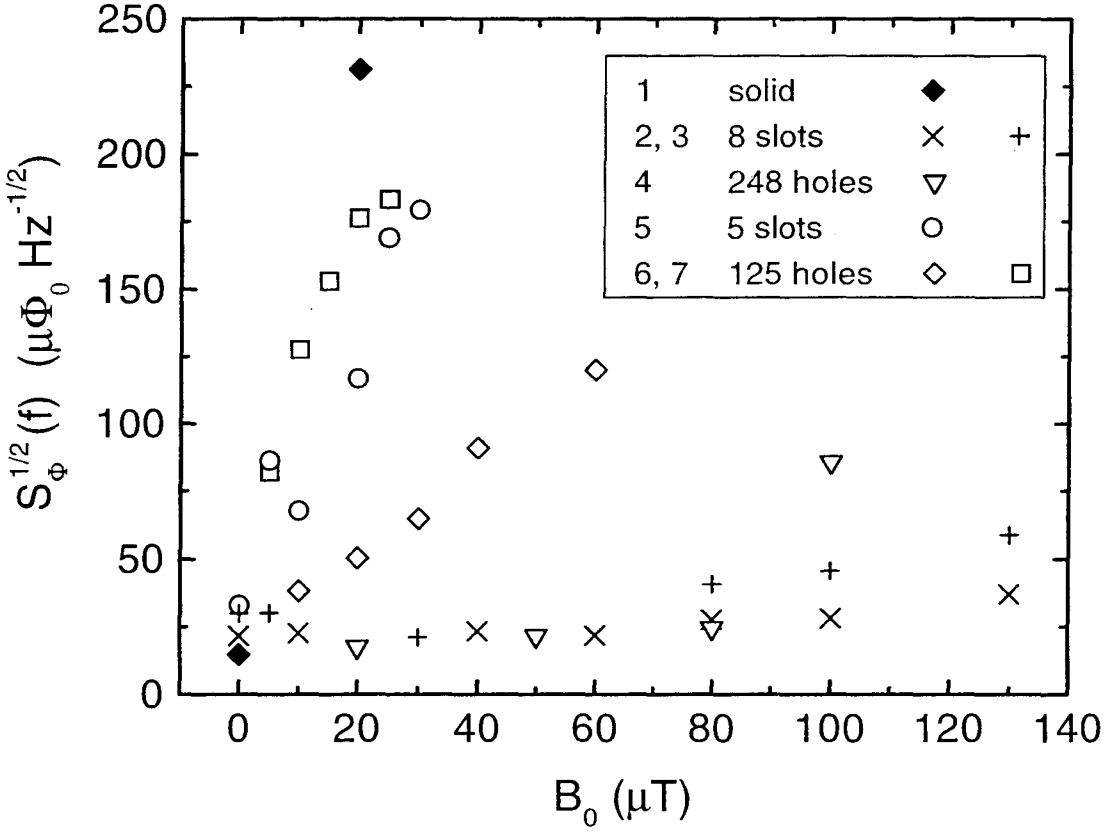

Figure 12.3: Flux noise $S_\Phi^{1/2}$(1 Hz) vs. cooling field B_0 for the seven devices listed in Table 12.1

penetrated by vortices even at relatively low cooling fields, exhibiting a 1/f noise spectrum. The intermediate cases, SQUIDs with 5 slots or 125 holes, had less noise in a given field than the solid SQUID, presumably because there were fewer vortices, but the presence of the vortices in the outer band was sufficient to couple significant amounts of excess 1/f noise into the SQUID.

12.3.2 A_{eff} and Coupling

Another important issue was the question of how well these new SQUIDs couple to the input coil of a flux transformer. In the case of the solid SQUID, the washer acts as a superconducting ground plane for the input coil resulting in high coupling efficiency [14]. What happens if there are holes in the ground plane?

We first measured the effective area A_{eff} of each SQUID by using our solenoid to determine the amount of magnetic field required to produce one flux quantum. The results are summarized in Table 12.1. In all cases the presence of slots or holes *increased* A_{eff} over the value for the solid washer. This result is quite interesting and at first sight rather amazing. Some insight can be gained if one considers the simple scenario of say the SQUID with slots having only the outer and the inner 4 μm–wide loops. Now it is a simple directly coupled magnetometer and we can calculate A_{eff} using Equation 5.1 to yield $5.0 \times 10^{-3}\text{mm}^2$, the same as the value measured for the solid washer SQUID. It is not unreasonable to expect additional loops to add to the effective area. I note, however, that a more precise calculation of both area and inductance, for the SQUIDs with slots and holes, is required to fully understand this increase in area.

Table 12.1 also shows the mutual inductance M_i between three SQUIDs and a 7–turn input coil shown in Figure 12.1(f). The coil was fabricated on a glass substrate from thin films of Cu-Au separated by a layer of SiO and involved two vias and a crossover. The coil was coupled to each SQUID in a flip–chip arrangement with a 3 μm–thick mylar foil separating the two chips. The mutual inductance was measured by passing a small current through the coil. As seen in Table 12.1, the presence of slots or holes reduces M_i only modestly compared with the solid SQUID, by about 16% and 13% respectively. This important result suggests that a flux transformer would couple to a SQUID with slots or holes nearly as efficiently as to a solid SQUID of equal size.

12.4 Implications for Flux Transformers

We now analyze the total noise contribution of a flux transformer with a multiturn input coil coupled to one of these SQUIDs with slots or holes to form a magnetometer. Once again, there are two sources of such noise [51]: "direct noise", in which the motion of vortices in the input coil couples flux noise directly into the SQUID, and "indirect noise", in which vortex motion in both the input coil and the pickup loop generates a noise current in the flux transformer and thus a noise flux in the SQUID. The direct noise can be eliminated by making the linewidth of the input coil sufficiently narrow, say 4 μm or less, thereby excluding vortices from the film. However, it is desirable to increase the width of the pickup loop to 1 mm or more in order to keep its inductance low and thereby increase the sensitivity of the magnetometer. The pickup loop would then be interpenetrated by vortices but we can, once again, show that the contribution of these vortices to the 1/f noise in the SQUID is rather small.

Consider a flux transformer with a pickup loop of width w_p, perimeter ℓ_p and inductance L_p, and an n–turn input coil with inductance L_i inductively coupled to the SQUID inductance L via mutual inductance M_i. We assume $L_p = L_i$ and ideal coupling between the SQUID and the input coil so that $L_i = n^2L$ and $M_i = nL$ [14]. Following the steps in Section 11.6, it is straightforward to show that the spectral density of the flux noise coupled into the SQUID due to flux motion in the pickup loop is

$$S_\Phi(f) \approx S_\Phi^U(f)\left(\frac{\ell_p}{w_p}\right)\left(\frac{1}{16n^2}\right) \tag{12.1}$$

where $S_\Phi^U(f)$ is the spectral density of an unpatterned film. Taking as typical values $S_\Phi^U(1Hz) \lesssim 10^{-9}\Phi_0^2 Hz^{-1}$ [81, 26], $\ell_p = 40mm$, $w_p = 1mm$ and $n = 16$, we find $S_\Phi(1Hz) \lesssim 10^{-11}\Phi_0^2 Hz^{-1}$. This corresponds to a flux noise of about 3 $\mu\Phi_0\,\mathrm{Hz}^{-1/2}$, smaller than the lowest noise we have observed in our washer SQUIDs. We thus conclude that vortices in the flux transformer should not add significantly to the noise of the magnetometer cooled in a static magnetic field.

12.5 Discussion and Future Directions

In this chapter I have shown that holes or slots of appropriate configuration eliminate excess 1/f noise in large–area SQUIDs cooled in an ambient magnetic field. Although

it appears that the quality of the YBCO films, most likely at the edges, still plays a role in determining the properties of these devices, improvements in the edge quality have increased the threshold field for flux entry in all three SQUIDs uniformly penetrated by slots or holes to a value above 50 μT. In two of these devices, the threshold field is consistent with the prediction $B_T = \pi\Phi_0/4w^2$ [97]. The key factor in the design of these SQUIDs is the narrow linewidths of the YBCO films; the size of the slots or holes is unimportant provided the remaining YBCO is sufficiently narrow. The effective area of various devices with slots or holes is always greater than that of the solid device, indicating that they are more efficient in directing flux into the SQUID. It was particularly gratifying to observe that the coupling efficiency of a spiral input coil to the devices with 8 slots and 248 holes was not greatly reduced compared with the solid SQUID.

The results of this chapter imply that it should be possible to operate a sensitive magnetometer, based on a flux transformer with a multiturn input coil tightly coupled to a large–washer SQUID containing slots or holes, in the Earth's magnetic field without a significant increase in the 1/f noise. I showed that vortices in the relatively wide pickup loop should not couple significant amounts of 1/f noise into the SQUID while direct noise contribution of the input coil can be eliminated by making the linewidths sufficiently narrow. The fact that a flux transformer contains multilayers with potentially rough edges may still add some excess 1/f noise to the magnetometer above the level of the SQUID, as it did in Chapter 6, although in that case, the magnetic field sensitivity was still quite adequate for magnetocardiography. Investigation and improvement of edge quality in multilayers may be in order.

To conclude this chapter, our original goal was to develop high-T_c SQUID magnetometers into practical devices. In Parts III and IV, I showed that our devices have sufficient magnetic field resolution for many desired applications in the shielded environment. Now it appears that we can attain the same sensitivity in ambient magnetic fields. Certainly, we have eliminated the adverse influence of unshielded cooling and operation on the *intrinsic* noise properties of the SQUID. Methods to eliminate the influence of *extrinsic* noise sources are addressed next.

Chapter 13

A High-T_C Planar Gradiometer with an Asymmetric Flux Transformer

13.1 Introduction

In the last two chapters I addressed the effects on the *intrinsic* noise properties of a high-T_c SQUID cooled in a *static* magnetic field comparable to the Earth's. However, even with a sensor free of excess intrinsic noise, in many applications one would like to detect weak signals against a background of *external* magnetic noise that is many orders of magnitude higher. In urban environments, the dominant source of noise is the 50 or 60 Hz signals, plus a large number of harmonics, from power lines. Other electrical instruments such as computers, automobiles, and elevators also generate magnetic noise. For this reason, most sensitive magnetic measurements, particularly of biomagnetic signals, are currently made in magnetically shielded rooms (MSRs). However, even the best MSRs [87] do not reduce the 50 or 60 Hz noise sufficiently and they often produce low frequency noise. Therefore one requires a gradiometer to discriminate against the external noise in favor of the signal.

Until recently, the traditional low-T_c gradiometer was wound from niobium wire: two pickup loops wound in opposition and mounted on a common axis with a baseline (separation) typically 0.1 m are connected in series with an input coil, inductively coupled to the SQUID. If the loops are identical and parallel, then the gradiometer is *balanced* and

a uniform magnetic field B_z links zero net flux into the loop. A field gradient dB_z/dz, on the other hand, links a net flux into the loop and generates an output from the SQUID. Typically one of the loops is placed in close proximity to the source while the other serves as a reference to subtract away the noise from remote sources whose signals are uniform over the length of the baseline. Thus the output of the SQUID is ideally that of a magnetometer, placed at the location of the first loop, minus the environmental noise. In order to measure a magnetocardiogram completely unshielded, one is required to balance the gradiometer to about 1 part in 10^6 (i. e. to reject six orders of magnitude of common mode signal.) This is often impossible to achieve with a first-order gradiometer and requires the use of a second– or third–order device. [100].

The lack of suitable wire eliminates the option of a high-T_c wire–wound gradiometer. Two approaches have been adopted so far with high–T_c SQUIDs. One is an electronic gradiometer made by subtracting the signals from two magnetometers [101, 102]. This approach is also used with some low-T_c SQUID systems [88, 89]. Although one can easily select any baseline, the balance of an electronic gradiometer is limited by the linearity of the readout electronics and the common–mode rejection ratio of the subtraction system. Furthermore, in a multichannel system, one must use at least two SQUIDs per gradiometric sensor element. The second approach is to make a planar thin film version of the niobium wire wound gradiometer that measures $\partial B_z/\partial x$; this either involves a gradiometric flux transformer with two pickup loops connected to a multiturn input coil coupled to a SQUID [103] or employs two loops in parallel with a SQUID galvanometer measuring the current induced along the common line [104, 105, 106]. The main disadvantage of these high-T_c devices is a very short baseline, limited by the size of the substrate to typically 5–20 mm, and thus unacceptable for many biomagnetic measurements.

In this chapter, I describe a new type of planar high-T_c gradiometer with a baseline of 48 mm and a balance in the z–direction of about 1 part in 3000, both quite suitable for using this device as a biomagnetic sensor.

13.2 Concept

The asymmetric planar gradiometer is shown schematically in Figure 13.1(a). The gradiometer evolved from a design by Zimmerman [107] for a wire–wound, axial gradiometer coupled to a fractional–turn SQUID machined from niobium. It consists of a directly coupled

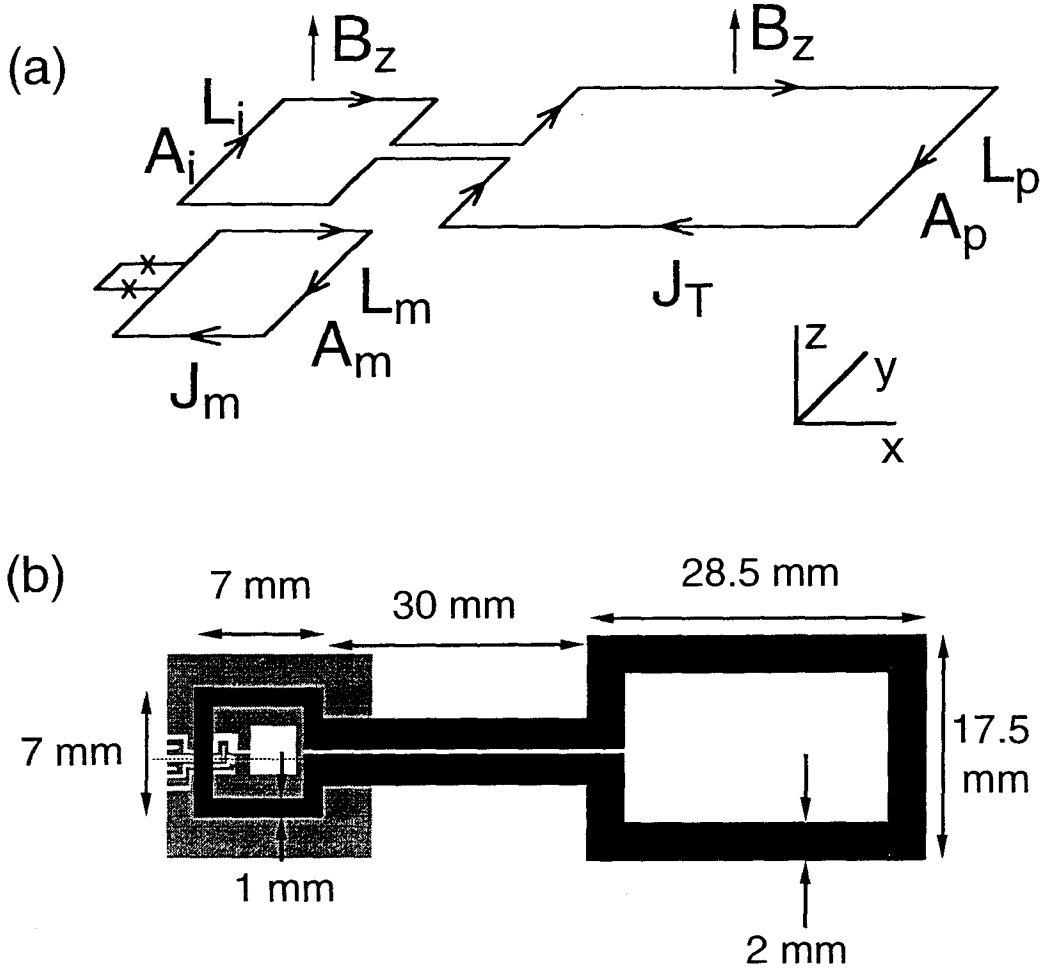

Figure 13.1: Asymmetric planar gradiometer consisting of a flux transformer and a directly coupled magnetometer. (a) Conceptual schematic showing key parameters. Note the coordinate axes. (b) Physical realization showing dimensions. The directly coupled magnetometer is shown in light shading.

magnetometer with a pickup loop of inductance L_m and area A_m, and a superconducting flux transformer with an input loop of inductance L_i and area A_i connected to a pickup loop of inductance L_p and area A_p. The mutual inductance between the input loop and the magnetometer is $M_i = \alpha(L_m L_i)^{1/2}$.

We first find the condition for the gradiometer to be balanced, that is, for the directly coupled magnetometer to produce zero response to a uniform magnetic field B_z (Figure 13.1(a)). Using flux conservation we find

$$B_z A_m - L_m J_m - M_i J_t = 0 \tag{13.1}$$

and

$$B_z(A_p + A_i) - (L_p + L_i)J_t - M_i J_m = 0, \tag{13.2}$$

where J_m and J_t are the screening supercurrents in the magnetometer loop and the transformer, respectively. To achieve the balance condition $J_m = 0$, we solve Equations 13.1 and 13.2 to find

$$\alpha = \frac{A_m}{\sqrt{L_i L_m}} \frac{L_p + L_i}{A_p + A_i}. \tag{13.3}$$

Obviously one must choose the parameters on the right–hand side of this equation so that balance is achieved for $\alpha < 1$.

We now consider the response to a gradient $\partial B_z/\partial x$. We apply a field δB_z to the magnetometer and input loop only, and again using flux conservation find

$$(\delta B_z)A_m - (\delta J_m)L_m - (\delta J_t)M_i = 0 \tag{13.4}$$

and

$$(\delta B_z)A_i - (\delta J_t)(L_p + L_i) - (\delta J_m)M_i = 0. \tag{13.5}$$

By solving Equations 13.4 and 13.5 we obtain the current induced in the magnetometer loop

$$\delta J_m = \delta B_z \frac{A_m}{L_m} \left[\frac{L_p/L_i + 1 - \alpha(A_i/A_m)\sqrt{L_m/L_i}}{L_p/L_i + 1 - \alpha^2} \right] \equiv \delta B_z \frac{A_m}{L_m} \eta \tag{13.6}$$

where the term $\delta B_z A_m/L_m$ is the usual current response of the magnetometer loop to a field δB_z and η represents the screening effect of the flux transformer. As we shall see, with appropriate design, η is only slightly less than unity, so that the sensitivity of the magnetometer itself is not significantly reduced by the presence of the flux transformer.

13.3 Design and Fabrication

Figure 13.1(b) illustrates the asymmetric planar gradiometer, showing the directly coupled SQUID magnetometer and a single–layer flux transformer. In this concept, through appropriate design, one selects suitable inductances and areas for the pickup and input loops of the transformer and for the magnetometer loop, and achieves final balance (Equation 13.3) by sliding the transformer over the magnetometer thereby varying α. The SQUID magnetometer is shown in Figure 5.6 and follows the design specifications outlined in that section. The outer and inner dimensions of the magnetometer loop are 10 mm and 2 mm, respectively, yielding an estimated inductance L_m of 4 nH and an estimated area A_m of 20 mm^2. Due to uncertainties involved with calculating accurate inductances of the transformer loops, it was necessary to carefully select the dimensions of the loops so that the right–hand side of Equation 13.3 is, say, between 0.4 and 0.8, a range of coupling coefficients that can be realistically achieved. After measuring the coupling between the magnetometer and a variety of input coils, we chose to use a square input coil with an outer and inner dimensions of 7 mm and 5 mm, respectively, yielding $L_i \approx 10$ nH and $A_i \approx 36$ mm^2. This somewhat simplifies the balance condition given by Equation 13.3, by introducing additional constraints $L_i \approx 2.5L_m$ and $A_i \approx 1.8A_m$, resulting in

$$\alpha \approx \frac{L_p/(1.6L_m) + 1.6}{A_p/A_m + 1.8}. \tag{13.7}$$

Finally I chose the dimensions of the pickup loop as shown in Figure 13.1(b). I estimate $L_p \approx 50 \pm 5$ nH, which included a 13 nH contribution from the stripline, and $A_p \approx 411$ mm^2. From Equation 13.3, these estimated values lead to $\alpha \approx 0.43 \pm 0.04$, required for balance, and from Equation 13.6 to $\eta \approx 0.95$; thus the presence of the flux transformer reduces the intrinsic sensitivity of the magnetometer by only 5%. The separation between the midpoints of the input and pickup loop, which we take as the baseline of the gradiometer, is approximately 48 mm[1].

The magnetometer was patterned by photolithography and Ar ion milling at normal incidence in a 150 nm–thick film of YBCO on a 10 × 10 mm^2 STO bicrystal. The linewidth of the SQUID loop was 4 μm. The junctions were approximately 1.3 μm wide. The critical current and resistance per junction were 200 μA and 1.2 Ω, respectively, and the transfer coefficient was about 41 μV/Φ_0. The flux transformer was patterned using

[1] A better definition of the baseline is given by measuring a known field gradient.

the Quintel Contact Aligner in a YBCO film co-evaporated on a 100 mm YSZ wafer by Z. Lu, V. Matijasevic and K. Char at Conductus. It was then wet etched in a 0.05% aqueous solution of HNO_3.

13.4 Results

For this experiment we used a probe which allowed us to slide the transformer parallel to the magnetometer using a linear motion mechanism that could be adjusted from outside the cryostat. The magnetometer was spring–loaded against the surface of the transformer. The transformer was held on a kinetic mount made from delrin; it was pushed forward in the x–direction by means of a screw; when the screw was released, it was pulled back by a set of return springs. In this way, we could vary α *in situ* to obtain the balance condition of Equation 13.3; the position of the flux transformer could be adjusted to about 2.5 μm. After some experimentation, I mounted the magnetometer and the flux transformer face–to–face separated by four layers of 50 μm–thick teflon tape. The gradiometer was immersed in liquid nitrogen with the x–axis vertical and the magnetometer at the lower end. There was no magnetic or rf shielding. I flux modulated the SQUID at 100 kHz and operated it in a a flux–locked loop without bias reversal. To assess the balance of the gradiometer I placed it at the center of a 1.2 m–diameter Helmholtz pair, with the axis of the coils perpendicular to the plane of the gradiometer (the z–axis). I injected an alternating current into the coils and averaged the output from the flux–locked loop 200 to 400 times, using a spectrum analyzer.

Figure 13.2 shows a plot of the output of the magnetometer for a 100 Hz magnetic field vs. the position of the flux transformer; at x=0 the position of the input loop of the transformer is entirely outside the central hole of the magnetometer loop, and the coupling between them is small. As I slide the input loop toward the magnetometer loop, the output of the flux–locked loop progressively decreases, dipping sharply near x=4.3 mm, and then increases again. Observations on an oscilloscope show that the phase of the 100 Hz output signal relative to the driving field changed sign across the minimum. The minimum represents the optimum balance point of the gradiometer, and corresponds to a reduction in the response to the uniformly applied magnetic field of approximately 2,930. This value may or may not represent the intrinsic balance limit; it is entirely possible that gradients introduced into the 100 Hz magnetic field by nearby steel objects were the limiting factor.

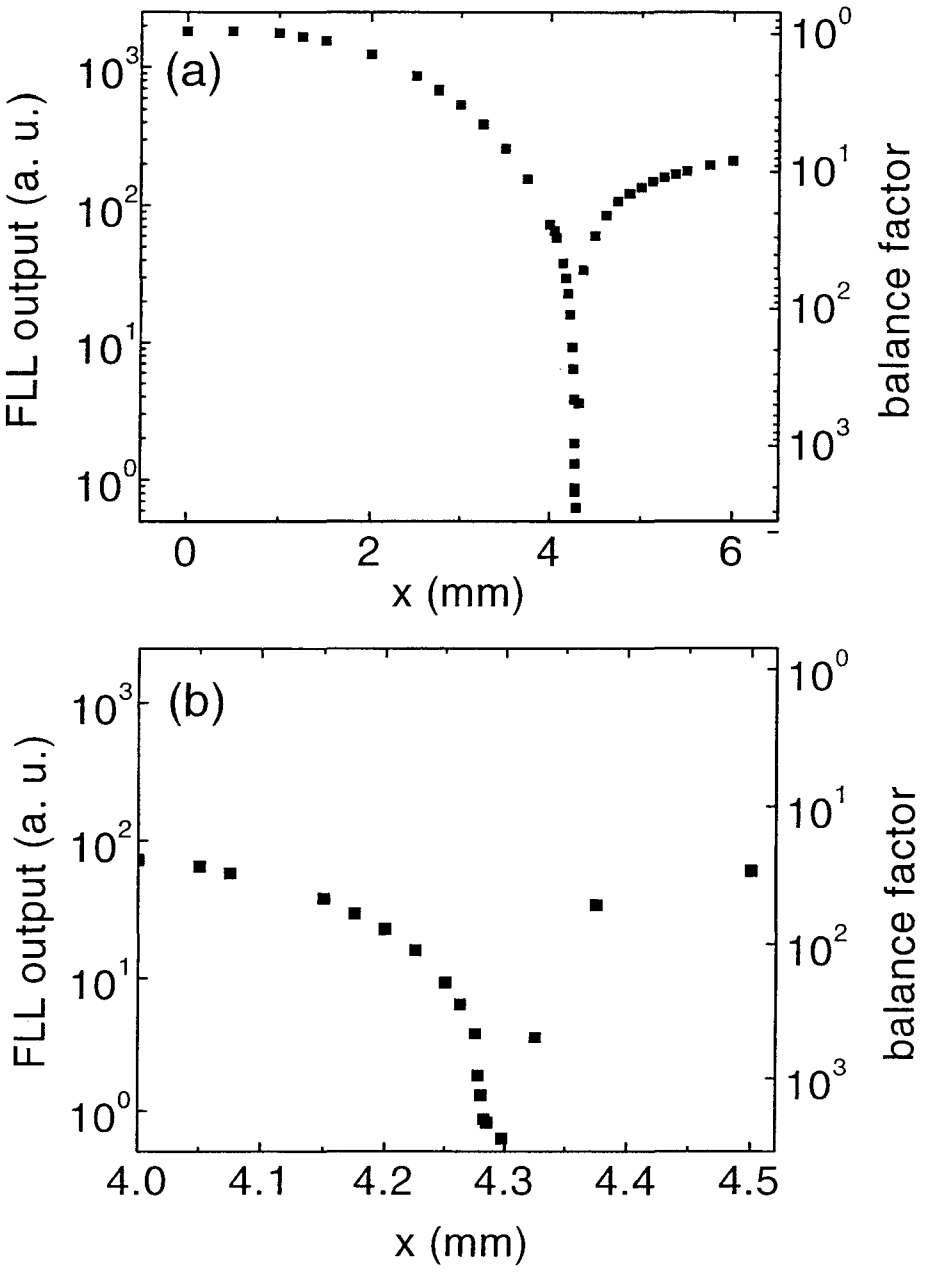

Figure 13.2: (a) Signal from the flux–locked loop (FLL) for a uniform 100 Hz magnetic field applied perpendicular to the plane of the gradiometer vs. position x of the input loop relative to the magnetometer. Right–hand ordinate is balance factor. (b) Expanded view about the position of optimal balance

The latter is consistent with the observation that uniformly applied magnetic fields at higher frequencies (1 kHz and up) were only reduced by a factor of a few hundred and that removal of metal objects from the room resulted in increased field rejection by the gradiometer.

An important criterion for a useful gradiometer is that the response to fields applied in the plane of the gradiometer should be low. To evaluate the response to fields in the y–direction, I applied a 100 Hz current to the Helmholtz coils. With the gradiometer unbalanced, I then rotated the dewar by approximately 90° to locate the precise angle θ_m at which the response to the 100 Hz signal is a minimum – this represented the direction perpendicular to the axis of the coils. I then restored the dewar to its original position, balanced the gradiometer using the uniform 100 Hz field as reference, and rotated it back to θ_m. I repeated this procedure several times and concluded that the signal measured by the *balanced gradiometer* at θ_m was on average 1,400 times less than the signal measured by the *magnetometer* with its plane perpendicular to the axis of the Helmholtz pair. Therefore the rejection in the y–direction was about 1 part in 1,400. Once again, either this residual response was intrinsic to the gradiometer, for example caused by the flux transformer not mounted exactly parallel to the magnetometer, or it was caused by the nonuniformity of the 100 Hz field.

As a demonstration of the reduction in ambient noise, Figure 13.3 shows the output of the magnetometer for the unbalanced (x=0) and the optimally balanced cases, with the signal from the Helmholtz pair switched off. The 60 Hz peak is reduced by a factor of 1,600. It is possible that the residual signal is due to a gradient in the 60 Hz field.

Finally, I measured the response of the balanced gradiometer to a gradient field by passing a 100 Hz current through a long wire in the y–direction placed below the gradiometer and parallel to its plane. The gradient produced by a long wire is given by $(\mu_0 I)/(2\pi r^2)$. I varied the distance of the wire from the midpoint of the baseline from r=0.5 m to r=0.75 m, distances substantially greater than the baseline. The gradiometer response vs. distance is plotted in Figure 13.4. The least–squares fitted slope on this log–log plot is -1.92 $\pm$ 0.04, close to the expected value of -2. Distortions is the applied gradient due to nearby metal objects, and, particularly, a slight residual response to a uniform magnetic field, will cause deviations from the ideal $1/r^2$ behavior.

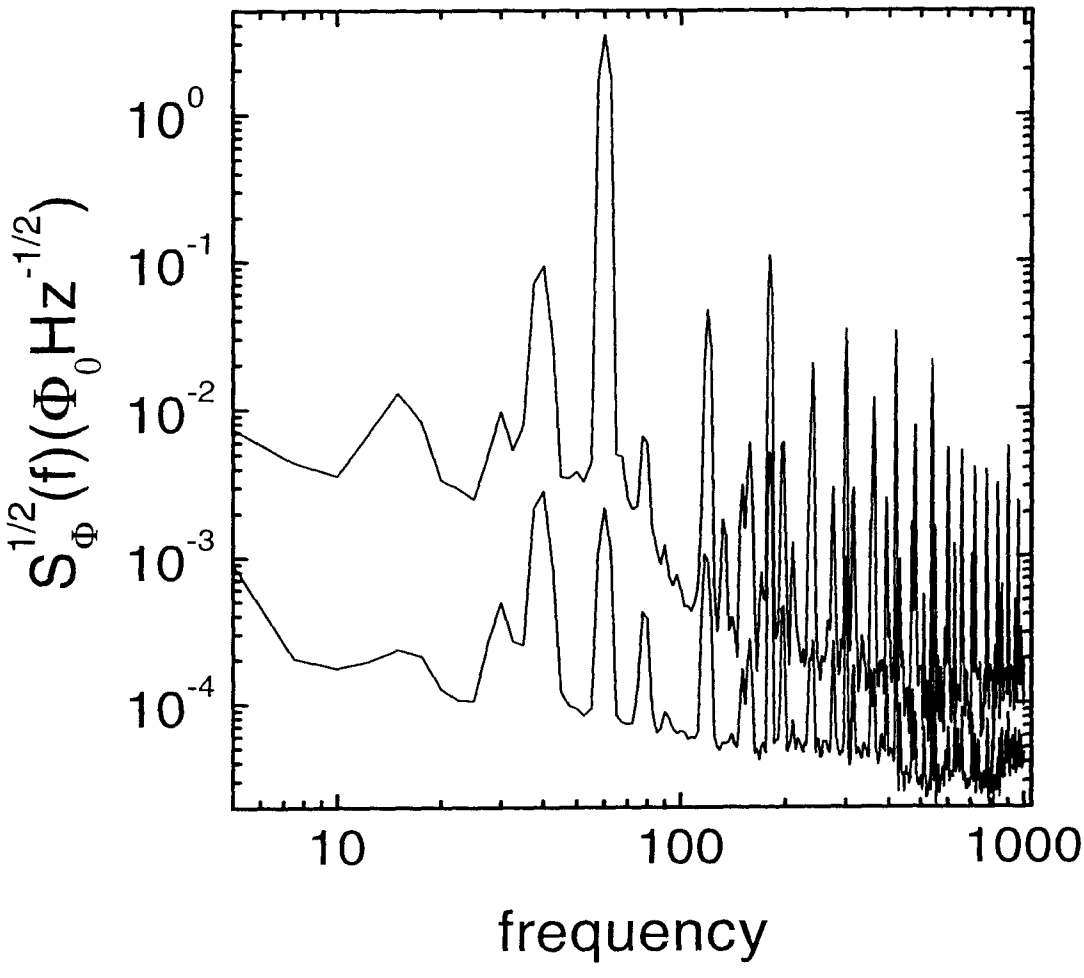

Figure 13.3: Output of the flux–locked loop for unshielded gradiometer unbalanced (upper trace) and at optimal balance (lower trace), showing reduction of the ambient noise.

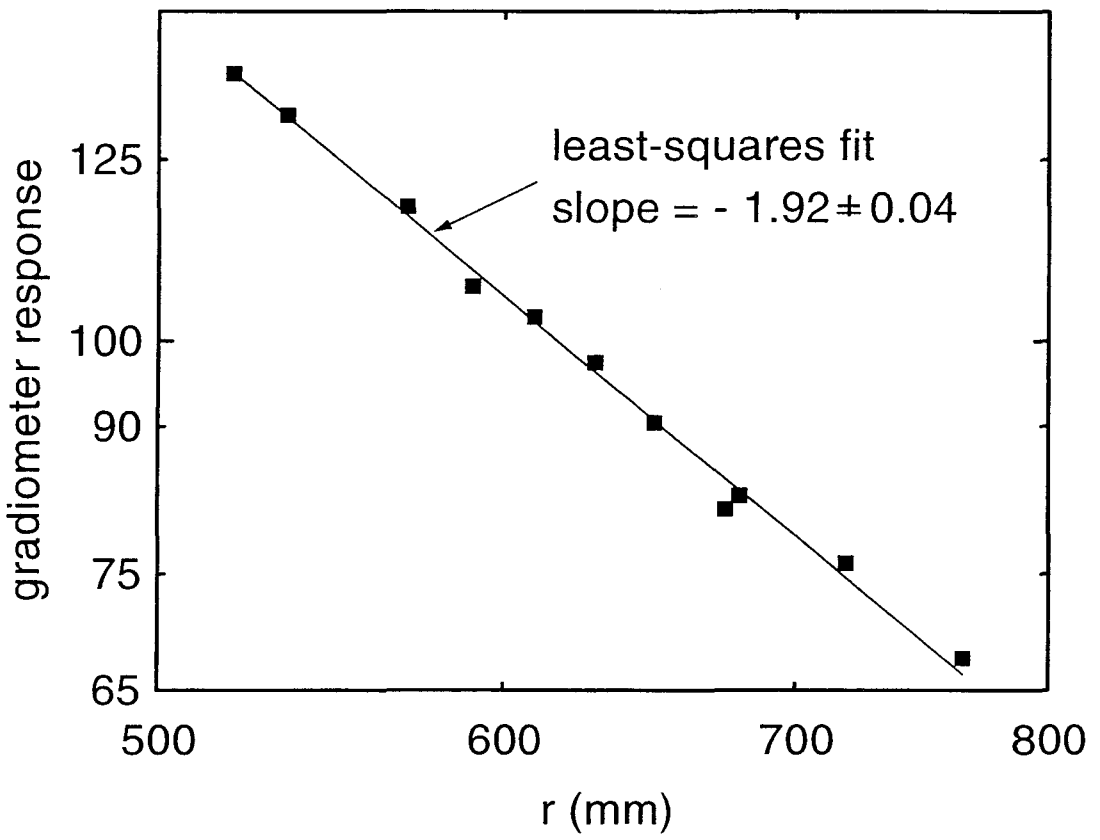

Figure 13.4: Signal from the flux–locked loop for balanced gradiometer vs. the distance r of a wire carrying a 100 Hz current below the centerline of the gradiometer.

13.5 Discussion

This approach to planar gradiometers has several advantages. The flux transformer involves only a single layer of YBCO, and its length could be readily extended to, say, 100 mm thereby increasing its baseline. Furthermore, it should not be necessary to use particularly high–quality films; I showed in Chapter 5 that vortex motion in the pickup loop of a flux transformer with relatively large area and inductance does not contribute significantly to the 1/f noise in the SQUID [50]. Thus, it may be possible to use sintered YBCO films on inexpensive polycrystalline substrates, like the YBCO tube that was used as a magnetic shield in some of the experiments mentioned in Part III [69]. The fact that the intrinsic sensitivity of the magnetometer is only reduced by a few percent by the presence of the flux transformer is particularly appealing. Needless to say, one could use high-T_c SQUID magnetometers that are more sensitive than the directly coupled magnetometer used in this experiment, for example, a magnetometer with a multiturn flux transformer (Chapters 6 and 7) or the multiloop magnetometer (Chapter 8).

This asymmetric first order gradiometer has a baseline of 48 mm and a measured balance of about 1 part in 3000 with respect to magnetic field perpendicular to its plane. Direct measurements and the observed reduction in the 60 Hz noise indicate an in–plane rejection of better than 1 part in 1000. This combination of balance and relatively long baseline, together with the minimal reduction of the sensitivity of the magnetometer, make this gradiometer eminently suitable for multichannel biomagnetic measurements. This device has further advantages of using only one SQUID per *gradiometric* sensor element, carrying over three orders of magnitude of ambient noise rejection. One could subtract signals among the gradiometers of an array to achieve higher order gradients, further reducing ambient noise pick–up. In combination with a magnetometer using a SQUID with slots or holes [63], this approach may well lead to a SQUID system that operates with high field sensitivity, completely unshielded.

Chapter 14

Conclusions and Future Directions

The objective of this work was to develop high-T_c SQUID magnetometers suitable for practical applications. Through improvements in fabrication of YBCO thin films and YBCO–STO–YBCO multilayers, we systematically reduced the low frequency 1/f flux noise that limited the performance of early devices. Thereby, we increased the magnetic field resolution of YBCO magnetometers to levels where clinical quality magnetocardiograms are attainable in a magnetically shielded room. Our best device (currently the best in the world) was a flip–chip magnetometer with a field resolution of 27 fT $Hz^{-1/2}$ at 1 Hz and 8.5 fT $Hz^{-1/2}$ at 1 kHz, representing a reduction of about 5 orders of magnitude in noise power at 1 Hz with respect to YBCO SQUID magnetometers made six years ago. The next challenge was to retain this level of performance in YBCO SQUIDs when they are cooled and operated in ambient magnetic fields. By redesigning the SQUID washer, we were able to eliminate the *intrinsic* excess 1/f flux noise, due to thermally activated hopping of flux vortices, in YBCO SQUIDs when they are cooled in static magnetic fields. New devices whose washers are interpenetrated by an array of empty slots or holes exclude flux vortices in fields of up to 100 μT. We have also introduced a new type of high-T_c gradiometer, based on a SQUID magnetometer coupled to a flux transformer, that combines a balance of about 1 part in 3,000 with a baseline of 48 mm and retains 95% of the field resolution of the bare magnetometer.

The progress made during the last six years represents a transition of high-T_c SQUID magnetometers from demonstrated working devices into the realm of useful ultra–sensitive magnetic field detectors that are beginning to operate in the ambient environment. I believe, however, that there is a number of improvements that must be made before this

technology draws substantial interest from outside of the community that developed it. I shall provide a list of challenges that lie ahead, based on my personal observations and opinions.

(1) *Josephson junction technology*: All of the SQUID magnetometers reported in this thesis were based on bicrystal grain boundary junctions in $SrTiO_3$. The critical currents and resistances of these junctions, however, vary by as much as a factor of two on each chip and by as much as an order of magnitude from chip to chip. I suspect that the variability of junction parameters is partly due to variation in the process used to fuse the bicrystal, partly to microstructural variation along a given grain boundary, and partly to lack of control of oxygen interdiffusion into the completed YBCO junction. Whatever the cause may be, the result is limited yield of high-T_c SQUID magnetometers, which raises their production cost. Although, there is considerable work being done to understand the microstructure and transport in grain boundary junctions, to my knowledge, there is nothing that suggests an improvement over the present lack of control. Other junction technologies, such as step–edge or ramp–edge, may turn out to be more promising but they face a similar lack of reproducibility, particularly in the range of interest for SQUIDs namely, $I_0R \gtrsim 200\,\mu V$ and $R \approx 10\,\Omega$ at T=77 K. The present low yield of SQUIDs with optimal junction parameters might be circumvented by making magnetometers in the flip–chip arrangement, although it would be preferable to increase the yield of junctions to the level of present day Nb–Al_2O_3–Nb junctions, which may involve a new junction technology or simply greater control of one of the existing processes.

(2) *High–T_c multilayers*: The earliest challenge in high-T_c multilayers with respect to SQUID magnetometers was to develop an interconnect technology suitable for flux transformers. The next challenge, largely undertaken in the course of this work, was to reduce the excessive 1/f flux noise in these multilayers. We have demonstrated that we can fabricate low–noise flux transformers; however, the process takes a certain amount of skill and may include some unnecessary steps. It would be desirable to streamline the process in order to move it closer to mass production, necessary for multichannel SQUID systems. In that vein, one would like to work with larger substrates, say 50 to 100 mm–diameter wafers to make large numbers of flux transformers or integrated magnetometers in one run. Only then could one possibly compete with the production costs of low-T_c devices.

(3) *White noise of high-T_c SQUIDs*: An unresolved mystery in high-T_c SQUIDs is that their white noise is as much as an order of magnitude higher than the value predicted by

$16k_BTR$ [11]. Not only is this fact puzzling from a fundamental point of view, it naturally limits the sensitivity of a SQUID or magnetometer in the white noise regime. This is of particular importance now that the 1/f noise in YBCO structures has been suppressed. The answer may be found by examining higher frequency ($\gtrsim$ 1 MHz) dynamics in high-T_c SQUIDs; one can speculate, for example, that the "white noise" that we measure around 1 kHz, is actually the low–frequency plateau of a Lorenzian spectrum generated by one or more random telegraph signals at higher frequencies.

(4) *Flux trapping in YBCO thin film structures*: Even in YBCO SQUIDs and magnetometers nominally free of 1/f noise, one can still trap flux vortices with little effort, in contrast with low-T_c SQUIDs. The weakly pinned vortices move under thermal activation, generating random telegraph signals, raising the flux noise of the SQUID. Normally one can remove these effects by raising the temperature of the SQUID above T_c and gradually lowering it again. For a system with a small number of channels, incorporation of a heater onto each SQUID chip is essential but ultimately may not be sufficient for a truly practical system. It would be highly desirable to eliminate vortex trapping. One can speculate that cleaner edges may be conducive to vortex exclusion, as already demonstrated by Sun *et al.* [98] and by ourselves [63]. Further work, possibly involving high resolution SQUID microscopy [96], may be required to identify vortex trapping sites.

(5) *Low magnetic field noise in ambient environments*: The next exciting step to be taken with the material presented in this thesis is to produce a high-T_c SQUID magnetometer system that is capable of detecting a clinical quality magnetocardiogram completely unshielded. The system that we envision consists of two or three asymmetric gradiometers (Chapter 13), each involving a single layer flux transformer coupled to a sensitive SQUID magnetometer. Each asymmetric gradiometer provides 3 orders of magnitude of ambient uniform field cancellation; the remaining cancellation would be done by electronically subtracting the outputs from two separate gradiometers to form a second derivative or among three gradiometers to form a third derivative. For maximum field sensitivity, each magnetometer would consist of a flux transformer with a multiturn input coil coupled to a square washer SQUID interpenetrated by an array of slots or holes, thereby also eliminating the intrinsic noise due to cooling the device in the Earth's static field (Chapter 12).

Although there are still challenges facing high-T_c SQUID magnetometers, I am inclined to believe (and history has shown) that issues involving materials, design, processing, operating in a field, and developing multichannel systems are wholly solvable through

good engineering. High-T_c SQUID magnetometers in all likelihood will reach the level of performance of their low-T_c counterparts. There is, in my opinion, a greater challenge facing all of these devices. We must refocus our attention on applications. Until now, the most common application of low-T_c SQUID magnetometers has been magnetoencephalography for the purposes of pure research, trying to understand the dynamics of the brain. This was hardly a tool for diagnosis used by the mainstream medical community. The same can be said for cardiography, NDE, and geophysics – there are other techniques used in these applications, and SQUID–based magnetometry, although likely to offer complementary information, will only be accepted when it is conclusively shown to do so. As an example, there is evidence that risk assessment for sudden cardiac death can be done through magnetocardiography [108]. One must, however, assess a large number of patients ($\sim$ 1000) and demonstrate that the technique offers advantages of speed, cost and/or reliability over competing methods before the medical community is likely to accept it. The next stage in the development of SQUID magnetometers (high or low–T_c) will likely involve intimate ties with other industries – biomedical, aeronautical, geophysical. Already high-T_c SQUIDs are marketed by companies including Conductus, Oxford Instruments, NKT, and Sumitomo Electric. The interesting question is: Will SQUID magnetometers remain a tool for pure research or will they enter the mainstream and be used to prospect for minerals, diagnose disease, save lives?

Bibliography

[1] R. C. Jaklevic, J. Lambe, A. H. Silver, and J. E. Mercereau. Quantum interference effects in Josephson tunneling. *Phys. Rev. Lett.*, 12:159, 1964.

[2] G. L. Romani, S. J. Williamson, and L. Kaufmann. Biomagnetic instrumentation. *Rev. Sci. Instrum.*, 53:1815, 1982. for example.

[3] BTi, Inc.,. San Diego, CA.

[4] Neuromag. Helsinki, Finland.

[5] J. G. Bednorz and K. A. Müller. Possible high-T_c superconductivity in the Ba-La-Cu-O system. *Z. Phys. B*, 64:189, 1986.

[6] M. K. Wu, J. R. Ashburn, C. J. Torng, P. H. Hor, R. L. Meng, L. Lao, Z. J. Huang, Y. Q. Wang, and C. W. Chu. Superconductivity at 93 K in a new–mixed–phase Y–Ba–Cu–O compound at ambient pressure. *Phys. Rev. Lett.*, 58:908, 1987.

[7] John Clarke. SQUID fundamentals. In Harold Weinstock, editor, *SQUID Sensors: Fundamentals, Fabrication and Applications*, pages 1–62. Kluwer Academic Press, Dordrecht, 1995.

[8] B. D. Josephson. Possible new effects in superconductive tunneling. *Phys. Lett*, 14:251, 1962.

[9] W. C. Stewart. Current–voltage characteristics of Josephson junctions. *Appl. Phys. Lett.*, 12:277, 1968.

[10] D. E. McCumber. Effect on dc voltage–current characteristics of Josephson junctions. *J. Appl. Phys.*, 39:3113, 1968.

[11] Claudia D. Tesche and John Clarke. dc SQUID: noise and optimization. *J. Low Temp. Phys.*, 37:397, 1979.

[12] R. H. Koch, John Clarke, W. M. Goubau, J. M. Martinis, C. M. Pegrum, and D. J. Van Harlingen. Flicker (1/f) noise in tunnel junction dc SQUIDs. *J. Low Temp. Physics*, 51:207, 1983.

[13] J. M. Jaycox and M. B. Ketchen. Planar coupling scheme for ultra low noise dc SQUIDs. *IEEE Trans. Mag.*, MAG-17:400, 1981.

[14] M. B. Ketchen and J. M. Jaycox. Ultra–low noise tunnel junction dc SQUID with tightly coupled planar input coil. *Appl. Phys. Lett.*, 40:736, 1982.

[15] V. Ambegaokar and B. I. Halperin. Voltage due to thermal noise in the dc Josephson effect. *Phys. Rev. Lett.*, 22:1364, 1969.

[16] John Clarke and Roger H. Koch. The impact on high–temperature superconductivity on SQUIDs. *Science*, 242:217, 1988.

[17] D. Koelle, A. H. Miklich, F. Ludwig, E. Dantsker, D. T. Nemeth, and John Clarke. dc SQUID magnetometers from single layers of $YBa_2Cu_3O_{7-x}$. *Appl. Phys. Lett.*, 63:2271, 1993.

[18] K. Enpuku, Y. Shimomura, and T. Kisu. Effect of thermal noise on the characteristics of a high-T_c superconducting quantum interference device. *J. Appl. Phys.*, 73:7929, 1993.

[19] Reinhold Kleiner. unpublished.

[20] R. H. Koch, C. P. Umbach, G. J. Clark, P. Chaudhari, and R. B. Laibowitz. Quantum interference devices made from superconducting oxide thin films. *Appl. Phys. Lett.*, 51:200, 1987.

[21] A. I. Braginski. Fabrication of high–temperature SQUID magnetometers. In Harold Weinstock, editor, *SQUID Sensors: Fundamentals, Fabrications and Applications*, pages 235–288. Kluwer Academic Press, Dordrecht, 1995.

[22] H. Kinder, P. Berberich, W. Prusseit, R. Semerad, and B. Utz. Very large area double sided evaporation of high quality YBCO films. In *Proceedings of ISTEC–MRS*, page 182, 1995.

[23] J. J. Kingston. *The Fabrication and Performance of* $YBa_2Cu_3O_{7-x}$ *SQUID Magnetometers.* PhD thesis, University of California at Berkeley, 1992.

[24] Amobeads AB3×2×3W. Mitsui and Co., San Francisco, CA, USA.

[25] F. C. Wellstood, J. J. Kingston, and John Clarke. Thin–film multilayer interconnect technology for $YBa_2Cu_3O_{7-x}$. *J. Appl. Phys.*, 75:683, 1994.

[26] M. J. Ferrari, Mark Johnson, F. C. Wellstood, J. J. Kingston, T. J. Shaw, and John Clarke. Magnetic flux noise in copper oxide superconductors. *J. Low. Temp. Phys.*, 94:15, 1994.

[27] F. Ludwig, E. Dantsker, D. T. Nemeth, D. Koelle, A. H. Miklich, John Clarke, S. Knappe, H. Koch, and R. Thomson. Fabrication issues in optimizing $YBa_2Cu_3O_{7-x}$ flux transformers for low 1/f noise. *Supercond. Sci. Technol.*, 7:273, 1994.

[28] K. Char, M. S. Colclough, S. M. Garrison, N. Newman, and G. Zacharchuk. Bi–epitaxial grain boundary junctions in $YBa_2Cu_3O_{7-x}$. *Appl. Phys. Lett.*, 59:733, 1991.

[29] D. Dimos, P. Chaudhari, J. Manhart, and F. K. LeGoues. Orientation dependence of grain–boundaries in $YBa_2Cu_3O_{7-x}$bicrystals. *Phys. Rev. Lett.*, 61:219, 1988.

[30] D. Dimos, P. Chaudhari, and J. Manhart. Superconducting transport propeties of grain boundaries in $YBa_2Cu_3O_{7-x}$bicrystals. *Phys. Rev. B*, 41:4038, 1990.

[31] A. H. Miklich. *Low-Frequency Noise in High-*T_c *Superconductor Josephson Junctions, SQUIDs and Magnetometers.* PhD thesis, University of California at Berkeley, 1994.

[32] A. H. Miklich, D. Koelle, E. Dantsker, D. T. Nemeth, J. J. Kingston, R. F. Kromann, and John Clarke. Bicrystal YBCO dc SQUIDs with low noise. *IEEE Trans. Appl. Supercond.*, 3:2434, 1993.

[33] M. S. DiIorio, S. Yoshizumi, K. Y. Yang, J. Zhang, and M. Maung. Practical high T_c Josephson junctions and dc SQUIDs operating above 85 K. *Appl. Phys. Lett.*, 58:2552, 1991.

[34] R. W. Simon, J. F. Burch, K. P. Daly, W. D. Dozier, R. Hu, A. E. Lee, J. A. Luine, H. M. Manasevit, C. E. Platt, S. M. Schwarzbeck, D. St. John, M. S. Wire, and M. J. Zani. Progress towards a YBCO circuit process. In R. D. McConnell and R. Noufi, editors, *Science and Technology of Thin Film Superconductors 2*, page 549, New York, 1990. Plenum Press.

[35] K. Char, M. S. Colclough, T. H. Geballe, and K. E. Myers. High-T_c superconductor–normal–superconductor Josephson junctions using $CaRuO_3$ as the metallic barrier. *Appl. Phys. Lett.*, 62:196, 1993.

[36] Q. X. Jia, X. D. Wu, D. Reagor, S. R. Foltyn, C. Mombourquette, and D. E. Peterson. Edge–geometry SNS dc SQUIDs using Ag–doped $YBa_2Cu_3O_{7-x}$ electrodes. *Electronics Lett.*, 32:499, 1996.

[37] Y. Zhang, U. Krüger, R. Kutzner, R. Wördenweber, J. Schubert, W. Zander, E. Sodtke, A. I Braginski, and M. Strupp. Single layer YBCO rf SQUID magnetometers with direct–coupled pickup coils and flip–chip flux transformers. *Appl. Phys. Lett.*, 65:3380, 1994.

[38] D. Reimer, M. Schilling, S. Knappe, and D. Drung. Integrated $YBa_2Cu_3O_{7-x}$ multi–loop magnetometers at 77 K. *IEEE Trans. Appl. Supercond.*, 5:2342, 1995.

[39] R. Scharnweber and M. Schilling. Integrated $YBa_2Cu_3O_{7-x}$ magnetometer with flux transformer and multiloop pick–up coil. *Appl. Phys. Lett.*, 69:1303, 1996.

[40] A. H. Miklich, J. J. Kingston, F. C. Wellstood, John Clarke, M. S. Colclough, K. Char, and G. Zaharchuk. Sensitive $YBa_2Cu_3O_{7-x}$ thin–film magnetometer. *Appl. Phys. Lett.*, 59:988, 91.

[41] R. F. Kromann, J. J. Kingston, A. H. Miklich, L. T. Sagdal, and John Clarke. Integrated $YBa_2Cu_3O_{7-x}$ SQUID magnetometers with only two superconducting layers. *Appl. Phys. Lett.*, 63:559, 1993.

[42] J. J. Kingston, F. C. Wellstood, P. Lerch, A. H. Miklich, and John Clarke. Multilayer $YBa_2Cu_3O_{7-x} - SrTiO_3 - YBa_2Cu_3O_{7-x}$ films for insulating crossovers. *Appl. Phys. Lett.*, 56:189, 1990.

[43] D. Grundler, R. Eckart, B. David, and O. Dössel. Highly sensitive YBCO dc SQUID magnetometer with thin film flux transformer. *Appl. Phys. Lett.*, 63:2700, 1993.

[44] N. Missert, T. E. Harvey, R. H. Ono, and C. D. Reintsema. High-T_c multilayer step–edge Josephson junctions and SQUIDs. *Appl. Phys. Lett.*, page 1690, 1993.

[45] F. Ludwig, D. Koelle, E. Dantsker, D. T. Nemeth, A. H. Miklich, John Clarke, and R. E. Thomson. Low noise $YBa_2Cu_3O_{7-x} - SrTiO_3 - YBa_2Cu_3O_{7-x}$ multilayers for improved superconducting magnetometers. *Appl. Phys. Lett.*, 66:373, 1995.

[46] Y. Q. Shen, Z. J. Sun, R. Kromann, T. Holst, P. Vase, and T. Freloft. Integrated high-T_c superconducting magnetometer with multiturn input coil and grain boundary junctions. *Appl. Phys. Lett.*, 67:2081, 1995.

[47] Y. Zhang, M. Mück, K. Hermann, J. Schubert, W. Zander, A. I. Braginski, and C. Heiden. Sensitive rf SQUIDs and magnetometers operating at 77 K. *IEEE Trans. Appl. Supercond.*, 3:2465, 1993.

[48] Mark B. Ketchen, W. J. Gallagher, A. W. Kleinsasser, S. Murphy, and John R. Clem. dc SQUID flux focuser. In H. D. Hahlbohm and H. Lübbig, editors, *SQUID '85 – Superconducting Quantum Interference Devices and Their Applications*, pages 865–871. Walter de Gruyter, Berlin, 1985.

[49] M. Matsuda, Y. Murayama, N. Kasai S. Kiryu, S. Kashiwaya, M. Koyanagi, and T. Endo. Directly–coupled SQUID magnetometers made of Bi–Sr–Ca–Cu oxide films. *IEEE Trans. Magn.*, 27:3043, 1991.

[50] D. Koelle, A. H. Miklich, E. Dantsker, F. Ludwig, D. T. Nemeth, John Clarke, W. Ruby, and K. Char. High-pertformance dc SQUID magnetometers with single layer $YBa_2Cu_3O_{7-x}$ flux transformers. *Appl. Phys. Lett.*, 63:3630, 1993.

[51] M. J. Ferrari, J. J. Kingston, F. C. Wellstood, and John Clarke. Flux noise from superconducting $YBa_2Cu_3O_{7-x}$ flux transformers. *Appl. Phys. Lett.*, 58:1106, 1991.

[52] L. P. Lee, J. Longo, V. Vinetskiy, and R. Cantor. Low–noise $YBa_2Cu_3O_{7-x}$ direct–current superconducting quantum interference device magnetometer with direct signal injection. *Appl. Phys. Lett.*, 66:1539, 1995.

[53] R. Cantor, L. P. Lee, M. Teepe, V. Vinetskiy, and J. Longo. Low–noise single–layer $YBa_2Cu_3O_{7-x}$ dc SQUID magnetometers at 77 K. *IEEE Trans. Appl. Supercond.*, 5:2927, 1995.

[54] L. P. Lee, M. Teepe, V. Vinetskiy, R. Cantor, and M. S. Colclough. Key elements for a sensitive 77 K direct current superconducting quantum interference device magnetometer. *Appl. Phys. Lett.*, 66:3058, 1995.

[55] F. Ludwig, E. Dantsker, D. Koelle, R. Kleiner, A. H. Miklich, and J. Clarke. Multilayer magnetometers based on high-T_c SQUIDs. *Appl. Superconductivity*, 3:383, 1995.

[56] Dietmar Drung. private communication.

[57] E. Dantsker, F. Ludwig, R. Kleiner, John Clarke, M. Teepe, L. P. Lee, Neil Alford, and Tim Button. Addendum:"Low noise $YBa_2Cu_3O_{7-x} - SrTiO_3 - YBa_2Cu_3O_{7-x}$ multilayers for improved superconducting magnetometers". *Appl. Phys. Lett.*, 67:725, 1995.

[58] L. P. Lee, K. Char, and G. Zaharchuk M. S. Colclough. Monolithic 77K dc SQUID magnetometer. *Appl. Phys. Lett.*, 59:3051, 1991.

[59] J. W. M. Hilgenkamp, G. C. S. Brons, J. G. Soldevilla, R. P. Isselsteijn, J. Floksrta, and H. Rogalla. Four layer monolithic integrated high-T_c SQUID magnetometer. *Appl. Phys. Lett.*, 64:3497, 1994.

[60] M. S. DiIorio, K.-Y. Yang, and S. Yoshizumi. Biomagnetic measurements using low–noise integrated SQUID magnetometers operating in liquid nitrogen. *Appl. Phys. Lett.*, 67:1926, 1995.

[61] Frederic C. Wellstood, C. Heiden, and John Clarke. Integrated SQUID magnetometer with high slew rate. *Rev. Sci. Instrum.*, 55:953, 1984.

[62] V. Foglietti, W. J. Gallagher, M. B. Ketchen, A. W. Kleinsasser, R. H. Koch, and R. L. Sandstrom. Performance of dc SQUIDs with resistively shunted inductance. *Appl. Phys. Lett.*, 55:1451, 1989.

[63] E. Dantsker, S. Tanaka, and John Clarke. SQUIDs with slots and holes: Low 1/f noise in ambient magnetic fields. *Appl. Phys. Lett.*, 70:2037, 1997.

[64] D. Drung, F. Ludwig, W. Müller, U. Steinhoff, L. Trahms, H. Koch, Y. Q. Shen, M. B. Jensen, P. Vase, T. Holst, T. Freltov, and G. Curio. Integrated $YBa_2Cu_3O_{7-x}$ magnetometer for biomagnetic measurements. *Appl. Phys. Lett.*, 68:1421, 1996.

[65] J. E. Zimmerman. Sensitivity enhancement of superconducting quantum interference devices through the use of fractional-turn loops. *J. Appl. Phys.*, 42:4483, 1971.

[66] D. Drung, R. Cantor, M. Peters, H. J. Scheer, and H. Koch. Low-noise high-speed dc superconducting quantum interference device magnetometer with simplified feedback electronics. *Appl. Phys. Lett.*, 57:406, 1990.

[67] D. Drung, S. Knappe, and H. Koch. Theory for the multiloop dc superconducting quantum interference device and experimental verification. *J. Appl. Phys.*, 77:4088, 1995.

[68] F. Ludwig, E. Dantsker, R. Kleiner, D. Koelle, John Clarke, S. Knappe, D. Drung, H. Koch, Neil McN. Alford, and Tim Button. Integrated high-T_c multiloop magnetometer. *Appl. Phys. Lett.*, 66:1418, 1995.

[69] T. W. Button, N. McN. Alford, F. Wellhoffer, T. C. Shields, J. S. Abell, and M. Day. The processing and properties of high-T_c thick films. *IEEE Trans. Mag.*, 27:1434, 1991.

[70] D. Drung, E. Dantsker, F. Ludwig, H. Koch, R. Kleiner, John Clarke, S. Krey, D. Reimer, B. David, and O. Doessel. Low noise $YBa_2Cu_3O_{7-x}$ SQUID magnetometers operated with additional positive feedback. *Appl. Phys. Lett.*, 68:1856, 1996.

[71] R. C. Black, A. Mathai, F. C. Wellstood, E. Dantsker, A. H. Miklich, D. T. Nemeth, J. J. Kingston, and J. Clarke. Magnetic microscopy using a liquid nitrogen cooled $YBa_2Cu_3O_{7-x}$ superconducting quantum interference device. *Appl. Phys. Lett.*, 63:2128, 1993.

[72] R. C. Black, F. C. Wellstood, E. Dantsker, A. H. Miklich, J. J. Kingston, D. T. Nemeth, and J. Clarke. Eddy current microscopy using a 77–K superconducting sensor. *Appl. Phys. Lett.*, 64:100, 1994.

[73] R. C. Black. *Magnetic Microscopy Using a Superconducting Quantum Interference Device.* PhD thesis, University of Maryland, 1995.

[74] Thomas S. Lee, Eugene Dantsker, and John Clarke. High–transistion temperature superconducting quantum interference device microscope. *Rev. Sci. Instrum.*, 67:4208, 1996.

[75] T. D. Gamble, W. M. Goubau, and J. Clarke. Magnetotellurics with remote magnetic reference. *Geophysics*, 44:53, 1979.

[76] J. Clarke, T. D. Gamble, W. M. Goubau, K. H. Koch, and R. F. Miracky. Remote–reference magnetotellurics: equipment and procedures. *Geophysical Prospecting*, 31:149, 1983.

[77] ElectroMagnetic Instruments, Inc. Richmond, CA.

[78] H. Kado. Applied Superconductivity Conference, Boston, MA, October 1994. unpublished.

[79] E. Dantsker, D. Koelle, A. H. Miklich, D. T. Nemeth, F. Ludwig, J. Clarke, J. T. Longo, and V. Vinetskiy. High-T_c three–axis dc SQUID magnetometer for geophysical applications. *Rev. Sci. Instrum.*, 65:3809, 1994.

[80] Taylor–Wharton Cryogenics, Inc.

[81] A. H. Miklich, D. Koelle, T. J. Shaw, F. Ludwig, D. T. Nemeth, E. Dantsker, J. Clarke, Neil McN. Alford, Tim Button, and M. S. Colclough. Excess low frequency excess noise in $YBa_2Cu_3O_{7-x}$ dc superconducting quantum interference devices cooled in static magnetic fields. *Appl. Phys. Lett.*, 64:3494, 1994.

[82] E. Dantsker, S. Tanaka, P.-Å. Nilsson, R. Kleiner, and John Clarke. Reduction of 1/f noise in high-T_c dc superconducting quantum interference devices cooled in an ambient magnetic field. *Appl. Phys. Lett.*, 69:4099, 1996.

[83] CTF Systems, Inc.,. Port Coquitlam, B.C., Canada.

[84] D. S. Barth, W. Sutherling, J. Engel Jr., and J. Beatty. Neuromagnetic evidence of spatially distributed sources underlying epileptiform spikes in the human brain. *Science*, 223:293, 1984.

[85] L. Trahms, M. Burghoff, K. Brockmeier, and L. Schmitz. Vortex current detected by the magnetocadiogram. In *Proceedings of Biomag 96*, Santa Fe, NM, February 1996.

[86] Y. Zhang, Y. Tavrin, H.-J. Krause, H. Bousack, A. I. Braginski, U. Kalberkamp, U. Matzander, M. Burghoff, and L. Trahms. Applications of high temperature SQUIDs. *Appl. Superconductivity*, 3:367, 1995.

[87] S. N. Erné, H. D. Hahlbohm, H. Scheer, and Z. Trontetelj. The Berlin magnetically shielded room. In S. N. Erné, H. D. Hahlbohm, and H. Lübbig, editors, *Biomagnetism*, pages 79–87. de Gruyter, Berlin, 1981.

[88] D. Drung, R. Zimmermann, R. Cantor, S. N. Erné, and H. Koch. A 37 channel dc SQUID magnetometer system. *Clin. Phys. Physiol. Meas.*, 12:21, 1991.

[89] Dietmar Drung. The PTB 83–SQUID system for biomagnetic applications in a clinic. *IEEE Trans. Appl. Supercond.*, 5:2112, 1994.

[90] Dietmar Drung. Advanced SQUID read–out electronics. In Harold Weinstock, editor, *SQUID Sensors: Fundamentals, Fabrications and Applications*, pages 63–116. Kluwer Academic Press, Dordrecht, 1995.

[91] W. N. Podney. Electromagnetic microscope for deep, pulsed, eddy current evaluation of airframes. unpublished.

[92] E. Dantsker, S. Tanaka, P. Å. Nilsson, R. Kleiner, and John Clarke. Low excess flux noise in $YBa_2Cu_3O_{7-x} - SrTiO_3 - YBa_2Cu_3O_{7-x}$ dc SQUIDs cooled in static magnetic fields. *IEEE Trans. Appl. Supercond.*, 1997.

[93] V. N. Glyantsev, Y. Tavrin, W. Zander, J. Schubert, and M. Siegel. The stability of dc and rf SQUIDs in static ambient fields. *Supercond. Sci. Technol.*, 9:A105, 1996.

[94] J. M. Schmidt, L. P. Lee, A. Matlashov, M. Teepe, V. Vinetskiy, R. Cantor, and M. S. DiIorio. Low-noise, single layer YBCO dc SQUID magnetometers for shielded and unshielded operation. In *Proceedings of Biomag 96*, Santa Fe, NM, February 1996.

[95] M. I. Faley, U. Poppe, K. Urbana, H. Hilgenkamp, H. Hennes, W. Aawink, J. Flokstra, and H. Rogalla. Noise properties of direct current SQUIDs with quasiplanar YBCO josephson junctions. *Appl. Phys. Lett.*, 67:2087, 1995.

[96] J. R. Kirtley, M. B. Ketchen, K. G. Stawiasz, J. Z. Sun, W. J. Gallagher, S. H. Blanton, and S. J. Wind. High–resolution scanning SQUID microscope. *Appl. Phys. Lett.*, 66:1138, 1995.

[97] J. R. Clem. Vortex expulsion from a superconducting strip in perpendicular applied magnetic fields. unpublished.

[98] J. Z. Sun, W. J. Gallagher, and R. H. Koch. Initial–vortex–entry–related hysteresis in thin–film SQUID magnetometers. *Phys. Rev. B*, 50:13664, 1994.

[99] A. H. Miklich, D. Koelle, F. Ludwig, D. T. Nemeth, E. Dantsker, and John Clarke. Picovoltmeter based on a high transition temperature SQUID. *Appl. Phys. Lett.*, 66:230, 1995.

[100] J. Vrba, V. Angus, K. Betts, M. B. Burbank, T. Cheung, A. A. Fife, G. Haid, P. R. Kubik, S. Lee, J. McCubbin, J. McRay, D. McKenzie, S. E. Robinson, M. Smith, P. Spear, B. Taylor, M. Tillotson, D. Cheyne, and H. Weinberg. 143 channel whole-cortex meg system. In *Proceedings of Biomag 96*, Santa Fe, NM, February 1996.

[101] Y. Tavrin, Y. Zhang, M. Mück, A. I. Braginski, and C. Heiden. YBCO thin film SQUID gradiometer for biomagnetic measurements. *Appl. Phys. Lett.*, 62:1824, 1993.

[102] R. H. Koch, J. R. Rozen, J. Z. Sun, and W. J. Gallagher. Three SQUID gradiometer. *Appl. Phys. Lett.*, 63:403, 1993.

[103] W. Eidelloth, B. Oh, R. P. Robertazzi, W. J. Gallagher, and R. H. Koch. YBCO thin-film gradiometers: Fabrication and performance. *Appl. Phys. Lett.*, 59:3473, 1991.

[104] Mark B. Ketchen, Wolfgang M. Goubau, John Clarke, and Gordon B. Donaldson. Superconducting thin-film gradiometer. *J. Appl. Phys.*, 49:4111, 1978.

[105] V. Zakosarenko, F. Schmidl, H. Schneidewind, L. Dorrer, and P. Seidel. Thin-film dc SQUID gradiometer using a single YBCO layer. *Appl. Phys. Lett.*, 65:779, 1994.

[106] V. Schultze, R. Stolz, R. Ijsselsteijn, V. Zakosarenko, L. Fritzsch, F. Thrum, E. Il Integrated SQUID gradiometers for measurement in disturbed environments. *IEEE Trans. Appl. Supercond.* to be published.

[107] James E. Zimmerman. SQUID instruments and shielding for low–level magnetic measurements. *J. Appl. Phys.*, 48:702, 1977.

[108] A. Link, L. Trahms, R. Zimmerman, and M. Oeff. Complex binomial bandpass filters for analysing phase and envelope of high frequency components in cardiac signals. In *Computers in Cardiology*, page 617. IEEE Computer Society Press, California, 1994.